Studies on Some Novel Methods of Synthesis and Sintering of Nanocrystalline Ceramics

By

SANJAY KUMAR. D

(Enrolment No: CHEM 02 2011 04 001)

Indira Gandhi Centre for Atomic Research, Kalpakkam

A Thesis Submitted to the
Board of Studies in Chemical Sciences
In partial fulfillment of requirements
For the Degree of

DOCTOR OF PHILOSOPHY
of
HOMI BHABHA NATIONAL INSTITUTE

July, 2017

Studies on Some Novel Methods of Synthesis and Sintering of Nanocrystalline Ceramics

By

SANJAY KUMAR. D

(Enrolment No: CHEM 02 2011 04 001)

Indira Gandhi Centre for Atomic Research, Kalpakkam

A Thesis Submitted to the
Board of Studies in Chemical Sciences
In partial fulfillment of requirements
For the Degree of

DOCTOR OF PHILOSOPHY
of
HOMI BHABHA NATIONAL INSTITUTE

July, 2017

Homi Bhabha National Institute

Recommendations of the Viva Voce Committee

As members of the Viva Voce Committee, we certify that we have read the dissertation prepared by **Mr. Sanjay Kumar. D** entitled "**Studies on Some Novel Methods of Synthesis and Sintering of Nanocrystalline Ceramics**" and recommend that it may be accepted as fulfilling the thesis requirement for the award of Degree of Doctor of Philosophy.

Chairman – **Dr. S. Anthonysamy** **Date:**

Guide / Convener – **Dr. K. Ananthasivan** **Date:**

Member 1 – **Dr. N. V. Chandra Shekar** **Date:**

Member 2 – **Dr. V. Jayaraman** **Date:**

Final approval and acceptance of this thesis is contingent upon the candidate's submission of the final copies of thesis to HBNI.

I hereby certify that I have read this thesis prepared under my direction and recommend that it may be accepted as fulfilling the thesis requirement.

Date:

Place: IGCAR, Kalpakkam

Dr. K. Ananthasivan
Guide

STATEMENT BY AUTHOR

This dissertation has been submitted in partial fulfillment of requirements for an advanced degree at Homi Bhabha National Institute (HBNI) and is deposited in the Library to be made available to borrowers under rules of the HBNI.

Brief quotations from this dissertation are allowable without special permission, provided that accurate acknowledgement of source is made. Requests for permission for extended quotation from or reproduction of this manuscript in whole or in part may be granted by the Competent Authority of HBNI when in his or her judgment the proposed use of the material is in the interest of scholarship. In all other instances, however, permission must be obtained from the author.

Sanjay Kumar. D

DECLARATION

I, hereby declare that the investigation presented in the thesis has been carried out by me. The work is original and has not been submitted earlier as a whole or in part for a degree/diploma at this or any other Institution / University.

Sanjay Kumar. D

List of Publications

Journal

a. <u>Published</u>

1. Bulk synthesis of nanocrystalline urania powders by citrate gel-combustion method

D. Sanjay Kumar, K. Ananthasivan, R. Venkata Krishnan, S. Amirthapandian, Arup Dasgupta, J. Nucl. Mater. 468 (2016) 178-193.

2. Studies on the synthesis of nanocrystalline Y_2O_3 and ThO_2 through volume combustion and their sintering

D. Sanjay Kumar, K. Ananthasivan, R. Venkata Krishnan, S. Amirthapandian, Arup Dasgupta, J. Nucl. Mater. 479 (2016) 585-592.

3. A novel gel combustion procedure for the preparation of foam and porous pellets of UO_2

D. Sanjay Kumar, K. Ananthasivan, R. Venkata Krishnan, Arup Dasgupta, J. Nucl. Mater. 483 (2017) 199-204.

4. Synthesis of monoclinic and cubic (metastable) nanocrystalline HfO_2 through the nitrate fusion technique

D. Sanjay Kumar, K. Ananthasivan, R. Venkata Krishnan, S. Amirthapandian, T. R. Ravindran, S. Balakrishnan, Ceram. Int. 43 (2017) 12623-12632.

5. Citrate gel-combustion synthesis and sintering of nanocrystalline ThO_2 powders

D. Sanjay Kumar, K. Ananthasivan, S. Amirthapandian, Arup Dasgupta, G. Jogeswara Rao, J. Nucl. Mater. 497 (2017) 16-29.

6. Reaction mechanism and kinetic analysis of citrate gel-combustion synthesis of nanocrystalline urania

D. Sanjay Kumar, K. Ananthasivan, R. Venkata Krishnan, Abhiram Senapathi, J. Therm. Anal. Calorim. 2017 (DOI: 10.1007/s10973-017-6695-4).

b. **Manuscript under revision**

1. Nitrate fusion synthesis and two-step sintering of nanocrystalline yttria stabilized hafnia powders

D. Sanjay Kumar, K. Ananthasivan, Abhiram Senapathi, S. Amirthapandian, Arup Dasgupta, Ceram. Int. **2018 (accepted)**.

2. Low Temperature Two-Step Sintering of nanocrystalline UO_2

D. Sanjay Kumar, K. Ananthasivan, Arup Dasgupta, J. Nucl. Mater. **2018.**

c. **Other publications (not included as a part of the thesis)**

1. Gel-Combustion Synthesis of Nanocrystalline Cerium Oxide and Its Powder Characteristics

S. Balakrishnan**, D. Sanjay Kumar,** K. Ananthasivan**,** T. Indian I. Metals **2015**, 68 S243-S252.

2. High pressure Raman spectroscopic studies on nanocrystalline ThO_2,

K. Kamali, K. Ananthasivan, T. R. Ravindran, **D. Sanjay Kumar**, J. Nucl. Mater. 493 (2017) 77-83.

3. High pressure studies on Thorium-Praseodymium mixed oxides,

K. A. Irshad, **D. Sanjay Kumar, G. Paneerselvam,** K. Ananthasivan, N. V. Chandra Shekar, S. Kalavathi, J. Nucl. Mater. 498 (2018) 221-226.

Papers / Posters presented in National / International Conferences

1. TEM study of nanocrystalline UO_2 prepared by gel-combustion method,

D. Sanjay Kumar, K. Ananthasivan, S. Balakrishnan, Amrita Pandian, Arup Dasgupta, K. Nagarajan, International Conference on Electron Microscopy and XXXIV Annual Meeting of the Electron Microscope Society of India (EMSI-2013), SINP, Kolkata, India, July 2013.

2. Citrate gel-combustion synthesis of nanocrystalline cerium oxide

   S. Balakrishnan, **D. Sanjay Kumar**, K. Ananthasivan, International Symposium for Research Scholars on Metallurgy, Materials Science and Engineering (ISRS 2014), IIT-M, Chennai, India, December 2014.

3. Carbon coated urania foam (CCUF)

   D. Sanjay Kumar, K. Ananthasivan, Arup Dasgupta, International Conference on Electron Microscopy and XXXVI Annual Meeting of the Electron Microscope Society of India (EMSI-2015), BARC, Mumbai, India, July 2015.

4. Stabilization of the cubic structure in nanocrystalline (nc) HfO_2

   D. Sanjay Kumar, K. Ananthasivan, S. Amirthapandian, International Conference on Electron Microscopy and XXXVI Annual Meeting of the Electron Microscope Society of India (EMSI-2015), BARC, Mumbai, India, July 2015.

5. Low Temperature Two-Steps Sintering (LTTSS) - An Innovative Method for Consolidating Porous UO_2 Pellets

   D. Sanjay Kumar, K. Ananthasivan, Abhiram Senapati, R. Venkata Krishnan, Chemistry in nuclear technology (CHEMNUT-2015), IGCAR, Kalpakkam, India, July 2015.

6. Microstructural investigations of nanocrystalline yttria stabilized hafnia prepared by nitrate fusion technique

   D. Sanjay Kumar, K. Ananthasivan, S. Amirthapandian, Arup Dasgupta, International Conference on Electron Microscopy and XXXVII Annual Meeting of the Electron Microscope Society of India (EMSI-2016), IIT-BHU, Varanasi, India, June 2016.

7. TEM investigation of nanocrystalline ThO_2 prepared by citrate gel-combustion

   D. Sanjay Kumar, K.Ananthasivan, S. Amirthapandian, Arup Dasgupta, International Conference on Electron Microscopy and XXXVII Annual Meeting of the Electron Microscope Society of India (EMSI-2016), IIT-BHU, Varanasi, India, June 2016.

Sanjay Kumar. D

Dedicated

To

Mother Nature

ACKNOWLEDGEMENTS

I would like to thank the people who were directly involved in the process of making this thesis a reality.

I am profoundly indebted to my Supervisor, Dr. K. Ananthasivan, for believing in me, for guiding me during the PhD and for the opportunities that I received from him, for his teaching, advice and constant support during the course of my PhD work. I owe my deepest gratefulness and respect to him.

I would like to thank the members of my doctoral committee, Dr. K. V. G. Kutty, Dr. A. Bharathi, Dr. V. Jayaraman, Dr. N. V. Chandra Shekar and Dr. S. Anthonysamy for their valuable suggestions, tough questions and encouragement which helped me gain deeper insights and intensify my quest to explore the research in different perspective

I would like to thank Homi Bhabha National Institute (HBNI) and Department of Atomic Energy (DAE) for funding my research work. I would like to thank former Director of the Indira Gandhi Centre for Atomic Research (IGCAR) Shri. S. C. Chetal, for offering me the opportunity to carry out my research work at Materials Chemistry & Metal Fuel Cycle Group (MC&MFCG), IGCAR. I am deeply grateful to the subsequent Directors, Dr. P. R. Vasudeva Rao and Dr. Satya Murthy and also to the current Director, Dr. A. K. Bhaduri for allowing me to carry forward my research work in this esteemed institute (IGCAR).

I extend my sincere gratitude to the Directors of the MC&MFCG, IGCAR, Dr. K. Nagarajan (former) and Dr. U Kamachi Mudali (former) and Dr. M. Joseph (present) for allowing me to carry out majority of the experimental work in this renowned institute.

I would like to further thank all my colleagues from the Advanced Fuel Studies Section, Materials Processing Chemistry Section and Analytical Chemistry & Spectroscopy Section for their willingness to share their knowledge and helping me to carry out experiments. Special thanks to Dr. V. Chandramouli for allowing me to carry out sintering experiments with the Molybdenum heating element furnace and for helping me in the measurements on the sintered densities, Dr. R. Sudha for helping me in the SEM investigation, Dr. S. Balakrishnan and Ms. N. Ambika for TG-DTA-MS analysis, Mr. R. Raja Madhavan for helping me with the X-ray diffraction analysis and allowing me to use M/s. Carbolite furnace, Mr. Abhiram Senapathi for DSC analysis, Mr. G. Jogeswara Rao for Particle size distribution analysis and Ms. Annie David for helping me with carbon analysis. I would also like to thank Dr. R. Kumar, Dr. Suddhasattwa Ghosh and Dr. R. Kumaresan for their valuable inputs and comments.

I express my sincere thanks to Dr. Arup Dasgupta and Dr. S. Amirthapandian for helping me in Scanning Electron Microscopy (SEM) and Transmission Electron Microscopy (TEM) respectively at UGC-DAE-CSR, Kalpakkam node. I thank Dr. T. R. Ravindran for helping me with the Raman analysis. I owe my sincere gratitude to Dr. Kitheri Joseph and Dr. R. Venkata Krishnan for their valuable suggestions in the kinetic studies. I extend my sincere thanks to Dr. Srinivasa Rao Bakshi for allowing me to carryout Spark Plasma Sintering (SPS) experiments at IIT-M.

Special thanks to Ms. S. Prema for the valuable comments, suggestions, good company and encouraging me at all times. I have to express my thankfulness as well to my friends Dr. C. Joel, Mr. Bharath Ramalingam, Dr. K. Benadict Rakesh, Dr. D. Karthikeyan, Mr. Samba Siva Rao Kamba, Ms. Gayathri, Ms. P. K. Shruthi, Mr. Thangam, Mr. Balakrishnan, Mr. K. G. Raghavendra, Mr. M. Siva Kumar and Mr. V. Yuvaraj who had accompanied me during these years of good and stressed moments.

Infinite thanks to my wonderful family; Father Mr. N. Devendhar Singh, Mother, Ms. R. Manju Devi, Brother Mr. D. Sujeeth Kumar and Sister Ms. Neethu Devi and Ms. Khusbhu for all that I learned and received from them during all along my life.

[Sanjay Kumar. D]

CONTENTS

Chapter 2: Experimental 31

Chapter 8: Conclusions 233

Synopsis

Nuclear energy plays an important role in meeting the energy demand of the world without the release of CO/CO_2 to the environment[1]. In the Indian context, the increase in energy demand vis-a-vis the non-availability of sufficient alternate conventional sources of energy have necessitated the nuclear energy to play a key role in meeting the energy demand[2]. International nuclear communities have taken initiatives to resolve the problems related to the efficient utilization of fuels, the management and minimization of radiotoxic waste, economics, recycling, non-proliferation and transmutation of minor actinides (Am, Np and Cm). Oxide fuels with enhanced performance characteristics are being developed to be deployed in the Generation IV reactors[3]. They are pertinent in the Indian context as well. The class of advanced materials developed for such applications are broadly known as "nuclear materials". In this work, an effort has been made to synthesize and characterize some "advanced nuclear materials" pertinent to fission reactors. Recent research on nano nuclear materials reveals that nanocrystalline (nc) fission reactor fuels exhibit superior properties (both physical and chemical) as compared to their microcrystalline counterparts[45]. Hence, R&D on these materials are useful and relevant to nuclear technology.

Nc-Y_2O_3, nc-HfO_2 and nc-yttria stabilized hafnia (YSH) are used extensively in high temperature applications. HfO_2 and YSH (both pure and doped with aliovalent cations) find application in the nuclear industry owing to their low thermal expansion coefficient, structural stability and chemical inertness even at high temperature[6]. Since, Y_2O_3, HfO_2 and YSH are thermodynamically compatible with molten uranium at temperatures above 1400 K; crucibles made out of HfO_2 and YSH would be useful for applications involving containment of molten U.

Current challenges in the preparation of nano nuclear materials include scaling-up the preparation of nc powders (about 100g), optimizing their consolidation parameters and choice of an advanced sintering method. In view of the above two novel techniques, viz., citrate gel-combustion (nc-urania, nc-thoria and nc-yttria) and salt melt synthesis (nc-HfO_2 and nc-YSH) have been investigated in this study for synthesizing nc nuclear materials in bulk. The systematic dependence of the reaction as well as the properties of these (nc-urania and nc-thoria) powders on the composition of the combustion mixture [R = fuel to nitrate (mole ratio)] was investigated. It was demonstrated for the first time that "volume combustion reaction (VCR)" takes place in citrate gels containing thorium nitrate, yttrium nitrate and uranyl nitrate with citric acid at an R value of 0.125, 0.17 and 0.25 respectively. Reaction mechanism pertaining to citrate gel-combustion and salt melt synthesis (SMS) was also investigated. It was demonstrated for the first time that nc-HfO_2 powders (30 g) i.e. either the thermodynamically stable monoclinic phase or the metastable cubic phase could be synthesized by tailoring the nitrite to nitrate mole ratio (Φ) in eutectic mixtures containing the nitrates of potassium and sodium along with $NaNO_2$. Similarly, bulk quantities of monodisperse nc-YSH (30 g) powders were also prepared for the first time by using SMS at a temperature as low as 673 K. The powder properties, compaction pressure and mode of sintering of nanocrystalline materials play an important role in the fabrication of dense monoliths. Hence, all these powders were characterized by different techniques. Further, it is difficult to sinter nc materials to dense monoliths with uniform microstructure and submicron grains due to significant grain coarsening. Hence, these powders were sintered by different methods viz., conventional sintering (CS), two-step sintering (TSS) and Spark Plasma Sintering (SPS). The utility of two-step sintering proposed by Chu et al.[7] (TSS_C) and Chen and Wang[8] (TSS_{CW}) was also investigated. Both the synthesis and sintering procedures were optimized to obtain dense small sintered crucibles made out of nc-HfO_2 and nc-YSH. Further, the utility of these small crucibles for holding molten U (compatibility test) was also investigated. An attempt has been made to prepare fine grained sintered bodies from nc-Y_2O_3, nc-HfO_2 and nc-YSH powders by using SPS as well.

Direct oxide reduction (DOR)[9] of metal oxide to metal is an attractive alternative compared to the conventional pyrometallurgical process for the production of uranium. In the DOR process, open porosity plays a key role in the complete reduction of uranium, necessitating a porous sintered body an important prerequisite. In this context, a novel gel based procedure was devised for the first time to obtain a dense UO_2 foam and porous UO_2 pellets. The procedure was optimized by controlling various parameters viz., fuel (sucrose / citric acid) to nitrate content, carbon residue, compaction pressure and mode of sintering.

Chapter 1 – Introduction

Chapter 1 presents a brief introduction highlighting the importance of nuclear energy and India's three stage nuclear power programme. The importance of high burn-up structure observed in the irradiated fuel has also been brought out. Nano nuclear materials, their preparation, properties and their potential applications in the nuclear power industry are also discussed. Different conventional and advanced methods used in their consolidation and sintering are discussed in detail. Advanced sintering techniques which are used to densify nanocrystalline powders without grain coarsening are discussed.

Chapter 2 – Experimental

Chapter 2 describes the details pertaining to the starting materials, experimental procedure and details of instrumental analyses. This chapter explains in detail about the different synthetic procedures adopted for the scaled-up synthesis of nc urania, ThO_2, Y_2O_3, HfO_2 and YSH powders. Chapter 2 also explains a novel gel-combustion procedure used in the preparation of foam and porous pellets of UO_2. Methods of characterization of powders, green pellets, sintered pellets, foam and porous pellets are described in this chapter. Methods used in the microstructural investigation of these powders [scanning electron microscopy (SEM) and transmission electron microscopy (TEM) coupled with electron energy loss spectroscopy (EELS)] are presented in detail. Thermal methods of analysis used to elucidate the plausible mechanism of the gel-combustion reaction and SMS by using differential scanning calorimetry (DSC), simultaneous thermogravimetry and differential thermal analysis coupled with mass spectrometry (TG-DTA-MS) are also described in detail. The green pellets made out of the powders derived in this study were sintered by using three different methods viz., CS and TSS (TSS_C and TSS_{CW}). This chapter also describes the details pertaining to the SPS investigations on Y_2O_3, HfO_2 and YSH powders. Experiments carried out to find out the critical compaction pressure have also been described. Details of the experiments performed to ascertain the compatibility of sintered HfO_2 and YSH cups with molten U have also been detailed in this chapter. The procedure used in the preparation of samples for microstructural investigations have also been described.

Chapter 3 – Synthesis, Characterization and Sintering of Nanocrystalline Urania

Chapter 3 deals with the bulk synthesis (60 g) of nanocrystalline (nc) free flowing urania powders with crystallite size ranging from 38-252 nm for the first time. A systematic study of the influence of the fuel (citric acid) to nitrate ratio (R) on the characteristics of the powders has also been carried out. Mixtures with an “R” value 0.25 exhibited a vigorous auto-ignition reaction (VCR). This reaction was investigated with DSC and in-situ TG-DTA-MS. SEM investigation of some of these powders revealed the presence of agglomerates with irregular exfoliated morphology, while analysis of their TEM images confirmed nanocrystallinity. EELS of some calcined (α-U_3O_8) and hydrogen reduced (UO_2) powders, testified the covalent nature of the U-O bond. The reaction mechanism and kinetic parameters pertaining to citrate gel-combustion synthesis of nc-urania were determined. All powders were consolidated at different compaction pressures and were sintered (CS and TSS). The extent of sintering in all sintered products was determined by measuring their sintered density, porosity and shrinkage characteristics. A maximum sintered density of 98.0 ± 0.4 % theoretical density (T.D) was obtained in this study. Selected samples of sintered specimens were characterized by using XRD and SEM to determine the constituent phases and the influence of the powder characteristics on their microstructure sizes of pores and grains and the final sintered density. The sintered pellets comprised sintered grains with grain size ranging from 1 – 15 μm.

Chapter 4 – Preparation of UO_2 foam and porous pellets of UO_2

Chapter 4 reports the first time preparation of UO_2 foam (sucrose gel-combustion) and porous pellets of UO_2 (citrate gel-combustion). The final products possessed a high matrix density and interconnected porosity. The utility of TSS (1073 K, 30 min and 1473 K, 4 h) for obtaining these porous bodies was also demonstrated for the first time. The foams and pellets possessed meso and macro pores. Sucrose to nitrate mole ratio of 2.4 was best suited for obtaining urania foam with good handling strength. The porous pellets were found to be more suitable for the end application for they had lesser carbon residue and a higher overall density. A citric acid to nitrate mole ratio of 0.25 and a compaction pressure of 180 MPa were found to be optimal for obtaining a pellet with 40 % porosity.

Chapter 5 – Synthesis, Characterization and Sintering of Nanocrystalline Thoria

Chapter 5 deals with the bulk synthesis (60 g) of nc free flowing ThO_2 powders. These investigations helped to establish the influence of R on the characteristics of the final product. It was also demonstrated that VCR occurs at a fuel (citric acid) to oxidant (nitrate) ratio close to that demanded by the stoichiometry (0.125) in mixtures containing Th^{4+}. The extent of sintering in all sintered products (R = 0 to 0.50) was determined by measuring their sintered density, porosity and shrinkage characteristics. In this study, it was observed that TSS led to the formation of highly sintered products compared to CS. ThO_2 with a maximum sintered density of

98.8 ± 0.3 % T.D could be obtained by using TSS. The sintered density of ThO_2 reported in this study is the highest among the values reported so far, for the pellets made from nc-ThO_2 derived through citrate gel-combustion. The sintered pellets comprised faceted sintered grains with a uniform size distribution with grain size ranging between 6 – 15 μm. It was also demonstrated that the two-step heating restricts "runaway" sintering and yields products with controlled microstructure.

Chapter 6 – Synthesis, Conventional Sintering and SPS of Nanocrystalline Yttria

Chapter 6 describes the experiments on the VCR in the citrate gels containing the $Y(NO_3)_3$. It was also demonstrated that volume combustion occurs at a fuel (citric acid) to oxidant (nitrate) ratio close to that demanded by the stoichiometry in mixtures containing Y^{3+}. These powders were pelletized at various compaction pressures ranging from 60-353 MPa. Green pellets were subjected to both CS as well as TSS. It was demonstrated that sintered Y_2O_3 pellets with a density as high as 98.9 ± 0.1 % T. D. could be produced by using the TSS method at a final temperature as low as 1673 K (grain size < 3 μm). The sintered density of Y_2O_3 reported in this study is the highest among the values reported so far, for the pellets made from nc-Y_2O_3 derived through citrate gel-combustion method. Selected samples of powders and monoliths were also characterized by using SEM investigation. The sintered pellets comprised faceted sintered grains with a uniform size distribution. It was also demonstrated that the two-step heating yields products with controlled microstructure. SPS of these samples had also been carried out. A maximum sintered density of 99.3 ± 0.2 % T.D was obtained by using SPS with grain size ranging from 6 – 12 μm. However, further optimization of experimental parameters is required in order to obtain nanograined Y_2O_3 pellets by using SPS.

Chapter 7 – Synthesis, Characterization and Sintering of Nanocrystalline HfO_2 and YSH powders by SMS

Chapter 7 demonstrates for the first time that nc-HfO_2 powders (30 g) i.e. either the thermodynamically stable monoclinic phase or the metastable cubic phase could be synthesized by tailoring the nitrite to nitrate mole ratio (Φ) in eutectic mixtures containing the nitrates of potassium and sodium along with $NaNO_2$. In addition, nc-YSH powders (30 g) were synthesized for the first time through salt melt synthesis. TEM reaffirmed the values of crystallite size estimated through XRD investigations as well as the constituent phases. Raman spectroscopy also confirmed the phases present. It was demonstrated that the SMS could be used as a simple method for producing bulk quantities of these nc powders. All "as prepared" powders were compacted at different pressures (60 to 353 MPa) and were sintered by using three different sintering methods viz., CS, TSS and SPS. The sintered products were characterized for their phase (XRD) and microstructure by using SEM. Elemental mapping confirmed the homogeneous distribution of yttrium in YSH. Maximum sintered densities of (TSS) 97.2 ± 0.4 % T.D and 98.2 ± 0.3 % T.D were obtained for HfO_2 and YSH powders respectively. SPS technique was used for the preparation of sintered pellets and the characteristics of the sintered products were compared with that of the products obtained by CS. SEM investigation revealed that the grain size varies from 1 - 3 μm (HfO_2 derived by using TSS) and 5 - 12 μm (YSH derived by using TSS). By using SPS, a maximum sintered density of 98.8 ± 0.1 % T.D and 97.3 ± 0.6 % T.D. were obtained for HfO_2 and YSH powders respectively. SEM investigation revealed that the grain sizes were varying from 5 - 25 μm (both HfO_2 and YSH derived by using SPS). Selected powders of HfO_2 and YSH were used in the fabrication of cups and the compatibility of these cups with molten U at 1410 K was tested. These investigations revealed that these could be used for U metal melting since the cups were compatible with molten U at 1410 K. These results are consolidated and are discussed in detail in this chapter.

Chapter 8 – Summary and conclusions

The highlights of this dissertation and conclusions of the studies carried out in understanding the bulk scale synthesis and sintering of nanocrystalline ceramic powders are summarized in chapter 8. The key findings of the thesis are highlighted as follows:

1. nc-ceramic powders of about 60 g (UO_2, ThO_2, Y_2O_3) and 30 g (HfO_2 and YSH) were successfully prepared by using both (aqueous) citrate gel-combustion method and (non-aqueous) salt melt synthesis;
2. The systematic dependence of the reaction as well as the properties of these (nc-urania and nc-thoria) powders on the composition of the combustion mixture (R) was investigated;
3. Variation in lattice strain in the nc-powders derived through citrate gel-combustion and their correlation with the X-ray crystallite size is being reported for the first time;

4. It was demonstrated for the first time that volume combustion reaction (VCR) takes place in citrate gels containing thorium nitrate, yttrium nitrate and uranyl nitrate with citric acid at an R value of 0.125, 0.17 and 0.25 respectively;
5. Porous UO_2 (both foam and sintered pellets) were prepared by using gel-combustion (sucrose and citric acid gels) method;
6. Salt melt synthesis (SMS) and a modified SMS were formulated to synthesize nanocrystalline m-HfO_2, c-HfO_2 and YSH powders in bulk, with near uni-modal size distribution of grains;
7. For the first time TEM and EELS investigations were carried out on the products obtained through volume combustion reaction (nc-UO_2, nc-ThO_2 and nc-Y_2O_3) and SMS [nc-HfO_2 (both the monoclinic and cubic phases) and nc-YSH];
8. The utility of TSS in obtaining a final product with high density and uniform microstructure was investigated
9. For the first time shrinkage anisotropic factor (α) was estimated to understand the importance of obtaining dense monoliths with uniform shrinkage and
10. SPS of nc-Y_2O_3 (VCR), nc-HfO_2 (SMS) and nc-YSH (SMS) was carried out for the first time to prepare dense monoliths (99 % T.D).

---

[1] M. M. Abu-Khader, Prog. Nucl. Energ. 51 (2009) 225.

[2] K. Saidi, M. B. Mbarek, Prog. Nucl. Energ. 88 (2016) 364.

[3] G. Locattelli, M. Mancini, N. Todeschini, Energy Policy, 61 (2013) 1503.

[4] S. Dey, J. W. Drazin, Y. Wang, J. A. Valdez, T. G. Holesinger, B. P. Uberuaga, R. H. R. Castro, Sci. Rep. 5 (2015) 7746.

[5] J. Spino, H. S. Cruz, R. J. Abril, R. Birtcher, C. Ferrero, J. Nucl. Mater. 422 (2012) 27.

[6] J. Tang, F. Zhang, P. Zoogman, J. Fabbri, S. W. Chan, Y. Zhu, L. E. Brus and M. L. Steigerwald, Adv. Funct. Mater. 15 (2005) 1595.

7 M.-Y. Chu, L.C. De Jonghe, M.K.F. Lin, F.J.T. Lin, J. Am. Ceram. Soc. 74(11) (1991) 2902-2911.

8 I.W. Chen, X.H. Wang, Nature 404(6774) (2000) 168-171.

9 G. Z. Chen, D. J. Fray, T. W. Farthing, Nature, 407 (2000) 361.

List of Abbreviations

a	Acoustic mode
"A"	As prepared powders
ADS	Accelerator Driven System
AFCI	Advanced Fuel Cycle Initiative
AHWR	Advanced Heavy Water Reactor
ADU	Ammonium diuranate
AISI	American Iron and Steel Institute
AR	Analytical reagent
ASTM	American Society for Testing and Materials
AUC	Ammonium uranyl carbonate
BARC	Bhabha Atomic Research Centre
c	Cubic
"C"	Calcined powders
CCD	Charge Coupled Device
CGC	Citrate gel-combustion
Comm	Commercial powder
CP	Compaction pressure
CS	Conventional Sintering
CVD	Chemical Vapor Deposition
D	Direct denitration
DBP	DiButyl Phthalate
DC	Direct current
DOR	Direct Oxide Reduction
DSC	Differential Scanning Calorimetry
DTA	Differential Thermal Analysis
DTG	Derivative thermo-gravimetric
DTGS	Deuterated Triglycine Sulfate
EDS	Energy dispersive X-ray spectroscopy
EELS	Electron Energy Loss Spectroscopy
EGA	Evolved gas analysis
FAS	Ferrous ammonium sulphate
FBR	Fast Breeder Reactor
FBTR	Fast Breeder Test Reactor

FE-SEM	Field Emission Scanning Electron Microscope
FFT	Fast Fourier Transform
GIF	Generation IV International Forum
GIXRD	Grazing Incidence X-ray Diffraction
GWd/tHM	Giga Watt days days/metric ton of heavy metal
HBS	High Burn-up structure
HBRP	High Burn-up Rim Project
HCHCr	High Carbon - High Chromium
HEBM	High energy ball milling
HP	Hot Pressing
HRTEM	High Resolution Transmission Electron Microscopy
HW	Hall-Williamson method
IAEA	International Atomic Energy Agency
ICP-MS	Inductively Coupled Plasma – Mass Spectrometer
IFFT	Inverse Fast Fourier Transform
IGCAR	Indira Gandhi Centre for Atomic Research
IMF	Inert Matrix Fuel
INPRO	International Project on Innovative Nuclear Reactors and Fuel Cycles
IP	Isostatic Pressing
IR	Infrared mode
IREL	Indian Rare Earths Limited
JCPDS	Joint Committee on Powder Diffraction Standards
KAS	Kissinger-Akahira-Sunose
m	monoclinic
M	Molarity
MA	Minor Actinides
MOX	Mixed Oxide
MPa	Mega Pascal
MS	Mass Spectrometry
N	Normality
Nc/nc	Nanocrystalline
NFC	Nuclear Fuel Complex
NIST	National Institute of Standards and Technology
Ox de	Oxalate decomposition
P	Porous agent (Vol %)
P&T	Partition and Transmutation

PCS	Photon Correlation Spectroscopy
PFBR	Prototype Fast Breeder Reactor
PHWR	Pressurized Heavy Water Reactor
PIR	Photochemically induced reaction
P_OSD	Pore size distribution / Distribution of pores
ppm	Parts per million
PSD	Particle size distribution / Distribution of particles
PTFE	Polytetrafluoroethylene
R	Raman mode
R	Fuel (citric acid / sucrose) to Nitrate (in mole ratio)
RC	Carbon residue
RCS	Rate Controlled Sintering
Re-Ox	Reduction-Oxidation
RF	Radio Frequency
RO	Re-oxidized
S	External gelation sol-gel technique
SAED	Selected Area Electron Diffraction
Sc	Scherrer method
SEM	Scanning Electron Microscopy
SMS	Salt Melt Synthesis
SPS / FAST	Spark plasma Sintering / Field-Assisted Sintering Technology
SRM	Standard Reference Material
SSA	Specific Surface Area
STEM	Scanning transmission electron microscopy
TBP	TriButyl Phosphate
T.D	Theoretical density
TEM	Transmission Electron Microscopy
TG	Thermogravimetry
TG-DTA-MS	Thermogravimetry-Differential Thermal Analysis coupled with Mass Spectrometry
Thde	Thermal decomposition
Th-Ox	Thorium oxalate
TSS	Two-step Sintering
TSS_C	Two-step Sintering proposed by Chu
TSS_{CW}	Two-step Sintering proposed by Chen and Wang
TWh	Terawatt hours
UV-VIS-NIR	Ultraviolet-visible-near infrared

VCR	Volume combustion reaction
XCS	X-ray crystallite size
XRD	X-ray Diffraction
YSH	Yttria Stabilized Hafnia
2-D	Two dimension

List of Symbols

K	Temperature dependent constant
K	Crystallite shape factor
ρ	Relative density
G	Grain size
n	Exponent that depends on the type of diffusion mechanism
D_l	Lattice diffusion coefficients
D_{gb}	Grain boundary diffusion coefficients
Ω	Atomic volume
γ_{sv}	Surface particle / pore interfacial energy
T	Temperature
δ_{gb}	Width of the grain boundary
T_m	Melting Point of that substance expressed in Kelvin
k	Boltzmann constant
F(ρ)	Unspecified function of density (ρ)
D	Grain boundary diffusivity
ρ_B	Bulk density
ρ_G	Green density
ρ_S	Sintered density
S/N	Signal to Noise ratio
V_m	Volume fraction of monoclinic phase
I	Integrated intensity of the X-ray diffraction lines
λ	X-ray Wavelength
ε	Strain distribution within the material
β	Full width at half maxima in radians / Heating rate
α	Degree of conversion / Shrinkage anisotropy factor
R	Gas constant
f(α)	Conversion function
A	Pre-exponential factor
T_P	Peak temperature
E_a	Activation energy
g(α)	Integral form of f(α)

g	Geometrical density
Ψ	Dihedral angle
γ_{gb}	Grain boundary energy
N	Number of grains surrounding the pores
N_c	Critical coordination number
ΔS	Relative shrinkage parameter
B	Branching ratio
K_{Eq}	Equilibrium constant

List of Figures

List of Tables

Chapter 1

Introduction

Nuclear energy is one of the best alternatives that could help us meet the growing energy demands with zero green house gas emission [1-3]. Although issues related to waste disposal are still a concern [3-5], it is the only available large-scale alternative that could be a major provider of green energy. However, as of now, the global share of nuclear power is rather meager [India (3 %) – 32 TWh] in comparison with coal, natural gas and hydropower [6]. In order to enhance the share of nuclear power in the global power production novel strategies are necessary [5, 7]. Some of the new strategies include minimization of the radiotoxic burden and destruction of the “long-lived” radiotoxic waste [5, 7]. In this context advanced nuclear fuels and advanced structural materials are particularly important [8-12]. India is aiming to meet 25 % of her power demand through the nuclear means by 2050 [6]. International agencies [International Atomic Energy Agency (IAEA) and Generation IV International Forum (GIF)] have also started programs viz., International Project on Innovative Nuclear Reactors and Fuel Cycles (INPRO) and Advanced Fuel Cycle Initiative (AFCI) [8, 13-15], that aim at coordinating the research and development to deploy innovative nuclear fission reactors (Generation IV reactors) with special emphasis to address certain challenges. These challenges are, efficient utilization of fuels, economics, safety, reliability, minimizing radiological toxic waste and partitioning and transmutation (P&T) of long lived radioactive elements in the nuclear waste (minor actinides (MA)) [5, 15].

India’s nuclear energy programme was initiated by Homi Bhabha about sixty years ago keeping in view the limited uranium and surplus thorium reserves of this nation [3, 16]. India has adopted the well-known three stage nuclear programme with closed fuel cycle reprocessing in order to utilize nuclear fuels completely and to reprocess the spent nuclear fuel[1] (nuclear waste management) [3, 16-18]. The first stage is primarily based on the Pressurized Heavy Water Reactors (PHWRs) which use natural uranium and heavy water as moderator[2] and coolant[3] [3, 16]. With the successful operation of Fast Breeder Test Reactor (FBTR) and the experience gained, the country has embarked on to the second stage programme based on Sodium cooled Fast Breeder Reactor (FBR) [3, 19]. One such Prototype Fast Breeder Reactor (PFBR) being built at Kalpakkam envisages the use of U, Pu mixed oxide (MOX) (with ≈ 21wt% and ≈ 28wt% Pu) as fuel [3, 20]. Thorium (^{232}Th) which is present around the core[4] in this reactor (blanket material) would be transmuted into ^{233}U, which will fuel the reactors in the third stage [3, 17, 18]. India has also designed an Advanced Heavy Water Reactor (AHWR) which would use mixed oxide (MOX) fuels comprising solid solutions of the oxides of ^{233}U & ^{232}Th or ^{233}U & ^{239}Pu [3, 21, 22]. AHWR would help shorten the period of thorium utilization [3, 21, 22]. India has also initiated a programme on Accelerator Driven Subcritical System (ADS) [3] to burn long lived minor actinides and to generate fissile ^{233}U from thorium. The third stage would involve generation of ^{233}U from ^{232}Th in PHWRs [3, 17, 18, 21, 22].

The fission reactors mentioned above, deploy a variety of special materials which are collectively called as nuclear materials [23]. In general the term "nuclear materials" include fuel,

---

[1] Nuclear fuel reprocessing / reprocess the spent nuclear fuel - The process by which spent fuel is separated into waste material for disposal and into material such as uranium and plutonium to be reused as fuel [http://www.srscro.org/].

[2] Moderator - Material used in a nuclear reactor to decelerate neutrons from the high velocities at which they are released. Neutrons lose velocity by scattering collisions with nuclei of the moderator. A good moderator has high scattering cross section, low atomic weight, and low neutron-absorption cross section [9].

[3] Coolant - Any fluid circulated through the core of a reactor to extract heat liberated in the fission process [https://nucleus.iaea.org].

[4] Core - The central portion of a nuclear reactor, which contains the fuel assemblies, moderator, neutron poisons, control rods, and support structures. The reactor core is where fission takes place [www.nrc.gov].

clad[5], coolant, moderator, reflector[6], control rod[7], shielding material[8], thermal insulation material and the structural materials[9] [9]. These materials are often subjected to an extremely harsh environment viz., intense radiation, prolonged exposure to coolant, thermal and mechanical stresses [8, 9]. Hence, investigations on the synthesis, characterization and fabrication of nuclear materials are pertinent to nuclear technology which aims at power production at an economically viable cost.

1.1 Nuclear fuels

The most common physical form of a nuclear fuel is “sintered cylindrical pellet” [9]. Less common forms include rod [9], microspheres [9, 19] and plates [19]. Nuclear fuels could be broadly classified into metallic (alloys containing U / Pu), ceramic (oxides, nitrides and carbides) and dispersion fuels [9].

As highlighted in the foregoing section, UO_2, PuO_2, ThO_2 and mixed oxides of U,Th or U,Pu (MOX) are important driver fuels[10] for fission nuclear reactors [3, 9, 17-19, 21, 22, 24]. Sintered UO_2 is most widely used in the nuclear power reactor because of its high melting point, compatibility with the cladding materials (stainless steel and zircaloy[11]) and chemical stability

---

[5] Clad - Tightly bound (usually metallic) casing directly surrounding the nuclear fuel which protects it against a chemically active ambience (cooling water) and prevents the escape of fission products into the cooling water [www.euronuclear.org].

[6] Reflectors - Layer of material surrounding the core of a nuclear reactor that serves to deflect escaping neutrons and return mainly to the core [9].

[7] Control rods - Device containing material with a high neutron absorption cross section that is used to govern the fission rate of a nuclear reactor by absorbing excess neutrons [9].

[8] Shielding materials - A mass of material surrounding a source of radiation that reduces radiation intensity, for the purposes of protection of equipment, material or personnel. Dense concrete, several metres thick, is used for shielding [https://nucleus.iaea.org].

[9] Structural materials - The materials used to encase the fuel in fuel rods, to hold fuel rods together in fuel assemblies, and to hold fuel assemblies in place, materials used in control rods and core monitoring instruments and their supporting structures are all considered as structural materials [www.iaea.org].

[10] Driver fuel - Fissionable material that has been enriched to a composition that will support a self-sustaining fission chain reaction when used to fuel a nuclear reactor, thereby producing energy (usually in the form of heat or useful radiation) for use in other processes., e.g., ^{233}U, ^{235}U, ^{239}Pu (and higher odd isotopes) [www.nrc.gov].

[11] Zircaloy - Zirconium alloy used as a tube to contain uranium oxide fuel pellets in a fuel rod (part of a reactor fuel assembly) [https://infcis.iaea.org].

towards water and well established fabrication technology [9]. The oxide fuels are fabricated through conventional powder metallurgical processes [9, 17-19, 24]. The fuels used in almost all the commercial oxide fuelled reactors are produced by this process [9, 17, 18, 24].

1.2 Advanced fuels – oxides, carbides and nitrides

Nuclear fuels which incorporate the concept of recycling, incineration of minor actinides, higher breeding ratio[12] (in turn short doubling time[13]) for waste minimization, higher power density and higher fuel reliability are generally termed as “advanced actinide fuels” [25, 26]. These fuels have significant advantages over the conventional fuels but are yet to be commercialized. Similarly “advanced fuel fabrication method” refers to a method that is advantageous over the conventional methods but is yet to be commercially deployed.

Table 1.1 enlists an intercomparision of the thermo-physical properties of some of the advanced fuel forms vis-à-vis that of the conventional oxide fuel [19].

The preparation of advanced oxide fuel forms containing ^{233}U, ^{239}Pu and Minor Actinides (MA) which call for improvised “advanced techniques” owing to the higher radiotoxicity of the latter is a typical example that necessitates the deployment of alternate fuel fabrication techniques [5, 10, 12-14, 18-20, 25]. Nitride, carbide and metallic fuels are considered as “advanced fuels” for they possess better thermo-physical and thermo-chemical properties as compared to the mixed oxide (Table 1.1) [19, 26].

The sol-gel method is considered as an ideal alternative “advanced method” for the fabrication of oxide fuels because it is dust free, easy to remotize and is a cost-effective technique [18, 24]. This process was successfully implemented for the preparation of sintered

---

[12] Breeding ratio - The ratio of fissile material obtained to spent fissile material after the use of a fuel mixture of fissile and fertile material in a reactor [www.euronuclear.org].

[13] Doubling time - The time during which the fissile material input of a breeding reactor doubles. Depending on the breeding reactor concept, doubling times of 8 to 20 years result [www.euronuclear.org].

microspheres of different size fractions of UO_2, ThO_2, mixed metal oxides (MOX) of U & Pu or U & Th and $(U, MA)O_2$ [18, 24].

Carbide fuel was considered as an advanced fuel for Fast Reactors [3, 19]. However, due to difficulties in fabrication, reprocessing and economics, the carbide fuel technology did not take off [19, 24]. Even though the Fast Breeder Test Reactor (FBTR) at Kalpakkam, India uses a plutonium rich mixed uranium and plutonium carbide fuel, PFBR, the commercial fast reactor being commissioned at Kalpakkam, would use only the MOX fuel [3, 19, 24].

Table 1.1 Comparison of some characteristics of the fuels used in Fast Reactor [19]

		Oxide fuel	**Carbide fuels**	**Nitride fuels**	**Metallic fuels**
		$U_{0.8}Pu_{0.2}O_2$	$U_{0.8}Pu_{0.2}C$	$U_{0.8}Pu_{0.2}N$	U-19Pu-10Zr
T.D (g cm^{-3})		11.04	13.58	14.32	15.73
T_m (K)		3083	2750	3070	1330
Crystal structure (Space group)		Fluorite (Fm3m)	NaCl (Fm3m)	NaCl (Fm3m)	Multi-phase
Breeding ratio		1.1	1.2-1.3	1.2-1.3	1.4-1.5
Swelling		Moderate	High	High	High
Handling atmosphere		Air	Inert gas	Inert gas	Inert gas
Dissolution and amenability to reprocessing		Demonstrated for industrial scale for aqueous and pilot scale for pyro reprocessing	Difficult-yet to be demonstrated industrially	Easy but risk of C^{14} in waste management	Pyro - reprocessing demonstrated on pilot scale
Fabrication/irradiation experience		Good	Limited	Very little	limited
Thermal conductivity (W m^{-1} ^{0}K)	1000 K	2.6	18.8	15.8	40
	2000 K	2.4	21.2	20.1	-
Compatibility with	Clad	Average	Carburization	Good	Low melting eutectics
	Coolant	Average	Good	Good	Good

T_m – Melting point and T.D – Theoretical density

1.3 "In-reactor" behavior of nuclear fuels

During its life in a reactor the nuclear fuel would undergo substantial physical, microstructural and chemical changes apart from radiation induced changes [19]. In order to improve the economics of the nuclear power production it is desirable to extract the maximum possible power from a given fuel. This necessitates a longer residence time or "burn-up"[14] of the fuel [8, 15, 27-29]. Increasing the fuel burn-up in the reactor would require the development and testing of advanced fuels and structural materials that would withstand the extended operation [8, 15]. Recently, Idaho National Laboratory had established a facility for the testing of advanced fuels and materials [15]. The investigations carried out in this facility would throw light on fuel performance, economics, safety and reliability [15]. Several countries including India are regularly monitoring and updating their tests for enhancing the performance of fuels and materials for the current and future advanced reactors [15].

1.3.1 High Burn-up Structure/phase (HBS)

Studies carried out in the past on LWR (oxide) fuels with a burn-up of about 60 GWd/tHM revealed that this fuel had undergone significant restructuring[15], comprised pores and a fine grained microstructure at its rim [27, 30, 31]. This feature was initially termed as the "rim structure" and later it was called as the "high burn-up structure" (HBS) [27, 30, 31]. Studies carried out earlier in the 1950-60s by Barney and Wemple [32] and Belle [33] were the first investigations on HBS. However, the significance of HBS was not known at that time and hence it was not investigated in detail [27]. But in the late 1990s, the HBS was rediscovered in

---

[14] Burn-up - Measure of the number of fissionable atoms that have undergone fission. It is usually expressed as the atomic percent of the total uranium atoms that have fissioned in the fuel, as megawatt-days of energy generated per ton of uranium, or as gigajoules of energy per kg of uranium. Other definitions include fissions/cc or atomic percent of fissions per total atoms present in the fuel [9].

[15] Restructuring – The increase in the local burn-up of the nuclear fuels leads to the formation of cracks followed by self healing and eventually redistribution of actinides and porosity in the fuels. Thus the fuel yields a new morphology. These processes are collectively termed as restructuring of the fuel [27].

"modern reactor fuels" and for the past two decades, research is being carried out world over [for e.g. High Burn-up Rim Project - HBRP] in order to understand the formation mechanisms, properties and significance of HBS [27]. It is now surmised that the HBS is formed due to the capture of epithermal neutrons with energies matching the resonance absorption cross-section of ^{238}U leading to ^{239}Pu build-up at the "rim" of the fuel [27, 30]. Further, it was observed that the Pu content at the rim of the UO_2 fuel is 2 to 3 times higher than that of the average Pu content in the fuel at an average burn-up of 60 GWd/tHM [27, 29]. Unlike the fresh fuel which possesses microcrystalline UO_2 grains with a size of about 10 μm, HBS was found to contain grains with size ranging from 100-300 nm (grain subdivision ≈ 10^4 times) [27, 30]. Further, it was found that it contains closed intergranular macropores with a porosity fraction of about 20 % (Fig. 1.1) [27, 29]. Significant amount of fission gases were entrapped in these closed pores [29, 31]. Microstructural analysis of HBS revealed that the restructured fuels were devoid of any defects [27, 30] and a thin section of HBS at the rim of the fuel extends to the inner region of the fuel pellet with increasing burn-up [27, 30]. It was found that the fuel with the average burn-up of about 60 GWd/tHM comprised HBS of about 8 % of the fuel volume [1]. HBS is not only observed in UO_2 fuel and U-Mo alloy fuel but also in other fuels viz., MOX, carbide and nitride fuels used in the FBRs [27, 30]. Lozano et al. [34] had identified two types of grains in the HBS viz., polyhedral (bulk of HBS) and round (around pores and open surface) grains.

Studies on HBS revealed that it possesses the following advantageous features, i) retention of 90% of fission gases in the closed pores, ii) lack of enhanced fission gas release, iii) improved thermal conductivity, iv) increased fracture toughness and plasticity and v) stability towards radiation and elimination of defects by itself (self healing mechanism) [27, 31]. All these properties are most suitable for achieving higher burn-up. Further, recent investigations on HBS analogue materials (partially stabilized zirconia doped with 4 mol% yttria by Spino et al. [31] revealed that nanocrystalline (nc) UO_2 is a potential candidate material to be used in reactors which aim at a higher burn-up as well as in inert matrix fuels (IMF)[16] [27, 30].

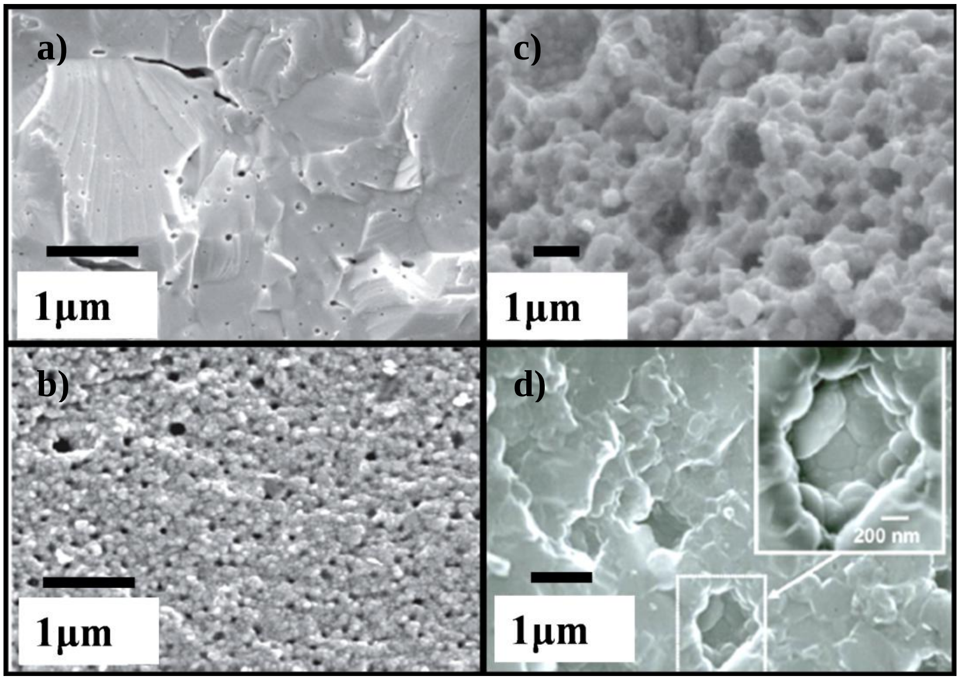

Figure 1.1 Scanning Electron Microscopy micrographs showing fuel fracture surfaces: (a) unirradiated UO_2 fuel; the pores visible in the as-fabricated fuel structure are removed in-pile during the early stage of irradiation by fuel densification processes, (b) Fuel with local burn-up of ~75 GWd/tHM showing the typical HBS morphology (HBRP [27]), (c) High magnification SEM fracture surface micrograph of LWR UO_2 fuel with a local burn-up of around 160 GWd/tHM. The image shows in detail the morphology of HBS, characterized by sub-micron grains and micron-sized intergranular pores and (d) High magnification scanning electron microscopy image of 75 GWd/ tHM *UO_2 showing HBS morphology. Polyhedral sub-grains are present in the bulk while round sub-grains (see inset) occur mainly around pores and open surfaces (HBRP) (Figure reproduced from [27])*

The mechanism leading to the formation of HBS is not understood completely due to the interplay of many complex factors. However, various researchers had tried to explain this

---

[16] Inert matrix fuels – IMF is a type of nuclear reactor fuel that consists of a neutron-transparent matrix and a fissile phase that is either dissolved in the matrix or incorporated as macroscopic inclusions. The matrix plays a crucial role of diluting the fissile phase to the volumetric concentrations required by reactor control considerations, the same role ^{238}U played in conventional low enriched uranium (LEU) or MOX fuel. The key difference is that replacing fertile ^{238}U with a neutron-transparent matrix eliminates plutonium breeding as a result of neutron capture [IAEA TECDOC 1516].

phenomenon by using different theories and models [27]. Some of these theories pertaining to the mechanism of HBS formation need to be modified as the recent findings indicate conflicting results [27]. Hence, several novel experiments are being devised for a better understanding of the HBS [35, 36]. Also new models / theories are being developed with these new results [27]. Many researchers are of the view that the formation of small grains could possibly be due to either recrystallization (formation of a subgrain which ultimately grow into recrystallized nanograins) or polygonization (formation of micro-domain of an over structure of the UO_2 which results in planar defects) [27, 29, 30]. Recent investigations provide enormous evidence pointing towards the polygonization mechanism [27]. *Thus investigations on nc-*UO_2 *have become very pertinent to advanced nuclear fuel forms.*

1.4 Foam and porous pellets

In addition to the above application nanostructured oxide foams and porous pellets also are relevant to advanced metal production viz., the direct oxide reduction (DOR) process. Uranium metal is a starting material for the preparation of uranium bearing alloys that are candidate fuels for the Fast Reactors. Usually the preparation of metallic uranium is accomplished by the reduction of its fluoride through the expensive fluoro-metallothermic process. Recent research carried out at the University of Cambridge has brought about a paradigm shift in the reduction of metal oxides [37]. This research group has reduced TiO_2 to Ti through a novel direct electrochemical reduction called DOR process [37]. This process is an attractive alternative to the expensive conventional metallothermy. Plutonium is presently being recovered from the spent nuclear fuel through aqueous nuclear fuel reprocessing technology [18]. Production of metallic Pu through direct electrochemical reduction coupled with reprocessing would serve as an attractive alternative method for the production of Pu metal.

This "advanced" DOR method is particularly advantageous because it is cost effective and less cumbersome than the "conventional bomb reduction"[17].

In view of the above, a research program on DOR is currently being pursued in some countries (including India), world over [38, 39]. Although, this method involves many process variables, percolation of the molten salt (into the MO_2 / pre-form used for the reduction) is one of the principal prerequisites that determine the complete conversion of the oxide to the metal. The oxide "pre-form" used in the reduction needs to have a high matrix density in order to have a good electrical conductivity vis-à-vis high porosity to facilitate complete reduction of the oxide. Hence, preparation of porous UO_2 bodies (either foam or a pellet) is necessary. Recently, a patent which describes a novel method for the fabrication of porous pellets has been registered [40]. In this study, we had investigated the possibility of producing both porous urania and urania foam through two different techniques, appropriate precursors.

The third application which warrants the use of nanocrystalline oxide ceramics in nuclear technology is the fabrication of chemically inert crucibles to be used in melting metallic U or alloys bearing U and Pu. This application encompasses both thermodynamic investigations as well as fuel fabrication [41, 42].

1.5 Crucibles for uranium melting

Experimental determination of the properties of U and its alloys, viz., self diffusion, melting, electrical resistivity and magnetic susceptibility are relevant to nuclear technology [43]. Data on the solidus temperature[18] of uranium bearing alloys serve as useful inputs for nuclear

---

[17] Conventional bomb reduction - Ames process or bomb reduction is a process by which high pure uranium is prepared. It involves the heating of mixtures of uranium halides and magnesium powder.

[18] Solidus temperature - It is the highest temperature up to which an alloy / solid solution could be heated without melting.

fuel design [41]. Liquid uranium bearing alloys are highly oxyphilic and have to be held at high temperatures in ceramic containers without any chemical interaction with the latter [43-45].

The use of many inert ceramic crucibles have been reported in the literature [41, 43-45]. These include crucibles made out of MgO [43, 45], Al_2O_3 [43, 44], UO_2 [43], BeO [43, 45], ThO_2 [41], yttria stabilized zirconia (YSZ) [41, 43] and graphite [43].

From a simple Ellingham diagram analysis, it is evident that both Y_2O_3 and HfO_2 are very stable in presence of molten U [42, 46, 47]. Hence crucibles made out of HfO_2 or Y_2O_3 are best suited for this application.

Reactions with impurities including those introduced through the additives (binders) used while making crucibles could contaminate the molten uranium [43]. Therefore, it is desirable to use binderless process for the production of crucibles for uranium melting. Hence, we undertook investigations on the fabrication of high density crucibles out of HfO_2 [$P2_1/c$ (14)] and Y_2O_3 [Ia-3 (206)]. HfO_2 undergoes a phase transformation from the monoclinic [$P2_1/c$ (14)] to quadratic[19] ($P4_2/nmc$) phase at 1973 K and the quadratic phase transforms into the cubic phase (Fm3m) at 2873 K [47, 48]. Monoclinic hafnia is less dense compared to the quadratic phase and hence thermal cycling of hafnia is accompanied by a volume expansion (+3.4%) [48]. This results in cracking of the sintered (1973 K) hafnia products [47-49]. Hence, yttria stabilized hafnia was prepared and crucibles were made out of the same. In view of their high sinterability nc powders were chosen for fabricating the crucibles.

1.6 Preparation of nanocrystalline (nc) oxides

Nanocrystalline materials possess superior material properties as compared to their microcrystalline counterparts [50]. The challenges in the fabrication of crucibles from nc

---

[19] Quadratic ($P4_2/nmc$) phase - Alternate name for tetragonal crystal system.

powders include preparation of nc materials in bulk quantities, optimizing the powder processing and consolidation parameters as well as choosing a suitable sintering technique [51-55].

There are many methods reported in the literature that could be used to synthesize nanocrystalline ceramics which include chemical vapor deposition (CVD) [56], pyrolysis [57], precipitation [52], sol-gel [52] and high-energy ball milling (HEBM) [51, 52]. However, some of these methods have their own limitations. Among these, the precipitation synthesis is most commonly used, in the preparation of nanocrystalline oxides in bulk quantities [52, 58].

In the precipitation method two or more reactants are mixed together (in an aqueous / non-aqueous solution) to precipitate the precursor. Subsequently the product is separated by filtration [52, 58]. The liquid solvent residue in the precipitate is removed by a suitable "post-processing" [52]. The product thus obtained is decomposed to yield the desired product. This method yields a homogeneous product [52, 58]. Typical examples include the preparation of ThO_2 powders from thorium oxalate [59] and BeO from $Be(OH)_2$ [60].

1.6.1 Challenges involved in the preparation of nanocrystalline materials

The primary challenge in the synthesis of nanocrystalline powders is the amenability of a given method to scale-up and its ability to control both the size and size distribution of particles, surface contamination and degree of agglomeration [52, 55, 61, 62]. CVD and chemical pyrolysis produce powders with a high degree of agglomeration with particle size over a wide range [52, 61]. In general, precipitation synthesis is carried out in aqueous media and in the subsequent stages moisture is removed by drying [55, 58, 62]. During drying hard agglomerates could be formed [52, 55, 62]. Some authors [52, 55, 62] had used dispersants during the synthesis or had washed the precipitates with an organic solvent and removed the latter subsequently by evaporation / decomposition at a higher temperature [55, 63]. In most cases, this heat treatment leads to localized densification and formation of harder agglomerates leading to heterogeneous density distribution in the green compacts [52, 55, 63]. This could lead to differential densification while these are sintered later [52, 55, 64]. Often these powders require high compaction pressures (to break the hard agglomerates) and very high temperature for sintering, if a dense product is to be obtained by consolidation [52, 55, 62]. On the other hand, gel based methods are promising alternatives for the preparation of nanopowders with control over both particle size and the distribution of sizes [52, 55]. HEBM has been used for grain refinement and for the preparation of novel nanomaterials which includes metastable phases [52, 65]. However, mechanical attrition generally leads to contamination and yields powders with a wide size distribution of particles [52].

Monoliths made out of nc materials densify at a faster rate (enhanced diffusion kinetics) at the surface than at the interior of the sample [54, 55, 62, 66]. In agglomerated powders, densification is strongly dependent on the agglomerate size rather than the crystallite size because of larger pores (both inter and intra agglomerate) [54, 55]. These larger pores are much stable and lead to a lower densification rate [54, 55, 62, 66]. Hence, control of agglomeration is a key parameter in the preparation of nc powders.

1.6.2 Advanced preparation techniques for the bulk preparation of nanocrystalline powders

Among the methods that are cited in the literature for the synthesis of nc materials only a few are useful for scale-up [52]. Presence of undesirable impurities, generation of a large volume of liquid waste and economic viability are the main factors that decide the scalability of a given method [52].

The precipitation method could be modified (for a scale-up) by adding surfactants / capping agents [67] or by changing the experimental conditions (e.g. high P [68], high T [58], and hydrothermal method [69])**.** Further, different post-processing techniques (e.g. freeze drying [70] and azeotropic distillation [71]) could be used for treating the powders or precipitates. Ananthasivan et al. [72] have prepared nc-ThO_2 powders by “oxalate ultrasonic deagglomeration” method.

Complex and uniform nanocrystals could also be prepared by carrying out the synthesis in non-aqueous media [73, 74]. Several mechanisms had been proposed for the non-aqueous synthesis of nanocrystals but the role played by solvent and surfactant in defining the specific structure of nanocrystals is yet to be completely understood [75]. Typically, a mixture containing a definite proportion oleic acid, oleyl amine, organic solvent and precursor salt are used in some procedures. This mixture is heated in a stream of an inert gas in an enclosed polytetrafluroethylene (PTFE) vessel [75, 76]. UO_2, ThO_2 and mixed oxides of U and Th of monodisperse nanocrystals have been successfully prepared by using this non-aqueous method [74].

1.6.3 Gel-Combustion Synthesis

Yet another promising advanced method for the preparation of nc-ceramic (UO_2, ThO_2 and Y_2O_3) powders is the combustion synthesis [77, 78]. Combustion synthesis involves the thermal decomposition of a mixture containing an oxidant and a reducing agent (fuel). Based on the physical state of the reactants this technique is further subdivided into solid state combustion synthesis and solution-combustion synthesis [79]. The latter is being widely used in the preparation of nc-oxide materials as it is simple, economical, fast and amenable to scale-up [80]. This method involves the thermal decomposition of a homogeneous aqueous gel containing a metal nitrate (oxidant) and an organic ligand (fuel: citric acid, urea, glycine, hydrazine, etc.) [79]. It is established that the composition of the combustion mixture (R = fuel to nitrate mole ratio) influences the characteristics of the final product [78]. Among the fuels citric acid is preferred for it produces moderate reactions and leaves behind lesser carbon residue in the product [81].

So far no reports are available in the literature pertaining to the citrate gel-combustion synthesis of nc-UO_2 powders while synthesis of nc-ThO_2 [78], solid solution of urania-thoria [82] and yttria [83] have been reported. Purohit et al. [84] have prepared nc-ThO_2 by using glycine gel combustion. These authors have carried out combustion synthesis with both fuel lean and fuel rich mixtures. However, they [84] did not investigate the systematic dependence of R on the characteristics of the final product. Chandramouli et al. [78] have used both urea and citric acid for the preparation of the nc-ThO_2, and also studied the influence of different modes of heating (hot plate and microwave) on the characteristics of the final product. So far, no report has been published in which the influence of fuel to nitrate mole ratio, in the fuel lean region (R = 0 - 0.31) on the citrate gel-combustion synthesis of nc-ThO_2 powders has been studied. Several authors had reported the preparation of nc-Y_2O_3 by using gel-combustion method [83, 85, 86]. However, no reports have so far been made on the preparation of nc-Y_2O_3, nc-UO_2 and nc-ThO_2 powders through “volume combustion reaction”[20] of citrate gels. Hence, we investigated these citrate gels of specific composition, in this study.

1.6.4 Salt Melt Synthesis (SMS)

The SMS is a non-aqueous molten salt technique that is very useful for the preparation of nc-oxides. The SMS involves the decomposition of a precursor [$M(NO_3)_x$ or MCl_x or $M(SO_4)_x$]

---

[20] Volume combustion reaction (VCR) – It is a kind of solution combustion synthesis wherein the entire reactive solution or gels is preheated uniformly to the boiling point of the solvent and held at this temperature for certain period until the mixture self propagates (exothermic) itself in the form of combustion wave. This mode is also called volume combustion mode [A. Verma et al. Chem. Rev. 116 (3) (2016) 14493-14586].

in a pool of molten metal nitrate [87-89]. The reaction between the precursor and molten salt could be viewed as an acid-base reaction (Lux-Flood concept [90]) wherein a base (NO_3^-) donates its oxide ion to an acid (M^{n+}). Extensive work has been carried out on SMS by Kerridge et al. [91] and Durand et al. [92]. These authors were able to prepare metastable nanocrystalline ceramics (t-ZrO_2, c-ZrO_2 and γ-Al_2O_3) by using SMS [91, 92].

Recent reports on the salt melt synthesis [88, 89] explain in detail about the preparation of metastable materials with different structures by tuning either one or more experimental parameters. The latter include varying the composition of the eutectic mixture, its basicity, reaction conditions (closed or open), heating rate, soaking temperature and duration of reaction [88, 89]. The SMS could be used to prepare nanocrystalline materials in bulk and is particularly suitable for the preparation of nc-HfO_2 and nc-YSH. However, nc-HfO_2 and nc-YSH has not so far been prepared in bulk quantities by using this method. Hence, we investigated the preparation of nc-HfO_2 and nc-YSH on a 30 g scale by using this method.

1.7 Sintering of nanocrystalline powders

Sintering is a thermal treatment for bonding particles into a coherent, predominately solid structure via mass transport events that often occur at the atomic scale. The bonding leads to improved strength and lower system energy [93]. The main driving forces for sintering are curvature of the particle surface, and (or) an externally applied pressure and a chemical reaction [93, 94]. The phenomenon of sintering in microcrystalline powders is well studied and many treatises are available on the same [62]. However, the sintering of nc powders are not fully understood [55, 62, 66]. Sintering in a real system involves many complex variables and many theories and models were developed in the past (scaling law, numerical simulations, analytical models, topological models, statistical models and phenomenological equations) to analyze the densification process [62, 94]. In general, these theoretical approaches indicate that the densification of nanocrystalline powders is affected significantly by the following variables viz., high SSA, agglomeration of particles, size distribution of particles, particle packing in green compacts, pores, heating schedule, sintering atmosphere and other process variables [52, 54, 55, 62]. Although, these factors affect the microcrystalline materials as well, the magnitude of their impact is more pronounced in the former [54]. Sintering of nc powders are greatly affected by their green density (ρ_G) and the compaction process as well [52, 55, 62]. It is observed that the nc powders do not yield green bodies with a high density due to the restricted sliding and rearrangement of particles during compaction owing to the presence of large interparticle frictional resistance [52, 54, 94]. In addition nc ceramic powders are prone to get agglomerated due to the presence of weak van der Waals force of attraction viz., Keesom forces, Debye induction forces and London dispersion forces [62].

During sintering, densification occurs due to grain boundary diffusion (grain boundaries to the pores) [62, 94]. Therefore increase in grain size would increase the diffusional path which in turn results in suppression of the densification rate (Fig 1.2) [94].

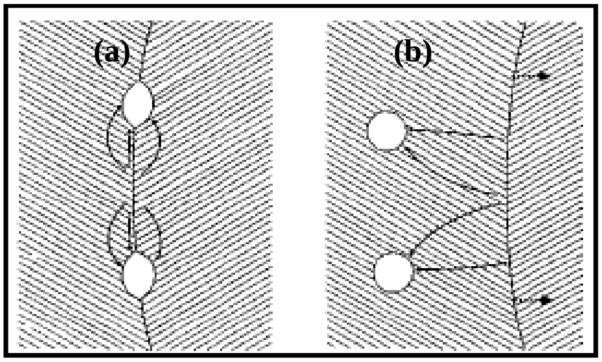

Figure 1.2 (a) Densification mechanisms for porosity attached to a grain boundary. The arrows indicate paths for atom diffusion and (b) Densification mechanisms for porosity separated from a grain boundary. The solid arrows indicate paths for atom diffusion, and the dashed arrows indicate the direction of boundary migration [94]

The relation between densification rate and the size of the grain boundary [63] is given by eqn. (1.1).

$$\frac{1}{\rho}\frac{d\rho}{dt} = \frac{K}{G^n} \tag{1.1}$$

where K is a temperature dependent constant, ρ is relative density, G is the grain size, n is an exponent that depends on the type of diffusion mechanism that prevails [n = 3 for lattice diffusion from the surface and 4 grain boundary diffusion].

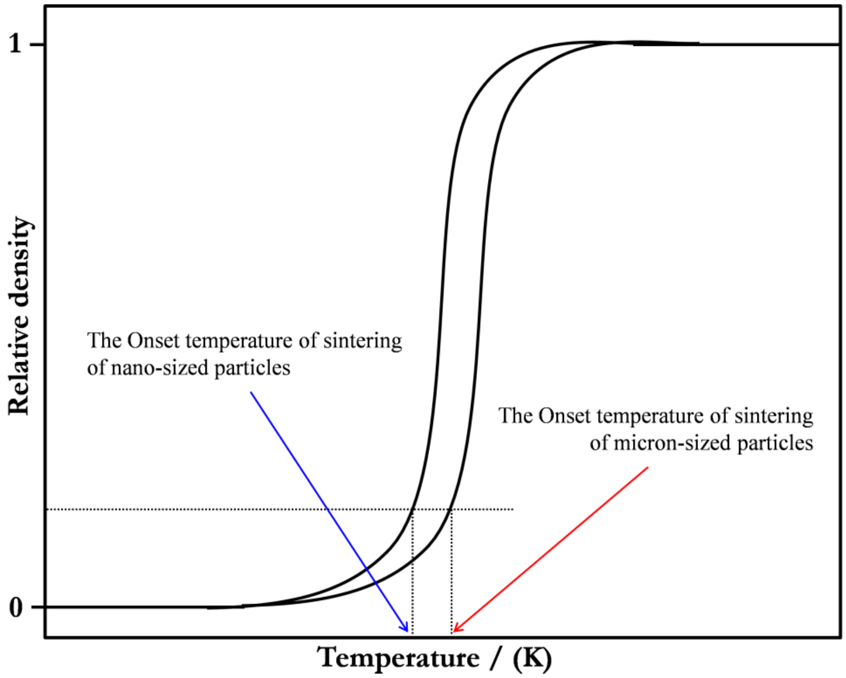

Figure 1.3 Schematic diagram illustrating different onset temperatures of sintering of nano- and micro-meter sized particles based on the model proposed by Fang [54]

Thus, to obtain highly dense monoliths it is necessary that the powder should contain small particles with unimodal size distribution and that the sintering is carried out in a controlled environment with normal grain growth [52, 53, 55, 62, 66]. The latter is a thermally activated microstructure evolution process wherein curvature driven grain rotation and grain boundary migration occurs [95]. In general, microcrystalline materials exhibit normal grain growth [95]. However, in some instances abnormal grain growth could occur due to the faster mobility of atoms at the grain boundary [95]. It is observed that the materials that comprise impurities and defects at the interface, as well as nc materials exhibits abnormal grain growth [95]. From the foregoing it is evident that considerable attention must be given during all the processing steps in the sintering of nc materials.

Herring's scaling law predicts that the sintering rate in a nc material could be as much as twelve orders higher than that of its microcrystalline counterpart [62]. Nanoparticles bear a high concentration of defects and unsatiated valence at their surface [66]. Therefore the mobility of atoms on the surface of such a particle is higher compared to that of the atoms at its interior [66]. Thus, the temperature at which sintering starts in a nc material is lower as compared to its microcrystalline counterpart (Fig.1.3) [54, 66].

Fang and Wang [54] have termed the "onset sintering temperature" as "rapid densification stage" due to the lack of demarcation between the coarsening and the densification processes. Further, these authors had also reported that due to the large surface to volume ratio prevailing in nc materials, surface premelting could also result in rapid densification [54]. Recent experimental investigation on laser heating of nc-UO_2 [96] had revealed that the nanostructured UO_2 compacts had melted at a lower temperature 2790 ± 60 K as compared to microcrystalline UO_2 (3120 ± 30 K) [97]. Rahaman [94] had reported that the reduction in particle size increases the diffusion rate which in turn increases the densification rate (eqns. 1.2-1.3):

$$\text{Lattice diffusion} = \frac{1}{\rho}\frac{d\rho}{dt} \approx \frac{10 D_l \gamma_{sv} \Omega}{\rho G^3 kT} \tag{1.2}$$

$$\text{Grain boundary diffusion} = \frac{1}{\rho}\frac{d\rho}{dt} \approx \frac{4}{3}\frac{D_{gb}\gamma_{sv}\Omega\delta_{gb}}{\rho(1-\rho)^3 G^4 kT} \tag{1.3}$$

where, ρ is relative density, D_l and D_{gb} are lattice and grain boundary diffusion coefficients, k is the Boltzmann constant, T is temperature, δ_{gb} is the width of the grain boundary, γ_{sv} is the specific energy of the solid-vapor interface and Ω is the atomic volume. Groza [61] had reported that the depression in sintering onset temperature for nc materials is in the range of 0.2 T_m to 0.3 T_m (where, T_m = melting point of that substance expressed in Kelvin) while in microcrystalline materials it is in the range of 0.5 T_m to 0.8 T_m.

Recent studies [52, 55, 62] had revealed that nanopowders comprising smaller aggregates and narrow unimodal size distribution of particles undergo homogeneous particle packing which in turn results in small pores with a narrow size distribution during sintering. Thus, homogeneous particle packing leads to uniform densification and yields a final product with controlled microstructure [55, 62, 94]. Further, the densification rate is higher when nc powders with a narrow unimodal size distribution of particles are used [55, 66].

1.8 Advanced sintering methods

Several studies were carried out pertaining to microstructure refinement by optimizing the sintering curve profile which includes Rate Controlled Sintering (RCS) [98], Two-Step Sintering (TSS) [99-102] and Spark Plasma Sintering (SPS) [103-105]. In RCS, the relationship between the densification and grain growth rate is obtained which in turn helps to identify the soaking temperature and duration of sintering for obtaining dense ceramics [101].

1.8.1 Two-step sintering (TSS) method proposed by Chu [102]

Chu et al. [102] had devised a novel two-step procedure (TSS_C) to sinter powders with wide size distribution of particles to high density. In this method [101, 102], the green compacts are subjected to “pre-heat treatment” at a low temperature (T1) followed by high temperature sintering (T2) [$T1 < T2$] (Fig. 1.4). Chu et al. [102] had successfully sintered conventional alumina (Al_2O_3) and magnesia (MgO) powders to a very high density and uniform microstructure (grain refinement) by using TSS_C. These authors [102] claim that “pre-heat treatment" eliminates fine particles by Ostwald ripening and delays the onset of abnormal grain growth, thus preventing differential densification. Thus, TSS_C method devised by Chu et al. [102] is a promising one to obtain a dense ceramic body with uniform microstructure and smaller grain sizes.

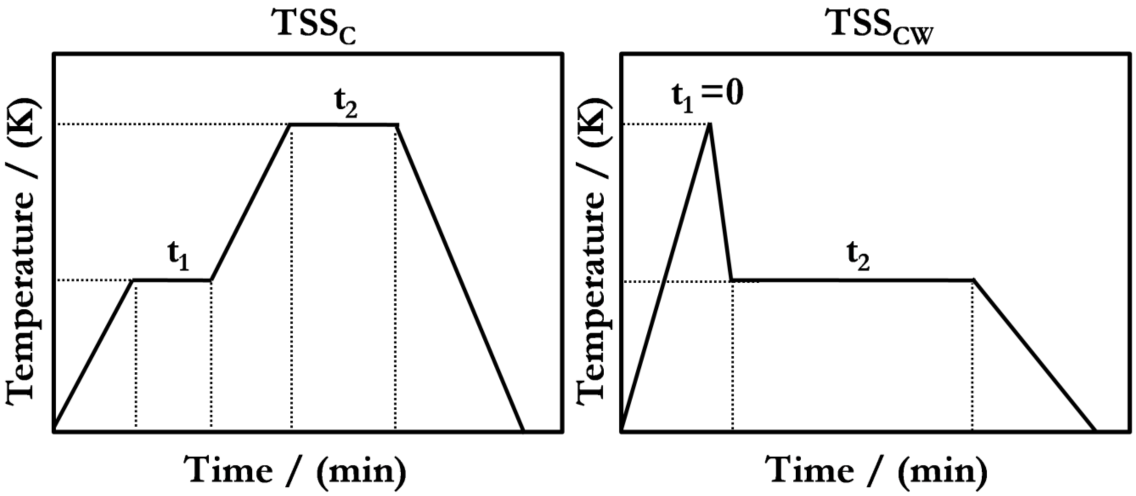

Figure 1.4 *Illustrative representation of the TSS_C and TSS_{CW} sintering plots as illustrated by Loh et al. [101](where TSS_C and TSS_{CW} denotes two-step sintering methods proposed by Chu [102] and Chen and Wang [99])*

1.8.2 Two-step sintering (TSS) method proposed by Chen and Wang [99]

Another TSS method devised by Chen and Wang [99] is the most widely used sintering technique to obtain dense ceramic body with controlled microstructure from an nc powder. This (TSS_{CW}) proposed by Chen and Wang [99] limits "runaway" sintering and yields a product with uniform grain size. In this method the sample is taken to a very high temperature [T_1] for a short duration (critical density: $\rho \geq 75$ % T.D) and then cooled and held at a lower temperature [T_2], for a longer duration (T1 > T2). Chen and Wang [99] had reported that during the first step in the TSS_{CW} the compact should attain a relative density of about 75 % in order to obtain unstable pores (Fig. 1.4). While in the second stage the grain growth is suppressed and the densification occurs with a frozen microstructure and a slower kinetics.

It is well known that the sintering phenomenon of real materials could not be explained by using models as it were built on various assumptions (for instance: uniform shape and size). However, it is reported that the diffusion kinetics of “two-step sintered” products could be estimated by measuring their normalized densification rate (final product) and comparing it with Herring’s dimensional theory [99]. The normalized densification rate ($d\rho/\rho dt$, where ρ is relative density and t is time) is given as (eqn. 1.4):

$$\frac{d\rho}{\rho dt} = F(\rho)\left(\frac{\gamma\Omega}{GkT}\right)\left(\frac{\delta D}{G^3}\right) \tag{1.4}$$

where, $F(\rho)$ is a unspecified function of density (ρ) which is independent of the grain size, γ is the surface energy, Ω is the atomic volume, G is the grain size, δ is the grain boundary thickness, k is the Boltzmann constant and D is grain boundary diffusivity. It is also reported that densification without grain growth requires not only suppression of grain boundary migration but also retention of active grain boundary diffusion [100]. Grain boundary migration and grain boundary diffusion are activation controlled processes [100]. The activation energy of the former is higher than that of the latter [100]. Hence grain boundary migration is suppressed at lower temperatures. It is now being perceived that in the TSS_{CW} higher T1 temperature is required for bringing about a different sintering mechanism below and above a critical density [100]. Particle coarsening and repacking are possible mechanisms for densification below this critical density [54, 106]. Otherwise pores would grow as predicted by the Kingery and Francois theory [107]. Particle coarsening takes place at a lower temperature itself since the activation energy for surface diffusion is lower than that of grain boundary diffusion [54, 106]. However, particle repacking would require a higher energy [106]. Hence a higher T1 is employed [106]. Once the critical density is achieved grain boundary diffusion alone is sufficient for densification at T2. However, T2 should not be too low to weaken the diffusion process [106].

1.8.3 Field-Assisted Sintering Technology / Spark plasma sintering (FAST/SPS)

The field-assisted sintering technique or Spark Plasma Sintering is a technique which involves consolidation of the powders or green compacts under the simultaneous action of a low-voltage, pulsed direct current (DC) and mechanical pressure [103]. Though it is similar to hot pressing (HP) wherein the powders or green pellet is sintered under the action of a thermal and mechanical stress, it differs from HP in the mode of heating (heat production and its transmission through the material) [103-105]. In HP, the heating element indirectly heats the punch, die and the powder through radiation, conduction and convection [104]. The passage of electric current through the heating element produces heat (Joule heating or ohmic heating or resistive heating) and the power of heat generated depends on current and resistance of the heating element [103, 104]. Further, the heating rate depends exclusively on the heat transfer modes (radiation, conduction and convection) [104]. However, in SPS the electric current and heat (Joule heat) are passed directly through the punches. The electric current density is of the order > 10 kA cm^{-2} and the heating rate of the powder could reach 10^6 Ks^{-1} [104]. Further details about this technique and the experimental conditions (electric effects, thermal effects, mechanical effects and sintering atmosphere) which would affect the final densification are explained in ref. [103]. This method is particularly useful for producing oxides with high density and very small grain size (< 1 μm) [62, 103, 108].

Sintering data pertaining to SPS of nc-HfO_2, nc-YSH and Y_2O_3 are rather limited. Tyrpekl et al. [109] had prepared YSH ($Hf_{0.85}Y_{0.15}O_{2-x}$) by employing the external gelation method and the derived beads were sintered by using SPS (57 MPa; 1873 K; 5 min). Further, no reports have been published so far on the SPS of nc-HfO_2 powders. Bu et al. [110] had sintered ball milled YSH powders by using both the conventional and SPS techniques (100 MPa; 1923 K;

3 min). Chapter 6 and Chapter 7 elaborate in detail about the SPS studies carried out by various authors on nc-Y_2O_3 and HfO_2 (microcrystalline) and YSH powders. Hence, in this study we carried out the preliminary investigations on the SPS of nc-Y_2O_3, nc-HfO_2 and YSH. Further, the SPS studies of volume combustion derived nc-Y_2O_3 powders and SMS derived nc-HfO_2 and YSH powders reported in this study are first of its kind.

References

[1] I. Pioro, R. Duffey, J. Nucl. Eng. Rad. Sci. 1(1) (2015) 011001-19.

[2] K. Saidi, M. Ben Mbarek, Prog. Nucl. Energy 88 (2016) 364-374.

[3] S. Banerjee, H.P. Gupta, Prog. Nucl. Energy 101 (2017) 4-18.

[4] M.M. Abu-Khader, Prog. Nucl. Energy 51(2) (2009) 225-235.

[5] M. Salvatores, G. Palmiotti, Prog. Part. Nucl. Phys. 66(1) (2011) 144-166.

[6] India Energy Outlook, Organisation for Economic Co-operation and Development (OECD), International Energy Agency (IEA), France, 2015.

[7] Potential Benefits and Impacts of Advanced Nuclear Fuel Cycles with Actinide Partitioning and Transmutation, OECD - NEA, Paris, 2011.

[8] P. Yvon, F. Carré, J. Nucl. Mater. 385(2) (2009) 217-222.

[9] M.T. Simnad, Nuclear Reactor Materials and Fuels A2 - Meyers, Robert A, Encyclopedia of Physical Science and Technology (Third Edition), Academic Press, New York, 2003.

[10] L. Ge, Processing of Uranium Dioxide Nuclear Fuel Pellets using Spark Plasma Sintering, PhD Thesis, University of Florida, 2014.

[11] R. Jovani-Abril, Synthesis and Characterization of nanocrystalline UO_2 ceramics, PhD Thesis, Universidad de Santiago de Compostela (USC), Institute for Transuranium Elements (ITU), 2014.

[12] S. Yeo, UO_2-SiC Composite Reactor Fuels with enhanced Thermal and Mechanical properties prepared by Spark Plasma Sintering, PhD Thesis, University of Florida, 2013.

[13] Report to Congress on Advanced Fuel Cycle Initiative: The Future Path for Advanced Spent Fuel Treatment and Transmutation Research, U.S. Department of Energy (DOE), Office of Nuclear Energy, Science and Technology, 2003.

[14] IRSN - Review of Generation IV Nuclear Energy Systems, France, 2014.

[15] T. Allen, J. Busby, M. Meyer, D. Petti, Mater. Today 13(12) (2010) 14-23.

[16] A. Gopalakrishnan, Annu. Rev. Energy Env., 27(1) (2002) 369-395.

[17] OECD, Introduction of Thorium in the Nuclear Fuel Cycle - Short to long consideration, Nuclear Science, OECD, 2015.

[18] Thorium Fuel Cycle - Potential Benefits and Challenges, International Atomic Energy Agency (IAEA), Vienna, 2005.

[19] R.J.M. Konings, (Ed.), Comprehensive Nuclear Materials, Elsevier, Amstersam, 2012.

[20] A.K. Sengupta, R. Agarwal, H.S. Kamath, Carbide Fuel A2 - R.J.M. Konings, (Ed.) Comprehensive Nuclear Materials, Elsevier, Amstersam, 2012, 55-86.

[21] R.K. Sinha, Energy Procedia 7 (2011) 34-50.

[22] R.K. Sinha, A. Kakodkar, Nucl. Eng. Des., 236(7) (2006) 683-700.

[23] The Statute of the International Atomic Energy Agency (IAEA) XX: Definitions, Vienna, Austria, 2013.

[24] Experiences and Trends of Manufacturing Technology of Advanced Nuclear Fuels, International Atomic Energy Agency (IAEA), Vienna, 2012.

[25] Development Status of Metallic, Dispersion and Non-oxide Advanced and Alternative Fuels for Power and Research Reactors, International Atomic Energy Agency (IAEA), Vienna, 2003.

[26] B.J. Lewis, E.N. Onder, A.A. Prudil, Fundamentals of Nuclear Engineering, Wiley, United Kingdom, 2017.

[27] V.V. Rondinella, T. Wiss, Mater. Today 13(12) (2010) 24-32.

[28] Impact of High Burnup Uranium Oxide and Mixed Uranium-Plutonium Oxide Water Reactor Fuel on Spent Fuel Management, International Atomic Energy Agency (IAEA), Vienna, 2011.

[29] P. Fors, P. Carbol, S. Van Winckel, K. Spahiu, J. Nucl. Mater. 394(1) (2009) 1-8.

[30] J. Noirot, L. Desgranges, J. Lamontagne, J. Nucl. Mater. 372(2) (2008) 318-339.

[31] J. Spino, H. Santa Cruz, R. Jovani-Abril, R. Birtcher, C. Ferrero, J. Nucl. Mater. 422(1) (2012) 27-44.

[32] W.K. Barney, B.D. Wemple, Metallography of UO_2-Containing Fuel Elements, Technical Report KAPL-1836, Knolls Atomic Power Lab., Schenectady, New York, 1958.

[33] J. Belle, Uranium Dioxide: Properties and Nuclear Applications. In: Naval Reactors Physics Handbook, United States Atomic Energy Commission, Washington, 1961.

[34] N. Lozano, L. Desgranges, D. Aymes, J.C. Niepce, J. Nucl. Mater. 257(1) (1998) 78-87.

[35] M. Teague, B. Gorman, J. King, D. Porter, S. Hayes, J. Nucl. Mater. 441(1) (2013) 267-273.

[36] M. Teague, B. Gorman, B. Miller, J. King, J. Nucl. Mater. 444(1) (2014) 475-480.

[37] G.Z. Chen, D.J. Fray, T.W. Farthing, Nature 407(6802) (2000) 361-364.

[38] D. Sri Maha Vishnu, N. Sanil, G. Panneerselvam, R. Sudha, K. S. Mohandas, K. Nagarajan, J. Electrochem. Soc. 160(9) (2013) D394-D402.

[39] J.-M. Hur, S.M. Jeong, H. Lee, Electrochem. Commun. 12(5) (2010) 706-709.

[40] S.H. Na, D.Y. Song, K.H. Kim, S.O. Bae, J.M. Park, C.G. Ji, H.J. Hwang, Porous UO_2 sintered pellet for electroreduction process, and preparation method thereof, US 2014/0093733 A1, 2014.

[41] K. Ananthasivan, Development of Methods and Materials for the Determination of Solid to Liquid Phase Transformation Temperatures in Alloys, PhD Thesis, University of Madras, 2002.

[42] S. Balakrishnan, K. Ananthasivan, K.C. Hari Kumar, J. Alloys Compd. 689 (2016) 751-758.

[43] W.D. Wilkinson, Uranium Metallurgy, first ed., Vol. 2, Interscience Publishers, New York 1962.

[44] H.M. Feder, N.R. Chellew, C.L. Rosen, Interaction of uranium and its alloys with ceramic oxides, Argonne National Laboratory, U.S.A, 1957.

[45] G. Billings, Refractory crucibles and molds for containing reactive molten metals and salts, US 2001/0033950 A1, 2001.

[46] M.P. Bochiechio, J.J. Marcin, A.D. Cetel, D.M. Shah, K.W. Schlichting, Crucible for master alloying, US 8323559 B2, 2012.

[47] P. Piluso, M. Ferrier, J.P. Bonnet, Refractory ceramic material having a high solidus temperature, its manufacturing process and structural part incorporating said material, US 8236414 B2, 2009.

[48] P. Piluso, M. Ferrier, C. Chaput, J. Claus, J.-P. Bonnet, J. Eur. Ceram. Soc. 29(5) (2009) 961-968.

[49] J. Wang, H.P. Li, R. Stevens, J. Mater. Sci. 27(20) (1992) 5397-5430.

[50] C. Suryanarayana, Int. Mater. Rev. 40(2) (1995) 41-64.

[51] C. Suryanarayana, C.C. Koch, Hyperfine Interact. 130(1) (2000) 5.

[52] A. Mukhopadhyay, B. Basu, Int. Mater. Rev. 52(5) (2007) 257-288.

[53] A.V. Ragulya, Adv. Appl. Ceram. 107(3) (2008) 118-134.

[54] Z.Z. Fang, H. Wang, Advances in Applied Ceramics 53(6) (2008) 326-352.

[55] R. Chaim, M. Levin, A. Shlayer, C. Estournes, Adv. Appl. Ceram. 107(3) (2008) 159-169.

[56] H. Hahn, Nanostruct. Mater. 9(1) (1997) 3-12.

[57] C. N. R. Rao, P. J. Thomas, G. U. Kulkarni, Synthesis of Nanocrystals, Nanocrystals: Synthesis, Properties and Applications, Springer Berlin Heidelberg, New York, 2007.

[58] A.R. West, Solid State Chemistry and Its Applications, Wiley India Pvt. Ltd., New Delhi, 1987.

[59] V. Tyrpekl, J.-F. Vigier, D. Manara, T. Wiss, O. Dieste Blanco, J. Somers, J. Nucl. Mater. 460 (2015) 200-208.

[60] R.C. Rau, J. Am. Ceram. Soc. 47(4) (1964) 179-184.

[61] J.R. Groza, Nanostruct. Mater. 12(5) (1999) 987-992.

[62] R. Castro, K. Van Benthem, Sintering: Mechanisms of Convention Nanodensification and Field Assisted Processes, Springer Berlin Heidelberg, 2012.

[63] M.N. Rahaman, Ceramic Processing and Sintering, Marcel Dekker Inc., New York, 2003.

[64] M.N. Rahaman, Sintering Process Variables and Sintering Practice, Sintering of Ceramics, CRC Press, Florida, 2008, 305-370.

[65] T. Klassen, M. Oehring, R. Bormann, Acta Mater. 45(9) (1997) 3935-3948.

[66] K. Lu, Int. Mater. Rev. 53(1) (2008) 21-38.

[67] H.F. Lu, R.Y. Hong, H.Z. Li, J. Alloys Compd. 509(41) (2011) 10127-10131.

[68] H. Casanova, L.P. Higuita, Chem. Eng. J. 175 (2011) 569-578.

[69] Y. Lai, M. Meng, Y. Yu, X. Wang, T. Ding, Appl. Catal. B, 105(3) (2011) 335-345.

[70] G. Chen, W. Wang, Drying Technol. 25(1) (2007) 29-35.

[71] S. Zha, Q. Fu, Y. Lang, C. Xia, G. Meng, Mater. Lett. 47(6) (2001) 351-355.

[72] K. Ananthasivan, S. Anthonysamy, A. Singh, P.R. Vasudeva Rao, J. Nucl. Mater. 306(1) (2002) 1-9.

[73] Z. Zhang, M. Lu, H. Xu, W.-S. Chin, Chem. Eur. J. 13(2) (2007) 632-638.

[74] D. Hudry, C. Apostolidis, O. Walter, T. Gouder, E. Courtois, C. Kübel, D. Meyer, Chem. Eur. J. 18(27) (2012) 8283-8287.

[75] M. Niederberger, G. Garnweitner, Chem. Eur. J. 12(28) (2006) 7282-7302.

[76] N. Pinna, G. Neri, M. Antonietti, M. Niederberger, Angew. Chem. Int. Ed. 43(33) (2004) 4345-4349.

[77] S. Ekambaram, K.C. Patil, J. Mater. Chem. 5(6) (1995) 905-908.

[78] V. Chandramouli, S. Anthonysamy, P.R. Vasudeva Rao, J. Nucl. Mater. 265(3) (1999) 255-261.

[79] S.T. Aruna, A.S. Mukasyan, Curr. Opin. Solid State Mater. Sci. 12(3) (2008) 44-50.

[80] F.-t. Li, J. Ran, M. Jaroniec, S.Z. Qiao, Nanoscale 7(42) (2015) 17590-17610.

[81] H. Palneedi, V. Mangam, S. Das, K. Das, J. Alloys Compd 509(41) (2011) 9912-9918.

[82] S. Anthonysamy, K. Ananthasivan, V. Chandramouli, I. Kaliappan, P.R. Vasudeva Rao, J. Nucl. Mater. 278(2) (2000) 346-357.

[83] S. Balakrishnan, K. Ananthasivan, K.C. Hari Kumar, Ceram. Int. 40(5) (2014) 6777-6785.

[84] R.D. Purohit, S. Saha, A.K. Tyagi, Curr. Opin. Solid State Mater. Sci. 288(1) (2001) 7-10.

[85] R.V. Mangalaraja, J. Mouzon, P. Hedström, C.P. Camurri, S. Ananthakumar, M. Odén, Powder Technol. 191(3) (2009) 309-314.

[86] S. Biamino, P. Fino, M. Pavese, C. Badini, Ceram. Int. 32(5) (2006) 509-513.

[87] T. Kimura, Molten Salt Synthesis of Ceramic Powders, in: C. Sikalidis (Ed.), Advances in Ceramics - Synthesis and Characterization, Processing and Specific Applications, InTech, Rijeka, 2011.

[88] P. Afanasiev, C. Geantet, Coord. Chem. Rev. 178 (1998) 1725-1752.

[89] X. Liu, N. Fechler, M. Antonietti, Chem. Soc. Rev. 42(21) (2013) 8237-8265.

[90] H. Flood, T. Forland, Acta Chem. Scand. 1 (1947) 592-604.

[91] D.H. Kerridge, Pure Appl. Chem. 41 (1975) 355-371.

[92] B. Durand, J.P. Deloume, M. Vrinat, Mat. Sci. Forum (152-153) (1994) 327-330.

[93] R.M. German, Sintering Theory and Practice, John Wiley & Sons Inc, New York, 1996.

[94] M.N. Rahaman, Sintering of Ceramics, CRC Press, Boca Raton, Florida, 2007.

[95] P.K. Kulriya, T. Yao, S.M. Scott, S. Nanda, J. Lian, J. Nucl. Mater. 487 (2017) 373-379.

[96] F. Cappia, R. Jovani-Abril, J. Spino, L. Luzzi, A. Janßen, D. Manara, Prog. Nucl. Energy, 72 (2014) 11-16.

[97] D. Manara, C. Ronchi, M. Sheindlin, M. Lewis, M. Brykin, J. Nucl. Mater. 342(1) (2005) 148-163.

[98] J. Wang, R. Raj, J. Am. Ceram. Soc. 73(5) (1990) 1172-1175.

[99] I.W. Chen, X.H. Wang, Nature 404(6774) (2000) 168-171.

[100] G. B. P. Ferreira, J. F. da. Silva Jr, R. M. do Nascimento, U. U. Gomes, A.E. Martinelli, Two-Step Sintering Applied to Ceramics, in: Arunachalam Lakshmanan (E.d.), Sintering of Ceramics - New Emerging Techniques, InTech., 2012.

[101] N.J. Lóh, L. Simão, C.A. Faller, A. De Noni, O.R.K. Montedo, Ceram. Int. 42(11) (2016) 12556-12572.

[102] M.-Y. Chu, L.C. De Jonghe, M.K.F. Lin, F.J.T. Lin, J. Am. Ceram. Soc. 74(11) (1991) 2902-2911.

[103] O. Guillon, J. Gonzalez-Julian, B. Dargatz, T. Kessel, G. Schierning, J. Räthel, M. Herrmann, Adv. Eng. Mater. 16(7) (2014) 830-849.

[104] G. Salvatore, S. Yoshio, M. Giovanni, Sci. Technol. Adv. Mater. 10(5) (2009) 053001.

[105] J.E. Alaniz, J.R. Morales, J.E. Garay, JOM 62(2) (2010) 58-62.

[106] X.-H. Wang, P.-L. Chen, I.W. Chen, J. Am. Ceram. Soc. 89(2) (2006) 431-437.

[107] W.D. Kingery, B. Francois, The Sintering of Crystalline Oxides, I. Interactions Between Grain Boundaries and Pores, in: S. Sōmiya, Y. Moriyoshi (Eds.), Sintering Key Papers, Springer Netherlands, Dordrecht, (1990) 449-466.

[108] R. Chaim, R. Marder, C. Estournés, Z. Shen, Adv. Appl. Ceram. 111(5-6) (2012) 280-285.

[109] V. Tyrpekl, M. Holzhäuser, H. Hein, J.-F. Vigier, J. Somers, P. Svora, J. Nucl. Mater. 454(1) (2014) 398-404.

[110] J. Bu, P.G. Jönsson, Z. Zhao, Ceram. Int. 41(2) (2015) 2611-2615.

Chapter 2

Experimental

In this chapter details pertaining to the chemicals, reagents and materials that have been used in this study and the experimental procedures and instruments that had been used for characterizing the powders, green pellets and sintered products are also presented.

2.1 Chemicals

Uranium oxide powders and thorium nitrate of nuclear grade purity were supplied by M/s. Indian Rare Earths Limited (IREL) and Nuclear Fuel Complex (NFC), India respectively. Uranium metal of 99.9 % pure was supplied by BARC, Mumbai. Nitric acid, phosphoric acid, sulphuric acid and hydrofluoric acid of AR grade were procured from M/s. Merck, India. Ferroin indicator (0.025 M) and citric acid of AR grade (>99.5 %) were obtained from Loba Chime Pvt. Ltd. India. Ferrous ammonium sulphate (AR grade) was procured from M/s. Merck, India. Hafnium (IV) chloride (99.9% pure) and yttrium nitrate hexahydrate (99.9% pure) were procured from M/s. Otto Chemie Pvt. Ltd. India. KNO_3 (GR 99.5 %) and $NaNO_3$ (GR 99.5 %) were obtained from M/s. Merck Specialties Pvt. Ltd, India. Propan-2-ol and silver nitrate (AR grade) were received from M/s. Merck, India. Dibutyl phthalate (DBP 99 % pure) was supplied by M/s. Ranbaxy Fine Chemicals Ltd, India.

2.2 Scaled-up synthesis of nanocrystalline oxide powders

Nanocrystalline powders of urania, thoria and yttria were prepared on a 60 g scale by using citrate gel-combustion method. Hafnia and yttria stabilized hafnia (YSH) were prepared on a 30 g scale by using the SMS.

2.2.1 Preparation of nanocrystalline powders by gel-combustion method

2.2.1.1 Preparation of uranyl nitrate

Urania powder was converted quantitatively into U_3O_8 powders by heating in air at 773 K for 4 h. An appropriate amount of this powder was taken and dissolved in concentrated nitric acid (12 *M*). This solution was heated on a hot plate to dryness to obtain uranyl nitrate crystals, which were dissolved subsequently in distilled water. The amount of nitrate present in this solution was quantitatively determined by titrimetry [1]. For this estimation, a known quantity of uranyl nitrate solution was taken along with 25 mL of 0.2 *N* ferrous ammonium sulphate (FAS), acidified with 10 mL of (12.2 *M*) HCl and 25 mL H_2SO_4 (18.4 *M*) and titrated against $K_2Cr_2O_7$ (0.1 *N*) by using ferroin indicator under ice cold condition. The exact amount of fuel (citric acid or sucrose) required for carrying out the combustion reaction with a particular value of fuel to nitrate mole ratio (R) was calculated from the estimated value of the concentration of nitrate.

2.2.1.2 Preparation of yttrium nitrate and thorium nitrate

Yttrium nitrate solution was prepared by dissolving preheated (473 K, 2 h) Y_2O_3 in 12 *M* nitric acid by warming it on a hot plate. In a typical experiment, yttrium nitrate / thorium nitrate solution was prepared by dissolving an appropriate quantity of the metal nitrate in a minimum quantity of distilled water. The nitrate content of this solution was estimated by using titrimetry [1] (Section 2.2.1.1).

2.2.1.3 Citrate gel-combustion synthesis of nc-urania, nc-thoria and nc-yttria powders

In a typical gel-combustion synthesis (urania, thoria and yttria), desired quantities of the fuel and oxidant were dissolved in a minimum quantity of demineralized water and warmed on a hot plate. R values chosen for the preparation of nc-urania, nc-thoria and nc-yttria powders are presented in Table 2.1.

Table 2.1 R values of the mixtures employed in citrate gel-combustion experiments

S. No.	Materials	Index			Value of R & index "XX"								
		A	C	H									
1	nc-urania	U_CXXA	U_CXXC	U_CXXH	R	0	0.05	0.10	0.25	0.50	0.75	0.90	1.00
					XX	0	05	10	25	50	75	90	100
2	nc-thoria	T_CXXA	T_CXXC	-	R	0	0.05	0.125	0.17	0.25	0.50		
					XX	0	05	12.5	17	25	50		
3	nc-yttria	Y_CXXA	Y_CXXC	-	R	0.17							
					XX	17							

The combustion mixture was gelated on a hot plate. Upon prolonged heating the gel got dehydrated and auto ignition ensued leaving behind a carboneous residue. These powders were named as "as prepared" powders (A). These powders were calcined in air in a furnace fitted with SiC heating element at 1073 K for 4 h to remove the residual carbon. The powders thus derived were named as the "calcined" powders (C).

"Calcined" urania powders were subsequently reduced to UO_2 in a flowing stream of hydrogen (flow rate = 400 mL min^{-1}) at a pressure of 49 to 98 kPa in a custom made furnace equipped with inconel sample holders at 1123 K for 5 h 30 min. The powders thus derived were named as "hydrogen reduced" powders (H). The indices used to denote the different "combustion derived" samples are presented in Table 2.1

2.2.2 SMS of nc-Hafnia and nc-YSH

Fine grained nc-hafnia and nc-YSH were prepared in bulk quantities (30 g) by using SMS. In a typical experiment an appropriate quantity of the eutectic salt mixture ($NaNO_3$-KNO_3) was mixed with either $HfCl_4$ and $NaNO_2$ (for preparing nc-HfO_2 powders) or $Y(NO_3)_3.6H_2O$ and $HfCl_4$ (for synthesizing nc-yttria stabilized hafnia powders). The weight ratio of metal salts to that of the eutectic mixture was maintained at 1:4. This reaction mixture was transferred into a

180 mm long one end closed quartz reaction tube, which in turn was placed into a quartz muffle tube (400 mm long, 100 mm outer diameter, 2.5 mm thick) [Fig. 2.1].

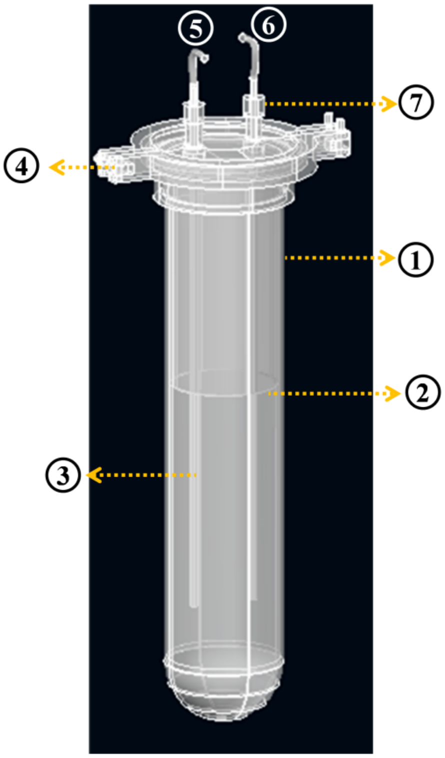

1. **One end closed quartz tube: 400mm long**
2. **One end closed quartz tube: 180mm long**
3. **Quartz tube**
4. **Teflon enclosure**
5. **Argon inlet**
6. **Argon outlet**
7. **Veco coupling**

Figure 2.1 A schematic of the experimental set-up used in the SMS of nc-HfO_2 and nc-YSH

The entire assembly was lowered into a pit type nichrome wire wound resistance furnace (M/s. High Temp Ind, Kochi, India). The mouth of this muffle tube was covered with a lid fabricated out of poly tetra fluoro ethylene (PTFE) that had provisions for purging argon through the reaction mass. The reaction mixture was heated under an argon flow of 250 mL min^{-1} at 673 K, for an hour and then cooled. Subsequently the whole assembly was cooled to room temperature. The contents were discharged from the reaction tube and treated with demineralized water, upon which the chlorides and nitrates dissolved leaving behind an insoluble oxide residue. Washing was repeated many times and the supernatant liquid was tested for chloride residue. The washing was stopped when the supernatant liquid did not yield either turbidity or a white precipitate upon treating with a few drops of $AgNO_3$ solution (0.1 wt/vol %). The powders thus obtained were washed and were dispersed in propan-2-ol and ultrasonicated for 1 h at 323 K. Subsequently, this suspension was subjected to vacuum filtration to obtain the product. The oxide residue was dried in an oven at 393 K in air for 5 h and stored in an air tight container for further processing. The preparation of nc-HfO_2 powder was carried out with five different salt mixtures that contained nitrite to nitrate in the mole ratio (Φ) of 0, 0.05, 0.11, 0.32 and 0.82 respectively (Flow sheet-Fig. 2.2). The details pertaining to the nomenclature used to denote the mixtures and products are given in Table 2.2.

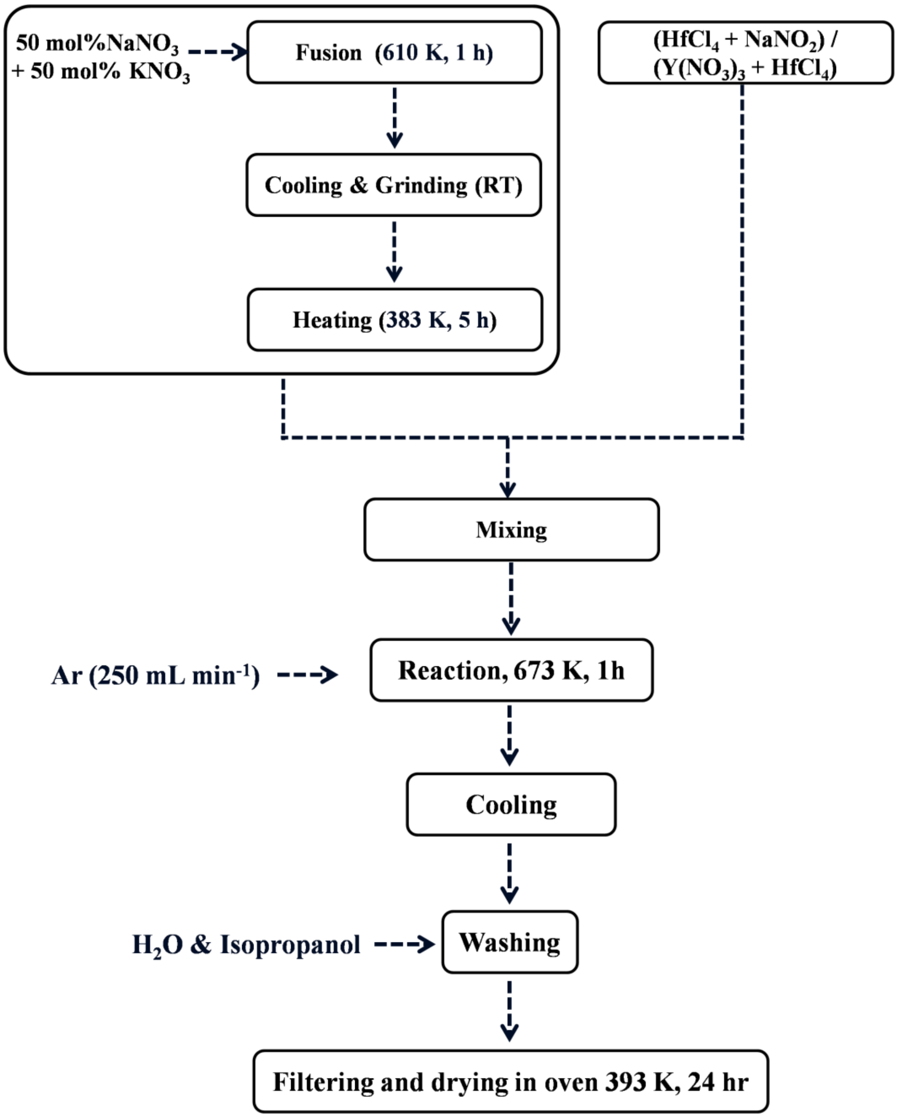

Figure 2.2 Flow sheet for the preparation of nc-HfO_2 / nc-YSH through SMS

Table 2.2 Φ values of the mixtures and indices of powders derived in SMS

S. No.	Materials	Index	Value					
1	nc-HfO_2	HfYD	Φ	0	0.055	0.11	0.32	0.82
			Y	0	5.5	11	32	82
2	nc-YSH	xxYSH	(mol% of Y)	6	10	14	20	30
			xx	6	10	14	20	30

where D – dried powders and $Y = \Phi * 100$

2.3 Preparation of porous UO_2

Porous UO_2 bodies (either foam or a pellet) were prepared by two different methods. UO_2 foam was prepared through the ignition of a gel made from sucrose and uranyl nitrate while the porous pellets were prepared from a nc powder derived through the citrate gel combustion of uranyl nitrate.

2.3.1 Novel gel-combustion process for the preparation of porous UO_2 pellets

In the preparation of porous UO_2 pellets a procedure similar to that employed in the preparation of UO_2 powders (Section 2.2.1) was used, except that the calcination and hydrogen reduction steps were excluded. The "as prepared" powders (R = 0.25 and 1.0) were consolidated at different pressures viz., 60, 120, 180, 243, 280, 317 and 353 MPa.

2.3.2 Novel gel-combustion process for the preparation of UO_2 foam

In a typical experiment the exact quantity of sucrose required to carry out the reaction with a predetermined sucrose to nitrate mole ratio (R) was calculated. This mixture containing sucrose and uranyl nitrate held in a polytetrafluorloethylene (PTFE) beaker (200 mL) was heated on a hot plate to form a dark viscous resin and subsequently the urania xerogel. These xerogel was heated at 393 K for 24 h in an oven. The product thus obtained was then cut into pieces of definite shapes.

2.4 Thermal analysis of gel-combustion reaction, salt melt reaction and products

2.4.1 Differential Scanning Calorimetry (DSC)

Heat flux differential scanning calorimetry (DSC) supplied by M/s. Mettler Toledo GmbH, Switzerland (model DSC821e/700) was used to determine the quantity of the heat liberated during the combustion reaction. For the DSC experiment, citrate gels containing thorium (R = 0.50) and uranyl ions (R = 0.25) were prepared, dried and loaded in a Pt pan of 70 µL capacity and heated at 10 K min^{-1} in flowing high purity O_2 (50 mL min^{-1}). At first, the sample was heated to 378 K and held at this temperature for about 10 min and subsequently cooled to room temperature in flowing O_2. Without altering the rates of heating and gas flow, the mixture was heated again from room temperature to 973 K. The details of the experimental procedure adopted for carrying out the calibration of the DSC instrument for the measurement of temperature, heating rate and heat flow are described elsewhere [2]. DSC experiments (similar to those described earlier) were also carried out with gels containing uranyl nitrate and citric acid (R = 0.25) at different heating rates viz., 5, 10, 15 and 20 K min^{-1} to elucidate the kinetics and mechanism of citrate gel-combustion reaction.

In the mixtures used for SMS, in order to ascertain the eutectic reaction temperature ($NaNO_3$-KNO_3), about 3 mg of the eutectic salt mixture was loaded in a Pt pan (70 µL) and heated at a rate of 10 K min^{-1} under flowing high purity Ar gas (flow rate = 50 mL min^{-1}) in the temperature range 298 K to 973 K.

2.4.2 Thermogravimetry-Differential Thermal Analysis coupled with Mass Spectrometry (TG-DTA-MS)

The thermal decomposition of the gel containing uranyl nitrate and citric acid was investigated with the help of simultaneous thermogravimetry (TG) coupled with differential thermal analysis (DTA) and mass spectrometry (MS). A TG-DTA-MS system SETSYS Evolution 16/18, supplied by M/s Setaram, France was used for this purpose.

Simultaneous thermogravimetry (TG) and differential thermal analysis (DTA) coupled with mass spectrometry (MS) analysis of gel containing thorium nitrate and citric acid as well as mixtures of KNO_3 and $NaNO_3$ (with and without $NaNO_2$) were carried out by using TG-DTA-MS (STA 449 - F3 Jupiter Model) supplied by Netzsch, Germany.

2.5 Characterization of the powders

2.5.1 Measurement of bulk density (ρ_B) of the powders

An electronic balance supplied by M/s. Scaltec, GmbH, Germany was used to estimate the bulk density of all the powders. Bulk densities of all the powders were measured from the weight of the powder that filled up to the rim of a cuvette of known volume (5 mL). The average values of five measurements are reported here.

2.5.2 Determination of size distribution of particles in the nc-powders

A particle size analyzer (laser light scattering, Mastersizer, M/s. Malvern, Worcestershire, UK) was used to measure the size distribution of particles. This equipment was calibrated with alumina standards supplied by NIST, USA. A suspension of the desired sample in demineralised water prepared by stirring was used to determine the particle size distribution (PSD). An appropriate quantity of sample was dispersed into the holder containing millipore water with stirring (2500 rpm). Average of ten measurements is reported. The size distribution of particles was deconvoluted using Origin® 6.1 software (OriginLab Corporation, USA).

2.5.3 Measurement of specific surface area (SSA) of the powders

Specific surface area (SSA) of all the powders was determined by using Thermo Scientific Surfer gas adsorption porosimeter (Thermo Fisher Scientific S.p.A, Milan, Italy). Blank analyses as well as calibration were carried out before analyses with the help of powder standards obtained from NIST. The powders were heated (degassed) at 393 K to remove surface adsorbed moisture and gases and were subsequently evacuated at a pressure of 0.1 Pa for 5 h by using a rotary pump (Pfeiffer-Model Duo1.6, Germany).

2.5.4 Determination of carbon residue (RC) of particles in the nc powders

Carbon residue present in all these samples was determined by using a carbon analyzer (Eltra CS 800, Germany). Mixtures containing about 200 mg of the samples and 1500 mg of tungsten were taken in an alumina crucible and heated in an induction furnace under flowing O_2. The CO_2 evolved was quantitatively measured by using an IR detector.

2.5.5 Determination of size and distribution of pores (P_OSD)

a) Mercury porosimetry

Analyses of the distribution of sizes of the pores (10 nm to 50 μm) present in the powders were carried out by using Pascal 140 and 440 mercury porosimeters (Thermo Fisher Scientific S.p.A, Milan, Italy) at an operating pressure range of 0.1 to 400 kPa and 0.1 to 400 MPa respectively. Blank analyses as well as calibration were carried out before analyzing the sample in the mercury porosimeter experiments by using alumina standards (SRM 1918) obtained from NIST.

b) Gas adsorption

Analyses of size distribution of pores (< 50 nm) present in the powders were also carried out by using Thermo Scientific Surfer gas adsorption porosimeter (Thermo Fisher Scientific S.p.A, Milan, Italy). Calibration was carried out by using powder standards obtained from NIST. Evaporation of the liquid N_2 condensate from the pores are related to the pore diameter. By using

Kelvin equation the pore diameter were derived from the volume of the gas desorbed (evaporated) from the pore.

c) Liquid immersion

Open and closed porosity in all the sintered pellets and cups were determined by employing ASTM C1039-85 procedure. DBP was used as the pycnometric liquid. Average of five different measurements is reported here. This method involved measuring the volume of the open pores from the volume of the liquid entrapped in them. The volume of closed pores was obtained by difference from the total and open porosity.

2.5.6 Spectroscopic analysis of starting materials, gels and powders

Uranyl nitrate and thorium nitrate samples were analyzed for impurity by using an Inductively Coupled Plasma – Mass Spectrometer (ICP-MS) [ELAN 250, M/s. Perkin Elmer, Canada]. ICP-OES measurements were carried out with Ultima C, HORIBA, Jobin Yvon, Longjumeau, France. This instrument was calibrated by measuring standard solutions of metals certified by National Institute of Standards and Technology (NIST).

Nitrate solutions were mixed with 4 *M* HNO_3 and equilibrated along with a drop of HF and tributyl phosphate (TBP) solution (30% TBP in dodecane). This process was repeated three times to remove uranium / thorium ions from the solution [3]. The aqueous solution thus obtained was diluted and subjected to ICPMS and ICPOES analysis.

The FTIR spectrum was recorded by using MB 100 FT-IR spectrometer (BOMEM, Canada). To obtain a good signal to noise (S/N) ratio, the samples were scanned for at least 8 times. This spectrometer has a resolution of 1 cm^{-1} and operated in the region of 4000-400 cm^{-1}. This instrument is equipped with deuterated triglycine sulfate (DTGS) detector. Calibration was carried out by using salicylic acid standard supplied by NIST.

UV-VIS-NIR spectrophotometer supplied by Shimadzu with model no. UV-3600 was used for spectrophotometric analysis. This instrument was equipped with three detectors, consisting of photomultiplier tubes for the ultraviolet and visible regions and InGaAs and cooled PbS detectors for near infrared region. The wavelength range of 200-1000 nm with double monochromator and rectangular cuvette made up of fused silica with an optical path length of 10 mm were used for measuring the absorbance of the metal complexes.

Micro Raman spectrometer supplied by M/s. Renishaw, (UK, model Invia) was used to record the Raman spectra. A laser excitation source of 514.5 nm was directed through a 10 μm pinhole and was focused by using a microscope on to the sample (a few mg) which is placed on transparent slide. A charge coupled device was used as the detector. Raman shift in the wave numbers was calibrated by using 520.5 nm Raman line from a Si single crystal.

2.6 Preparation of pellets and cups

A semi automatic double action (biaxial) hydraulic powder compacting press (Model No. 027) supplied by M/s. Sri Yugantak Engineers, Bangalore, India was used for compaction. Top punch, die and bottom punches made up of AISI D3 tool steel lined with tungsten carbide were used. These tools were cleaned with acetone before every compaction. To investigate the influence of the compaction pressures (CP) and to elucidate the critical compaction pressure each powder was compacted into green pellets (10 mm diameter) at different compaction pressures (CP) viz., 60, 120, 180, 220, 243, 280, 317 and 353 MPa.

Ceramic cups were compacted by using a double action hydraulic press which was supplied by M/s. Bemco hydraulics Ltd., Belgaum, India. The plungers were made out of high carbon - high chromium (HCHCr) steel while the die was made with tungsten carbide encased in tool steel. The green cups were of the following dimensions; outer diameter x inner diameter x height = 10 mm x 6 mm x 5 mm.

2.7 Sintering of nanocrystalline green bodies

2.7.1 Conventional Sintering (CS)

The CS method involved sintering the green pellet at an isothermal temperature for 4h. The samples nc-UO_2, nc-ThO_2, nc-Y_2O_3, nc-HfO_2 and nc-YSH were sintered by using this procedure. The temperature and procedure used along with the indices of the specimens are given in Table 2.3. All the urania samples were sintered under flowing Ar+8%H_2 (500 mL min^{-1}) while rest of the samples were sintered in air in a furnace equipped with $MoSi_2$ heating elements (M/s. Carbolite UK).

2.7.2 Two-step sintering (TSS)

Two different two-step sintering (TSS) routines were used. TSS_C method involved heating the sample at a lower temperature viz., 1073 K and then at a higher temperature 1473 or 1673 K for about 4 h. This method was used to sinter nc-UO_2 powders, nc-U_3O_8 powders and foam. The details pertaining to the sintering routine and nomenclature are given in Table 2.3.

In the second TSS_{CW} method the samples were held at a higher temperature 1873 K (held at this temperature for 30 min) and cooled to a lower temperature (either 1773 K or 1673 K) at 10 K min^{-1} and held at the latter for about 4 h. This procedure was used in the sintering of nc-ThO_2, nc-Y_2O_3, nc-HfO_2 and nc-YSH. The details pertaining to these sintering routines are presented in Table 2.3 along with the indices used for denoting different products.

Table 2.3 Nomenclature used for indexing the sintered monoliths

Sample		Form	Sintering method		Sintering schedule	Atm	Sample index
Urania	$\mathrm{UO_2}$	Pellet	Conventional sintering (CS)		1673 K; 4 h; 5 K $\mathrm{min^{-1}}$	$\mathrm{Ar+8\%H_2}$	$\mathrm{U_CXXS_C}$
			Two-step sintering ($\mathrm{TSS_1}$)		1473 K; 4 h; 3 K $\mathrm{min^{-1}}$		$\mathrm{U_CXXS_1}$
			Two-step sintering ($\mathrm{TSS_2}$)		**Step 1:** 1073 K; 2 h; 5 K $\mathrm{min^{-1}}$ **Step 2:** 1673 K; 4 h; 3 K $\mathrm{min^{-1}}$		$\mathrm{U_CXXS_2}$
	$\mathrm{UO_2}$	Foam	Two-step sintering ($\mathrm{TSS_3}$)		**Step 1:**1073 K; 30 min; 5 K $\mathrm{min^{-1}}$ **Step 2:** 1473 K; 4 h; 5 K $\mathrm{min^{-1}}$		USXXXS
	$\mathrm{U_3O_8}$	Pellet					$\mathrm{U_CXXA}$-CP
Thoria	$\mathrm{ThO_2}$	Pellet	Conventional sintering	Single step 1 ($\mathrm{CS_1}$)	1673 K; 4 h; 3 K $\mathrm{min^{-1}}$	Air	$\mathrm{T_C13S_{CS1}}$
				Single step 2 ($\mathrm{CS_2}$)	1773 K; 4 h; 3 K $\mathrm{min^{-1}}$		$\mathrm{T_C13S_{CS2}}$
			Two-step sintering	Two-step sintering ($\mathrm{TSS_1}$)	**Step 1:**1873 K; 30 min; 5 K $\mathrm{min^{-1}}$ **Step 2:** 1673 K; 4 h; 5 K $\mathrm{min^{-1}}$		$\mathrm{T_C13S_1}$
				Two-step sintering ($\mathrm{TSS_2}$)	**Step 1:**1873 K; 30 min; 5 K $\mathrm{min^{-1}}$ **Step 2:** 1773 K; 4 h; 5 K $\mathrm{min^{-1}}$		$\mathrm{T_CXXS_2}$
Yttria	$\mathrm{Y_2O_3}$	Pellet	Conventional sintering	Single step 1 ($\mathrm{CS^Y{}_1}$)	1673 K; 4 h; 3 K $\mathrm{min^{-1}}$	Air	$\mathrm{Y_C13S_{CS1}}$
				Single step 2 ($\mathrm{CS^Y{}_2}$)	1773 K; 4 h; 3 K $\mathrm{min^{-1}}$		$\mathrm{Y_C13S_{CS2}}$
			Two-step sintering	Two-step sintering ($\mathrm{TSS^Y{}_1}$)	**Step 1:**1873 K; 30 min; 5 K $\mathrm{min^{-1}}$ **Step 2:** 1673 K; 4 h; 5 K $\mathrm{min^{-1}}$		$\mathrm{Y_C13S_1}$
				Two-step sintering ($\mathrm{TSS^Y{}_2}$)	**Step 1:**1873 K; 30 min; 5 K $\mathrm{min^{-1}}$ **Step 2:** 1773 K; 4 h; 5 K $\mathrm{min^{-1}}$		$\mathrm{Y_CXXS_2}$
Hafnia	$\mathrm{HfO_2}$	Pellet	Conventional sintering	Single step 1 ($\mathrm{CS_1}$)	1673K; 4 h; 3 K $\mathrm{min^{-1}}$	Air	$\mathrm{HfYD_{CS1}}$
				Single step 2 ($\mathrm{CS_2}$)	1773K; 4 h; 3 K $\mathrm{min^{-1}}$		$\mathrm{HfYD_{CS2}}$
				Single step 3 ($\mathrm{CS_3}$)	1873K; 4 h; 3 K $\mathrm{min^{-1}}$		$\mathrm{HfYD_{CS3}}$
			Two-step sintering	Two-step sintering ($\mathrm{TSS_1}$)	**Step 1:**1873 K; 1 h; 3 K $\mathrm{min^{-1}}$ **Step 2:** 1673 K; 1 h; 3 K $\mathrm{min^{-1}}$		$\mathrm{HfYDS_1}$
				Two-step sintering ($\mathrm{TSS_2}$)	**Step 1:**1873 K; 30 min; 3 K $\mathrm{min^{-1}}$ **Step 2:** 1773 K; 4 h; 3 K $\mathrm{min^{-1}}$		$\mathrm{HfYDS_2}$
Yttria stabilized hafnia	YSH	Pellet	Conventional sintering	Single step 1 ($\mathrm{CS_1}$)	1673K; 4 h; 3 K $\mathrm{min^{-1}}$	Air	$\mathrm{xxYSH_{CS1}}$
				Single step 2 ($\mathrm{CS_2}$)	1773K; 4 h; 3 K $\mathrm{min^{-1}}$		$\mathrm{xxYSH_{CS2}}$
				Single step 3 ($\mathrm{CS_3}$)	1873K; 4 h; 3 K $\mathrm{min^{-1}}$		$\mathrm{xxYSH_{CS3}}$
			Two-step sintering	Two-step sintering ($\mathrm{TSS_1}$)	**Step 1:**1873 K; 1 h; 3 K $\mathrm{min^{-1}}$ **Step 2:** 1673 K; 1 h; 3 K $\mathrm{min^{-1}}$		$\mathrm{xxYSHS_1}$
				Two-step sintering ($\mathrm{TSS_2}$)	**Step 1:**1873 K; 30 min; 3 K $\mathrm{min^{-1}}$ **Step 2:** 1773 K; 4 h; 3 K $\mathrm{min^{-1}}$		$\mathrm{xxYSHS_2}$

$\mathrm{U_C}$, $\mathrm{T_C}$ and $\mathrm{Y_C}$ indicate citrate gel-combustion derived urania, thoria and yttria powders respectively; Atm – atmosphere; XX denotes R value in %; $_{\mathrm{CS}}$-conventional sintering; Y = Φ*100 and xx – mole fraction of yttrium (in %). Sintering schedule denotes soaking temperature, duration of soaking & heating/cooling rate.

2.8 Spark plasma sintering (SPS)

Spark Plasma Sintering (SPS) studies of nc powders were carried out using Dr. Sinter Spark Plasma unit (Model SPS-625, SPS Syntex Inc., Japan). Monoliths of HfO_2, YSH and Y_2O_3 were made by using uniaxial pressing under vacuum (≈ 0.133 Pa). The die and punches were made of high density graphite (HDG) material. The dimension of the die and plungers were as follows: inner diameter - 10 mm, outer diameter - 30 mm, height - 40 mm and a centre pin hole - 0.50 mm. Before filling the HDG die with nanocrystalline powders; the inner surface of HDG die was covered with a graphite foil of thickness 0.15 mm. The graphite foil helps to facilitate the easy removal of sintered monoliths. To minimize the radiative heat losses at high temperatures, the die was covered with graphite felt (except the central pin hole). K type thermocouple was used to measure temperature till 873 K. An optical pyrometer was used to measure temperature beyond 873 K and it was focused on to a pin hole on the periphery of the graphite die. SPS compacts had a thickness and diameter of about 2.0 mm and 9.5 mm respectively. The applied voltage, current, temperature and pressure were recorded by the instrumentation provided in the equipment. A compaction pressure (CP) of 50 MPa was applied from the start of the experiment, till the end. The compacts were heated to 1873 K and soaked at this temperature for 7 min with a heating rate of either 50 K min^{-1} (HfO_2) or 100 K min^{-1} (Y_2O_3 and YSH). The sintering experiment comprising die and plunger were cooled naturally to room temperature to remove monoliths from the graphite die.

2.9 X-ray diffraction analysis of powders and pellets

Phases present in the powder samples were identified by using X-ray diffraction (XRD) by using X'pert MPD system supplied by Philips, The Netherlands (Cu K_α radiation ($\lambda = 1.541\ A^0$)), equipped with a graphite monochromator and a scintillation detector. Calibration was carried out by using silicon and alumina standards supplied by NIST, USA. All the powder samples were used as such without any further processing, whereas the sintered pellets were grounded to a fine powder by using a mortar and pestle.

Spark Plasma sintered pellets were characterized by using Bruker X-ray diffractometer of grazing incidence X-ray diffraction (GIXRD), (Model: D8-Discover): Cu K_α radiation of wavelength 1.5418 Å was used. The incident angle in the GIXRD measurements was kept as 0.3° which could probe upto a depth of 184 nm. The collection angle was increased in steps of 0.05° from 25º to 95°.

By considering the multiplicity factor and linear absorption coefficient, the volume fraction of monoclinic hafnia phase in YSH was derived by making use of eqn. (2.1) [4].

$$\mathrm{V_m} = \frac{(1.6031 * \mathrm{I_m}(11\bar{1})}{1.6031 * \mathrm{I_m}(11\bar{1}) + \mathrm{I_c}(111)} \tag{2.1}$$

Where, $\mathrm{I_m}(11\bar{1})$ and $\mathrm{I_c}(111)$ represent the integrated intensity of the X-ray diffraction lines of the monoclinic $(11\bar{1})$ and cubic (111) phases respectively.

The size of the crystallites in all these samples was estimated from the width of peaks in the X-ray diffraction (XRD) patterns [5]. All XRD patterns that are presented in this work represent raw data and the peaks obtained were well resolved. Crystallite sizes of all these samples were calculated by using both the Scherrer formula (Sc) [eqn. 2.2] and the Hall-Williamson (HW) plots (eqn. 2.3), while the lattice strain was derived from the latter [5].

$$\mathrm{Sc_{XCS}} = \frac{K\lambda}{\beta \operatorname{Cos} \theta} \tag{2.2}$$

$$\beta \operatorname{Cos} \theta = \frac{K\lambda}{\mathrm{HW_{XCS}}} + 4\varepsilon \operatorname{Sin} \theta \tag{2.3}$$

Where, λ is the X-ray wavelength (Cu-K_α), K is crystallite shape factor, β is the full width at half maxima in radians, θ is Bragg angle and ε is strain distribution within the material.

2.10 Measurement of green density (ρ_G), radial and axial shrinkage and sintered density (ρ_S)

Relative ρ_G of the pellets were obtained from their weight and volume. Average of the values obtained in five such measurements is reported. Radial and axial shrinkage were obtained by measuring the dimension of green and sintered pellets. Their dimensions were measured by using a digital screw gauge (accuracy of ± 0.001 mm) supplied by Mitutoyo, Japan. Density of the sintered pellets was measured at room temperature by using Archimedes method (ASTM: B962-13) [6], in which, dibutyl phthalate ((DBP)[*]; density - 1.056 g cm^{-3} (293 K)) was used as the immersion liquid. The mean of the values obtained in five measurements is reported here.

2.11 Microstructural characterization

2.11.1 Scanning Electron Microscopy (SEM) and Energy Dispersive X-ray Spectroscopy (EDS) of powders and pellets

For carrying out the SEM analyses, a few milligrams of the powder was dispersed on to the carbon tape. The morphological analysis of these samples was carried out by using a Field Emission Scanning Electron Microscope (FE-SEM, Model-Helios NanoLab 600i), (FEG Quanta, Philips, The Netherlands). Pieces of a sintered pellet were polished and thermally etched at the corresponding sintering temperature. These were placed on a carbon tape and were coated with gold.

2.11.2 Transmission Electron Microscopy (TEM) and Electron Energy Loss Spectroscopy (EELS)

For the TEM analyses, a few milligram of the powder under investigation was suspended in propan-2-ol and deagglomerated by ultrasonication. A few drops of this solution were then

---

[*] Generally it is preferable to use a liquid with low surface tension low vapor pressure.DBP is inert, has low vapor pressure and has a surface tension compared with water.

dropped on to a holey carbon grid. TEM investigations were carried out in a LIBRA 200FE (Carl Zeiss) high resolution TEM operated at 200 kV equipped with energy dispersive X-ray spectroscopy (EDS) analysis, scanning transmission electron microscopy (STEM) and an in-column energy filter.

Both SEM and TEM images were analyzed by using CaRine v3.1® software.

2.12 Studies on the compatibility of molten uranium with crucibles made out of HfO_2 and YSH

Sintered hafnia and YSH crucibles were used to investigate the compatibility of these crucibles with the molten uranium. Experiments pertaining to these investigations were carried out by using a custom made “spot technique” instrumentation. The construction of this equipment and the principle behind the experiment are explained in detail in ref. [7-9]. Prior to the experiment, these crucibles together with the Knudsen cell in which they were held were degassed under high vacuum (2.7×10^{-7} mbar) for about 1 h by radio frequency (RF) induction heating at 1773 K (Fig. 2.3).

In a typical experiment, pieces of uranium were taken in a degassed sintered hafnia or YSH crucible. This crucible along with the Knudsen cell and its susceptor were heated by electromagnetic induction (RF) under vacuum (2.7×10^{-7} mbar). The Knudsen cell orifice was viewed by using a long distance optical microscope (QM1, M/s. Questar, Inc. USA). Temperature at which a spot is observed (fusion) was measured by focusing the black body hole (at the bottom of the Knudsen cell) on to a two color pyrometer (M78, M/s. Micron, USA). The corresponding video image of the sample surface was viewed through the Knudsen cell orifice by using a long distance optical microscope, fitted with a charge coupled device (CCD) camera

(WAT 207 A, M/s. Watec Co. Ltd., Japan). After the experiment these crucibles were recovered and were subjected to microstructural investigations by using SEM.

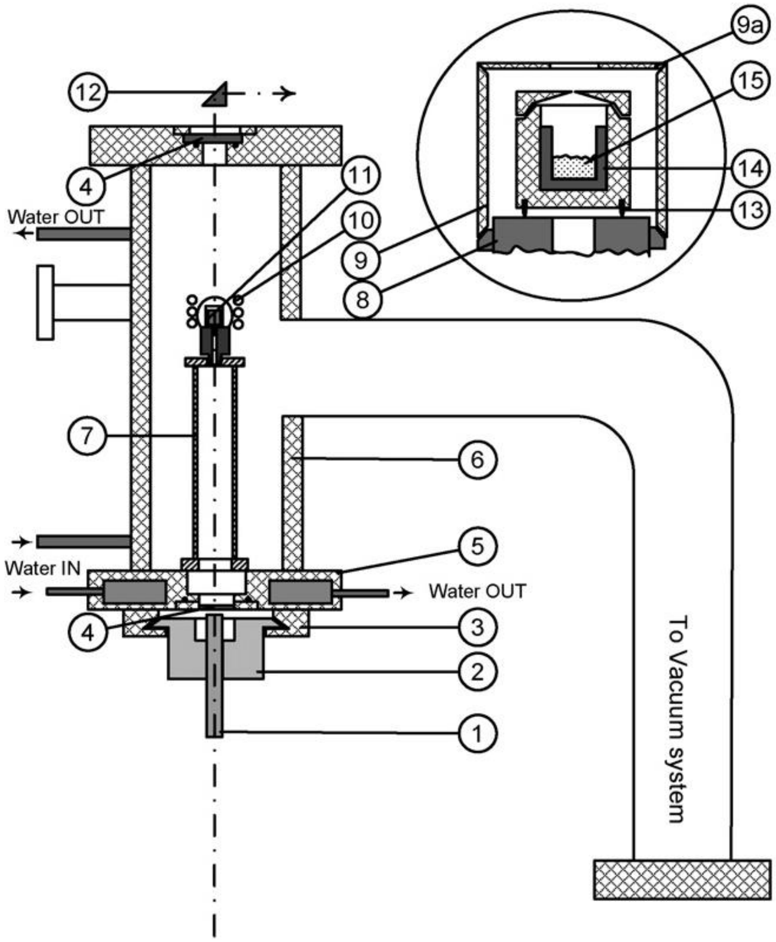

Figure 2.3 Schematic showing the experimental system used for the spot experiments: 1) IR two color pyrometer; 2) fixture for pyrometer; 3) optical rail; 4) quartz optical window; 5) bottom flange; 6) vacuum chamber; 7) sample support assembly; 8) molybdenum table; 9 & 9a) radiation shield; 10) RF coil; 11) Knudsen cell; 12) quartz prism; 13) tungsten legs; 14) crucible; 15) sample (Adopted from [9])

References

[1] W. Leithe, Anal. Chem. 20 (1948) 1082-1084.

[2] R. Venkata Krishnan, K. Nagarajan, Thermochim. Acta 440(2) (2006) 141-145.

[3] R. Venkata Krishnan, G. Panneerselvam, B.M. Singh, B. Kothandaraman, G. Jogeswararao, M.P. Antony, K. Nagarajan, J. Nucl. Mater. 414(3) (2011) 393-398.

[4] D.L. Porter, A.H. Heuer, J. Am. Ceram. Soc. 62(5-6) (1979) 298-305.

[5] V. Mote, Y. Purushotham, B. Dole, J. Theor. Appl. Phys. 6(1) (2012) 6.

[6] ASTM B962-13, Standard Test Methods for Density of Compacted or Sintered Powder Metallurgy (PM) Products Using Archimedes' Principle, ASTM International, West Conshohocken, PA.

[7] K. Ananthasivan, Development of Methods and Materials for the Determination of Solid to Liquid Phase Transformation Temperatures in Alloys, PhD Thesis, University of Madras, 2002.

[8] S. Balakrishnan, K. Ananthasivan, K.C. Hari Kumar, J. Alloys Compd. 689 (2016) 751-758.

[9] K. Ananthasivan, S. Balakrishnan, I. Kaliappan, S. Anthonysamy, R. Pankajavalli, P. R. V. Rao, J. Alloys Compd. 468(1) (2009) 275-279.

Chapter 3

Synthesis, Characterization and Sintering of Nanocrystalline Urania

This chapter explains in detail about the investigations carried out on bulk synthesis of nc-UO_2 by using citrate gel-combustion method. An attempt was made to evaluate the mechanism and the kinetic parameters of the "volume combustion reaction" of an initial mixture with a citric acid to nitrate mole ratio (R) of 0.25. The utility of "two-step sintering" of nc-UO_2 powders was also investigated. The shrinkage, distribution of porosity as well as the microstructure of the sintered pellets were also studied.

3.1 Purity of the starting materials

The starting materials used in the preparation of the combustion mixtures were devoid of impurities that would significantly alter the characteristics of the gel-combustion derived powders as testified by the ICP-MS analysis of the starting urania powders (Table 3.1).

3.2 Gel-combustion synthesis

The gel-combustion synthesis [1-6] involves blending together an oxidizing agent (metal nitrate) and an organic complexing agent in a definite proportion to form a homogenous aqueous solution, followed by gelation and combustion. In this study, the composition of the combustion mixture was found to influence the properties of the product (Table 3.2). No attempt has been made, however, to measure the reaction temperatures as well as the heat of the reaction since these reactions were carried out in an open glass bowl and not in a thermally isolated environment. "Volume combustion" a vigorous reaction that involved sudden expulsion of gases

Table 3.1 Impurity analysis by ICPMS

Elements	Ni	Zn	Mo	Ba	Al	Mg	Ca	V	Cr	Mn	Fe	Cu	Ce	La	Sm	Eu	Gd	Dy	C
Conc. of impurities /ppm	8	2	9	<1	<1	<1	<1	<1	7	8	45	<1	1	6	<1	<1	28	<1	<100

Table 3.2 Characteristics of the urania powder synthesized by "gel-combustion"

Sample	**Mole ratio** $\frac{N_{CA}}{N_{NO_3^-}}$	**Color of the sample**			ρ_G **(Mg m^{-3})**			**RC (ppm)**			**SSA (m^{2}g^{-1})**			**O/U**		
		A	**C**	**H**	**A**	**C**	**H**	**A**	**C**	**H**	**A**	**C**	**H**	**C**	**H**	**H$_a$**
U	0	Y	Bl	Br	2.39	2.15	2.68	110	114	92	7	5	6	2.62 ± 0.05	2.02 ± 0.04	2.06 ± 0.04
U_C5.5	0.055	Or	Bl	Br	1.01	0.88	1.22	563	185	109	5	5	5	2.67 ± 0.02	2.06 ± 0.03	2.09 ± 0.03
U_C10	0.100	Ol	Ol	LBr	0.18	0.26	0.44	417	158	116	7	7	7	2.68 ± 0.04	2.06 ± 0.04	2.12 ± 0.04
U_C25	0.249	LOl	LOl	Ol	0.06	0.09	1.61	660	447	156	18	8	10	2.74 ± 0.07	2.15 ± 0.05	2.13 ± 0.04
U_C50	0.499	DGy	Bl	Re	1.79	1.59	3.73	877	631	229	6	5	6	2.74 ± 0.06	2.10 ± 0.06	2.14 ± 0.05
U_C75	0.750	DGy	Gy	Re	1.29	1.25	2.63	1270	552	274	6	5	6	2.75 ± 0.08	2.04 ± 0.03	2.12 ± 0.03
U_C90	0.899	DGy	Gy	Gy	1.18	1.11	2.42	1163	552	296	6	5	5	2.69 ± 0.02	2.12 ± 0.06	2.20 ± 0.02
U_C100	0.994	DGy	DGy	Bl	1.28	1.15	2.27	1004	698	310	6	5	5	2.73 ± 0.06	2.05 ± 0.02	2.19 ± 0.02

Y=Yellow; Bl - Black; Br/LBr – Brown/Light Brown; Gy/DGy - Grey/Dark Grey; Ol/LOl - Olive/Light Olive; Or - Orange; Re - Dark Red; CA - Citric acid; ***A, C & H*** *= "As-prepared", Calcined & Hydrogen reduced powders;* ***O/U*** *– mole ratio of oxygen to uranium;* ***H$_a$*** *- O/U of H after 52 days* that yields a very voluminous product was observed in the mixtures with R values of 0.10 and 0.25, whereas all the other gels decomposed through a reaction at a moderate pace followed by auto ignition with attendant smoldering.

3.3 IR spectroscopy of the precursor and products

The FTIR spectra of citric acid, uranyl nitrate and the products derived from a mixture with an R value of unity (“A”, “C” and “H” powders) are depicted in Fig. 3.1. The absorption minima observed in these specimens are enlisted in Table 3.3 are comparable to the standard spectra cited in Refs. [7-9].

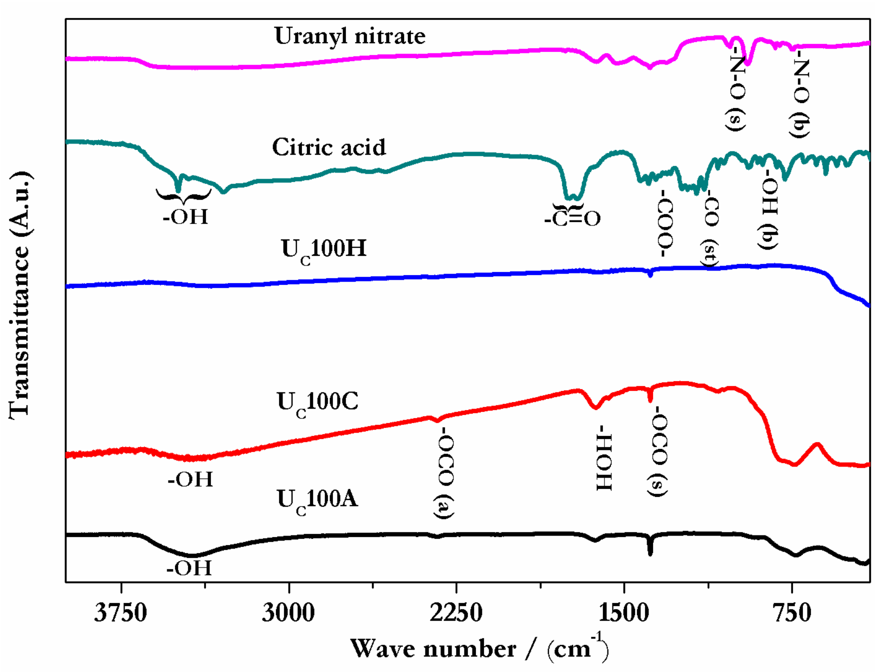

Figure 3.1 FTIR spectra of precursors and products [s-symmetric, a-asymmetric, st-stretching and b-bending]

Table 3.3 Absorption minima of starting materials and products

Functional group	Wave number (cm^{-1})
O-H	3300 - 3500 cm^{-1} (s); 1419 cm^{-1} (b)
C-O	1706 cm^{-1} (st)
COO^{-}	1384 cm^{-1} (st)
N-O	1021 cm^{-1}(st); 813 cm^{-1} (rocking); 740 - 750 cm^{-1} (s.b) and 710 cm^{-1} (a. b)

st – stretching, b – bending; s.b and a.b symmetric and asymmetric bending

The IR spectra pertaining to the sample U_C100A was devoid of the absorption signatures pertaining to citric acid and uranyl nitrate indicating that the reaction has proceeded to completion. In the spectra of the powder U_C100H, the intensities observed were the lowest, possibly due to the complete removal of the organic precursor and nitrates. The bands pertaining to O=C=O and O-H observed in the powders U_C100A and U_C100C could be ascribed to the presence of adsorbed CO_2 and moisture. However, since a quantitative determination of the constituent moieties was not attempted, inter comparison of these spectra would not be appropriate. The IR spectra, in general, suggest that the reaction has proceeded up to completion.

3.4 Thermal analysis

3.4.1 Analysis by using TG-DTA-MS

The results obtained in the TG-DTA-MS investigation of the pyrolysis of a gel prepared from a mixture with an R value of 0.25, are presented in Fig. 3.2 and Fig. 3.3. Two distinct weight loss regions were observed in the TG curve. The first step in the TG curve reveals a weight loss due to simultaneous reactions (slope change). In order to reaffirm this observation, the first TG curve was differentiated (DTG). The DTG curve, further confirmed that the TG curve could be resolved into two distinct peaks revealing that the simultaneous reaction did take place (inset in Fig. 3.2). This could be due to the dehydration of citric acid to form aconitic acid [10]. These two steps could therefore be attributed to the direct participation of citric acid in the combustion reaction as well as the participation of its dehydrated moiety (aconitic acid) [10]. A minor weight loss was observed (Fig. 3.2) at 625 K and at 830 K which may be due to the oxidation of trace amounts of carbon present in the sample. This is further substantiated by the mass spectrometric data of the gases evolved during combustion reaction (Fig. 3.3). Three exothermic peaks were observed in the DTA with onset temperatures at 430 K, 535 K and 625 K (Fig. 3.2).

The mass spectrometric analysis of the gases evolved at various stages from the sample is shown in Fig. 3.3. As seen in the figure (Fig. 3.3) the gases evolved corresponding to the first step of the mass loss are H_2O, N_2, CO_2, NO and NO_2. The gases evolved in the second step are H_2O, CO_2 and CO. The mass spectrometric, DTA and TG analyses suggest that the following reactions (eqns. 3.1-3.2) probably take place during the gel-combustion synthesis.

$$6UO_2(NO_3)_2 + 3C_6H_8O_7 + O_2 \rightarrow 2U_3O_8 + 3N_2 + NO_2 + 5NO + 18CO_2 + 12H_2O \tag{3.1}$$

$$3C_6H_8O_7 + 13.5O_2 \rightarrow 18CO_2 + 12H_2O \tag{3.2}$$

The reaction pertaining to the first exothermic peak given in eqn. 3.1 corresponds to the overall reaction. The second exothermic peak could therefore be attributed to the decomposition of residual unreacted fuel (citric acid) [eqn. 3.2]. This is also substantiated by the fact that the evolution of N_2 [11] which is a typical product of the combustion reaction [12, 13].

The third exothermic peak was observed at the 625 K. The weight loss (<1 wt %) observed at temperatures above 625 K is due to the oxidation of residual carbon present in the sample. The EGA analysis (Fig. 3.3) does show the evolution of CO_2 at temperatures above 625 K. Since the heat of the combustion of trace amounts of carbon would be quite low, it is reasonable to assign the third exothermic peak to the crystallization of uranium oxide (U_3O_8). The minor mass loss at 830 K corroborates well with the evolution of CO_2 at 830 K. The XRD patterns of nc-U_3O_8 phase (both “A” and “C”) are shown in Fig. 3.7. These analyses were carried out on samples retrieved immediately after the completion of combustion reaction (around 673 K) as well as beyond the latter (973 K).

Table 3.4 XCS of urania powders

Sample	A			C			H		
	Sc (nm)	HW (nm)	Strain x 10^{-3}	Sc (nm)	HW (nm)	Strain x 10^{-3}	Sc (nm)	HW (nm)	Strain x 10^{-3}
U	-	-	-	48	283	1.58	42	146	1.45
U_C5.5	14	-	-	45	252	1.69	40	113	1.36
U_C10	13	23	4.96	41	50	0.36	39	79	1.06
U_C25	20	32	2.75	36	38	0.10	32	47	0.77
U_C50	19	24	1.75	35	58	0.97	33	54	0.98
U_C75	18	24	1.42	34	69	1.34	35	85	1.39
U_C90	20	51	4.23	38	87	1.32	29	71	1.66
U_C100	24	90	4.63	38	98	1.61	27	45	1.22

Table 3.5 PSD and total pore volume of urania powders

Sample	Particle size distribution (vol %)										
	10 vol. % of sample has size less than (μm)			50 vol. % of sample has size less than (μm)			90 vol. % of sample has size less than (μm)			Total pore volume (mm^3g^{-1})	
	A	C	H	A	C	H	A	C	H	C	H
U	2	6	5	11	56	13	179	662	63	226	269
U_C5.5	6	10	7	42	53	33	229	246	141	433	521
U_C10	7	4	5	62	32	32	270	162	131	699	1116
U_C25	5	3	11	27	14	61	108	56	220	1549	4787
U_C50	2	4	3	24	28	21	411	304	371	320	281
U_C75	2	3	3	26	33	27	192	254	150	405	403
U_C90	2	3	3	29	31	35	196	245	149	434	381
U_C100	2	4	3	38	48	20	166	230	97	414	414

Both “A” and “C” samples revealed the presence of nc-U_3O_8 phase. However, the XRD peaks of the latter were more prominent and well resolved due to significant grain coarsening. The XCS computed by using the HW method for the sample is 24 nm at 673 K (Table 3.4). The nc-U_3O_8 when heated in air at 1073 K for 4 h yielded the product with a higher crystallite size of 58 nm. The XRD patterns of nc-U_3O_8 (both "A" and "C") are shown in Fig. 3.7.

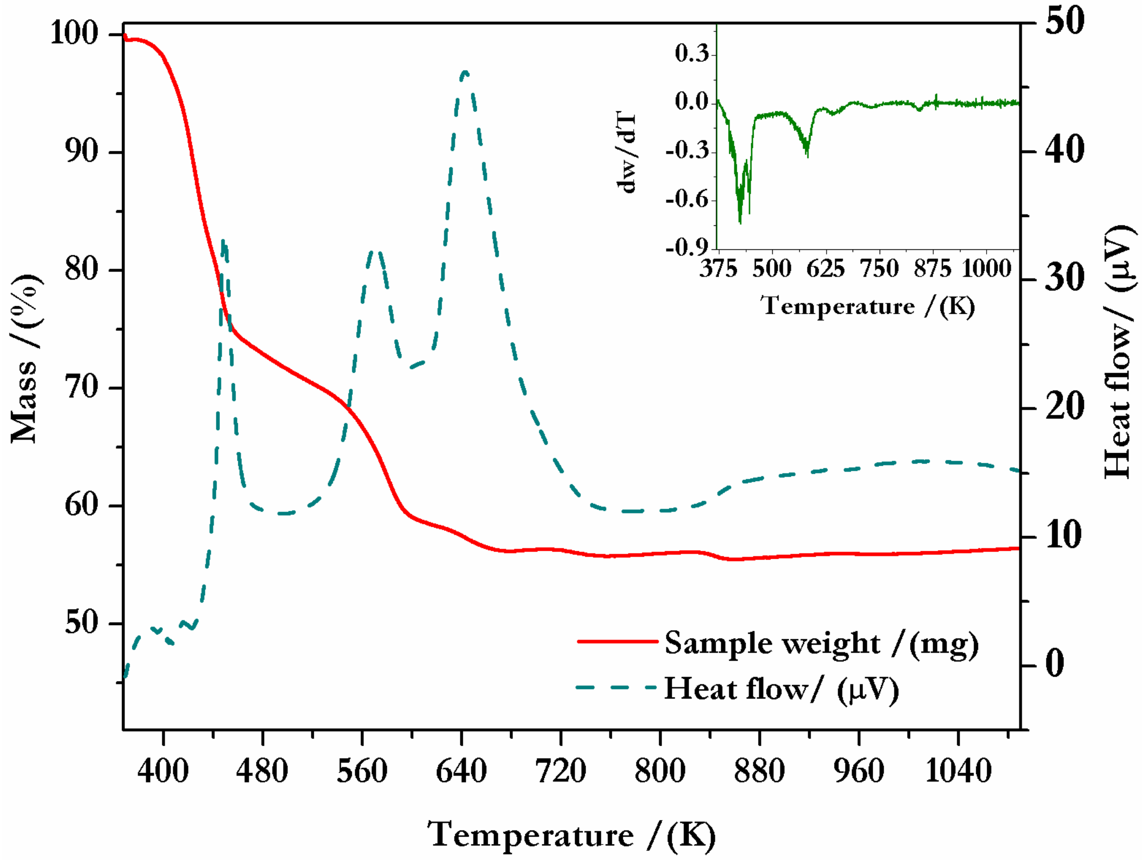

Figure 3.2 TG-DTA curve pertaining to the combustion reaction at a heating rate of 10 K min^{-1} in O_2 (inset shows the differential weight with respect to temperature)

3.4.2 Analysis by using DSC

The sample gel contains considerable amounts of adsorbed moisture. In order to avoid the thermal artifact due to the evaporation of the adsorbed moisture and to determine the quantum of heat evolved during the course of the reaction, the specimen gels were preheated before carrying out the actual experiments at 373 K for 30 min in O_2 atmosphere inside the DSC sample cell (Inset Fig. 3.4). The sample was cooled to room temperature and then again heated from 298 - 973 K.

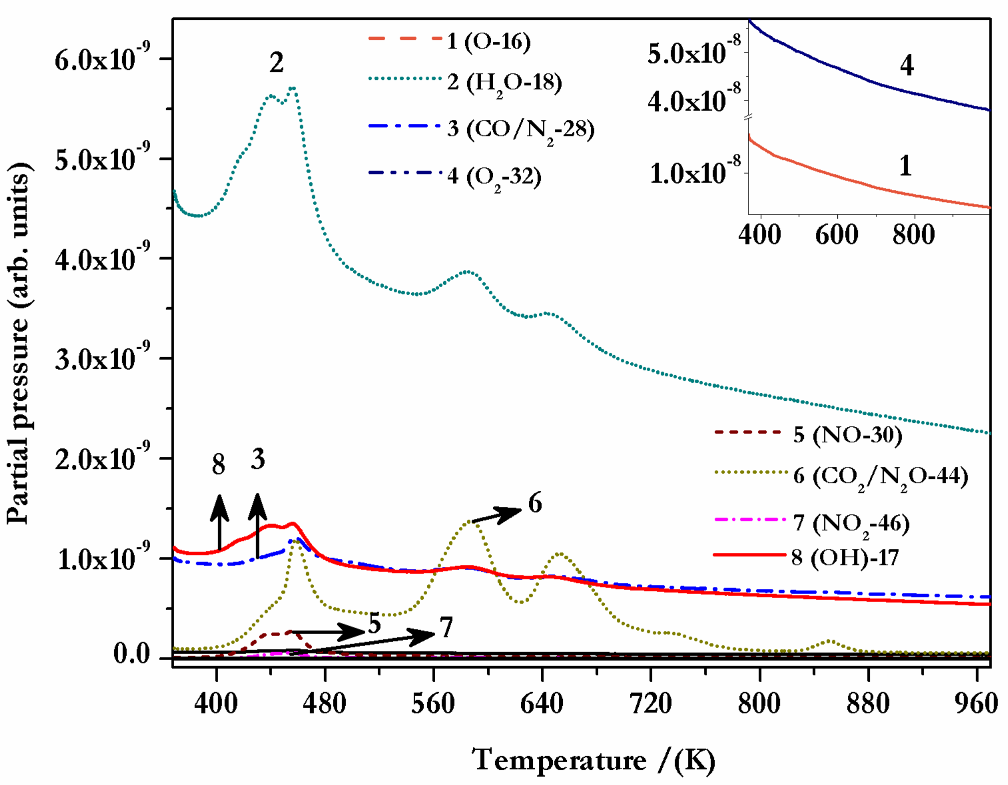

Figure 3.3 Mass spectrometric analysis of evolved gases during the citrate gel-combustion synthesis of nc-U_3O_8

The samples were subjected to different linear heating rates viz., 5, 10, 15 and 20 K min^{-1}. A heat flow rate curve obtained as a function of temperature at different heating rates is shown in Fig. 3.4. Similar to the DTA analysis, three exothermic peaks were observed. The onset temperature of these peaks is in good agreement with that obtained by using DTA. DSC curves also revealed that the peaks shift with the heating rate while the area under the curve differs significantly with the heating rate.

The optimum calcination temperature was chosen with the help of the results obtained in the thermogravimetric analysis of the U_C100A powders. The thermal analysis revealed that the weight of this sample remained nearly constant at temperatures beyond 1050 K. Hence the calcination was carried out at 1073 K in order to remove the carbon residue present in the “as prepared” powders.

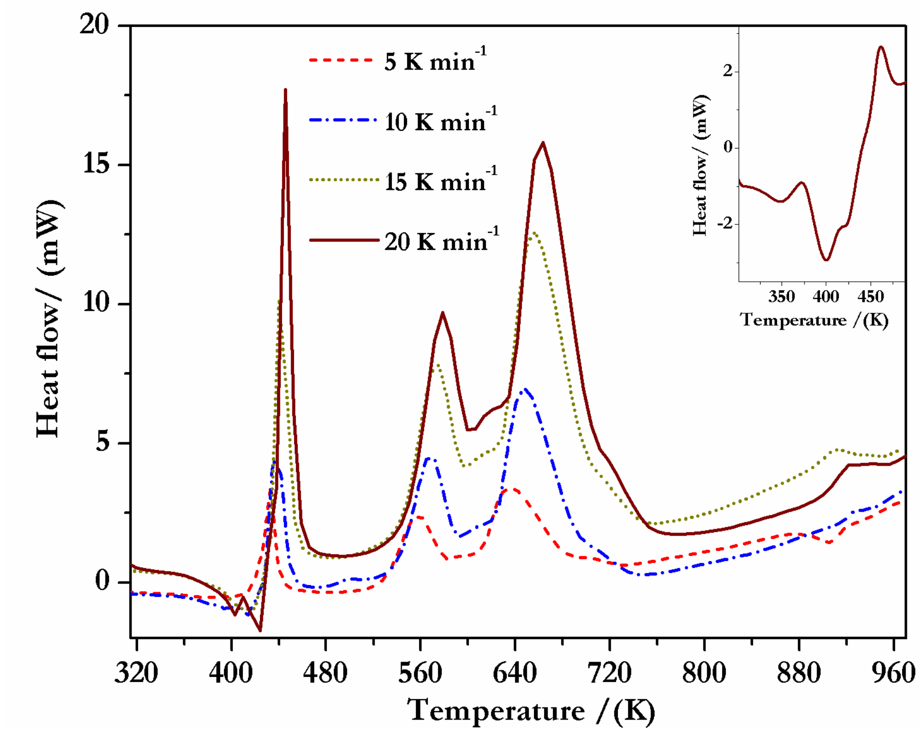

Figure 3.4 *DSC curves pertaining to the combustion reaction at various heating rates in O_2 atmosphere (Inset: DSC curve pertaining to dehydration)*

3.5 Characterization of the powders

3.5.1 Particle size distribution (PSD) and Bulk density (ρ_B)

The packing density of a powder depends on the size distribution of its constituent particles, mode of their packing, their flowability and shape. All these factors are directly linked to the powder preparation method [14, 15]. The same is true for the powders derived through combustion synthesis. Earlier, Anthonysamy et al. [16] showed that the mode of heating (microwave and hot plate) affected the PSD for urania-thoria solid solution prepared by using the citrate gel-combustion method and they have also reported that the difference in size distribution affected the sinterability of the final product. The properties of the powders prepared through citrate gel-combustion would depend strongly on the fuel to nitrate ratio [17]. These include their ρ_B, SSA, P_OSD and sinterability. The PSD in the “A”, “C” and “H” powders are presented in

Table 3.5 and in Fig. 3.5. In this Fig. 3.5 the thick solid line represents the experimentally observed size distribution of particles whereas the thin solid lines depict the deconvoluted size distribution derived from the former. The integral areas in percentage are given in the legend. The distribution of sizes among these particles was found to be in the range of 0.5 - 1000 µm. The size distribution histograms were deconvoluted in order to delineate the contribution pertaining to different size fractions. The "A" and "C" powders exhibited mono and poly modal size distributions while the hydrogen reduced powders revealed only poly modal size distribution. The product U_C25A possessed a unimodal distribution. U_C25C and U_C25H comprised a bimodal distribution of particles.

The bulk densities as well as the PSD in these powders (A, C and H) exhibited a systematic dependence on the value of R (Fig. 3.6a). In all these powders the number of different size fractions had a bearing on their ρ_B and the following trend was discernible $\rho_{B\ (tetra)} > \rho_{B\ (tri)} > \rho_{B\ (bi)} > \rho_{B\ (uni)}$. The variation in the ρ_B of the "A" powders exhibited the following trend:

$${\rho_B}^{\mathrm{U00A}}_{\mathrm{(tetra/tri)}} > {\rho_B}^{\mathrm{U_C50A}}_{\mathrm{(tri)}} > {\rho_B}^{\mathrm{U_C75A}}_{\mathrm{(tri/bi)}} \approx {\rho_B}^{\mathrm{U_C100A}}_{\mathrm{(tri/bi)}} > {\rho_B}^{\mathrm{U_C90A}}_{\mathrm{(tri)}} > {\rho_B}^{\mathrm{U_C5.5A}}_{\mathrm{(tri/bi)}} > {\rho_B}^{\mathrm{U_C10A}}_{\mathrm{(bi)}} > {\rho_B}^{\mathrm{U_C25A}}_{\mathrm{(uni)}}$$

In the above expression the type of distribution is indicated within the parenthesis. Powders with polymodal distribution of particulates exhibited higher bulk densities. More the number of size fractions higher was the value of the ρ_B. Among the powders, U_C25A was found to have the minimum bulk density, while U00A exhibited the highest ρ_B. This is evidently due to the better packing arising from appropriate distribution of size fractions i.e., when all the three size fractions are significantly populated, the ρ_B tends to be high. However in those powders that had a relatively less populated third size fraction the ρ_B was low. In powders with a bimodal distribution of particles the ρ_B was positively correlated with the quantities of the coarser fraction, indicating that in these powders the relative population of the heavier particles determined the former. U_C25A exhibited only a flat uni-modal distribution which spanned over a wide range of sizes and was found to possess the lowest ρ_B. The ρ_B and PSD in "calcined" urania powders followed the trend:

$$\rho_{B}{}^{\mathrm{U00C}}_{\mathrm{(tri)}} > \rho_{B}{}^{\mathrm{U_C50C}}_{\mathrm{(tri)}} > \rho_{B}{}^{\mathrm{U_C75C}}_{\mathrm{(tri)}} > \rho_{B}{}^{\mathrm{U_C100C}}_{\mathrm{(tri/bi)}} > \rho_{B}{}^{\mathrm{U_C90C}}_{\mathrm{(bi)}} > \rho_{B}{}^{\mathrm{U_C5.5C}}_{\mathrm{(bi)}} > \rho_{B}{}^{\mathrm{U_C10C}}_{\mathrm{(bi)}} > \rho_{B}{}^{\mathrm{U_C25C}}_{\mathrm{(bi/uni)}}$$

Calcined powders with tri, bi and uni modal distributions were found to possess the highest, intermediate and lowest ρ_B respectively. The ρ_B of the powders with a tri modal distribution, increased with the relative proportion of the fines. This could be ascribed to better packing of the particles facilitated by the percolation of fines into the interspaces of the larger particles. Thus the variation in ρ_B indicated in the above expression pertaining to the calcined powder and in Fig. (3.6a) could be substantiated.

"Calcined" powders with a bimodal distribution were found to possess a lower ρ_B than those with a tri modal distribution of particles. Unlike in the latter the bulk densities of the former bore an inverse correlation with the relative fraction of the fines. Possibly a higher fraction of the coarser agglomerates is necessary to compensate the relatively poorer packing in these powders as compared to their counterparts with three different size fractions. It is interesting to note that the pattern of PSD in a given calcined powder closely resembled that of its precursor. This suggests that these powders did not undergo significant self attrition during calcination and subsequent handling.

The ρ_B of "hydrogen reduced" UO_2 powders followed the trend:

$$\rho_{B}{}^{\mathrm{U_C50H}}_{\mathrm{(tetra)}} > \rho_{B}{}^{\mathrm{U00H}}_{\mathrm{(tetra/tri)}} \approx \rho_{B}{}^{\mathrm{U_C75H}}_{\mathrm{(tri/bi)}} > \rho_{B}{}^{\mathrm{U_C90H}}_{\mathrm{(tri)}} > \rho_{B}{}^{\mathrm{U_C100H}}_{\mathrm{(tri)}} > \rho_{B}{}^{\mathrm{U_C25H}}_{\mathrm{(tri/bi)}} > \rho_{B}{}^{\mathrm{U_C5.5H}}_{\mathrm{(tri/bi)}} > \rho_{B}{}^{\mathrm{U_C10H}}_{\mathrm{(bi)}}$$

From Fig. 3.5 it is evident that none of these powders exhibited uni modal distribution of sizes. This is due to the formation of multiple size fractions during the conversion of U_3O_8 to UO_2. U_C50H was found to exhibit a tetra modal distribution and the highest ρ_B. U_C10H comprised a larger coarser fraction and the least ρ_B. U00H was found to have the largest fraction of particles with an average size of 100 μm and much smaller fractions of the terminal sizes. Among the powders which exhibited a tri or tetra modal distribution of sizes those with the higher fraction of fines exhibited a higher value of ρ_B.

The bulk densities of hydrogen reduced powders were highest while that of the "as prepared" precursors were the least and that of the calcined powders were intermediate. Powders obtained from the mixture with an R value of 0.25 possessed the lowest ρ_B among the "A" and "C" powders. It is appropriate to compare the bulk densities of the powders obtained in the present study with those of the powders prepared through well established conventional processes cited in the literature (Table 3.6).

It is evident that UO_2 powders with the lowest ρ_B could be produced by employing citrate combustion mixtures with R values 0.10 and 0.25 (Table 3.2). These are the lowest ρ_B values reported so far, for UO_2. All the other powders synthesized in this study exhibited values of ρ_B that were comparable to those pertaining to the powders obtained by the ADU [18], AUC [18], dry ADU [19] and the atomization method [20]. Both, the exothermicity as well as the rate of the combustion depend upon the composition of the combustion mixture (R). The variation in the powder properties substantiates the fact that the combustion reaction is vigorous for mixtures with an R value of 0.25. Hence, these highly porous powders exhibit the lowest ρ_B.

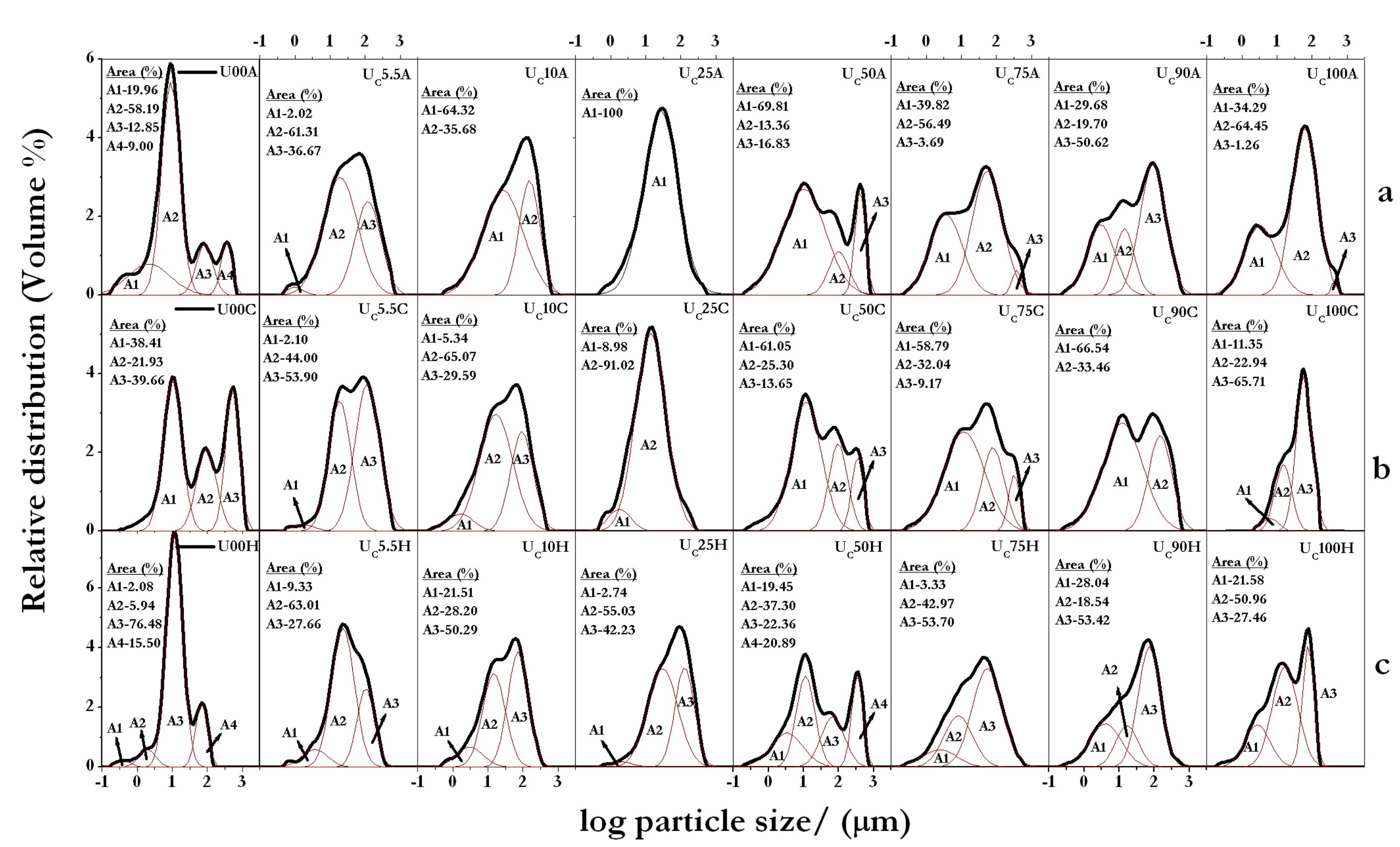

Figure 3.5 Distribution of sizes among particles in the "A", "C" and "H" urania powders (Thick solid lines – experimental curve, thin solid line – deconvoluted curves)

3.5.2. Specific surface area (SSA)

The dependence of SSA of the urania powders on the value of R is presented in Fig. 3.6b. From these data it is evident that the SSA of the “A” (SSA_A), “calcined” (SSA_C) and “H” (SSA_H) powders follow the trend: $SSA_A > SSA_H > SSA_C$.

U_C25A was found to have the highest SSA which decreased upon calcination, probably due to grain coarsening, as evidenced by a concomitant increase in the XCS. Hydrogen reduction of U_C25C yielded U_C25H with an enhanced SSA due to crumbling of the U_3O_8 particles. The powder U_C25A was found to be extremely reactive and underwent oxidation under ambient conditions and developed yellow patches on its surface upon prolonged exposure to air. XRD analysis suggested that these were streaks of UO_3. The surface oxidation is possibly accentuated by the nano pores (Fig 3.15a). While U_C25A and U_C25H were found to have significantly higher values of SSA compared to the rest of the powders, the values of SSA of all the other powders were comparable.

From Table 3.2 and Table 3.6 it is evident that the SSA of urania powders derived through citrate gel combustion method was moderate and comparable with those pertaining to the powders derived through ADU [18], dry ADU [19] and AUC [18] processes. The final product (hydrogen reduced powders) had a SSA ranging from 4.98 - 9.68 m^2g^{-1}.

3.5.3. Residual carbon

Table 3.2 depicts the variation in the quantity of carbon residue in the powders with the value of R. The data presented in Table 3.2 confirms that the quantity of carbon residue increases with R and decreases upon calcination and hydrogen reduction. The decrease in the quantity of carbon (residue) upon calcination is due to oxidation whereas during hydrogen reduction the residual carbon gets converted into hydrocarbons. The quantity of carbon residue varies between 100 and 700 ppm and 90 and 300 ppm in the "C" and "H" powders respectively.

Table 3.6 Comparison of ρ_B, SSA and XCS of urania powders reported values in the literature

References	Method	ρ_B (Mg m^{-3})	SSA (m^2 g^{-1})	XCS (nm)
[18]	AUC	2.08 - 2.24	4.29 – 6.66	-
	ADU	1.02	6.04	-
[19]	modified dry ADU	1.63 - 2.22	2.16 – 3.7	-
[20]	Atomization of uranyl nitrate	0.58 - 1.49	2.30 – 4.90	-
[21]	ADU	1.77 - 1.92	7.24 – 35.39	-
[22, 23]	AUC	-	0.50 – 5.96	-
[24]	AUC	-	4.70 – 14	10 – 100 (using SSA)
[25]	reoxidised U_3O_8	-	0.66 – 1.20	-
[26, 27]	ADU	-	1.1 – 6.2	15 – 32
[28]	Electrochemical method	-	10.3	4 – 6 (Sc)
[29]	Hydrothermal	-	28 (porous U_3O_8) 10.0 (U_3O_8)	80 - 100
[30]	ADU	1.5 – 1.8	5.82 – 10.4	-
[31]	Radiation chemical synthesis		60 – 70	22-35 (PCS) 9 (using SSA)
[32]	Hydrothermal (UO_2)	-	-	30 – 250 (Sc)
	Hydrothermal (U_3O_8)	-	-	44.1 – 51.1 (Sc)
[33]	Electrochemically reduced	-	-	3 (Sc)
[34]	Ox de 673 K 873 K 1h	-	-	9 (Sc)
	873 K 2h	-	-	11 (Sc)
	973 K 1h	-		20 (Sc)
	1073 K 1h	-	-	52 (Sc)
This study	A	0.06 - 2.39	5-18	23-90 (HW)
	C	0.09 - 2.15	5-8	38-283 (HW)
	H	0.44 - 3.73	5-10	45-146 (HW)

AUC - Ammonium uranyl carbonate; ADU - Ammonium diuranate-; PCS – photon correlation spectroscopy; and Ox de – oxalate decomposition

Y.W. Lee and M.S. Yang [18] produced urania powders by both ADU and AUC process with a residual carbon content of 110 ppm and 160 ppm respectively. The quantity of carbon residue found in the powders obtained in this study is comparable to those reported in ref. [18]. The residual carbon could assist presintering of the agglomerates as well as could influence O/U in these powders.

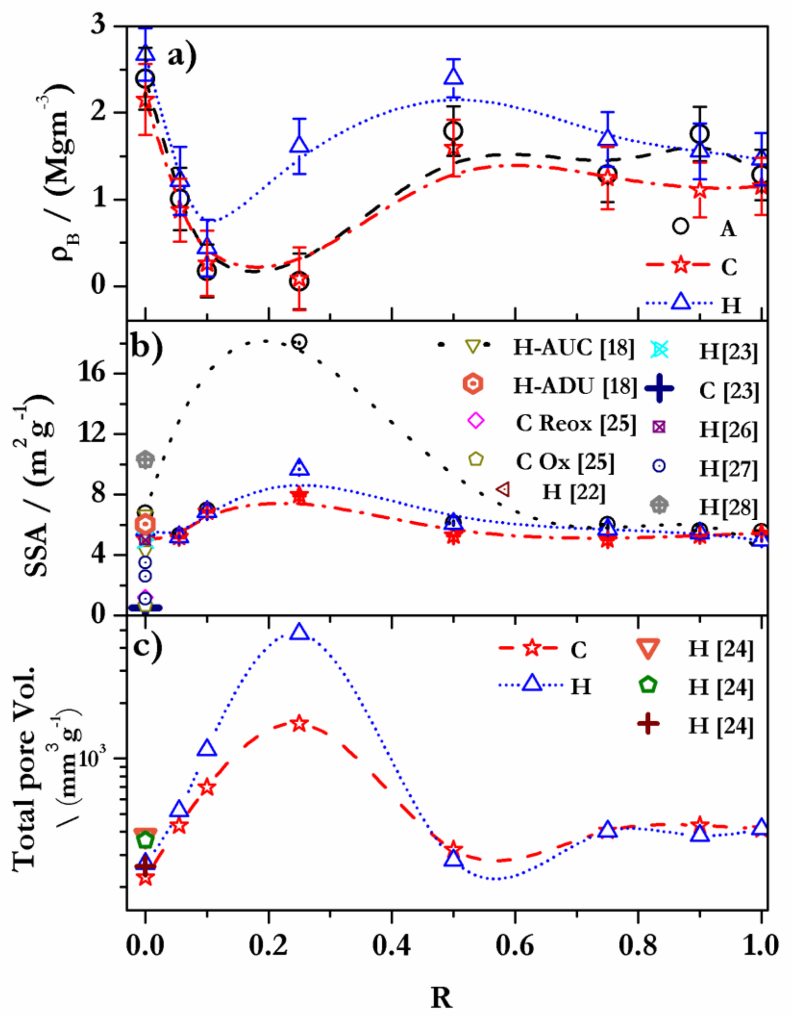

Figure 3.6 Dependence of (a) ρ_B of the powders; (b) SSA of the powders and (c) total pore volume on the value of R in, "C" U_3O_8 and "H" UO_2 powders

3.5.4. Phase characterization and XCS

XRD analyses of the urania powders synthesized in this study revealed that the "A" and "C" powders comprised U_3O_8 phase (JCPDS: 00-047-1493 & 00-031-1424) while the reduced

"H" powders consisted of the fluorite phase (JCPDS: 00-041-1422) (Fig. 3.7). These results are summarized in Table 3.4. The urania powders obtained through denitration without the addition of citric acid (U00A) were amorphous (Fig. 3.7). This product upon calcination yielded a U_3O_8 powder with a higher XCS. Subsequent reduction of this powder yielded UO_2 with a lower crystallite size. Except U00A and U_C5.5A, all the other "as prepared" powders comprised essentially U_3O_8 (Fig. 3.7). The constituent phases found in U_C25A were UO_2, UO_3 and U_3O_8 (major quantity). This powder was derived through volume combustion.

A limited supply of oxygen during the combustion reaction could have resulted in the formation of UO_2 along with U_3O_8. Later on these nc-phases would have got converted into UO_3 through oxidation in air. Air calcination of these powders resulted in their complete transformation into orthorhombic U_3O_8 phase as identified by the XRD pattern presented in Fig. 3.7. Subsequent hydrogen reduction of these powders yielded UO_2.

The estimates of XCS obtained by using the Sc formula were significantly different than those derived from the HW plots. All the "A" powders were found to be nc (XCS < 100 nm) and comprised smaller crystallites than the "C" powders. Both the XCS and the lattice strain of all the powders (A, C and H) exhibited a systematic dependence on the value of R (Fig. 3.8a and 3.8d). This variation is correlated with the rate of the combustion reaction. A faster rate led to a smaller XCS. Mixtures with R values between 0.25 and 0.75 yielded "A" powders with lower XCS than the rest of the mixtures. The powder U_C25A was distinctly different from the rest, in that it possessed the lowest XCS among all. "A" powders upon calcination and hydrogen reduction yielded "C" and "H" powders with enhanced XCS.

The combustion reaction is a self propagating and fast reaction (as evidenced by DSC) and does not allow enough time for the growth of the crystallites. This is the primary reason because of which the combustion synthesis yields nc powders. The dispersion of the mixture by the gaseous products further accentuates the reduction in the size of these crystallites.

In order to understand the trends in the variation of XCS observed in the powders synthesized in the present study as well as to compare the present observations with those reported in the literature (for both microcrystalline and nanocrystalline), the results reported by other workers are cited here (Table 3.6). V. Tyrpekl [34] reported the presence of carbonate residue and complete removal of carbon necessitated calcination at 1073 K. All the above methods cited in refs [28, 31-33] have been employed for producing only a few mg of nc-UO_2. Further, these processes as well as the citrate gel-combustion would require further optimization trials before they could be gainfully deployed for the production of nc-UO_2 in significant bulk quantities.

The results obtained in the present investigations show that the citrate gel-combustion is an easy method for the synthesis of nc-UO_2. The XCS (HW) of the product was found to vary from 45 - 113 nm for UO_2 and 38 - 252 nm for U_3O_8. These values compare well with those obtained in recently reported advanced methods [28, 31-34].

Upon storage the dioxide powders picked up oxygen from the ambience and got converted in to an oxide that was hyperstoichiometric with respect to oxygen (O/U > 2.00). There appeared to be a minor, yet noticeable variation in the oxygen stoichiometry of the freshly reduced powders (Fig. 3.9). In general the extent of hyperstoichiometry seems to depend on the relative fraction of fines in a given powder. However, this correlation defies a simple reasoning. The complex interplay of distribution of porosity and particle size as well as the specific surface area seem to determine the relative ease with which these powders would pick up oxygen when stored under identical conditions.

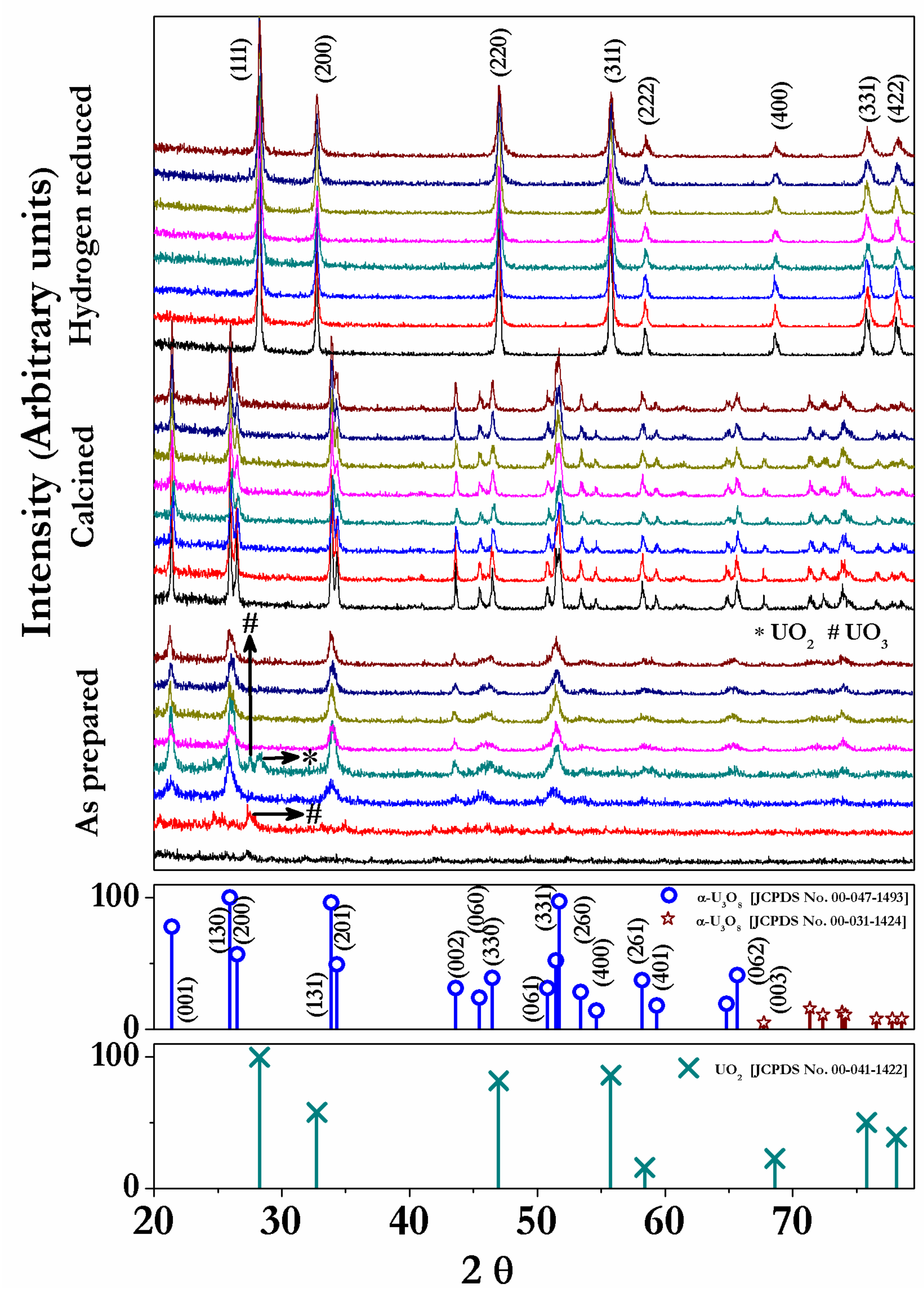

Figure 3.7 *XRD of the “U_CXXA”, “U_CXXC”, “U_CXXH” urania powders (Where XX = R value in %) 0, b) 5.5, c) 10, d) 25, e) 50, f) 75, g) 90 and h) 100*

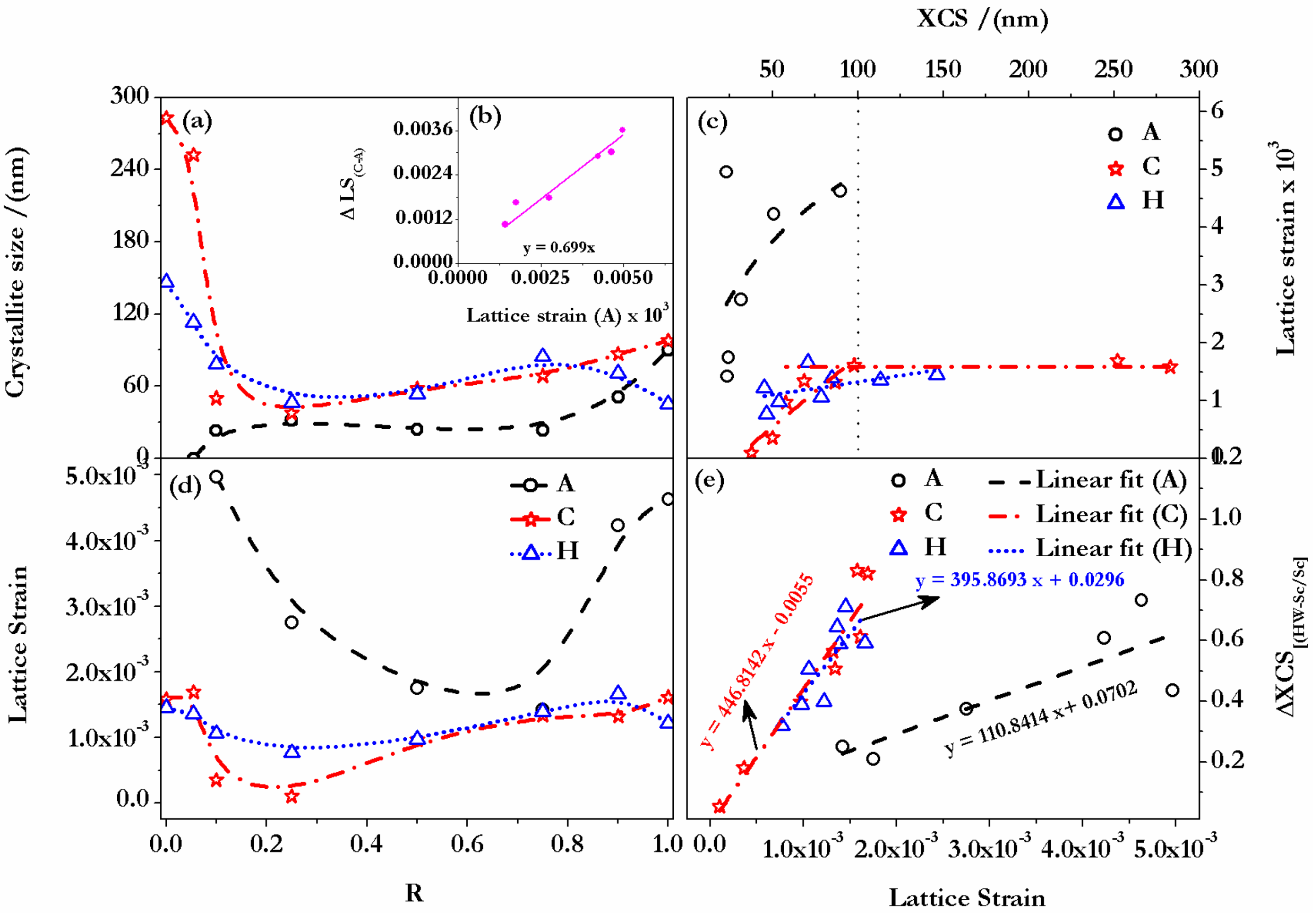

Figure 3.8 *(a) Variation of sizes of crystallites in the powders on R ratio by HW's method; (b) Dependence of difference in lattice strain between "C" and "A" powders with the lattice strain of "A" powders; (c) Variation of lattice strain with XCS; (d) Variation of lattice strain in crystallites with ratio R and (e) Variation of relative difference in XCS with the lattice strain*

In order to ascertain the variation in the lattice parameter with the oxygen to uranium ratio (O/U) in the hydrogen reduced UO_2 powders, their O/U was measured by quantitatively estimating the concentrations of U^{4+} and U^{6+} in the oxide by using a spectroscopic technique [35]. The lattice parameter was computed from the X-ray diffractograms. From the data presented in Fig. 3.9. It is evident that the lattice parameter decreases with a rise in the value of oxygen to metal ratio (O/U) as expected, and has a linear dependence on the O/U ratio in UO_{2+x} [36].

Thus it is evident that the urania powders obtained through citrate gel-combustion (except U_C25H and U_C10H) get stabilized after initial surface oxidation and that the hydrogen reduction yields a nearly stoichiometric product.

The dimensionless lattice strain obtained from the HW treatment [37] of the XRD data revealed many interesting aspects (Fig. 3.8b – 3.8e). The lattice strain in the “A” powders had a parabolic dependence on the value of R with a minimum at an R value of 0.50. Lattice strain in the “C” and “H” powders were much lower than that found in “A” and did not have a strong dependence on R. Insufficient time for the nucleation and growth during the combustion reaction and partial annealing during calcination substantiate these observations.

The lattice strain in all these powders was positively correlated with their XCS, indicating that the larger the crystallite more was the strain. Two regions viz., one below and the other above a critical value of 100 nm could be delineated in the plots depicting the variation in lattice strain with XCS (Fig. 3.8c). In the first region (XCS < 100 nm) a nearly linear correlation was observed while in the second (XCS > 100 nm) the lattice strain was more or less constant. Thus it is reasonable to conclude that when the powders coarsen and become microcrystalline (XCS > 100 nm) the strain approaches a constant value. Further, it was observed that the difference in the lattice strain in the “A” powders and the “C” powders was correlated with the magnitude of the lattice strain in the “A” powders. This indicates that the lattice strain tends to annul itself upon calcination (annealing), and higher its initial value more would be the tendency for this reduction.

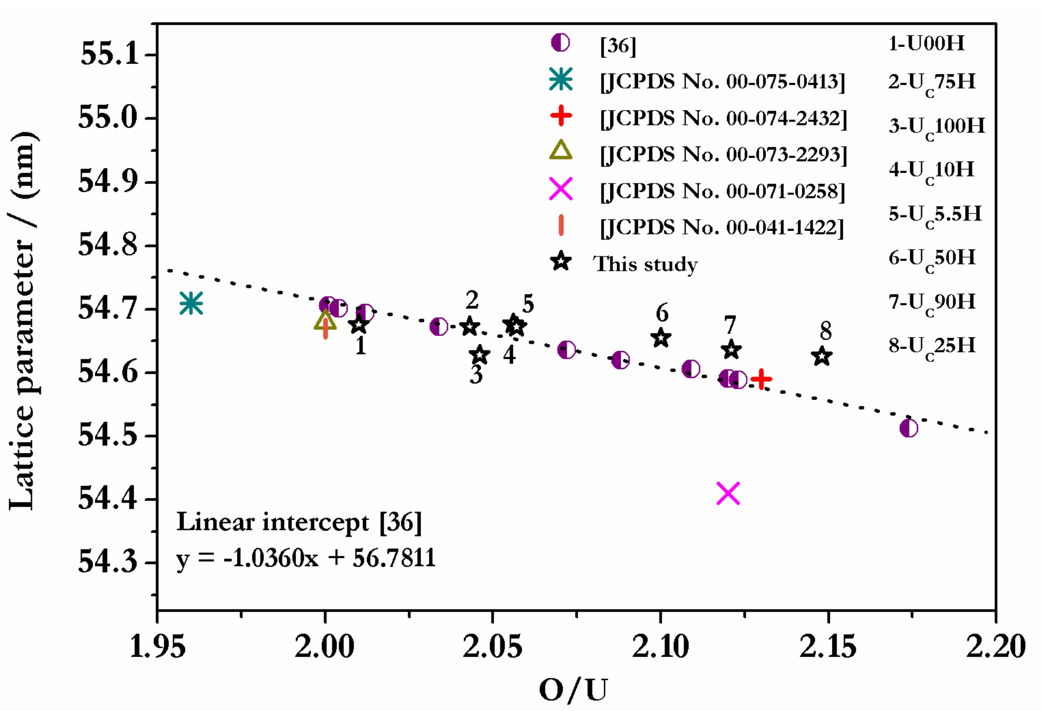

Figure 3.9 Dependence of the Lattice parameter of $UO_{2\pm x}$ on oxygen non-stoichiometry (O/U)

In order to compare the two methods (HW and Sc) used in deriving the XCS, the dimensionless relative crystallite size parameter ($\Delta XCS = (XCS_{HW} - XCS_{Sc}) / XCS_{HW}$) was considered. This parameter represents the error in the Sc estimate of the crystallite size and is caused by neglecting the contribution of lattice strain to the peak broadening. The variation in this parameter with the lattice strain given by eqn. 3.3 was found to be linear. The dependence of the error in the estimate on the lattice strain is given in Fig. 3.8e.

$$\Delta XCS = \frac{XCS_{HW} - XCS_{Sc}}{XCS_{HW}} = \frac{4 \in \tan\theta}{\beta} \qquad (3.3)$$

The slopes were found to be more or less identical for both the U_3O_8 and UO_2 powders, i.e. the “C” and “H” powders respectively. However, the error in the estimate caused by neglecting the strain component appears to be less for the “A” powders (higher value of slope) as compared to the “H” and “C” powders. Hence, care should be exercised in using the Sc estimates for arriving at the crystallite sizes for the gel-combustion derived products. Our results are in keeping with the observations made in ref [38]. Ideally, analysis of the lattice strain and the XCS in conjunction with the microstructure should be carried out, which is beyond the scope of this work.

3.5.5 Pore size distribution analysis

Cumulative pore size distribution (CPoSD) in the “C” and “H” powders estimated with the help of mercury porosimetry is presented in the Figs. 3.10 and 3.11 respectively. Fig. 3.6c depicts the total volume of the mercury intruded into the pores of “C” and “H” urania powders. From Fig. 3.10 it is clear that the volume (per unit mass of the powder) of mercury intruded into the pores of calcined urania powders increases with the value of R up to 0.25 (226 mm^3g^{-1} to 1549 mm^3g^{-1}).

The specific pore volume decreases with further increase in the value of R (0.50) to 320 mm^3g^{-1} and remains constant in the range 320 - 500 mm^3g^{-1} thereafter. The specific pore volume of calcined urania powders exhibits the following trend:

$$V_{U00C} < V_{U_C50C} < V_{U_C75C} < V_{U_C100C} < V_{U_C5.5C} \approx V_{U_C90C} < V_{U_C10C} < V_{U_C25C}$$

The total pore volume (V_T) of these powders was inversely correlated with their corresponding ρ_B (eqn. 3.4).

$$\rho_B(\mathrm{Mgm^{-3}}) \propto \frac{1}{V_T\ (\mathrm{mm^3g^{-1}})} \tag{3.4}$$

Similarly, the total pore volume of the "H" urania powders was found to increase with R when the latter was increased from 0 to 0.25. Further increase in the value of R led to a decrease in the total pore volume to 281 mm^3g^{-1}. A comparison of the total volume of mercury intruded into the "C" and "H" urania powders (Fig. 3.6c) indicates that additional pores are generated during hydrogen reduction which leads to an increase in the total pore volume. During the conversion of the orthorombic U_3O_8 into the fluorite UO_2 phase, new fine pores are generated [24]. This explains the increase in the total pore volume of "H" urania powders:

$$V_{U00H} < V_{U_C50H} < V_{U_C90H} < V_{U_C75H} < V_{U_C100H} < V_{U_C5.5H} < V_{U_C10H} < V_{U_C25C}$$

Systematic variation in the pore volume of the gel-combustion derived urania powders has not been investigated so far. However, limited data on the pore size distribution in urania powders prepared by the conventional AUC process has been cited by C. S. Choi et al. [24]. These authors have reported an average total pore volume of 260 - 380 mm^3g^{-1} for urania powders derived through the AUC process. This value is close to the lowest values of the total pore volume of urania powders prepared in this study.

3.5.6 Microstructure and morphology

The morphology of the powders U_C25C, U_C25H and U_C50H have been investigated by using SEM. Images pertaining to both U_C25C and U_C25H (Fig. 3.12 and Fig. 3.13a) were found to have a "broccoli like" exfoliated morphology. It appears that the gel-combustion derived UO_2 powders are pseudomorphic. High magnification image of the broccoli like pattern in Fig. 3.12 reveals embedded features with faceted cubic crystals and faceted cuboidal pores. The SEM images of U_C50H are presented in Fig. 3.13b. Hydrogen reduction leads to lattice restructuring of α-U_3O_8 to UO_2.

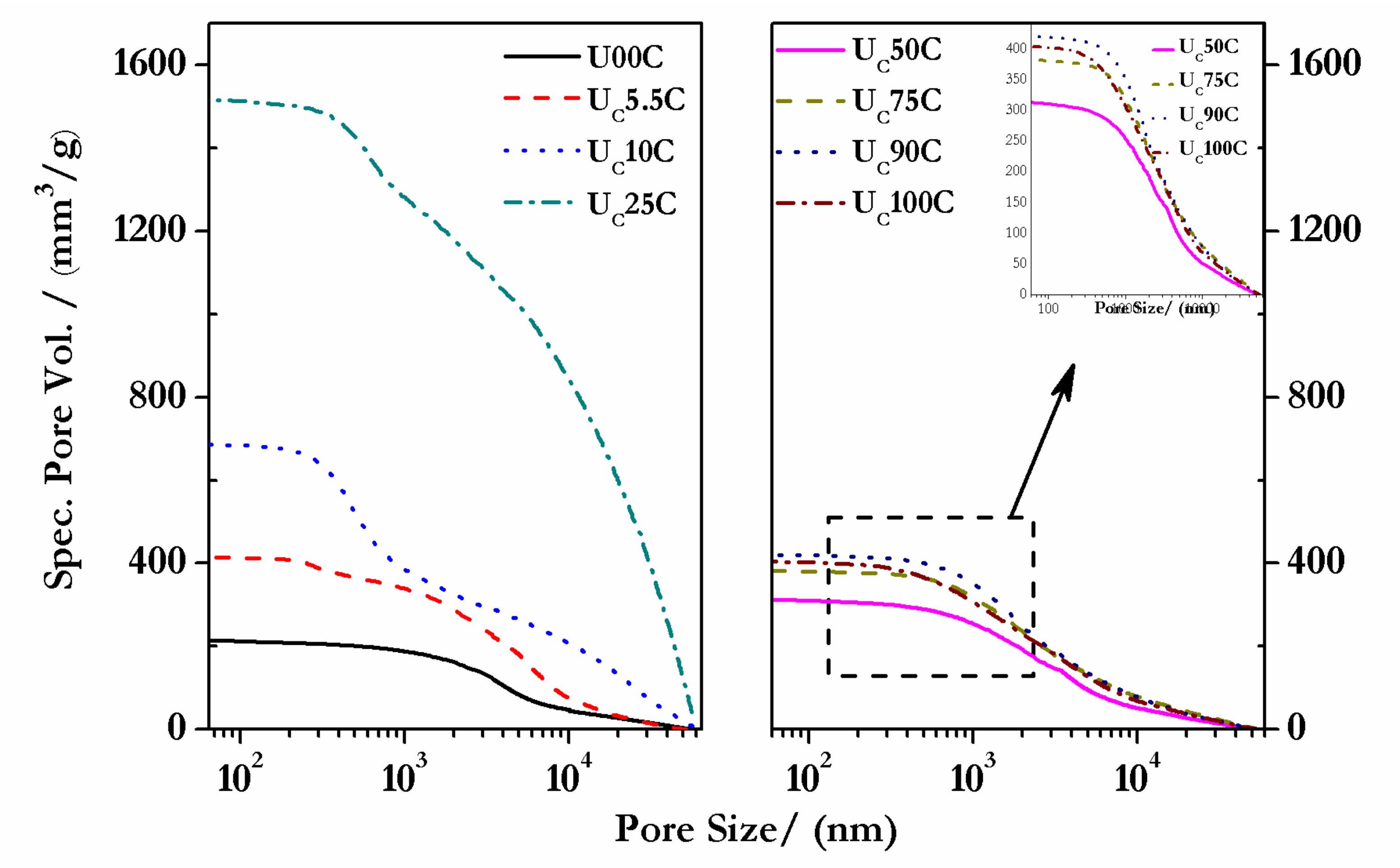

Figure 3.10 Cumulative size distribution of pores in "calcined" urania powders

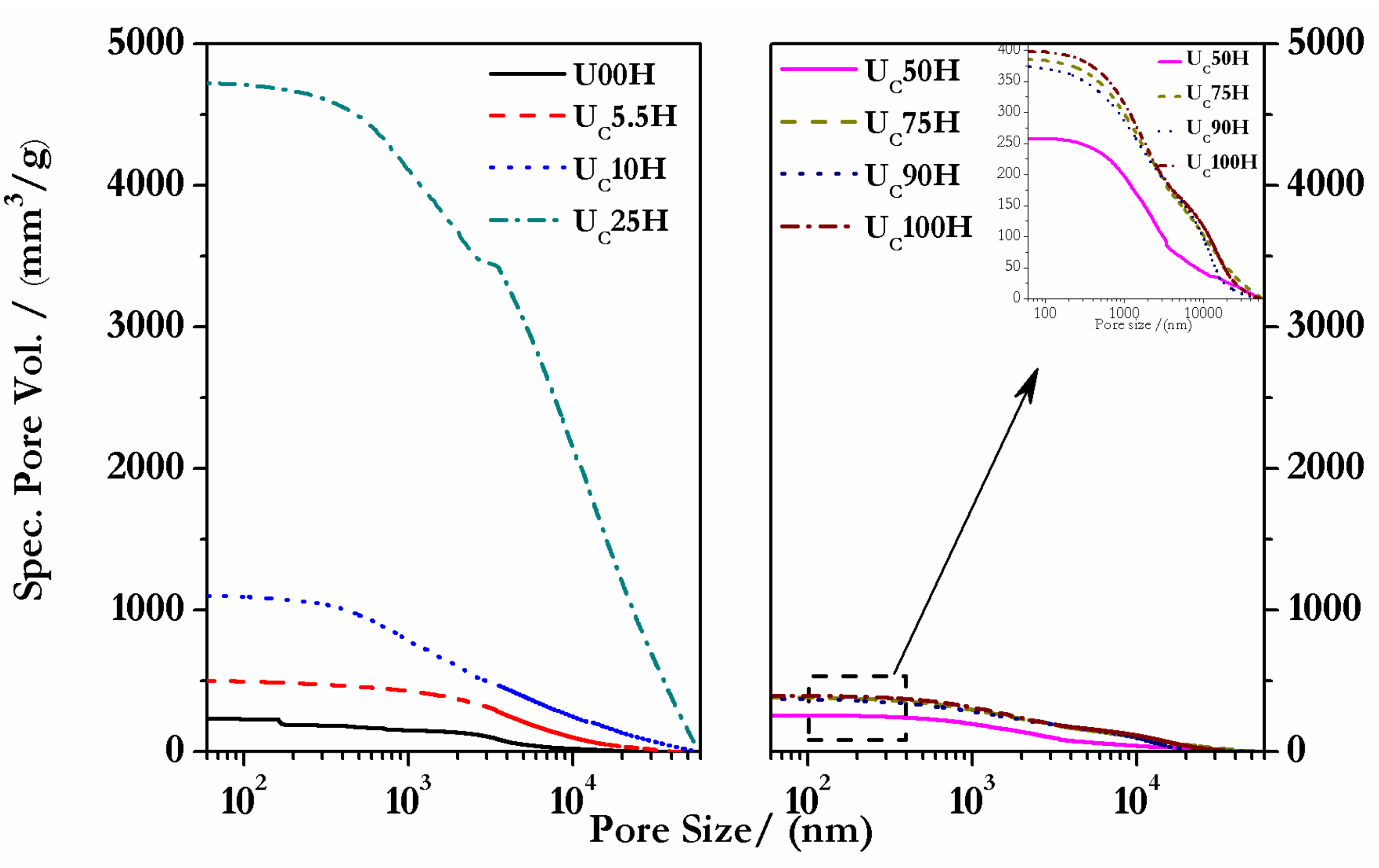

Figure 3.11 Cumulative size distribution of pores in "hydrogen reduced" urania powders

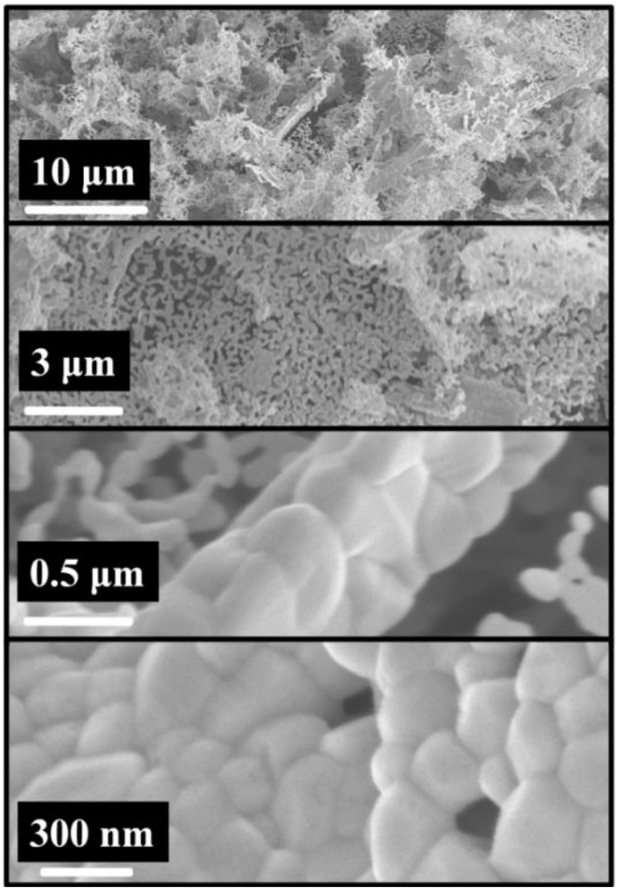

Figure 3.12 SEM images of "calcined" urania powers with an R value of 0.25

Microstructural analyses carried out by using TEM on the powders U_C25C and U_C25H are given in Figs. 3.14 – 3.16, which reveal the presence of macropores (20 nm). The selected area electron diffraction (SAED) pattern pertaining to these powders confirmed that the calcined and hydrogen reduced samples comprised orthorhombic α-U_3O_8 and fluorite UO_2 respectively. The d-spacings measured from the diffracted images were compared with those pertaining to the star JCPDS pattern. The inverse Fast Fourier Transform images (IFFT) were comparable with the IFFT image generated from CaRIne v3.1® software. By using these, the zone axes of the respective samples were also calculated. All the bright and dark field images testified the presence of nanoscopic grains. Macropores with interconnected porosity were also observed, a typical image of which is presented in Fig. 3.15a.

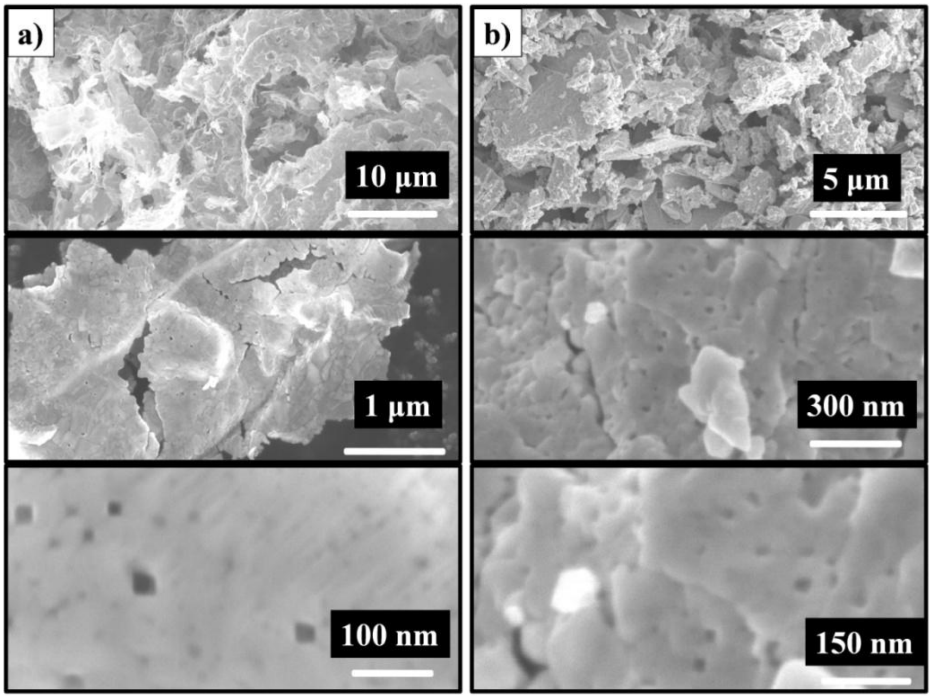

Figure 3.13 SEM images of "hydrogen reduced" urania powers with an R value of (a) 0.25 and (b) 0.50

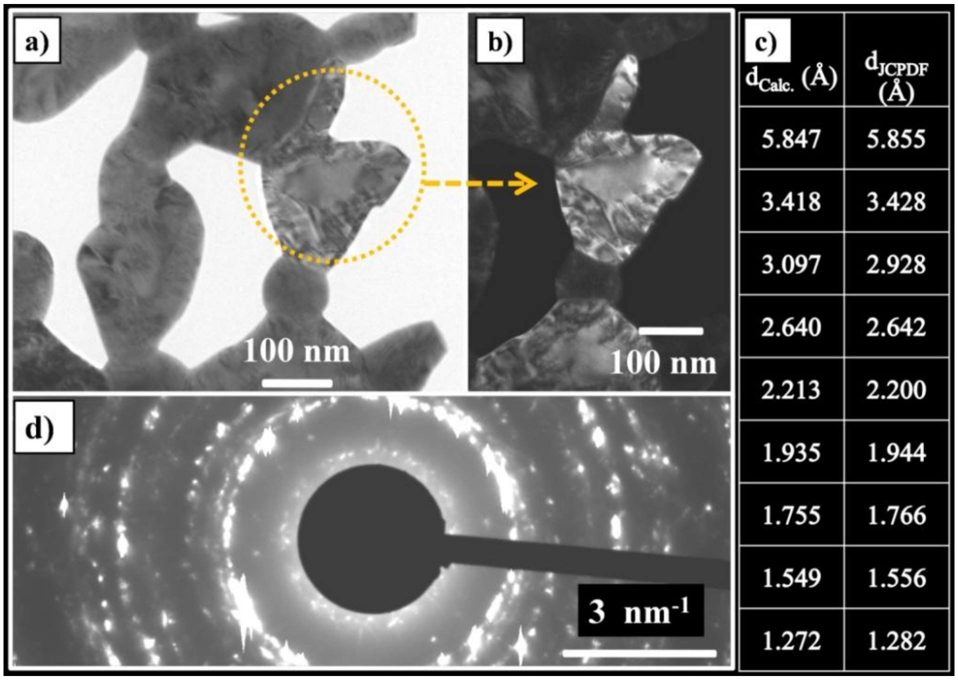

$d_{Calc.}$ (Å)	d_{JCPDF} (Å)
5.847	5.855
3.418	3.428
3.097	2.928
2.640	2.642
2.213	2.200
1.935	1.944
1.755	1.766
1.549	1.556
1.272	1.282

Figure 3.14 TEM images of U_C25C powders: (a) bright field image revealing nano grains; (b) dark field image revealing nano grains; (c) calculated and standard 'd' spacing from SAED image and (d) SAED image

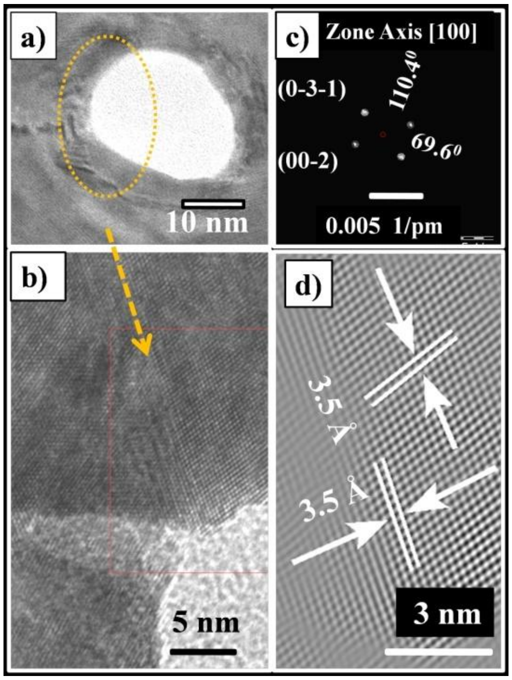

Figure 3.15 TEM images of U_C25C powders: (a) a typical nano pore; (b) HRTEM image with selected area; (c) FFT image revealing zone axis [100] and (d) IFFT image of zone axis [100]

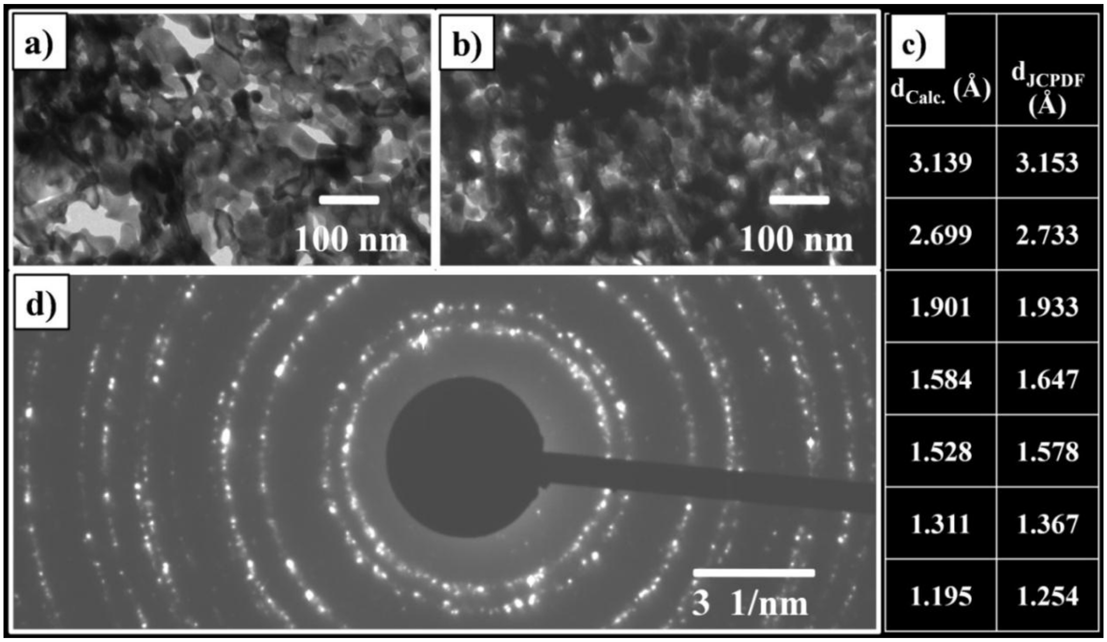

$d_{Calc.}$ (Å)	d_{JCPDF} (Å)
3.139	3.153
2.699	2.733
1.901	1.933
1.584	1.647
1.528	1.578
1.311	1.367
1.195	1.254

Figure 3.16 TEM images of U_C25H powders: (a) bright field image revealing faceted nano grains; (b) dark field image depicting nano grains; (c) calculated and standard 'd' spacing from SAED image and (d) SAED image

EELS [39-41] was used to ascertain the oxidation states as well as the nature of bonding in the specimen i.e., for α-U_3O_8 and UO_2. The powders U_C25C, U_C25H, U_C50C and U_C50H were examined. The corresponding O-K edge and $N_{4,5}$ (4d→ 5f) edges [39] pertaining to these powders are depicted in Fig. 3.17. In order to use the spin-orbit sum rule [42, 43], background correction was carried out initially, following which the branching ratio [$B=A_{5/2}/(A_{5/2}+A_{3/2})$] was calculated, wherein $A_{5/2}$ and $A_{3/2}$ are the integrated intensities of N_5 and N_4 peaks respectively. These values of B were used for calculating the spin-orbit interaction per hole, using eqn. 3.5 [39, 40].

$$\frac{< w^{110} >}{n_h} - \Delta = -\frac{5}{2}\left(B - \frac{3}{5}\right) \tag{3.5}$$

where, n_h is the number of the 5f holes, Δ is the correction factor as given by Cowan's relativistic Hartree-Fock code [44] and $<w^{110}>$ is the expectation value for the angular part of the spin-orbit (5f) parameter. These results are tabulated in Table 3.7. The branching ratio for the powders U_C25C and U_C50C are 0.665 and 0.632 respectively. The values of B pertaining to the powders U_C25H and U_C50H are 0.713 and 0.693 respectively. The above results indicate that due to the increase in N_4 peaks in UO_2 the branching ratio was found to be high whereas for U_3O_8 powders B value was minimum compared to UO_2 due to the substantial increase in N_4 integrated area. The results obtained with UO_2 samples were comparable to the results indicated by Moore et al. [40] for α-U metal and UO_2 powders. These features are typical for urania and are in keeping with the fact that both α-U_3O_8 and UO_2 are predominantly covalent.

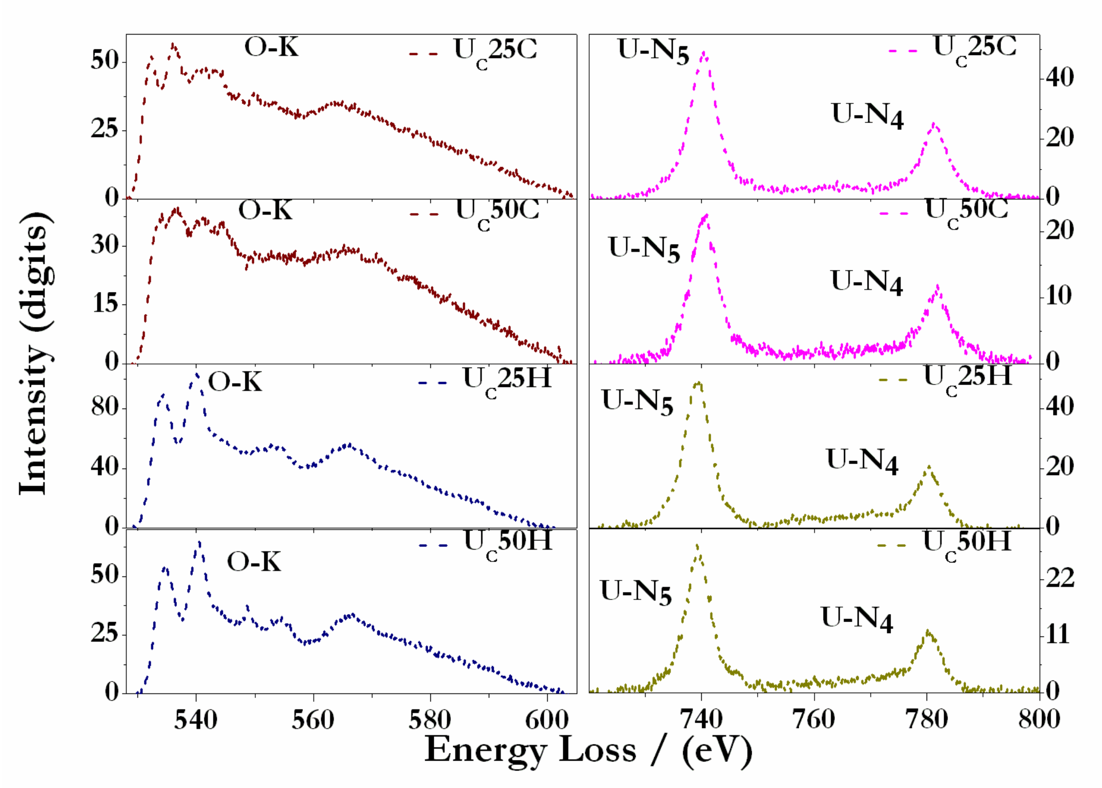

Figure 3.17 *EELS of powders U_C25C, U_C25H, U_C50C and U_C50H depicting both O-K edge and $N_{4,5}$ edges*

Table 3.7 Parameters derived from the EELS spectra of α-U_3O_8 and UO_2

Sample	f	B	$<w^{110}>/n_h - \Delta$	Phase
U_C25C	3	0.665	-0.163	α-U_3O_8
U_C50C		0.632	-0.080	α-U_3O_8
U_C25H		0.713	-0.283	UO_2
U_C50H		0.693	-0.233	UO_2

(Δ = -0.010 for n = 3)

3.6 Conclusions drawn from citrate gel-combustion synthesis of nc-urania

Nc-urania powders were synthesized by using citrate gel-combustion in bulk quantities for the first time. The systematic dependence of the reaction as well as the properties of these nanocrystalline powders on the composition of the combustion mixture (R) was investigated. The course of the combustion reaction is these mixtures were measured with the help of DSC for the first time. These results showed that the rate of this reaction is strongly influenced by the composition of the combustion mixture (R). Mixtures with an R value of 0.25 showed a markedly different behavior compared to the rest and underwent "volume combustion".

Upon storage the oxygen stoichiometry of the UO_2 powders was found to change with time, plausibly due to the facile oxidation of these nc powders. All the powders possessed a flaky morphology and comprised agglomerates of nanocrystallites of α-U_3O_8 or UO_2. The morphology and microstructure of the powders derived from the mixture with the R value of 0.25 were very different from the rest. HRTEM investigations reaffirmed the nanocrystallinity and revealed the presence of faceted nano crystallites and nano pores. The EELS study confirmed the covalency as expected.

It was observed that the ρ_B, XCS, size distribution of pores and particles, morphology of the powders and their microstructure showed a strong dependence on the value of R. The variation in the bulk density with R and its correlation with the size distribution of particles were investigated. For the first time an attempt was made to de-convolute the particle size distribution data. The contributions from the different size fractions were found to correlate well with the ρ_B.

The variation in lattice strain in nc-UO_2 derived through citrate gel-combustion and its dependence on size is being reported for the first time. Two distinct regimes viz., nc regime and the microcrystalline regime could be delineated by analyzing the variation in the lattice strain with the XCS. Further analytical models are required, in order to understand the relation between the lattice strain and the distribution of sizes. It appears that the combustion mixtures with R values ranging from 0.25 to 0.50 would yield powders that are most suitable further processing.

3.7 Reaction mechanism and kinetic analysis of citrate gel-combustion synthesis of nc-urania

The kinetics of the gel-combustion reaction in the mixture with R = 0.25 was investigated by using DSC and TG-DTA-MS. The results of thermal analysis (DSC and TG-DTA-MS) are explained in detail in section 3.4.

The general expression for Arrhenius type temperature dependence of rate constant in heterogeneous kinetics under isothermal condition [45] (eqn. 3.6) could be expressed as,

$$\frac{\partial\alpha}{\partial t} = Ae^{-\left(\frac{E_a}{RT}\right)} f(\alpha) \qquad (3.6)$$

Where α is degree of conversion (fraction reacted), T is temperature in Kelvin; R is the gas constant; E_a is activation energy of the reaction; t is time; $f(\alpha)$ is the conversion function which is dependent on the reaction mechanism and A is the pre-exponential factor. The expression for heterogeneous reaction under non-isothermal condition with constant heating rate [45] (β) is represented as,

$$\frac{\partial\alpha}{\partial T} = \frac{A}{\beta} e^{-\left(\frac{E_a}{RT}\right)} f(\alpha) \qquad (3.7)$$

where $\beta = \frac{\partial T}{\partial t}$; the integral form of eqn. 3.7 could be represented by eqn. (3.8) and this could be solved using numerical integration [46].

$$g(\alpha) \equiv \int_0^{\alpha} \frac{\partial\alpha}{\partial t} = \int_0^{T} \frac{A}{\beta} \exp\left(\frac{-E_a}{RT}\right) \partial T \qquad (3.8)$$

Where g(α) is the integral form of f(α). The E_a of the reaction could be obtained by using "model free classical kinetic methods" such as Kissinger method [47], Augis and Bennet method [48] and Mahadevan [49] method.

3.7.1 Kissinger method [47]

The activation energy (E_a) of the reaction could be obtained by knowing the peak temperature of the thermal analysis curve as a function of heating rate. The Kissinger equation [47] (eqn. 3.9) that employs the peak temperature (T_P) to evaluate E_a is given below.

$$\ln\frac{\beta}{T_p^2} = \text{constant} - \frac{E_a}{RT_p} \tag{3.9}$$

The plot of $\ln\frac{\beta}{T_p^2}$ vs $1/T_p$, would be a straight line with a slope ($-E_a/R$) from which activation energy could be derived.

3.7.2 Augis and Bennet method [48]

The expression used by Augis-Bennet [48] (eqn. 10), that employs a constant (k_0) for the determination of E_a is given below.

$$\ln\frac{\beta}{T_P} = \ln k_0 - \frac{E_a}{RT_p} \tag{3.10}$$

The value of k_0 and slope are derived from the graphical representation of the dependence of eqn. 3.10. The activation energy (E_a) could then be obtained from the slope.

3.7.3 Mahadevan method [49]

Mahadevan [49] proposed eqn. 3.11 for the determination of activation energy (E_a).

$$\ln\beta = \text{constant} - \frac{E_a}{RT_p} \tag{3.11}$$

The enumeration of the E_a in the Mahadevan method [49] is carried out by using the slope obtained from the plot of ln β against $1/T_p$.

The classical methods (Kissinger [47], Augis and Bennet [48] and Mahadevan [49]) of kinetic analysis assume single activation energy for the entire reaction, which may not be correct for a heterogeneous reaction. These classical methods provide a rough estimate of E_a. Hence it is essential to evaluate E_a of the reaction as a function of fraction reacted (α). Thus, it is necessary to obtain the E_a by using the isoconversional method [50, 51].

3.7.4 Kissinger-Akahira-Sunose (KAS) isoconversional method [50, 51]

Though the overall estimate of E_a could be carried out with the model free classical methods, it is essential to understand the dependence of the E_a on the fractional progress of the reaction (α). Hence, the isoconversional KAS [50, 51] method was used to evaluate the dependence of E_a on α.

The approximate solution was given by the KAS [50, 51] method (also known as the isoconversional method) employs the following eqn. 3.12 to evaluate the E_a as a function of α.

$$\ln\frac{\beta}{T_{\alpha,i}^2} = \text{constant} - \frac{E_\alpha}{RT_{\alpha,i}} \tag{3.12}$$

Where the subscript 'i' represents heating rates. The degree of conversion (α) was determined from the fractional area of the heat flow rate curve at different heating rates ($\alpha = \frac{A_F}{A_T}$ where A_F and A_T are fractional area and total area respectively) [52]. Before evaluating α, the baseline of the DSC curves were corrected by using blank run. This procedure was adopted for the curves obtained with different heating rates. From the temperature dependence of α obtained at different heating rates the effective E_a was computed, by using eqn. 3.12 from a plot of $\ln\frac{\beta}{T_{\alpha,i}^2}$ vs $\frac{1}{T_{\alpha,i}}$.

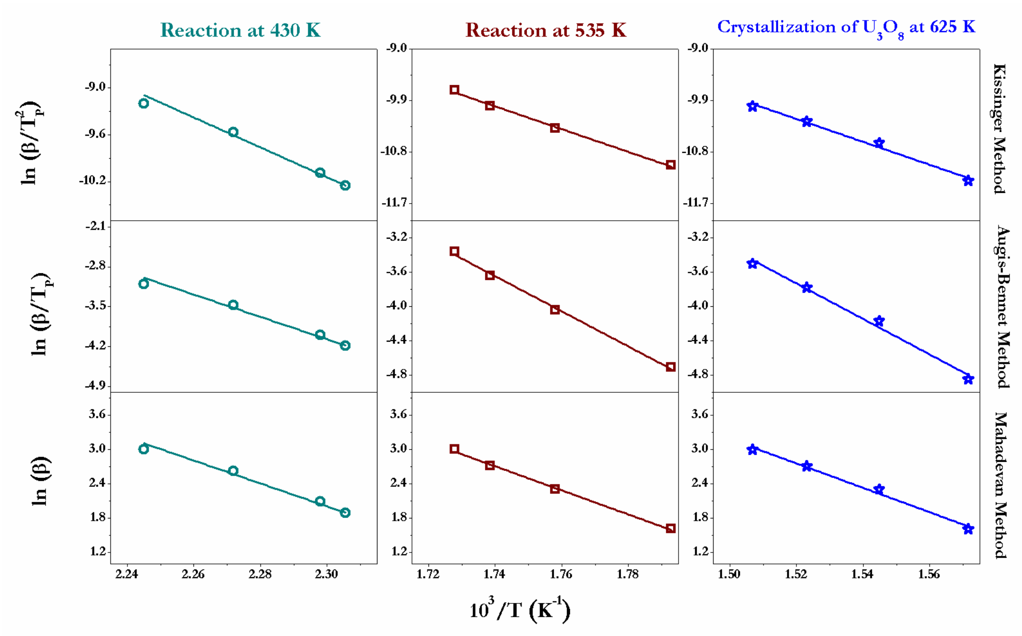

Figure 3.18 Temperature dependence of model variables pertaining to Kissinger [47], Augis and Bennet [48] and Mahadevan methods [49]

It should be mentioned here that the areas of the peaks pertaining to the thermal events varied with the rate of heating (β). It is well established that the peak area obtained in a heat flux technique would be dependent on β even if the mass of the sample does not vary. This had been demonstrated even in the case of simple melting [45, 46]. Since the heat effects measured here were not calibrated or quantified with respect to the peak area at a given β. The relative area of the peaks corresponding to the different thermal events in an experiment was nearly the same irrespective of the β. Hence, in the relative analysis of the progress of the reaction the variation in the area of the peak with β this is an experimental artifact, may not introduce errors in the estimate of the kinetic parameters.

3.8 Determination of activation energy

3.8.1 Classical models

The linear dependence of the model parameters on temperature pertaining to Kissinger [47], Augis - Bennet [48] and Mahadevan methods [49] corresponding to the first, second and third exothermic peaks are shown in Fig. 3.18. The activation energies computed by using these methods pertaining to the first and second exothermic events as well as that to the crystallization of uranium oxide are listed in Table. 3.8. From these data (Table 3.8) it is evident that the values of E_a are mutually in agreement within 5 %.

3.8.2 Isoconversional method

The DSC curves pertaining to the three exothermic events at different heating rates are shown in Fig. 3.19.

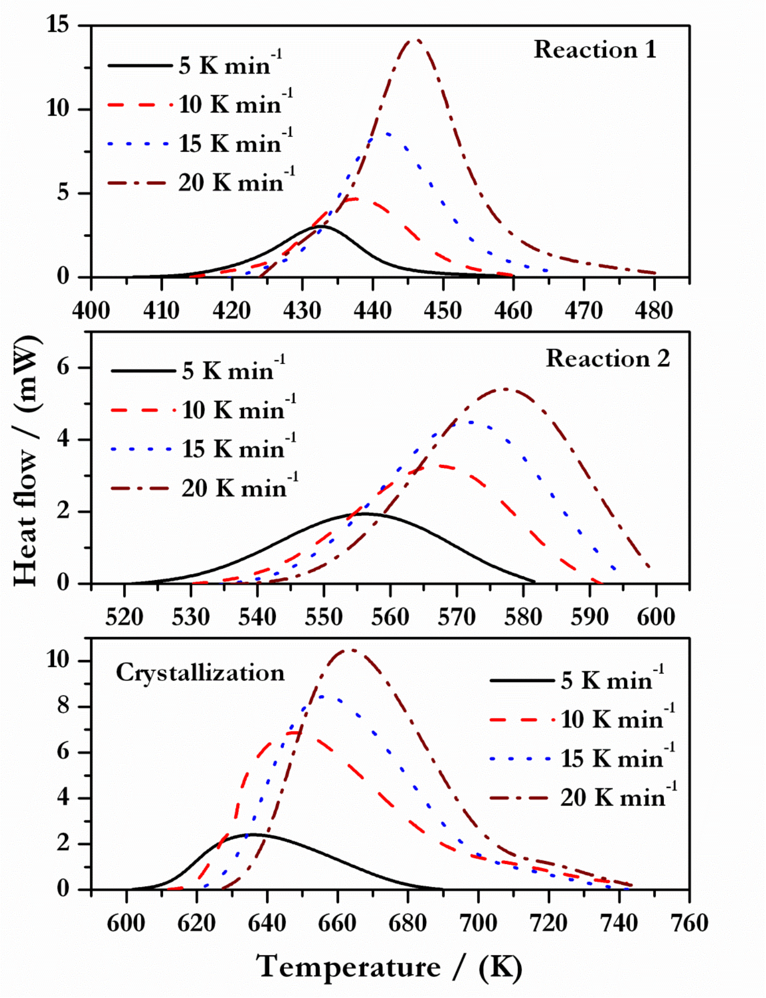

Figure 3.19 Exothermic peaks obtained in the DSC analysis at different steps of the combustion reaction

The variation in α as a function of temperature pertaining to the three exothermic events on α is shown in Fig. 3.20. The dependence of E_a on α pertaining to the three exothermic events is shown in Fig. 3.21. From these data it is clear that the effective E_a remains nearly constant for "α" values from 0.2 to 0.8. The average value of the E_a in the α range of 0.2 to 0.8 for the first, second and third thermal events were found to be 152 ± 6 kJ mol^{-1}, 179 ± 8 kJ mol^{-1} and 166 ± 7 kJ mol^{-1} respectively. Taylor et al. [53] had reported the E_a for the formation of U_3O_8 in the unirradiated UO_2 fuel is 146 ± 10 kJ mol^{-1}. The E_a values obtained by this method are in agreement with those obtained by other classical methods within 5% (Table 3.8).

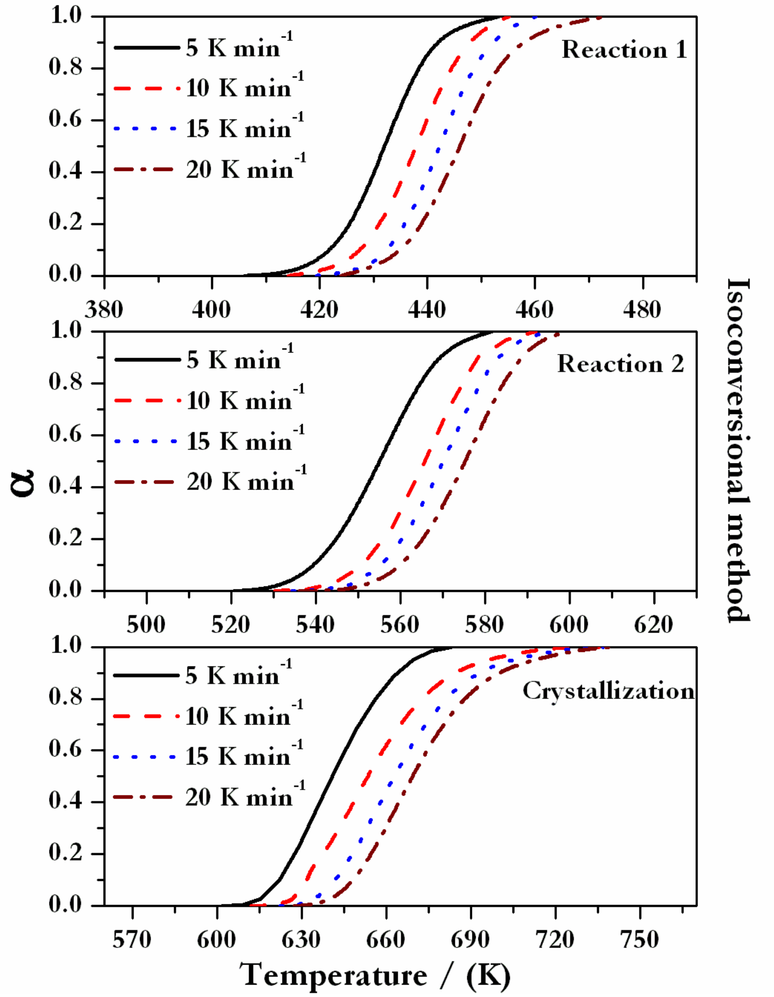

Figure 3.20 Degree of reaction (α) as a function of temperatures at different heating rates

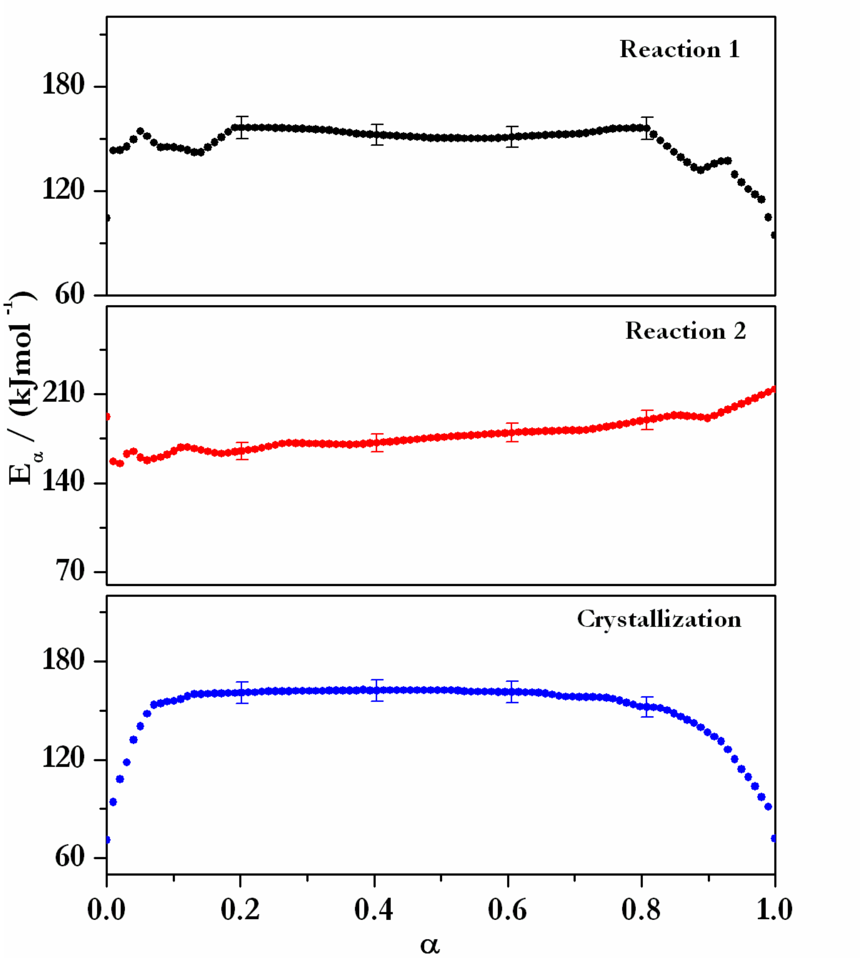

Figure 3.21 Dependence of the E_α pertaining to the thermal events (DSC)

The dependence of E_a on α pertaining to all the three thermal events could be explained as follows. As observed in Fig. 3.21, the activation energies do not vary much during the progress of the reaction (α = 0.2 to 0.8). In view of the fact that the reaction under investigation is heterogeneous and that many process are operating simultaneously, it is quite unlikely that the E_a would be independent of α. However, the E_a pertaining to these different processes viz., nucleation, growth, diffusion, localized sintering is operating simultaneously, get internally compensated leading to the consistency of E_a with α. In the first reaction, the activation energy appears to be nearly constant up to α = 0.8, beyond which it decreases indicating that the mechanism gets more complex with the formation of U_3O_8 and the growth and diffusion of the constituent phases [54].

Table 3.8 Computed activation energy by using various models

Methods	E_a (1st reaction) T_{onset} 430 K (kJ mol^{-1})	E_a (2nd reaction) T_{onset} 535 K (kJ mol^{-1})	E_a (Crystallization) T_{onset} 625 K (kJ mol^{-1})
Kissinger	159 ±2	166 ±3	167 ±1
Augis and Bennet	163 ±1	170 ±2	172 ±1
Mahadevan	167 ±4	175 ±1	177 ±2
Isoconversion (α from 0.20 to 0.80)	152 ± 6	179 ± 8	166 ± 7

During the second stage, though the overall activation energy does not vary much with respect to α, it shows an increasing trend with α. This is probably due to a parallel reaction [55] involving the growth of U_3O_8 nuclei and the combustion of citric acid. However, the effect due to the combustion dominates. In the third reaction involving no measurable weight change but only the crystallization of U_3O_8, the initial increase in the activation energy observed is probably due to the formation of a well-ordered crystalline U_3O_8. The activation energies pertaining to the formation of U_3O_8 from microcrystalline UO_2 reported by Taylor [53] are marginally lower than those estimated in this study. This is probably due to the additional energy barrier imposed by the nearly amorphous (nc) UO_2 formed during the combustion reaction used in this study. In the stages of the reaction beyond $\alpha = 0.8$, along with crystallization, diffusion of oxygen also competes and thus a general trend in decrease in E_a was observed beyond alpha of 0.80 [54].

3.9 Conclusions drawn from the kinetic analysis of citrate gel-combustion

Elucidation of a reaction mechanism for the combustion synthesis of uranium oxide was carried out for the first time. The sample gels were analyzed by using TG-DTA-MS and DSC. Three exothermic peaks were observed in both the DTA and DSC analyses. The proposed reaction mechanism was supported by the mass spectrometric analysis of the evolved gases. The E_a estimated for the first two thermal events were 152 ± 6 and 179 ± 8 kJ mol^{-1} respectively. The E_a for the third thermal event (crystallization of U_3O_8) was found to be 166 ± 7 kJ mol^{-1}. In this study gels with a fuel to oxidant ratio of 0.25 were investigated. However, the reaction mechanisms and the activation energies will depend on the fuel (citric acid) to oxidant (nitrate) ratio of the gels. Further investigations are required to study the systematic variation of citrate gel-combustion of urania with different fuel to nitrate ratio (R).

3.10 Compaction and sintering of nc-UO_2

3.10.1 Green density (ρ_G)

The variation in the ρ_G with the compaction pressures pertaining to U_CXXH powders is presented in Fig. 3.22 and Table 3.9. The ρ_G of these pellets was found to vary from 44.6 – 57.2 % T.D. The lowest ρ_G was observed for the sample U_C90H (44.6 % T.D) when compacted at 60 MPa while the highest ρ_G (57.2 % T.D) was obtained for the U_C25H powders at a CP of 353 MPa. All the powders except U_C10H could be compacted to a ρ_G more than 50 % T. D. at a pressure above 180 MPa. To obtain a pellet with good handling strength (except U00H) a CP of about 60 MPa was found necessary. However to consolidate the powder U00H into a defect free pellet with good handling strength a minimum CP of 120 MPa was required. U_C5.5H and U_C25H exhibited nearly identical compaction behavior (Fig. 3.22). Their ρ_G are found to increase linearly with the CP up to 210 MPa. Probably at this pressure the harder agglomerates undergo fracture and rearrangement leading to a further increase in the ρ_G with pressure. The powder U00H and U_C10H exhibit a multimodal size distribution of particles. Hence, it is reasonable to assume that these powders would undergo a better packing. From the results depicted in Fig. 3.22 it is evident that upon compaction, the powders U_C10H and U00H yield a higher ρ_G

than the powders U_C5.5H and U_C25H. It is also clear from Fig. 3.22 that the powders U_C50H, U_C75H, U_C90H and U_C100H exhibit similar variation in ρ_G with CP with a sharp discontinuity in the pressure dependence at 280 MPa.

U00H yielded pellets with a maximum ρ_G of 58.3 % T.D at 280 MPa. Further increase in the CP up to 353 MPa did not bring about any appreciable change in the ρ_G. It is reported in the literature [56] that it is difficult to compact nc powders to a higher ρ_G as compared to their microcrystalline counterparts. This behavior is ascribed to the following reasons; viz, i) presence of higher friction during compaction, ii) fracturing of finer particles requiring excessive stress and iii) presence of steeper pressure gradients within the compact. However, the powders used in this study behaved very much like microcrystalline powders. Even though they possessed a nano-substructure, the size of the particle aggregates was as big as 10-100 μm. Thus the gel-combustion derived powders offer the dual advantage of possessing nano-crystallites and the microcrystalline particle aggregates.

In the literature [19, 22-27, 57-63], pressures in the range of 50-392 MPa has been reported (Table 3.12) for the consolidation of microcrystalline urania. The maximum ρ_G obtained is about 58 % T.D [19, 24]. While Sakamura [60], Ayaz [57], Furhrman [58], Harada [59], Ching-Tsven [19], Choi [24] and Yi-Ming [61] had used lubricants during compaction many others [22-27, 62, 63] have compacted without the aid of a lubricant. Most authors could obtain a ρ_G of about 50 % T.D. Murty et al. [64] reported that a CP of 250 - 275 MPa is best suited for the compaction of UO_2 derived through the ADU route. The ρ_G obtained in this work (44.6 to 57.2 % T.D) is comparable with those reported in the literature [18, 19, 22-24, 26, 27, 57-63]. Our results revealed that all the gel-combustion derived powders are suitable for binderless consolidation due to their good flowability and favorable size distribution.

Table 3.9 Green density (ρ_G) of UO_2 pellets derived through citrate gel-combustion method

CP (MPa)	**U00H**	**U_C5.5H**	**U_C10H**	**U_C25H**	**U_C50H**	**U_C75H**	**U_C90H**	**U_C100H**
	% T.D[x]							
60	-	45.0 ± 0.2	48.1 ± 0.5	46.0 ± 0.6	45.7 ± 0.8	45.1 ± 0.4	44.6 ± 0.6	45.2 ± 0.3
120	49.6 ± 0.4	48.3 ± 0.6	50.9 ± 0.5	48.8 ± 0.5	48.8 ± 0.7	48.9 ± 0.2	48.1 ± 0.5	48.7 ± 0.1
180	54.2 ± 0.9	50.7 ± 0.2	53.4 ± 0.5	51.1 ± 0.5	52.0 ± 0.2	51.1 ± 0.5	51.4 ± 0.2	51.4 ± 0.2
244	57.7 ± 0.7	52.5 ± 0.4	55.3 ± 0.4	52.5 ± 0.6	53.8 ± 0.4	53.0 ± 0.4	52.8 ± 0.6	53.3 ± 0.3
280	58.3 ± 0.5	52.7 ± 0.4	55.7 ± 0.4	52.9 ± 0.5	54.8 ± 0.6	54.4 ± 0.4	54.1 ± 0.4	53.9 ± 0.1
317	58.3 ± 0.9	54.2 ± 0.5	56.4 ± 0.7	54.4 ± 0.6	55.8 ± 0.4	55.2 ± 0.5	54.2 ± 0.6	54.3 ± 0.3
353	57.6 ± 0.3	54.9 ± 0.6	57.2 ± 0.2	55.3 ± 0.9	55.7 ± 0.4	56.1 ± 0.5	55.2 ± 0.3	54.8 ± 0.6

[x] *indicates the mean value of five independent measurements*

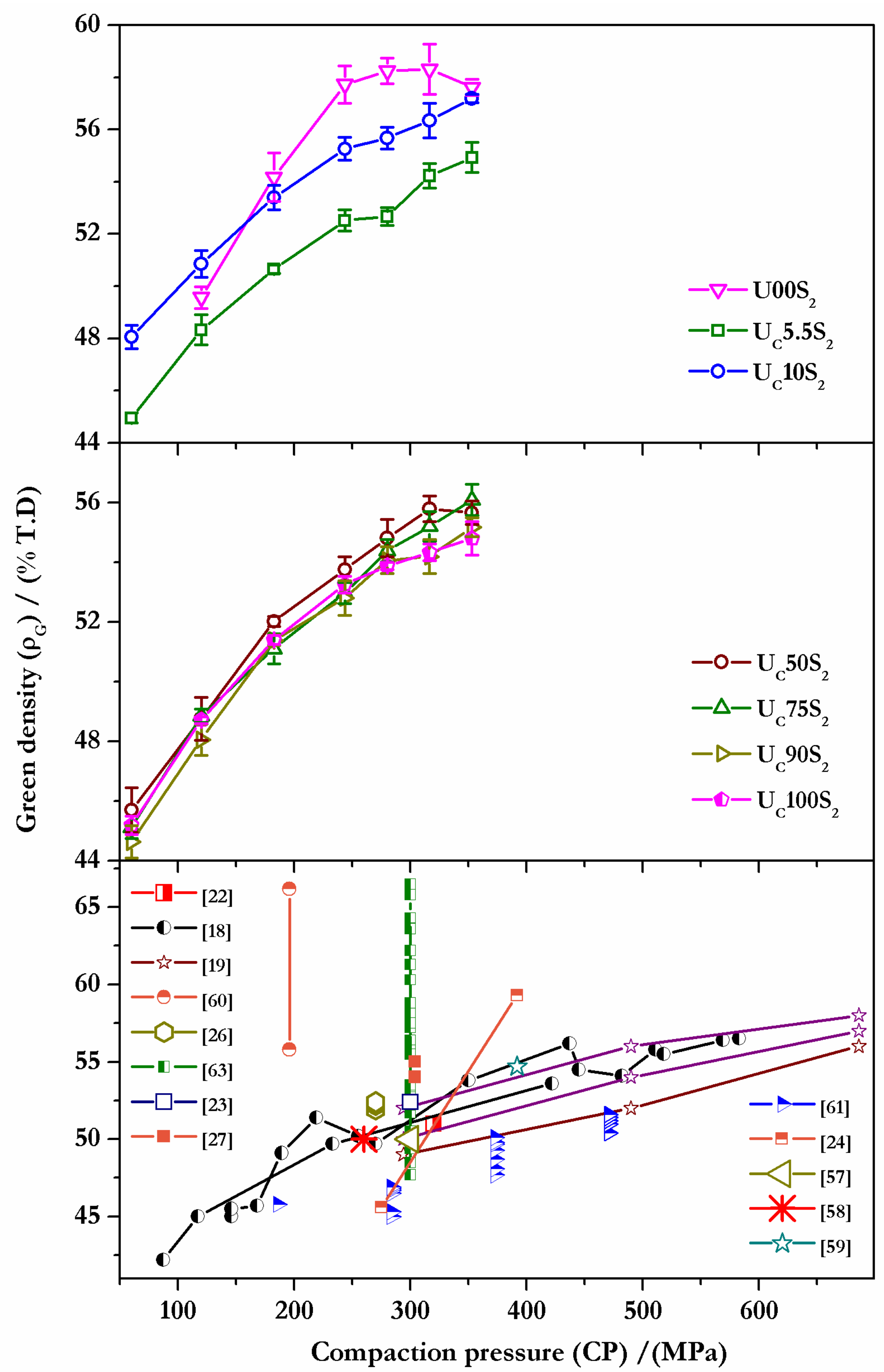

Figure 3.22 Variation in the ρ_G with CP ["hydrogen reduced" UO_2 powders]

3.10.2 Sintering studies on U_C25H

The densification of nc materials depends on many process variables viz., size distribution of particles, SSA of the powders, porosity, ρ_G, sintering temperature and sintering atmosphere [65]. The variables viz., stability of pores, the dihedral angle between the grains and the number of grains are indicative of the degree of densification. The densification could be enhanced by destabilizing the trapped pores which in turn depends mainly on the rate of sintering and final soaking temperature [65-67].

U_C25H exhibited powder properties markedly different from the rest and comprised smallest crystallites. From the data cited in the literature [68-71] it is evident that powders with small crystallites exhibit “run-away” sintering leading to a reduction in the sintered density when sintered at higher temperatures. Often modification of the sintering routine helps alleviate this problem. To study the difference between the CS and TSS [72] in the case of nc-UO_2, the powder U_C25H was chosen as a “typical” sample. The dependence of the relative ρ_S on the CP of the pellets U_C25S_C, U_C25S_1 and U_C25S_2 are presented in Fig. 3.23 and Table 3.10. These data reveal that CS yielded ρ_S ranging from 81.1 %T.D (at 60 MPa) to 95.9 % T.D (at 244 MPa). The ρ_S of the specimens U_C25_C is found to be increase linearly with the CP in the range 60 to 150 MPa, beyond which it is found to be independent of the latter. It is found that when CS is employed, the pellets compacted at 150 MPa, yield a ρ_S of 94.5 % T.D.

Porosity values reveal that beyond 150 MPa, the open pore fraction decreases to 1 %, leaving behind a closed porosity of about 3.5 %. It is also observed that the open pore fraction is inversely correlated with the CP. The total porosity in the sintered pellet decreases drastically from 19 % to 6 % in sintered UO_2 pellets when the CP is increased from 60 MPa to 150 MPa.

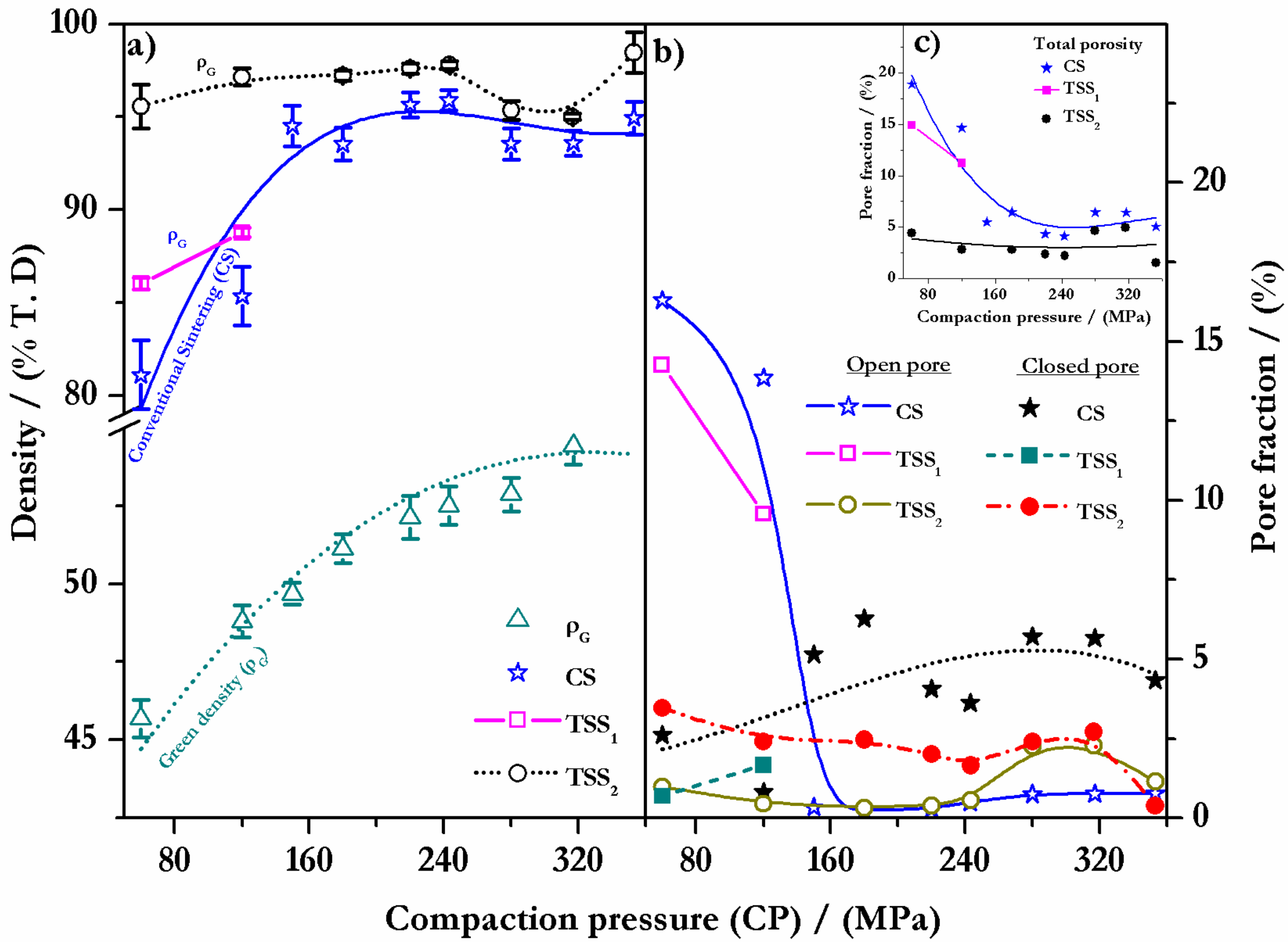

Figure 3.23 Compaction and sintering curves – U_C25H, under different sintering conditions: (a) dependance of green and sintered density with CP, (b) variation of open and closed pore fraction with CP and (c) variation of total porosity with the CP

Table 3.10 Sintered density (ρ_S) of UO_2 pellets obtained from U_C25H powders

Conventional sintering (CS) [Soaking temperature 1673 K 4 h]	
CP (MPa)	**% T.D^x**
60	81.1 ± 1.9
120	85.4 ± 1.6
150	94.5 ± 1.1
180	93.5 ± 0.9
220	95.7 ± 0.7
244	96.0 ± 0.5
280	93.6 ± 0.9
317	93.6 ± 0.7
353	94.9 ± 0.9
Two-step sintering (TSS_1) [Step 1: 1073 K 2h; Step 2: 1473 K 4 h]	
60	86.0 ± 0.3
120	88.8 ± 0.3
Two-step sintering (TSS_2) [Step 1: 1073 K 2h; Step 2: 1673 K 4 h]	
60	95.6 ± 1.2
120	97.2 ± 0.5
180	97.2 ± 0.3
244	**97.8 ± 0.2**
280	95.4 ± 0.5
317	95.0 ± 0.2
353	**98.5 ± 1.1**

^{x} *indicates the mean value of five different measurements*

It appears that at a CP of 150 MPa the ρ_G approaches 50% T.D, which is just about optimum for obtaining a defect free sintered product. A minimum CP of 150 MPa was found necessary in order to obtain a sintered product with a density above 90 % T.D. From the foregoing it could be concluded that the CS method when applied to nc-UO_2 powders yields a maximum density of 96 % T.D at 1673 K.

U_C25H powders were compacted at 60 and 120 MPa and sintered by using TSS_1 method (Fig. 3.23 and Table 3.10). The results indicate that U_C25S_2 compacts densified to marginally higher densities as compared to those sintered by CS (Table 3.10). A ρ_S of 86.0 % T.D (60 MPa) and 88.8 % T.D (120 MPa) were obtained by using TSS_1, while the CS had yielded a ρ_S of 81.1 % T.D (60 MPa) and 85.4 % T.D (120 MPa). It is further observed that the open pore fraction had decreased with the CP with a concomitant increase in the closed pore fraction.

Shrinkage data pertaining to these compacts also revealed that both the axial shrinkage (AS) and radial shrinkage (RS) decrease with the CP. Among them, the reduction in AS is found to be more pronounced (higher slope) than that in the RS. These results (ρ_S, shrinkage and porosity of U_C25S_1) suggest that even though TSS_1 has the potential to yield a better sintered product, the ρ_S needs to be improved by appropriate process optimization. Hence, a new procedure was devised by which higher densities could be realized. Our results (Fig. 3.24 & Table 3.10) revealed that U_C25H compacts could be sintered to a density of 95.6 ± 1.2 % T.D (60 MPa) and 97.2 ± 0.5 % T.D (120 MPa) by this new method. Hence, this “TSS” with a final sintering temperature of 1673 K (TSS_2) was used to sinter all the other powders.

3.10.3 Two-Step Sintering (TSS_2)

The ρ_S of the compacts sintered by TSS_2 are presented in Fig. 3.24 and Table 3.11. It was observed that the UO_2 compacts derived through the de-nitration method (U00H) had yielded the lowest ρ_S. The ρ_S of the $U00S_2$ monoliths increase with the CP up to 244 MPa (85.1 %T.D). Pellets compacted at 317 MPa showed a lower ρ_S (75.7 % T.D). This behavior could be explained by considering the porosity and shrinkage of the respective samples (Fig. 3.25).

Sintered UO_2 compacts (U00H) revealed that both AS and RS are negatively correlated with the CP (up to 317 MPa) and the monolith derived at 317 MPa exhibited the lowest shrinkage. Among all the U00H compacts maximum porosity was observed when the CP was in the range of 280 to 317 MPa. It is interesting to note that the open porosity in the sintered compacts have increased from 12 % to 24 % while the closed porosity remained constant at less than 1 % independent of the CP. The characteristics of the U00H powders and its sintering behavior were markedly different from the rest of the citrate gel-combustion derived powders.

Among the powders derived through citrate gel-combustion method a clear trend was discernible. The powders could be separated into two sets, viz., **set 1:** U_C5.5H, U_C10H and U_C25H and **set 2:** U_C50H; U_C75H, U_C90H and U_C100H. The powders in **set 1** exhibited higher sinterability (Table 3.10 & 3.11 & Figs. 3.23-3.24). The powders U_C10H and U_C25H which were derived through “volume combustion” yielded higher densities than U_C5.5H under identical conditions. All these three powders exhibited nearly similar shrinkage anisotropy and low open porosity and densified to a maximum density of 98 % T.D (317 MPa). The reduction in the ρ_S in these pellets (**set 1**) obtained by compacting at pressures between 200 and 240 MPa is due to the reasons cited in the foregoing discussions on U00H. The values of sintered densities of these compacts (with low ρ_S) bear an inverse relation with open porosity.

The shrinkage anisotropy [65] in highly densified monoliths U_C10S_2 and U_C25S_2 was pronounced and its correlation with the density was markedly different. From the forgoing it is evident that the nc-urania powders derived through volume combustion (U_C10H and U_C25H powders) could be sintered to a density of about 97.0 % T.D by employing a compaction pressure as low as 120 MPa and sintering with the TSS_2 method. Even though a CP of 317 MPa yielded higher densities, in order to maintain the shrinkage anisotropy (α) close to unity, it is found that a CP of 180 MPa would be most ideal for these powders (set 1).

The maximum density that could be realized with the powders in **"set 2"** was limited to 94 % T.D (U_C100S_2, 317 MPa). However, the reduction in ρ_S in the **"set 1"** compacts (280 MPa and 317 MPa) was not observed in these powders. The absence of harder agglomerates, testified by the dependence of the ρ_G on CP (Fig. 3.22) supports the fact that these powders undergo uniform compaction with less residual stress. Thus, it is evident that, apart from surface activity and sinterability, other physical characteristics, viz., flowability and particle size distribution contribute significantly towards the sinterability of nc-UO_2.

Table 3.12 and Fig. 3.26 enlists the data cited in the literature on CS of microcrystalline UO_2. From these data it is evident that the ρ_S in the range of 68.2 to 98.5 % T.D have been realized and that the sintering temperatures in the range of 1423 to 2053 K and CP in the range of 87 – 471 MPa have been employed by different authors [18, 24, 64, 73, 74]. Among these the work reported in ref. [25] and [74] are different and interesting variations. Kang et al. [25] had sintered UO_2 monoliths (2003 K; 4h; 294 MPa and H_2) derived through the ADU method and re-oxidation method (mixture of UO_2 and U_3O_8) to a ρ_S of 97.9 % T.D and 96.3 % T.D respectively. Yang et al. [74] had sintered UO_2 pellets which employed "additive type pellets" and "matrix type pellets" wherein the former involves mixing, compacting, crushing and pressing to form green pellets while the latter were prepared by mixtures containing UO_2 powders, ammonium oxalate (pore former) and zinc stearate (binder). These authors had obtained sintered monoliths of 93.3-94.0 % T.D and 94.3-94.8 % T.D (1673 K; 1-3 h & N_2-CO_2) respectively.

Table 3.11 Sintered density (ρ_S) of UO_2 pellets derived through TSS_2 method

CP (MPa)	$U00S_2$	$U_C5.5S_2$	U_C10S_2	U_C50S_2	U_C75S_2	U_C90S_2	U_C100S_2
	% T.D^x						
60	-	89.1 ± 0.9	95.2 ± 0.6	80.7 ± 0.5	86.4 ± 0.4	88.6 ± 0.4	87.5 ± 0.7
120	83.5 ± 0.5	92.8 ± 0.4	97.0 ± 0.7	83.4 ± 0.6	89.8 ± 0.5	90.1 ± 0.6	90.8 ± 0.3
180	84.5 ± 0.1	93.4 ± 1.4	97.2 ± 0.6	87.7 ± 0.1	91.6 ± 0.2	91.7 ± 0.7	91.8 ± 1.4
244	85.1 ± 0.6	92.0 ± 0.4	97.1 ± 0.1	88.9 ± 0.3	91.7 ± 0.3	91.8 ± 1.7	92.5 ± 0.4
280	76.3 ± 1.4	89.6 ± 0.7	93.6 ± 0.1	90.2 ± 0.2	92.0 ± 0.2	92.0 ± 0.6	92.7 ± 0.6
317	75.7 ± 1.3	97.0 ± 0.1	**98.0 ± 0.4**	90.6 ± 0.4	91.4 ± 0.7	90.8 ± 1.3	94.0 ± 0.2
353	84.4 ± 0.5	95.7 ± 0.2	97.8 ± 0.3	87.7 ± 1.4	86.4 ± 0.3	88.5 ± 0.9	89.8 ± 1.4

^{x} *indicates the mean value of five different measurements*

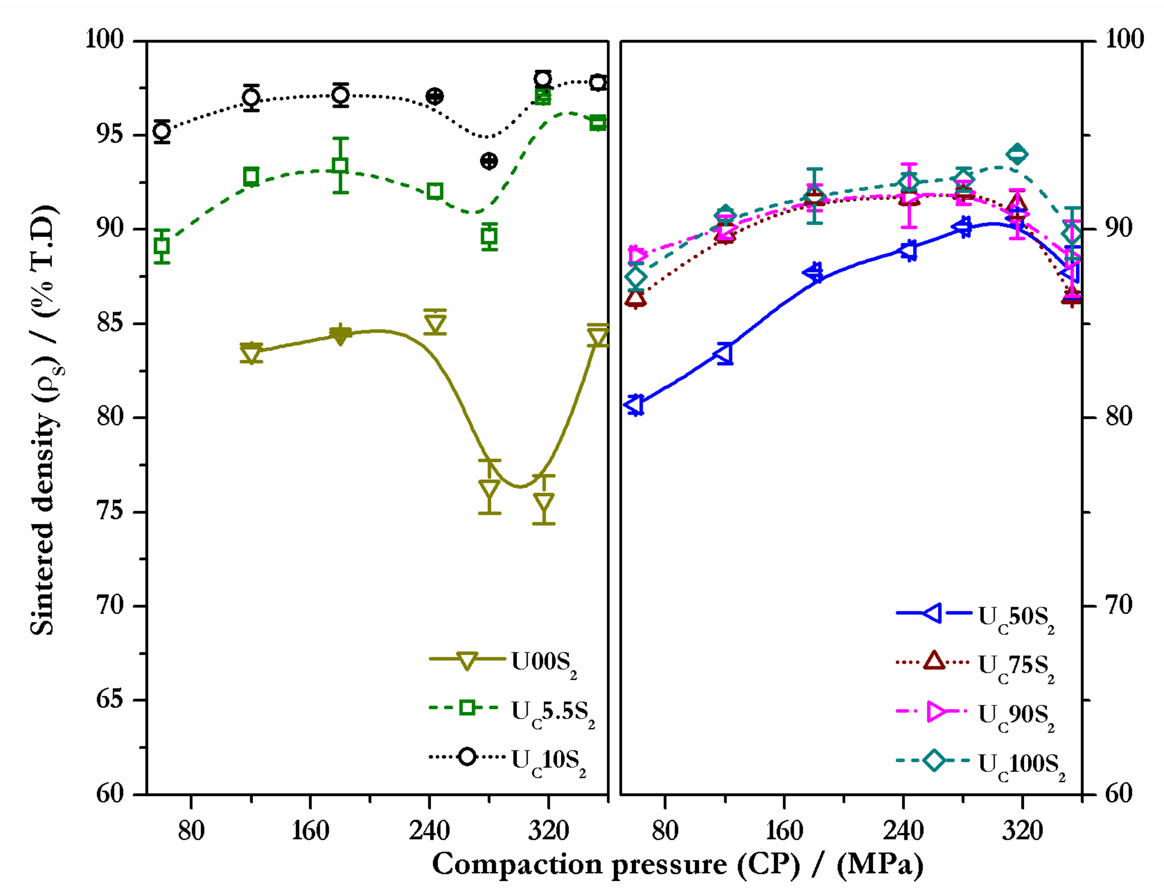

Figure 3.24 Sintered density (ρ_S) of TSS_2 compacts with the CP

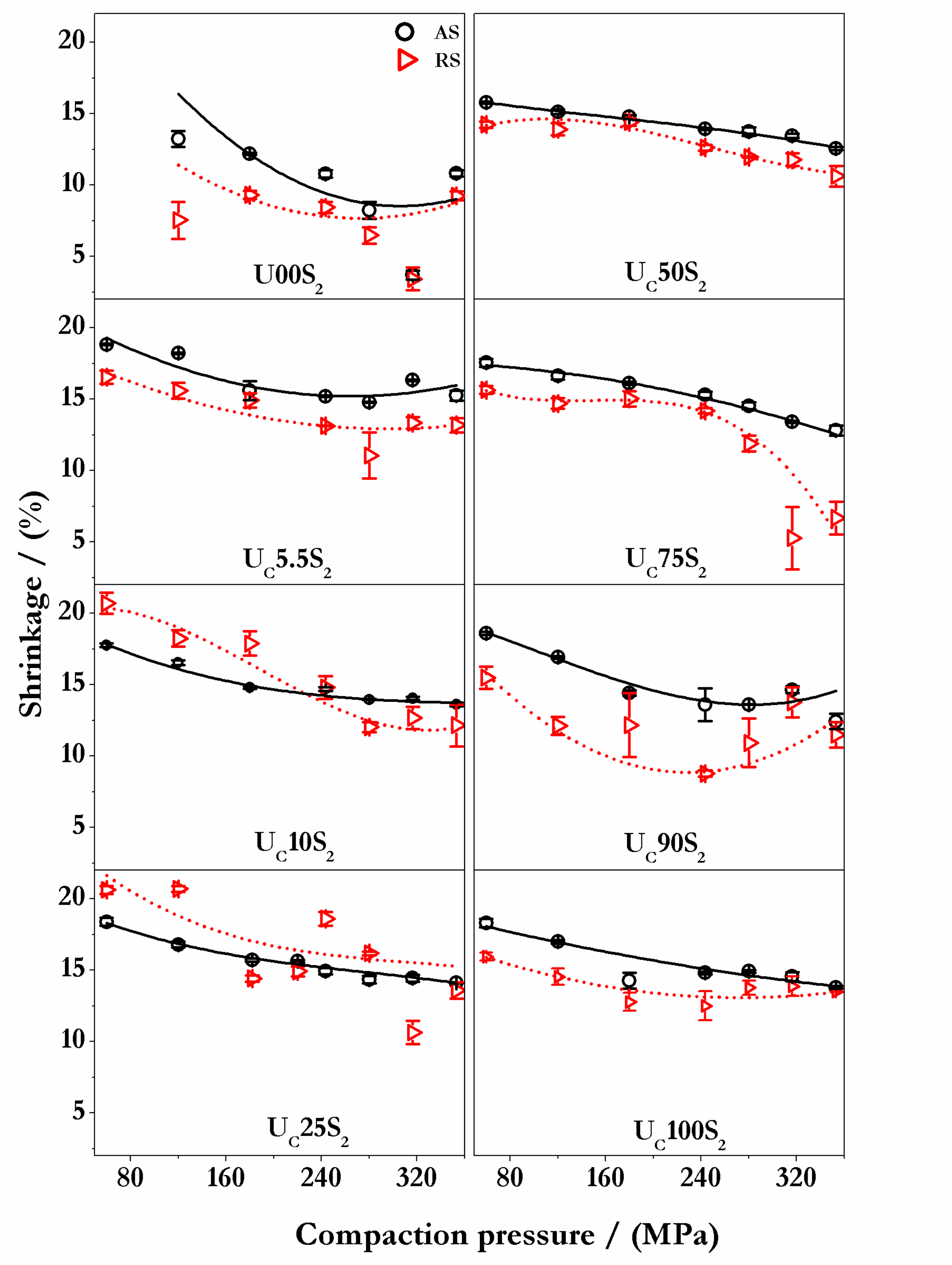

Figure 3.25 Axial (AS) and radial shrinkage (RS) in TSS$_2$ UO$_2$ pellets

From the data presented Table 3.12 it is evident that many authors had successfully prepared sintered UO$_2$ pellets from microcrystalline UO$_2$ with a density of 97 to 98 % T.D

(Fig. 3.26) without the addition of a binder or a lubricant. However, these authors (Table 3.12 and Fig. 3.26) had employed a temperature as high as 1973 K to realize such high densities. In the present study a density as high as 98 % T.D has been realized at a temperature as low as 1673 K by using nc-UO_2. Thus, it has been amply demonstrated that citrate gel-combustion derived nc-UO_2 undergoes facile densification even at lower temperatures, as compared to its microcrystalline analogue.

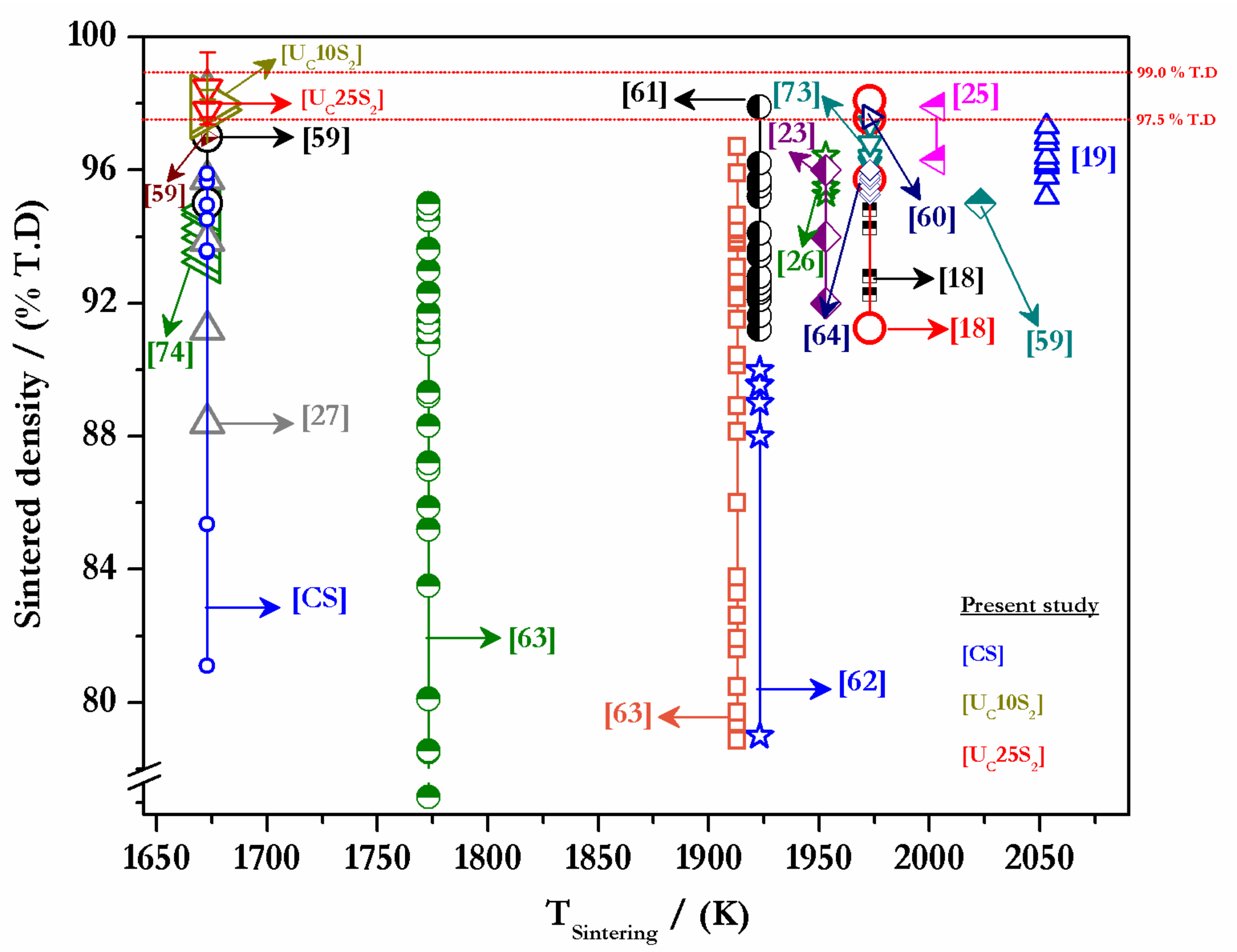

Figure 3.26 Effect of $T_{sintering}$ on the ρ_S of UO_2

Table 3.12 Comparison of UO_2 powder characteristics and ρ_S reported in the literature

$R^{binder/lubricant}$	Method	SSA (m^2g^{-1})	CP (MPa)	T_S / time / atmosphere	ρ_G (% T.D)	ρ_S (% T.D)
[22]	AUC	5.96	320	1573 / 0.1-40 h / (CO_2-H_2) 1773/0.1-40 h / (CO_2-H_2)	51.0	-
[18]^{ZS}	AUC	4.29-6.66	87-422	1973 / 2 h / H_2	45.6-56.5	92.3-97.6
	ADU	6.04	146-573		41-53.8	91.3-98.1
[19]^{SA}	ADU	2.16-4.9	343	2053 / 4 h / H_2	49-58	95.2-97.3
[73]	ADU	0.5	300	1973 / 4 h / H_2	-	96.2-97.4
[25]	ADU	0.6-1.4	294	2003 / 4 h / H_2	-	97.9
	RO					96.3
[74]^{ZS}	A	4.7	-	1673 / 1-3 h / N_2-CO_2	-	93.3-94.0
	M					94.3-94.8
[64]	ADU	-	250	1973 / - / cracked NH_3	-	95.3-96.0
[60]	-	-	196	1973 / 2 h / N_2-13% H_2	55.8-66.2	97.6
[62]	ADU	5.31	-	1923 / 3 h / H_2	38-54	79-90
[26]	AUC	5	270	1953 / 4 h / H_2	51.9-52.4	95.3-96.4
[63]	-	0.2-5.9	300	1773 / 4 h / H_2	47.7-66.5	68.2-95.0
				1913 / 4 h / H_2		71.9-96.7
[23]	AUC	5	300	1953 / 4 h / CO_2-H_2	52.4	92.0-96.0
[27]	ADU	1.1-6.2	304	1673 / 16 h / H_2	54.0-55.0	88.1-**98.5**
[61]^{SA}	AUC	7.5-10.6	186	1923 / 4 h / H_2	45.8	91.6
			284		45.0-46.9	91.2-95.2
			373		48.1-50.1	92.1-95.7
			471		50.4-51.4	92.8-**97.9**
[24]	AUC	4.5-5.5	275-392	-	45.6-59.3	93.0-96.6
[57]^{ZS}	ADU	4.8	300	1423 / 4 h / H_2O-CO_2-H_2	50	95.0
[58]^{PVA}	ADU		260	1473-1573 / 6 -7 h / N_2-H_2	50	92.0-**98.0** (g)
[59]^{ZS}	ADU	2.3-2.4	392	2023 / 5 h / H_2	54.7	95.0
				1673 / 8 h / (H_2/N_2)-air-(H_2-N_2)		97.0
				1673 / 4 h / (H_2/N_2)-air-(H_2-N_2)		95.0
This study	D	5.66	60-353	1673 / 4 h / 8 % Ar-H_2	49.6-58.3	75.7-85.1
	CGC	5-9.7		1473 / 4 h / 8 % Ar-H_2	44.6-56.4	81.1-95.9
				1673 (TSS_2) / 4 h / 8 % Ar-H_2		80.7-**97.8**

ADU - Ammonium diuranate; AUC - ammonium uranyl carbonate; CP – compaction pressure; TSS_2 – "two-step sintering"; g - geometrical density; A- Additive type; M-Matrix type; CGC-citrate gel-combustion; D-direct denitration; ^{PVA}-poly vinyl alcohol; ^{ZS}- zinc stearate; ^{SA}- stearic acid and T_S-Sintering temperature (K); RO-Re-Oxidised

3.10.4 Morphological analysis by using SEM

Selected samples of sintered UO_2 pellets were examined for their microstructure by using SEM (Figs. 3.27-3.29). All these pellets were investigated for the sizes of grains, pores and dihedral angle between the grains. SEM images revealed that these monoliths comprised grains with unimodal size distribution (fine grained monoliths). It was observed that the U_C25S_2 monoliths possessed faceted grains with well defined grain boundaries.

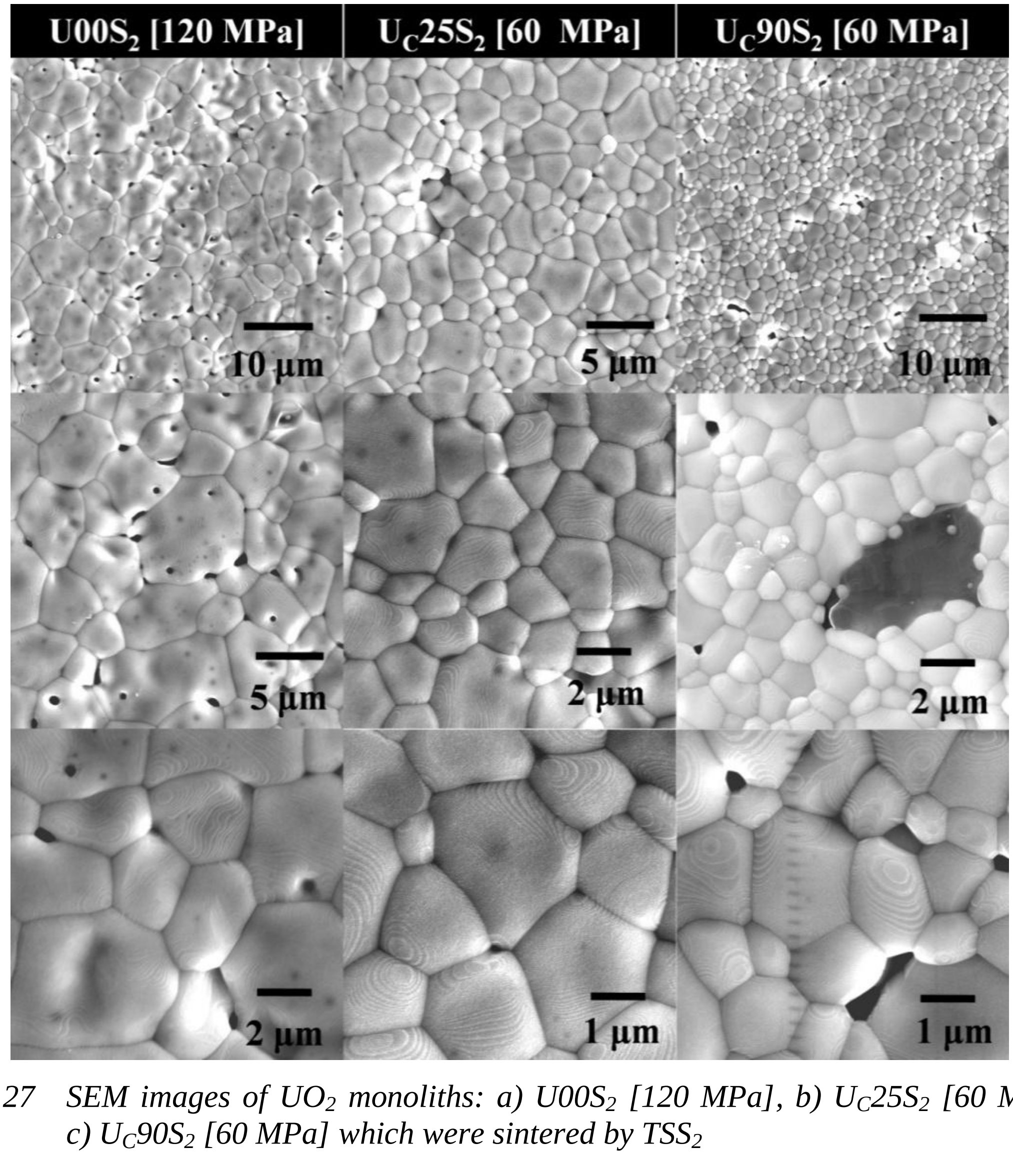

Figure 3.27 SEM images of UO_2 monoliths: a) $U00S_2$ [120 MPa], b) U_C25S_2 [60 MPa] and c) U_C90S_2 [60 MPa] which were sintered by TSS_2

On the other hand it was observed that U_C50S_2, U_C90S_2 and U_C100S_2 monoliths comprised grains in the submicron regime. This implies that powders derived through citrate gel-combustion (R > 0.25) would yield fine grained UO_2 pellets when sintered by using TSS_2.

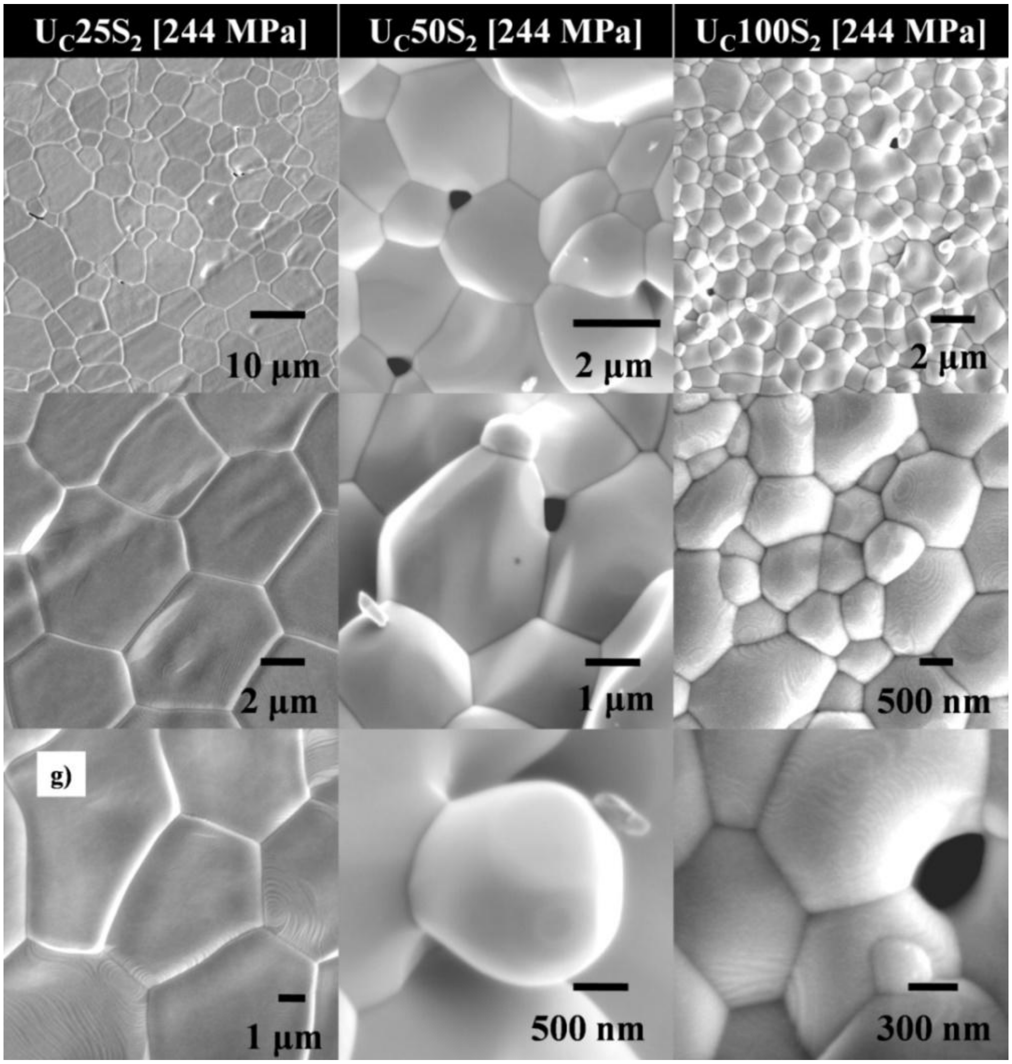

Figure 3.28 SEM images of UO_2 monoliths: a) U_C25S_2 [244 MPa], b) U_C50S_2 [244 MPa] and c) U_C100S_2 [244 MPa] which were sintered by using TSS_2

Fractured surface of these pellets were investigated for their pores both isolated (intragranular) and between the grains (intergranular), fissures and dihedral angle by using SEM. The most important characteristic of a sintered body is its porosity (open and closed). Besides pore size, its distribution also plays an important role during densification. Hence, to achieve a desired ρ_S it is vital to understand the pore characteristics viz., their morphology, size distribution, dihedral angle and coordination number [number of grains surrounding the pores (N)] in order to optimize the sintering process [65, 66]. Thermodynamically it could be shown that the stability of a pore depends on the Gibbs energy change during the shrinkage, the dihedral angle (Ψ) between the grains, grain boundary energy (γ_{gb}) and surface particle/pore interfacial energy (γ_{sv}). The equilibrium shape of the pore is related to its dihedral angle by eqn. 3.13 [65].

$$\cos\left(\frac{\Psi}{2}\right) = \frac{\gamma_{gb}}{2\gamma_{sv}} \qquad 3.13$$

Further, it can be shown in 2-D that the pores with N < 6 would shrink because the surface of the pore will move inward towards is centre of curvature (concave grain boundary) while with N > 6 would grow [65, 66]. In other words, the resultant Gibbs energy change indicates that the decrease in energy due to the reduction in the pore surface area is greater than the increase in energy due to growth of the grain boundary (N < 6). For N > 6, the Gibbs energy change is just the opposite [65, 66]. When N = 6 [critical coordination number (N_c)] the pore is said to be in a metastable state with a dihedral angle of 120^0 [65, 66].

Kingery and Francois [75] had reported that the stability of a pore could be ascertained by measuring its dihedral angle. Further, these authors had demonstrated that the pores with a dihedral angle beyond a certain threshold value (3D: critical angle = 120^0; critical number of grains surrounding the pore = 12) with a few grains surrounding them would shrink while those with a dihedral angle less than the critical angle and a large number of grains surrounding them would coarsen (pore growth). Rahaman [65] and Chaim [76] had reported that pores that are larger than the grains surrounding them would be thermodynamically stable and it is difficult to eliminate them. Thus, it is important to compact powders into a body with high ρ_G and with a uniform size distribution of smaller pores such that the value of N is smaller than 12 [76]. These pores could then be removed easily during sintering, resulting in a dense product. Anisotropic shrinkage would result in a defective sintered product [65]. Thus, in order to obtain a defect free sintered product, it is necessary to optimize the process parameters such that the shrinkage anisotropy and relative pore fraction are minimal.

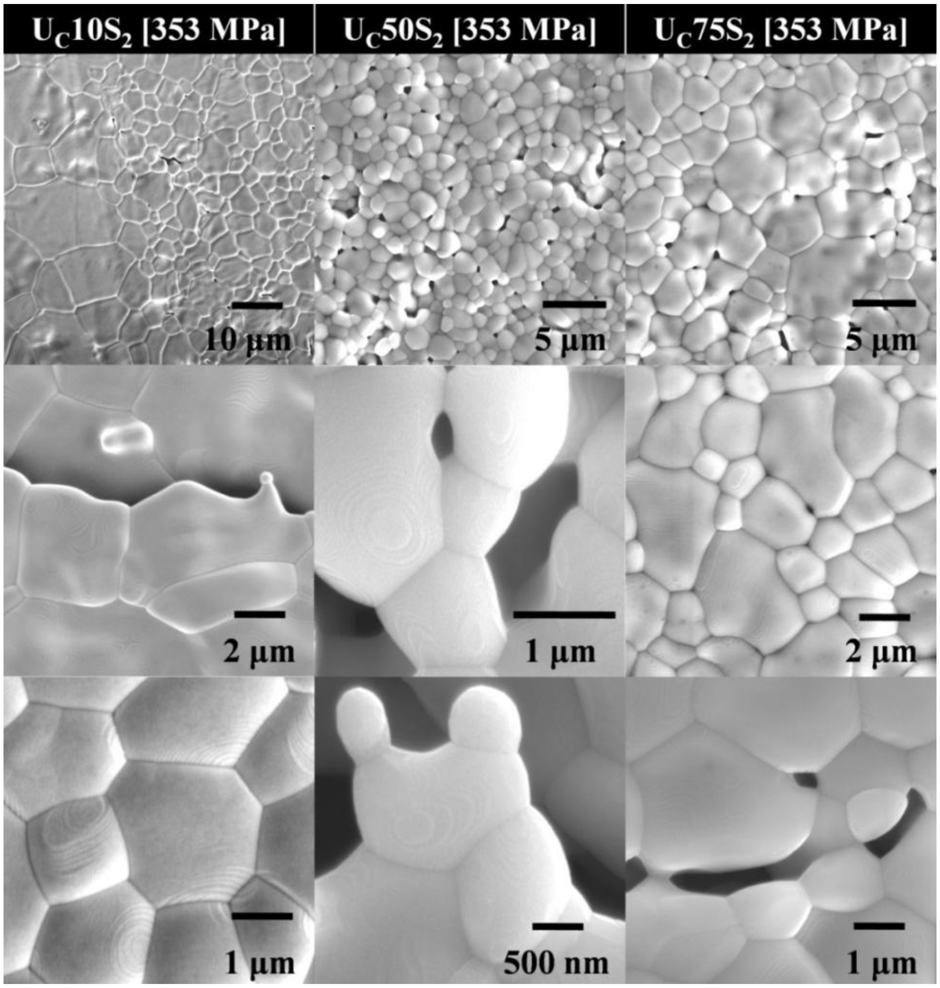

Figure 33.29 *SEM images of* UO_2 *monoliths: a)* U_C10S_2 *[353 MPa], b)* U_C50S_2 *[353 MPa] and c)* U_C75S_2 *[353 MPa] which were sintered by using* TSS_2

Shrinkage anisotropy factor (α) is defined as the ratio of AS to that of RS $[\propto = \frac{\mathrm{AS}}{\mathrm{RS}}]$ while the relative pore fraction is the ratio of open or closed porosity to that of total porosity (Figs. 3.30-3.31). The desirable value of α is about 1 while that of relative porosity is less than 1% [65].

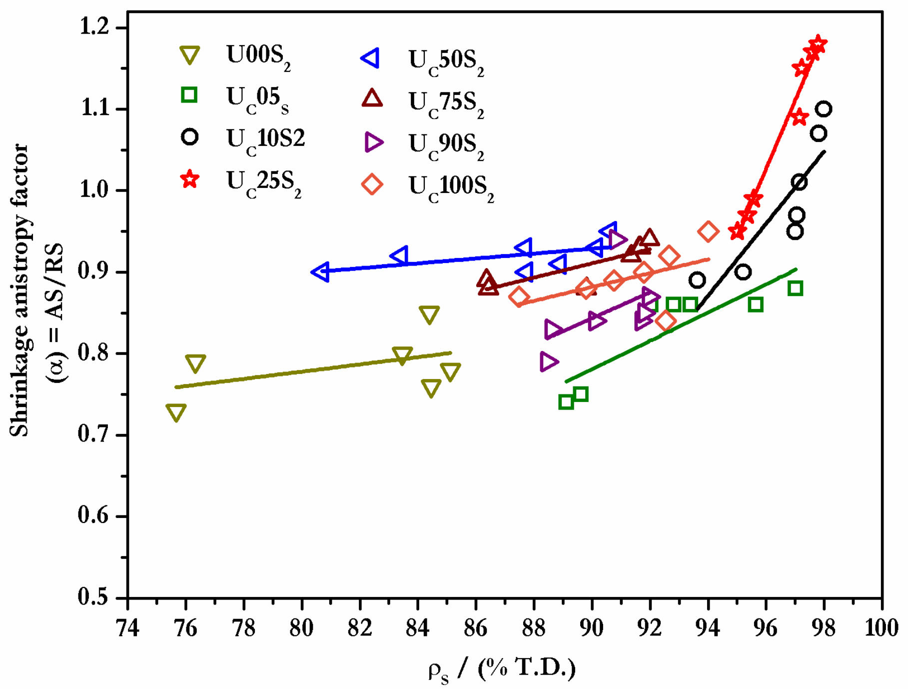

Figure 3.30 Dependence of shrinkage anisotropy factor (α = ratio of axial to radial shrinkage) on the ρ_S of UO_2 monoliths (TSS_2)

All other process variables viz., steps in the powder preparation and the characteristics of powders and green body and the sintering cycle need to be optimized such that an α close to unity and a closed porosity near to 1 % are achieved. In general, it is observed that α varies linearly with the ρ_S while the open pore fraction decreases with the same. The variation in closed porosity with the ρ_S plays a predominant role in the final stage of sintering [65, 76-78]. A study of the relative variation in the porosity and α with the ρ_S helps to optimize the critical CP wherein both closed and open pore fraction are nearly equal beyond which there would be no appreciable change in the ρ_S. Since most of the pores observed in the sintered pellets obtained in this study (Figs. 3.27-3.29 & 3.31) have dihedral angles between 115^0 to 128^0, it is reasonable to assume that they would shrink upon prolonged sintering. This testifies the fact that in the TSS_2 method sintering has been taken up to the “final stage”.

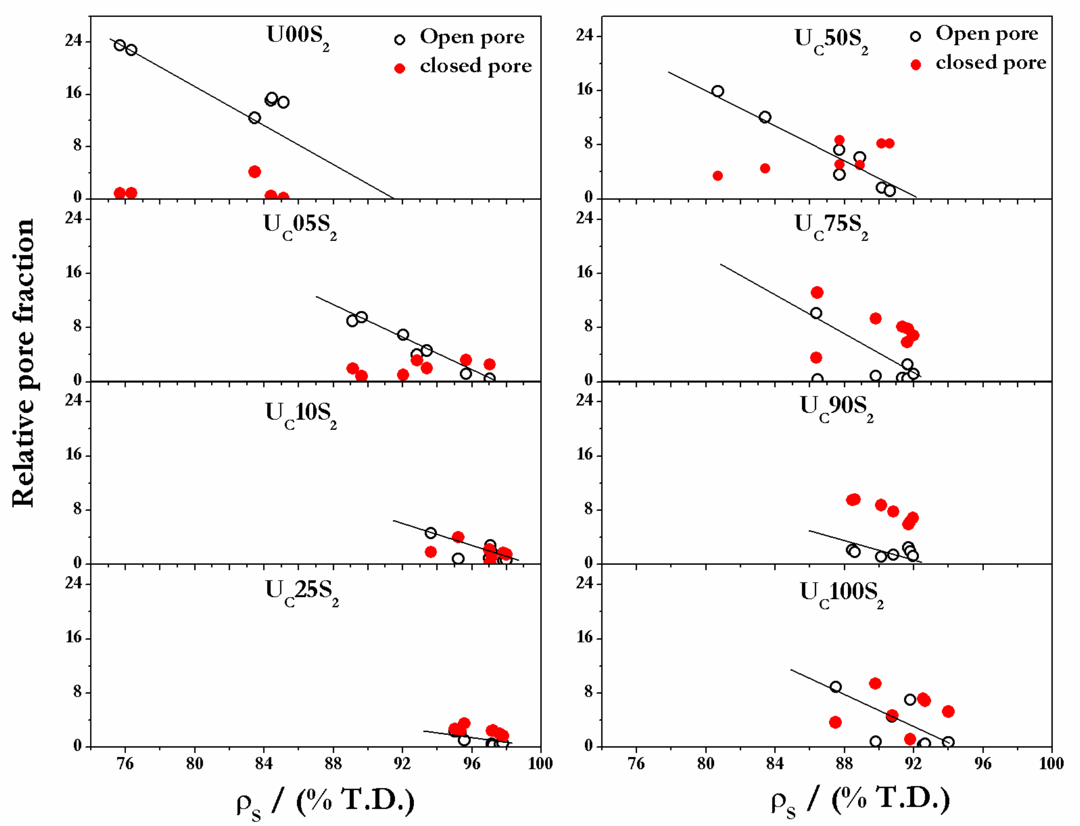

Figure 3.31 Dependence of the volume fraction of pores (open and closed) on the ρ_S

Nanocrystalline powders usually tend to yield sintered bodies with significant grain coarsening. Usually the grains size is in the range of 10-50 μm but often the distribution of sizes of these grains is not uniform. Our aim was to obtain dense compacts with near unimodal size distribution. In addition the sintered densities obtained with the method used in our study are much higher as compared to the methods proposed by other authors for sintering of nanocrystalline urania. However, further studies would help to optimize the process parameters to obtain nanostructured sintered monoliths. Probably a techniques that suppresses grains coarsening viz., SPS might yield a product with nanograins.

3.10.5 Phase characterization and residual carbon

XRD analysis of the sintered UO_2 pellets (selected samples) revealed that the sintered UO_2 compacts comprised the fluorite phase (Fig. 3.32).

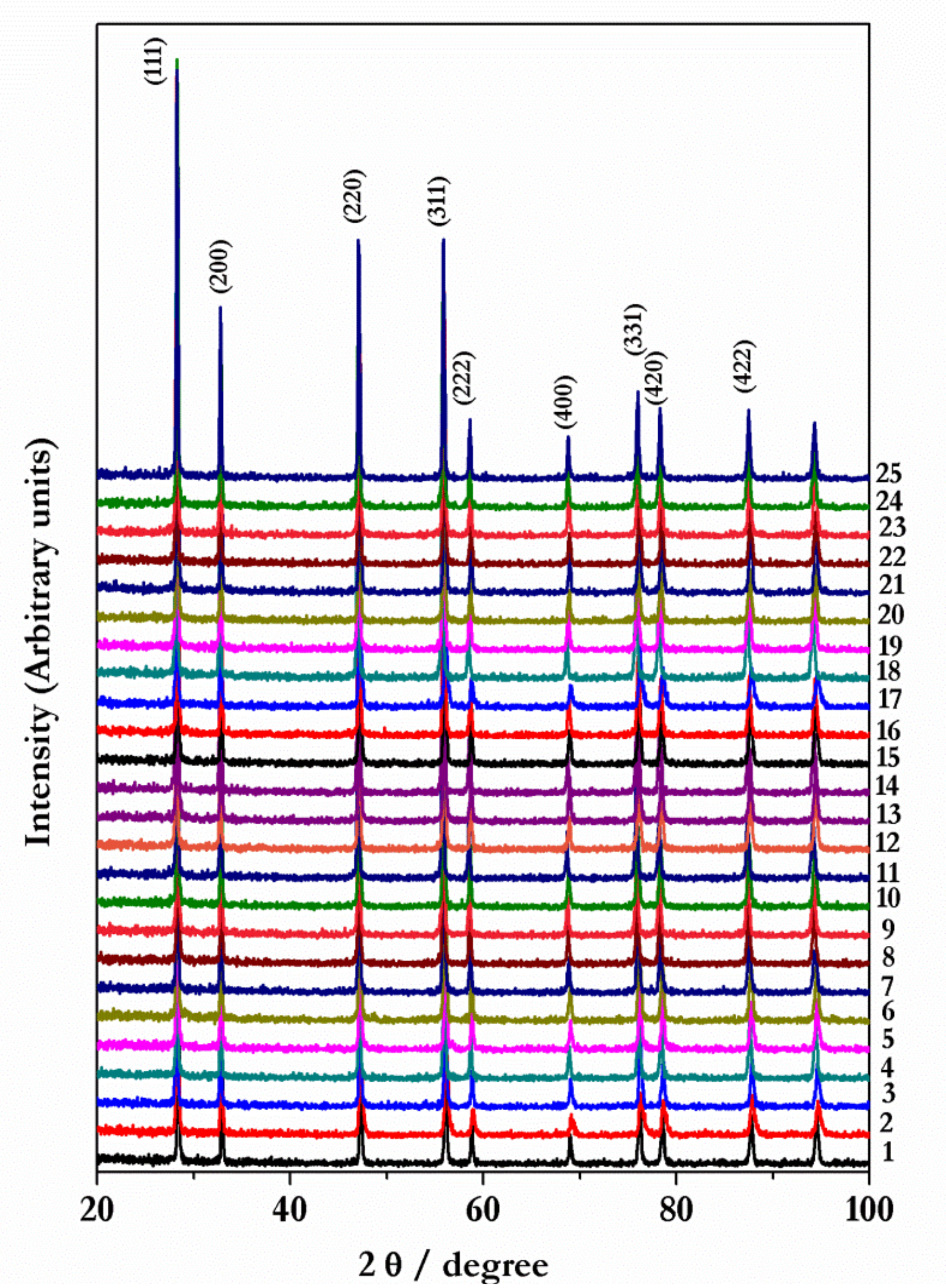

Figure 3.32 *XRD plot of U_CXXS_2-YYY samples [where -YYY indicates compaction pressure] 1) U_C100S_2-317, 2) U_C100S_2-280, 3) U_C100S_2-244, 4) U_C100S_2-120, 5) U_C90S_2-280, 6) U_C90S_2-244, 7) U_C90S_2-180, 8) U_C90S_2-060, 9) U_C50S_2-244, 10) U_C25S_2-353, 11) U_C25S_2-280, 12) U_C25S_2-244, 13) U_C10S_2-317, 14) U_C10S_2-280, 15) U_C10S_2-244, 16) U_C10S_2-120, 17) U_C10S_2-060, 18) U_C5.5S_L-317, 19) U_C5.5S_2-280, 20) U_C5.5S_2-244, 21) U_C5.5S_2-180, 22) U_C5.5S_2-120, 23) U00S_2-280, 24) U00S_2-244, 25) U00S_2-180*

Carbon residue present in the sintered UO_2 compacts was found to vary between 67 – 103 ppm (Table 3.13). The carbon residue in the sintered UO_2 pellets are well meet the specification of nuclear grade sintered UO_2 pellets (ASTM- CC776-06) [79]. Thus, the sintered UO_2 monoliths are comparable to the reactor grade sintered UO_2 pellets.

Table 3.13 Carbon residue in sintered UO_2 pellets derived through TSS_2

CP (MPa)	**$U00S_2$**	**$U_C5.5S_2$**	**U_C10S_2**	**U_C25S_2**	**U_C50S_2**	**U_C75S_2**	**U_C90S_2**	**U_C100S_2**
	(ppm)							
60	78	96	92	68	88	91	95	85
120	88	83	90	90	103	76	82	86
180	84	96	95	92	81	88	99	89
243	96	99	79	85	95	99	91	74
280	79	83	83	96	96	92	84	97
317	67	74	93	86	89	89	96	85
353	90	72	87	79	83	94	102	81

^{x} *indicates the mean value of five independent measurements*

3.11 Conclusion from investigations on the sintering of nc-UO_2

Systematic investigation on sintering of nc-UO_2 powders derived through citrate gel-combustion method was carried out, by using three different methods, viz., i) conventional method (CS), ii) two-step sintering (TSS_1) and iii) two-step sintering (TSS_2). Among these, the TSS_2 method was found most suitable. Powders derived from starting mixtures with an R value of 0.10 and 0.25 were found to be highly sinterable and yielded a maximum ρ_S of ≈ 98 % T.D with uniform grains (1 – 15 μm). Through optimization trials, 180 MPa and TSS_2 were found to be the ideal conditions to obtain high density UO_2 pellets from these powders. Shrinkage anisotropy factor (α) in the sintered UO_2 monoliths were investigated for the first time. Relative size fraction of open and closed pore fraction of sintered UO_2 monoliths were also investigated. The method employed in this study has led to a new fabrication procedure which would be an energy and cost efficient method for obtaining UO_2 pellets with a uniform grain size of about 1-15 μm.

References

[1] L.A. Chick, L.R. Pederson, G.D. Maupin, J.L. Bates, L.E. Thomas, G.J. Exarhos, Mater. Lett. 10(1) (1990) 6-12.

[2] J.J. Kingsley, K.C. Patil, Mater. Lett. 6(11) (1988) 427-432.

[3] J.J. Moore, H.J. Feng, Prog. Mater. Sci. 39(4) (1995) 243-273.

[4] P. Erri, P. Pranda, A. Varma, Ind. Eng. Chem. Res. 43(12) (2004) 3092-3096.

[5] K. Deshpande, A. Mukasyan, A. Varma, Chem. Mater. 16(24) (2004) 4896-4904.

[6] F.-t. Li, J. Ran, M. Jaroniec, S.Z. Qiao, Nanoscale 7(42) (2015) 17590-17610.

[7] S.E. Stein, "Infrared Specra" in NIST Chemistry WebBook, NIST Standard Reference Database No. 69, National Institute of Standards and Technology (NIST), Gaithersburg MD, 20899, 2015.

[8] B.M. Gatehouse, A.E. Comyns, J. Chem. Soc. 802 (1958) 3965-3971.

[9] J.I. Bullock, M.M. Patel, J.E. Salmon, J. Inorg. Nucl. Chem. 31(2) (1969) 415-423.

[10] D. Wyrzykowski, E. Hebanowska, G. Nowak-Wiczk, M. Makowski, L. Chmurzyński, J. Therm Anal. Calorim. 104(2) (2011) 731-735.

[11] K.C. Patil, Chemistry of Nanocrystalline Oxide Materials: Combustion Synthesis, Properties and Applications, World Scientific Publishing Co. Pvt. Ltd., Singapore, 2008.

[12] A. Saberi, F. Golestani-Fard, H. Sarpoolaky, M. Willert-Porada, T. Gerdes, R. Simon, J. Alloys Compd. 462(1) (2008) 142-146.

[13] K. Zupan, M. Marinsek, B. Novosel, Mater. Technol. 45 (2011) 439-445.

[14] H.Y. Sohn, C. Moreland, Can. J. Chem. Eng. 46(3) (1968) 162-167.

[15] G. Tarì, J.M.F. Ferreira, A.T. Fonseca, O. Lyckfeldt, J. Eur. Ceram. Soc. 18(3) (1998) 249-253.

[16] S. Anthonysamy, K. Ananthasivan, V. Chandramouli, I. Kaliappan, P.R. Vasudeva Rao, J. Nucl. Mater. 278(2) (2000) 346-357.

[17] H. Palneedi, V. Mangam, S. Das, K. Das, J. Alloys Compd. 509(41) (2011) 9912-9918.

[18] Y.W. Lee, M.S. Yang, J. Nucl. Mater. 178(2) (1991) 217-226.

[19] H. Ching-Tsven, J. Nucl. Mater. 199(1) (1992) 61-67.

[20] P. Lainetti, H.G. Riella, J. Nucl. Mater. 178(2) (1991) 135-142.

[21] S. Manna, P. Karthik, A. Mukherjee, J. Banerjee, S.B. Roy, J.B. Joshi, J. Nucl. Mater. 426(1) (2012) 229-232.

[22] S. Kun Woo, C. Woong Kil, J. Nucl. Mater. 203(2) (1993) 122-127.

[23] K.W. Song, K.S. Kim, Y.M. Kim, Y.H. Jung, J. Nucl. Mater. 277(2) (2000) 123-129.

[24] C.S. Choi, J.H. Park, E.H. Kim, H.S. Shin, I.S. Chang, J. Nucl. Mater. 153 (1988) 148-155.

[25] K.W. Kang, J.H. Yang, J.H. Kim, Y.W. Rhee, D.J. Kim, K.S. Kim, K.W. Song, J. Nucl. Sci. Technol. 45(11) (2008) 1150-1154.

[26] K.W. Song, K.S. Kim, Y.M. Kim, K.W. Kang, Y.H. Jung, J. Nucl. Mater. 279(2) (2000) 253-258.

[27] P. Das, R. Chowdhury, J. Nucl. Mater. 158 (1988) 261-266.

[28] G. Rousseau, M. Fattahi, B. Grambow, L. Desgranges, F. Boucher, G. Ouvrard, N. Millot, J.C. Nièpce, J. Solid State Chem. 182(10) (2009) 2591-2597.

[29] Q. Wang, G.-D. Li, S. Xu, J.-X. Li, J.-S. Chen, J. Mater. Chem. 18(10) (2008) 1146-1152.

[30] R. Lloyd, LWBR Development Program, Contract DE-AC11-76PN00014, Bettis Atomic Power Laboratory, 1980.

[31] O. Roth, H. Hasselberg, M. Jonsson, J. Nucl. Mater. 383(3) (2009) 231-236.

[32] R. Zhao, L. Wang, Z.-J. Gu, L.-Y. Yuan, C.-L. Xiao, Y.-L. Zhao, Z.-F. Chai, W.-Q. Shi, CrystEngComm 16(13) (2014) 2645-2651.

[33] D. Gil, R. Malmbeck, J. Spino, T. Fanghänel, E. Dinnebier Robert, Radiochim. Acta, 98 (2010) 77-89.

[34] V. Tyrpekl, J.-F. Vigier, D. Manara, T. Wiss, O. Dieste Blanco, J. Somers, J. Nucl. Mater. 460 (2015) 200-208.

[35] S. Kihara, T. Adachi, H. Hashitani, Fresenius' Zeitschrift für. anal. Chem. 303 (1980) 28-28.

[36] L. Lynds, W.A. Young, J.S. Mohl, G.G. Libowitz, X-Ray and Density Study of Nonstoichiometry in Uranium Oxides, Non-stoichiometric Compounds, in: Adv. in Chem Series, Vol. 39 (1963) 58-65.

[37] V. Mote, Y. Purushotham, B. Dole, J. Theor. Appl. Phys. 6(1) (2012) 6.

[38] B.R. Rehani, P.B. Joshi, K.N. Lad, A. Pratap, Indian J. Pure Appl. Phys. 44 (2006) 157-161.

[39] G. van der Laan, K.T. Moore, J.G. Tobin, B.W. Chung, M.A. Wall, A.J. Schwartz, Phys. Rev. Lett. 93(9) (2004) 097401.

[40] K.T. Moore, G. van der Laan, R.G. Haire, M.A. Wall, A.J. Schwartz, Phys. Rev. B 73(3) (2006) 033109.

[41] K.T. Moore, G. van der Laan, Ultramicroscopy, 107(12) (2007) 1201-1206.

[42] B.T. Thole, G. van der Laan, Phys. Rev. B 38(5) (1988) 3158-3171.

[43] G. van der Laan, B.T. Thole, Phys. Rev. Lett. 60(19) (1988) 1977-1980.

[44] R.D. Cowan, The Theory of Atomic Structure and Spectra, University of California Press, 1981.

[45] C.H. Bamford, C.F.H. Tipper, eds., Reaction in the Solids, Comprehensive Chemical Kinetics, Elsevier, Amstersam, 1980.

[46] E.B. Michael, K.G.e. Patrick, Handbook of Thermal Analysis and Calorimetry, Elsevier, Amsterdan, 2008.

[47] H.E. Kissinger, Anal. Chem. 29 (1957) 1702-1706.

[48] J.A. Augis, J.E. Bennett, J. Therm. Anal. 13(2) (1978) 283-292.

[49] S. Mahadevan, A. Giridhar, A.K. Singh, J. Non-Cryst. Solids 88(1) (1986) 11-34.

[50] A.A. Abu-Sehly, Thermochim. Acta 485(1) (2009) 14-19.

[51] A.A. Joraid, Thermochim. Acta 456(1) (2007) 1-6.

[52] A. Catalani, M.G. Bonicelli, Thermochim. Acta 438(1) (2005) 126-129.

[53] P. Taylor, R.J. McEachern, Quantitative procedure to determine the rate of U_3O_8 formation on UO_2, Proceedings of the fifth international conference on CANDU fuel, 31 (1997) 425-434.

[54] S. Vyazovkin, I. Dranca, Macromol. Chem. Phys. 207(1) (2006) 20-25.

[55] S.V. Vyazovkin, A.I. Lesnikovich, Thermochim. Acta 165(2) (1990) 273-280.

[56] A. Mukhopadhyay, B. Basu, Int. Mater. Rev. 52(5) (2007) 257-288.

[57] B. Ayaz, A.N. Bilge, J. Nucl. Mater. 280(1) (2000) 45-50.

[58] N. Fuhrman, L.D. Hower, R.B. Holden, J. Am. Ceram. Soc. 46(3) (1963) 114-121.

[59] Y. Harada, J. Nucl. Mater. 245(2) (1997) 217-223.

[60] Y. Sakamura, T. Omori, Nucl. Technol. 171(3) (2010) 266-275.

[61] P. Yi-Ming, M. Che-Bao, H. Nien-Nan, J. Nucl. Mater. 99(2) (1981) 135-147.

[62] K.C. Radford, R.J. Bratton, J. Nucl. Mater. 57(3) (1975) 287-302.

[63] W. Timmermans, A. van Heck-Hennen, F. Gorle, R. de Batist, J. Nucl. Mater. 71(2) (1978) 256-267.

[64] B. Narasimha Murty, P. Balakrishna, R.B. Yadav, C. Ganguly, Mater. Charact. 49(2) (2002) 103-111.

[65] M.N. Rahaman, Sintering of Ceramics, CRC Press, Boca Raton, Florida, 2007.

[66] R. Castro, K. van Benthem, Sintering: Mechanisms of Convention Nanodensification and Field Assisted Processes, Springer Berlin Heidelberg, 2012.

[67] R.M. German, Sintering Theory and Practice, John Wiley & Sons Inc, New York, 1996.

[68] O. Sudre, F.F. Lange, J. Am. Ceram. Soc. 75(3) (1992) 519-524.

[69] F.F. Lange, De-Sintering, A Phenomena Concurrent with Densification Within Powder Compacts: A Review, University of California, 1996.

[70] K. Ananthasivan, S. Anthonysamy, C. Sudha, A.L.E. Terrance, P.R. Vasudeva Rao, J. Nucl. Mater. 300(2) (2002) 217-229.

[71] K. Ananthasivan, S. Balakrishnan, S. Anthonysamy, R. Divakar, E. Mohandas, V. Ganesan, J. Nucl. Mater. 434(1) (2013) 223-229.

[72] N.J. Lóh, L. Simão, C.A. Faller, A. De Noni, O.R.K. Montedo, Ceram. Int. 42(11) (2016) 12556-12572.

[73] K.W. Song, K. Sik Kim, K. Won Kang, Y. Ho Jung, J. Nucl. Mater. 317(2) (2003) 204-211.

[74] X.-d. Yang, J.-c. Gao, Y. Wang, X. Chang, Trans. Nonferrous Met. Soc. China 18(1) (2008) 171-177.

[75] W.D. Kingery, B. Francois, The Sintering of Crystalline Oxides, I. Interactions Between Grain Boundaries and Pores, in: S. Sōmiya, Y. Moriyoshi (Eds.), Sintering Key Papers, Springer Netherlands, Dordrecht, (1990) 449-466.

[76] R. Chaim, M. Levin, A. Shlayer, C. Estournes, Adv. Appl. Ceram. 107(3) (2008) 159-169.

[77] Z.Z. Fang, H. Wang, Int. Mater. Rev. 53(6) (2008) 326-352.

[78] G. B. P. Ferreira, J. F. da. Silva Jr, R. M. do Nascimento, U. U. Gomes, A.E. Martinelli, Two-Step Sintering Applied to Ceramics, in: Arunachalam Lakshmanan (E.d.), Sintering of Ceramics - New Emerging Techniques, InTech., 2012.

[79] ASTM C776-06 (2001) Standard Specification for Sintered Uranium Dioxide Pellets, ASTM International, West Conshohocken, PA, 2001.

Chapter 4

Preparation of UO_2 foam and porous pellets of UO_2

In this chapter the results obtained in the investigations on the preparation of urania foam and porous pellets are discussed

4.1 Purity of starting material

Nuclear grade urania was used for the preparation of both UO_2 foam and porous UO_2 pellets. The reagents that were used in this study were devoid of any significant impurities that would influence sintering.

4.2 Preparation of UO_2 foam by using sucrose-gel combustion method

Since this is the first study on the preparation of urania foam through sucrose-gel combustion, the conditions best suited for the preparation of the foam had to be optimized. The value of R is a key parameter [1], and it had to be optimized in order to obtain UO_2 foam with desirable properties. Initial trials revealed that sucrose-uranyl nitrate gels with an R value below 1.5, yielded powders while those with an R value above 2.6 yielded foams that were too fragile to handle. Hence, investigations were carried out on gels prepared from mixtures whose R value was between 1.50 and 2.60. Sucrose gets hydrolyzed into glucose and fructose in the presence of hydronium ions. These in turn are oxidized into a mixture of hydroxy carboxylic acids viz., gluconic acid, saccharic acid, glycolic acid and tartaric acid, in acidic medium. Hence, heating a mixture containing uranyl nitrate and sucrose would lead to the formation of carbohydrate molecule followed by formation of mixtures of hydroxy carboxylic acids. Upon continued heating these mixtures polymerize to form a resin. This resin decomposes slowly upon continued heating to form CO, CO_2 and NO_x gases. Evolution of these gases from the resin leads to foaming. From the data presented in Table 4.1 it is seen that the specific surface area increases by two orders of magnitude (i.e. from 1.24 – 198.64 m^2g^{-1}) when the value of R was increased from 1.5 to 2.6. The carbon residue and porosity were found to increase with R, while the ρ_B decreased from 0.51 g cm^{-3} to 0.10 g cm^{-3}. Since the carbon residue would have a significantly lower density than urania the reduction in density could be attributed to the presence of a significant quantity of the former. While the XRD patterns (Fig. 4.1) pertaining to the sintered foam confirms the presence of UO_2, there is no evidence for the presence of graphite. Plausibly the final product comprises amorphous carbon (which has much lower density than graphite) (Fig. 4.1). In view of the above it is reasonable to argue that the reduction in density is due to the presence of significant amount of both amorphous carbon and porosity.

The SEM images of the UO_2 foam derived through sucrose gel precursor (R = 2.4 and 2.6) presented in Fig. 4.2 reveal that these foams are highly porous and comprise both meso and macro pores. In view of the fact that the presence of high carbon residue (that would lead to electronic conductivity, which is not desirable for the DOR process); they are not well suited for the intended end use.

4.3 Preparation of porous pellets by using citrate gel combustion method

In order to obtain porous monoliths devoid of significant quantities of carbon, citrate gel-combustion synthesis of nc-urania was pursued. In this investigation the R value was so tailored as to get a porous sintered pellet. In earlier investigation (Chapter 3) it was observed that the powders derived from mixtures with an R value of 0.25 (U_C25A) show very different properties than those derived from mixtures with other values of R. Hence a mixture with this R value (0.25) was chosen for investigation along with a powder derived from mixtures with an R value of 1.00 (U_C100A). Investigations on both these powders were carried out for comparison.

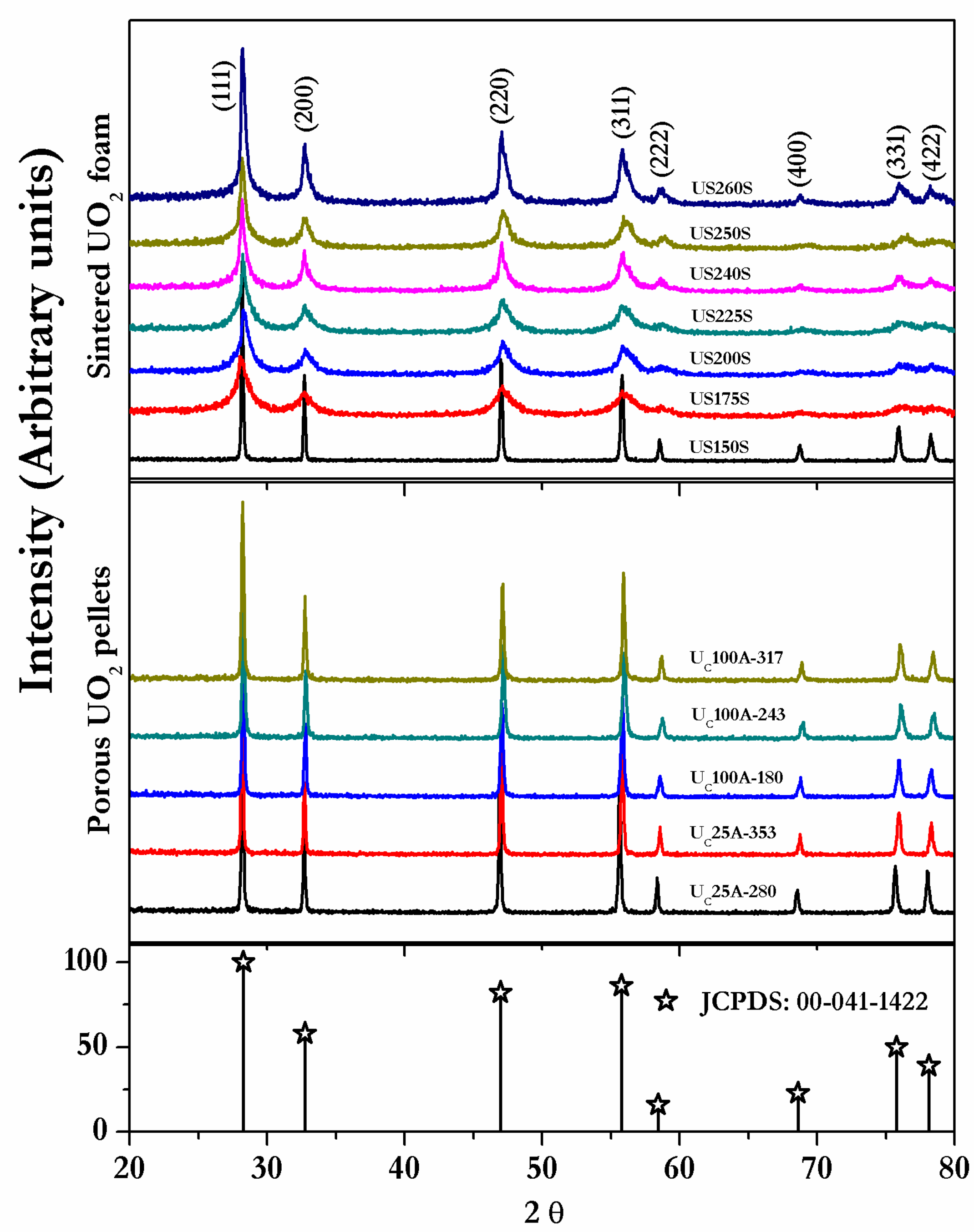

Figure 4.1 XRD of porous UO_2 foam and sintered UO_2 pellets [Sintered foams and porous UO_2 pellets were designated as USXXXS and UCXXA-P respectively, where XXX and XX indicates the value of "R" in % and the suffix S denotes that the foam is a sintered body, P denotes compaction pressure and "A" reflects the fact that the "as prepared" powder has been used as such in the sintering without calcination.]

The SSA pertaining to U_C25A and U_C100A were found to be 18 m^2g^{-1} and 6 m^2g^{-1} respectively. The ρ_G and ρ_S of the urania pellets (U_C25A and U_C100A), are presented in Figs 4.3a & 4.3b.

The ρ_G of all these urania pellets were found to increase linearly (from 45 to 60 % T. D) with the CP (60 to 180 MPa). When the CP was increased beyond 180 MPa and up to 353 MPa, this increase was less pronounced.

The ρ_S of U_C100A were nearly independent of the CP (being constant at 75 ± 5% T. D) while the ρ_S of U_C25A exhibited a greater variability. The following trend was observed in the compaction experiments carried out with the U_C25A powders. The ρ_S of U_C25A remained constant at 60 ± 5 % T. D between 60 and 180 MPa, increased sharply between 180 MPa and 320 MPa (90 ± 2 % T. D) and then declined to 70 ± 2 % T. D at 353 MPa. It must be noted that the sintering experiments carried out in this study are very different from those reported in section 3.10, the powders used here are the “as prepared” powders containing a high carbon residue not the “calcined” powders that are discussed in the former.

No evidence of cracks or other physical defects like layering, hour glassing and end capping was noticeable in these pellets (Fig. 4.4a & 4.4d). However, the variation in the shrinkage of these pellets with the CP exhibited a definite trend.

Murthy et al. [2] observed that UO_2 powders need to be compacted at a CP of about 250 – 275 MPa in order to get “defect free” sintered products. From the discussions presented in Chapter 3 (section 3. 11) it is evident that a critical compaction pressure of 180 MPa would best suit both U_C25H and U_C100H. However, the optimum pressure for **U_C25A** and **U_C100A** had to be experimentally optimized.

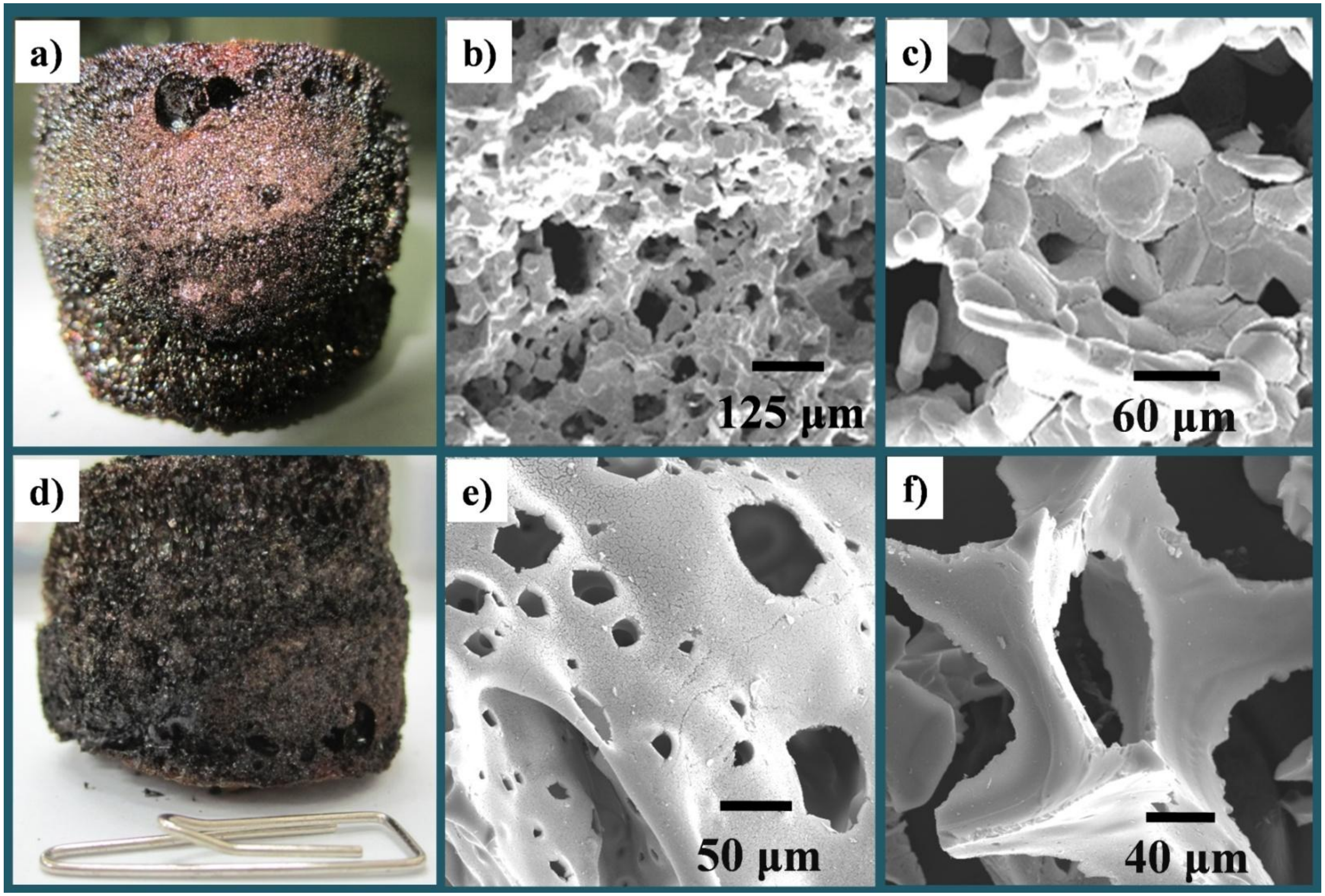

Figure 4.2 (a-c) Images of US240S: (a) Green foam (b-c) SEM images of sintered foam; (d-f) Images of US260S: (d) green foam, (e-f) SEM images of sintered foam

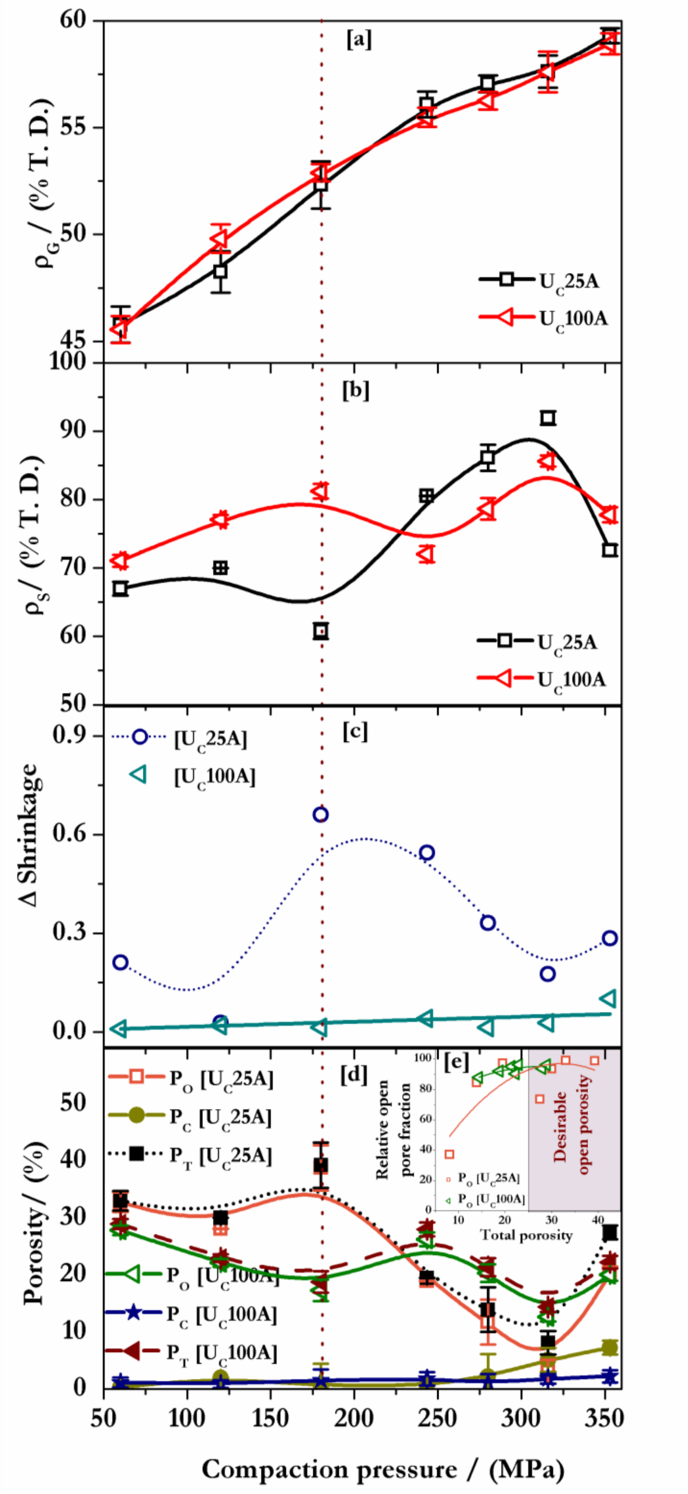

Figure 4.3 *(a) Variation of ρ_G with CP; (b) variation of ρ_S with CP, (c) dependence of shrinkage (ΔS) on CP; (d) interdependence of open and closed porosity with CP and (e) interdependence of the volume fractions of open porosity with total porosity [Where: P_O, P_C and P_T indicates open, closed and total porosity respectively; whereas the error bar shown in Fig (a-e) depict 1σ (standard deviation)]*

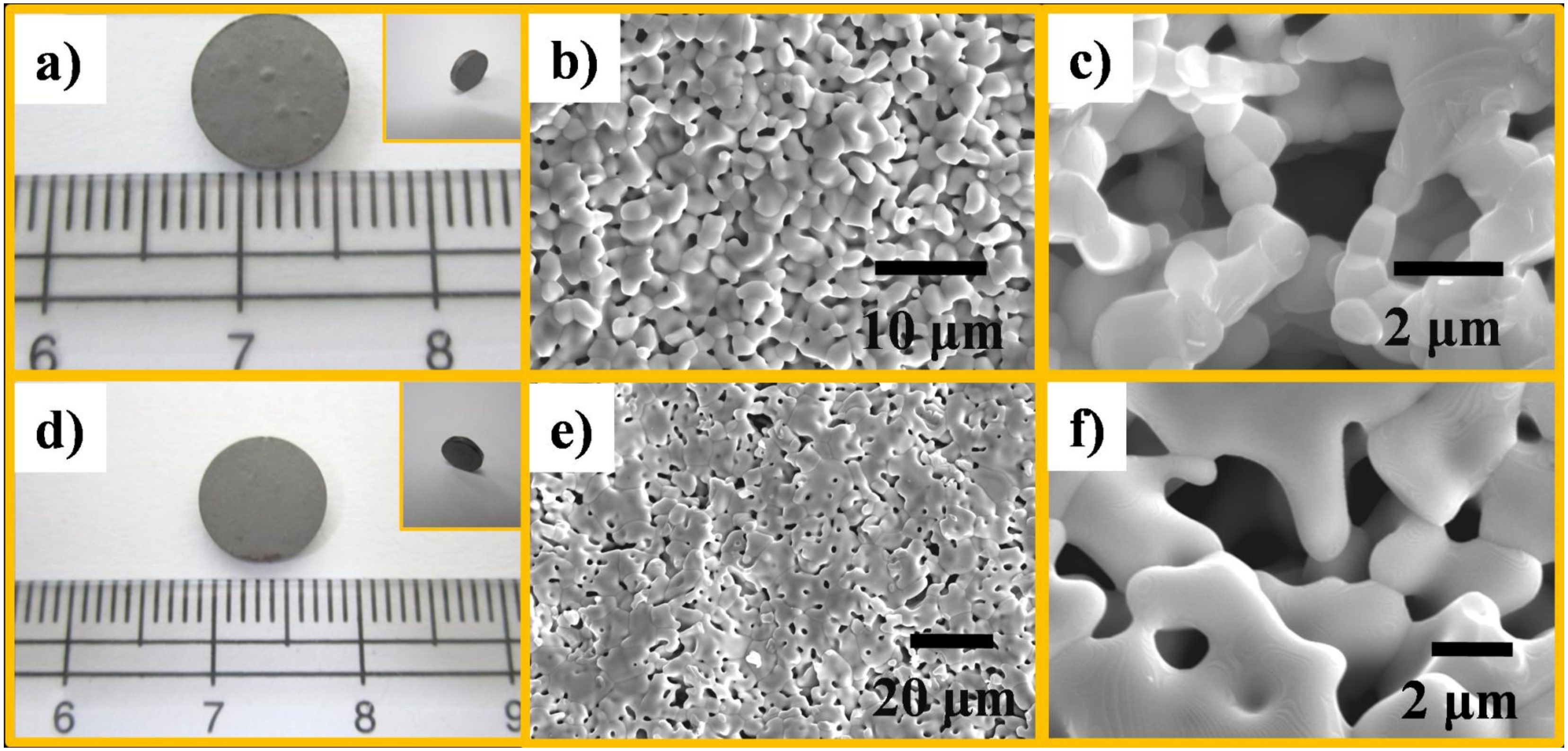

Figure 4.4 *Images obtained with sintered* UO_2 *pellets (180 MPa) derived from (a-c)* U_C25A *and (d-f)* U_C100A*: (a and d) Photograph showing porous sintered* UO_2 *pellets; SEM images of (b and e) the sintered surfaces (c and f) fractured surface*

Table 4.1 Characteristics of the UO_2 foams and pellets

Foam derived through sucrose gel precursor						Pellets derived through citrate gel precursor				
Sample	**ρ_B (g cm^{-3})**	**RC (wt %)**	**SSA (m^{2}g^{-1})**	**Porosity (%)**	**Total specific pore volume (mm^{3}g^{-1})**	**CP / MPa**	**U_C25A**		**U_C100A**	
							Density (% T. D)[#]			
							ρ_G	**ρ_S**	**ρ_G**	**ρ_S**
US150S	0.51	20	1	94.5	211	**60**	45.8 ± 0.9	66.9 ± 1.0	45.6 ± 0.6	71.1 ± 0.9
US175S	0.45	26	14	94.8	140	**120**	48.4 ± 0.0	70.0 ± 0.0	49.8 ± 0.7	77.1 ± 0.7
US200S	0.38	27	18	95.6	130	**180**	52.3 ± 1.1	60.8 ± 1.2	52.9 ± 0.4	81.2 ± 1.1
US225S	0.28	29	19	96.7	229	**243**	56.1 ± 0.6	80.5 ± 0.0	55.5 ± 0.5	72.0 ± 1.2
US240S	0.24	30	33	97.1	170	**280**	57.1 ± 0.4	86.1 ± 0.9	56.3 ± 0.4	78.7 ± 1.5
US250S	0.12	31	127	98.5	593	**317**	57.6 ± 0.8	92.0 ± 0.0	57.7 ± 0.0	85.6 ± 0.8
US260S	0.10	33	199	98.8	723	**353**	59.3 ± 0.4	72.6 ± 0.8	58.9 ± 0.5	77.8 ± 1.1

[#] *The values represent mean of five measurements*

In order to compare the sintering behavior of U_C25A and U_C100A the dimensionless relative shrinkage parameter (ΔS) of these powders was considered. This parameter is defined as follows; $\Delta S* = \frac{AS-RS}{AS}$. At the critical CP the value of ΔS would be zero. For the U_C100A powder the value of ΔS was found to be close to zero at all the CP employed in this study. However, in the case of U_C25A it was much higher than the corresponding values of ΔS pertaining to U_C100A for CP between 180 and 320 MPa. This could be attributed to the non uniform density within the compacts made with U_C25A. ΔS showed a progressive increase with the CP. It was however more pronounced in the case of U_C25A. However, the ΔS of the pellets made from U_C25A at CP below 180 MPa and above 320 MPa followed a trend similar to that exhibited by U_C100A, indicating that at these CP, distribution of density within the U_C25A compacts is rather uniform. To minimize the defects in the green compact, it is desirable to choose the minimum pressure [2] adequate to yield a good green compact. Hence, the pressure of 180 MPa would be well suited for compacting U_C25A powders.

From the data presented in Fig. 4.3a – 4.3e, it is clear that U_C25A powders yield a product with a higher porosity as compared to U_C100A at CP below 180 MPa. It is evident that open pores form a significant fraction of the total porosity and that the former increases with the total porosity (Fig. 4.3e). When the total porosity is more than 30 % (i.e. ρ_S = 70 % T.D) the relative fraction of open porosity is above 90%.

In view of the above, 180 MPa is the optimum pressure suitable to compact the powder U_C25A. Even though the pellets derived from U_C100A exhibit uniform sinterability, the pellets made out of U_C25A possess more open porosity and are hence, more desirable. The microstructures (Fig 4.4b-c & Fig. 4.4e-f) reveal that these samples contain interconnected pores

---

∗ The shrinkage values reported here cannot be compared with those mentioned in section 3.11, because these pellets were made from the U_C25A powders and not from the U_C25H powders which are typically a few micrometers in size. From the foregoing it is evident that U_C25A would be well suited for the DOR process.

4.4 Conclusions from the studies on foam and porous pellets of nc-UO_2

UO_2 foam was successfully prepared for the first time by using a sucrose-gel precursor. This comprised both meso and macro pores and possessed sufficient crush strength. However, the presence of large amounts of carbon residue would limit its utility for the intended application, viz., DOR, owing to the electronic conductivity brought about by carbon. Typically 30 to 40% porosity would be ideal for the DOR process. However, the densities of these foams are far lower than the optimum value suitable for the end use.

Porous urania pellets were successfully obtained for the first time from nc-urania powders obtained through citrate gel-combustion method. A fuel to oxidant ratio (R) of 0.25, a CP of 180 MPa and a TSS_3 (Sintering schedule (Table 2.3)) with a maximum temperature of 1473 K were found to be the optimum conditions for obtaining a product with a desirable density of about 60 to 70 % T. D.

References

[1] K.C. Patil, Chemistry of Nanocrystalline Oxide Materials: Combustion Synthesis, Properties and Applications, World Scientific Publishing Co. Pvt. Ltd., Singapore, 2008.

[2] B. Narasimha Murty, P. Balakrishna, R.B. Yadav, C. Ganguly, Mater. Charact. 49(2) (2002) 103-111.

Chapter 5

Synthesis, Characterization and Sintering of Nanocrystalline Thoria

This chapter deals with bulk synthesis of nc-ThO_2 by using citrate gel-combustion method. The nc-ThO_2 powders were compacted at different pressures and were sintered by using the "two-step sintering" method. The microstructural investigations on nc-ThO_2 powders were carried out by using both SEM and TEM.

5.1 Assay of starting material

Nuclear grade thorium nitrate crystals were used in this study. ICPMS analysis of thorium nitrate was carried out and the impurities present are given in Table 5.1. Since, the impurities present are insignificantly low, it is reasonable to conclude that their presence would not alter the gel-combustion synthesis as well as the sinterability of the powders.

5.2 Citrate gel-combustion synthesis

Nc-ThO_2 was prepared through citrate gel-combustion with a view to observe "volume combustion" in Th^{4+} ion containing gels as well as to re-establish the systematic dependence of powder properties on R. During the gel-combustion synthesis of nc-ThO_2, a white precipitate was formed and upon continued heating of the starting mixture it got re-dissolved subsequently. The white precipitate was probably due to the formation of thorium citrate [1, 2]. Upon heating, these mixtures underwent precipitation, re-dissolution of the precipitate, dehydration, gelation and decomposition (combustion reaction). All these reactions took place in an open glass bowl. No attempt was made to measure the reaction temperature. Among all the mixtures used, those with R = 0.125 and 0.17 were found to undergo a "vigorous" and "moderate volume combustion reaction" respectively while those mixtures with R values of 0.25 and 0.50 exhibited auto-ignition that ensued with smoldering. Earlier, Chandramouli et al. [1] had reported the citrate gel-combustion synthesis of nc-ThO_2 with R values ranging from 0.31 to 1.27. These authors did not observe "volume combustion" in the citrate gel-combustion of nc-ThO_2. Since, these authors [1] had used mixtures with a higher R value beyond the stoichiometric ratio (R = 0.125) for VCR, these authors could not observe VCR. In this study, the value of R was varied between 0 and 0.50. However, we observed for the first time that "volume combustion reaction (VCS)" [3] in the citrate gel-combustion synthesis of thoria takes place in mixtures with R = 0.125.

$$4\mathrm{Th(NO_3)_2} + 2\mathrm{C_6H_8O_7} + 5\mathrm{O_2} \rightarrow 4\mathrm{ThO_2} + 16\mathrm{NO_2} + 12\mathrm{CO_2} + 8\mathrm{H_2O} \qquad 5.1$$

5.3 Thermal analysis and evolved gas analysis of gel-combustion reaction

The thermogram, DTA curve, DSC curves as well as the evolved gas analysis pertaining to the pyrolysis of citrate gels containing Th^{4+} (R = 0.50) are presented in Fig. 5.1. The thermogravimetric curve (R = 0.50) shows three mass loss steps; their onset temperatures being 398 K, 438 K and 609 K respectively. The DSC curve of this mixture (R = 0.50) shows an endothermic peak at 398 K and three exothermic peaks at 438 K, 624 K and 659 K. Evolved gas analysis of this mixture (R = 0.50) revealed the evolution of water at 396 K and 438 K. The first peak could be ascribed to the dehydration of the gel (onset 396 K), while the other peak could be due to the pyrolysis of this gel (438 K). These observations were further substantiated by both the DSC and evolved gas analyses. The latter showed that loss of water begins at 398 K and the liberation of other gases (NO, NO_2, CO and CO_2) sets in at 418 K. So far evolved gas analysis of the combustion of Th^{4+} containing citrate gels had not been reported. In addition, it is also observed that H_2O (g), O (g), NO (g), NO_2 (g), CO (g) and CO_2 (g) evolve at 434 K close to the exothermic peak observed in the DSC curve (438 K). These observations confirm that this gel undergoes dehydration followed by the combustion reaction. The exothermic peak (438 K) in the DSC curve shows a minor hump that could not be resolved further. This could be attributed to simultaneous reactions. Further it is observed that in the combustion of Th^{4+} containing gels N_2 gas is not liberated. This is a new observation and is at variance with the general reaction proposed in the literature [4].

At still higher temperatures the thermogravimetric curve and the DSC curves show a weight loss (609 K onset) and two exothermic peaks (624 K and 659 K) respectively. The evolved gas analysis reveals the liberation of H_2O (g), O (g), CO (g) and CO_2 (g) at 619 K and CO (g) and CO_2 (g) at 658 K. These emanate from the combustion of the carbonaceous residue. It is interesting to note that a reduction in the O_2 availability is testified by the mass spectrum pertaining to O_2 at 424 K and 605 K. Probably, O_2 available in the ambience is consumed by the combusting mass. From the foregoing discussion it is clear that the the citrate gel-combustion synthesis of thoria is completed within 500 K and the subsequent reactions pertain to the combustion of the unburnt residue.

5.4 Characterization of the powders

5.4.1 Bulk density (ρ_B), PSD and SSA

The ρ_B of all the T_CXXA powders were lower compared to that of the T_CXXC powders (Table 5.2 & Fig. 5.2a). These were found to vary from 1.0 – 7.4 % T.D and 1.2 – 8.3 % T.D respectively. The powders derived from the simple denitration possessed a ρ_B of 18.5 % T.D (T_CXXA) and 32.1 % T.D (T_CXXC). The thoria powders (T_C13A) derived through VCR were found to be highly porous. This powder exhibited the lowest ρ_B (1.0 % T.D).

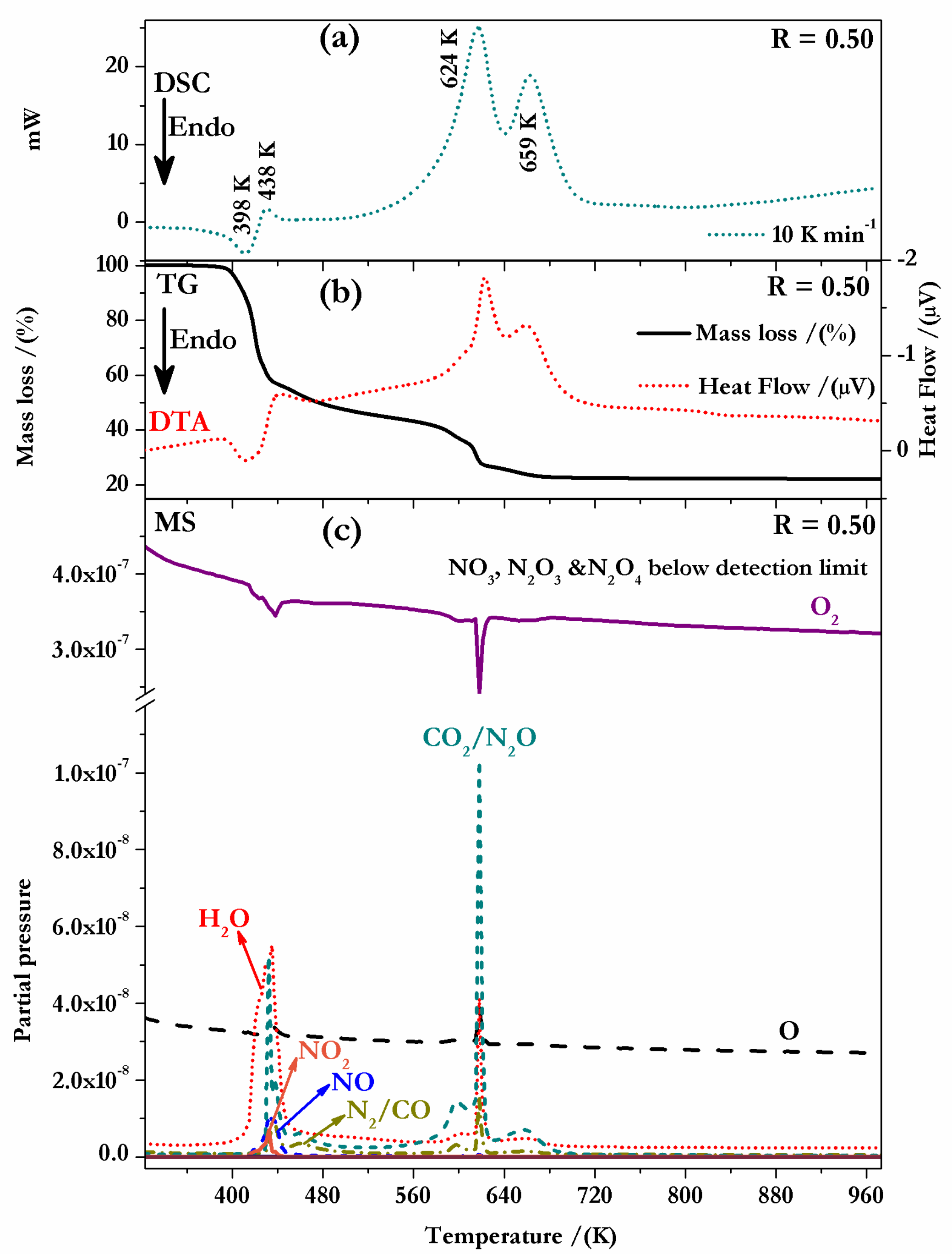

Figure 5.1 Thermal decomposition in a mixture with an R value 0.50 in O_2 atmosphere with 10 K min^{-1} heating rate by using (a) DSC (b) TG-DTA and (c) evolved gas analysis

Very much like nc-urania (Chapter 3) and nc-yttria (Chapter 6) obtained through volume combustion, nc-ThO_2 also exhibited lowest ρ_B. Ananthasivan et al. [5] had reported that the ρ_B of thoria powders derived through oxalate de-agglomeration was varying between 11.0 % T.D to

18.3 % T.D. Pope and Radford [6] found that the ρ_B of thoria powders prepared through precipitation and denitration were 10.0 % and 25.0 % T.D respectively. Thus, it is evident that the ρ_B of nc-ThO_2 powders prepared in this study through citrate gel-combustion are lower than those reported earlier [5, 6].

Table 5.1 Impurities in the thorium nitrate (ICP-MS)

Elements	Co	Mn	Mo	Ba	Al	Sr	Ti	Pb	Cr	Zn	Fe	Cu	V	Ni	Mg
Concentration of Impurities /ppm	<20	14	15	51	< 16	16	<20	<15	<17	<15	25	<25	<18	<17	6

Table 5.2 Characteristics of the nc-ThO_2 powder synthesized by "gel-combustion"

Sample	**Mole ratio (R)**	**ρ_B % T. D***		**RC^1 (ppm)**		**SSA^1 (m^2g^{-1})**	
		A	**C**	**A**	**C**	**A**	**C**
T00	0	18.5	32.1	137	105	27	16
T_C5.5	0.055	2.9	3.0	1206	560	34	18
T_C13	0.125	1.0	1.2	1528	537	37	24
T_C17	0.166	1.5	1.8	1553	425	25	17
T_C25	0.250	2.3	3.5	1591	323	20	15
T_C50	0.500	7.4	8.3	1501	568	21	16

^{1}and * - averaged of three and five independent measurements

SSA of the nc-ThO_2 powders prepared in this study is presented in Fig. 5.2b and in Table 5.2. It is observed that the SSA of T_CXXA powders is higher than that of T_CXXC powders. T_C13A and T_C13C which were derived through volume combustion reaction exhibited the highest SSA of 37 m^2 g^{-1} and 24 m^2 g^{-1} respectively. Rest of the powders were found to have a SSA of about 16 m^2 g^{-1}. Chandramouli et al. [1] had reported the dependence of SSA of citrate gel-combustion derived nc-ThO_2 on the value of R. The values of SSA of the powders obtained from mixtures with different “R” reported by these authors are as follows; a) hot plate (R = 0.64 m^2 g^{-1} to 1.01 m^2 g^{-1}, SSA = 14.93 m^2 g^{-1} to 15.18 m^2 g^{-1}) and b) microwave heating (R = 0.31 – 1.27, SSA = 9.92 – 15.18 m^2 g^{-1}). SSA of thoria powders reported by other authors is presented in Table 5.3.

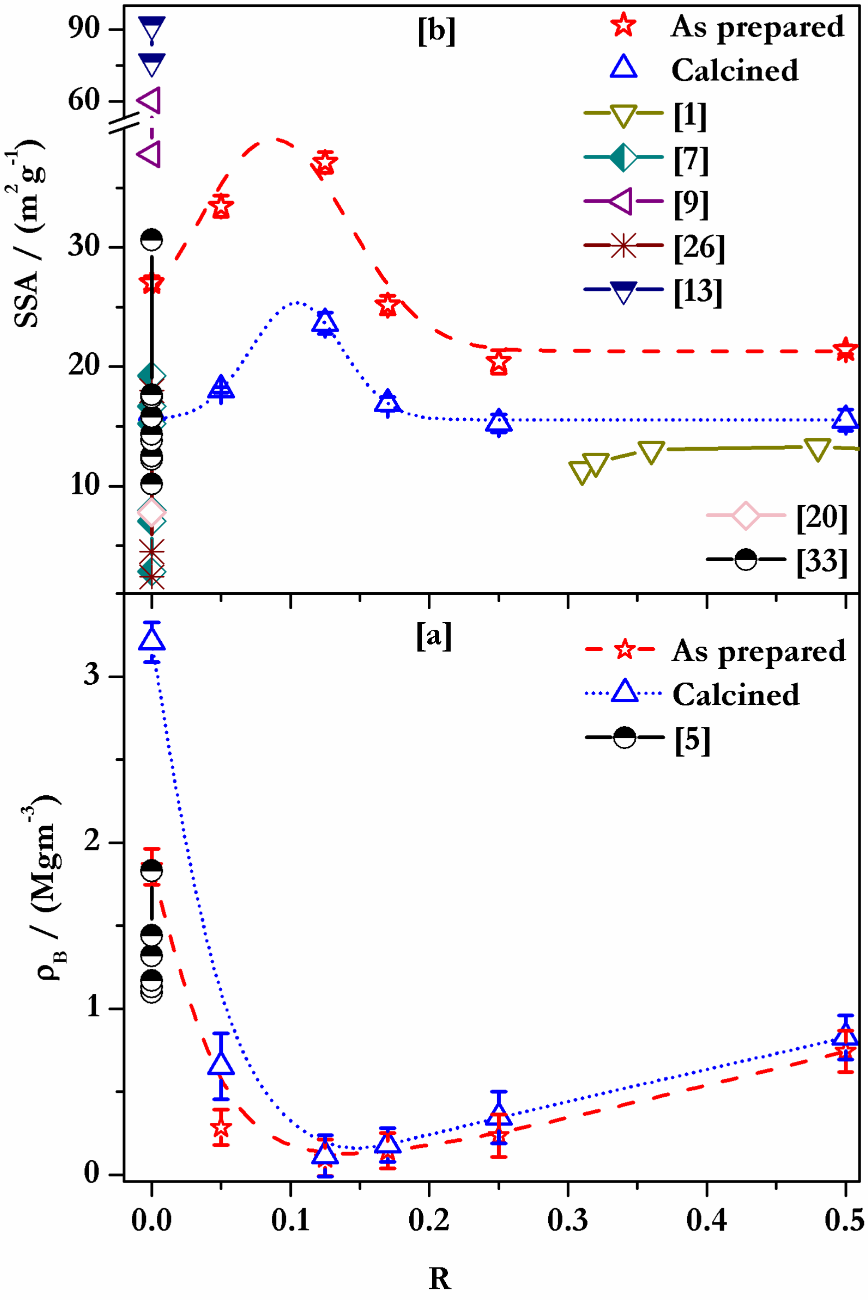

Figure 5. 2 Dependence of (a) ρ_B of the nc-ThO_2 powder and (b) SSA of the nc-ThO_2 powder on the value of R [14, 15, 24, 26-28, 40]

It should be noted that in the BET analysis, reliable values of SSA could be obtained only when the quantity of the powder sample taken for investigation is about half a gram or more. Also, representative sampling from the bulk has to be ensured. In view of the above, and the fact that we measured SSA values by using sufficient quantity of the sample (about 1g), our results are reliable.

Table 5. 3 Comparison of RC and SSA of thoria powders reported in the literature

Ref.	**Method**		**RC**	**SSA (m^2g^{-1})**	**Quantity / Batch size**
[7]	Th-Ox		20 – 1400 ppm	2.84 – 19.25	-
[5, 8]	Th-Ox (deagglomeration)		1000 – 1800 ppm	12.8 – 19.8	≈ 25 g
[9]	Hydrothermal		-	-	0.114 g
[10]	Th-Ox	873 K; 1h	1.9 wt % (as CO_3^{2-})	-	-
		873 K; 2h	1.6 wt % (as CO_3^{2-})		
		973 K; 2h	1.0 wt % (as CO_3^{2-})		
		1073 K; 2h	0.5 wt % (as CO_3^{2-})		
[11]	Glycine GC		0.3 – 0.4 wt %	53 – 90	-
[12]	PIR		≤ 0.3 %	7.8	-
[13]	electro-deposition		-	76.6 – 92.1	-

Th-Ox – thorium oxalate; GC – gel combustion and PIR- photo chemically induced reaction

In order to understand the packing and compaction behavior of the powders it is useful to investigate the dependence of size distribution of particles on the bulk density and SSA in the powders T_CXXA and “T_CXXC. The size distribution of particles in T_CXXA and T_CXXC powders are presented in Table 5.4 and in Fig. 5.3. The size distribution histograms were deconvoluted to delineate the contribution from different size fractions. The thick solid lines depict the experimentally observed particles while the thin solid lines depict the deconvoluted curves. It was observed that the size distribution of particles in T_CXXA exhibited both unimodal and bimodal size distributions while T_CXXC powders exhibited bimodal and trimodal size distribution of particles. It was observed that the T00A powders had the highest ρ_B while T_C13A had the lowest. T_C5.5A, T_C17A, T_C25A and T_C50A have moderately higher ρ_B than T_C13A.

The following general trends are discernible. T_C5.5C, T_C13C and T_C17C have markedly higher SSA than T00C, T_C25C and T_C50C. Probably the former set of powders possesses a higher fraction of pores. Among the first set the following trend was discernible: $\rho_{B(TC5.5C)} > \rho_{B(TC17C)} > \rho_{B(TC13C)}$. This trend positively correlates with the fraction of heavier particles present in the powders. A similar trend is also observed among the other powders i.e., $\rho_{B(T00C)} > \rho_{B(TC50C)} > \rho_{B(TC25C)}$. Nc-$ThO_2$ powders derived through oxalate deagglomeration method had exhibited multimodal size distribution of particles with their size ranging from 0.1 μm to 1000 μm. Rahaman et al. [14] had reported that the powders with variable size distribution of particles would undergo abnormal sintering leading to differential densification and a defective product. It is reported that the differential densification [14-16] could be averted by employing powders with near unimodal size distribution of particles. From the results presented above, it is evident that the powders derived with R values 0.125 and 0.17 are likely to undergo better densification as compared to other thoria powders prepared in this study.

Table 5.4 Particle size distribution in thoria powders

Sample	**Particle size distribution (vol %)**					
	10 vol. % of sample has size less than (μm)		**50 vol. % of sample has size less than (μm)**		**90 vol. % of sample has size less than (μm)**	
	A	**C**	**A**	**C**	**A**	**C**
T00	2	14	22	66	69	158
T_C5.5	4	10	23	67	89	266
T_C13	8	12	38	125	143	415
T_C17	15	8	111	106	371	480
T_C25	11	4	102	25	364	168
T_C50	11	10	76	65	304	241

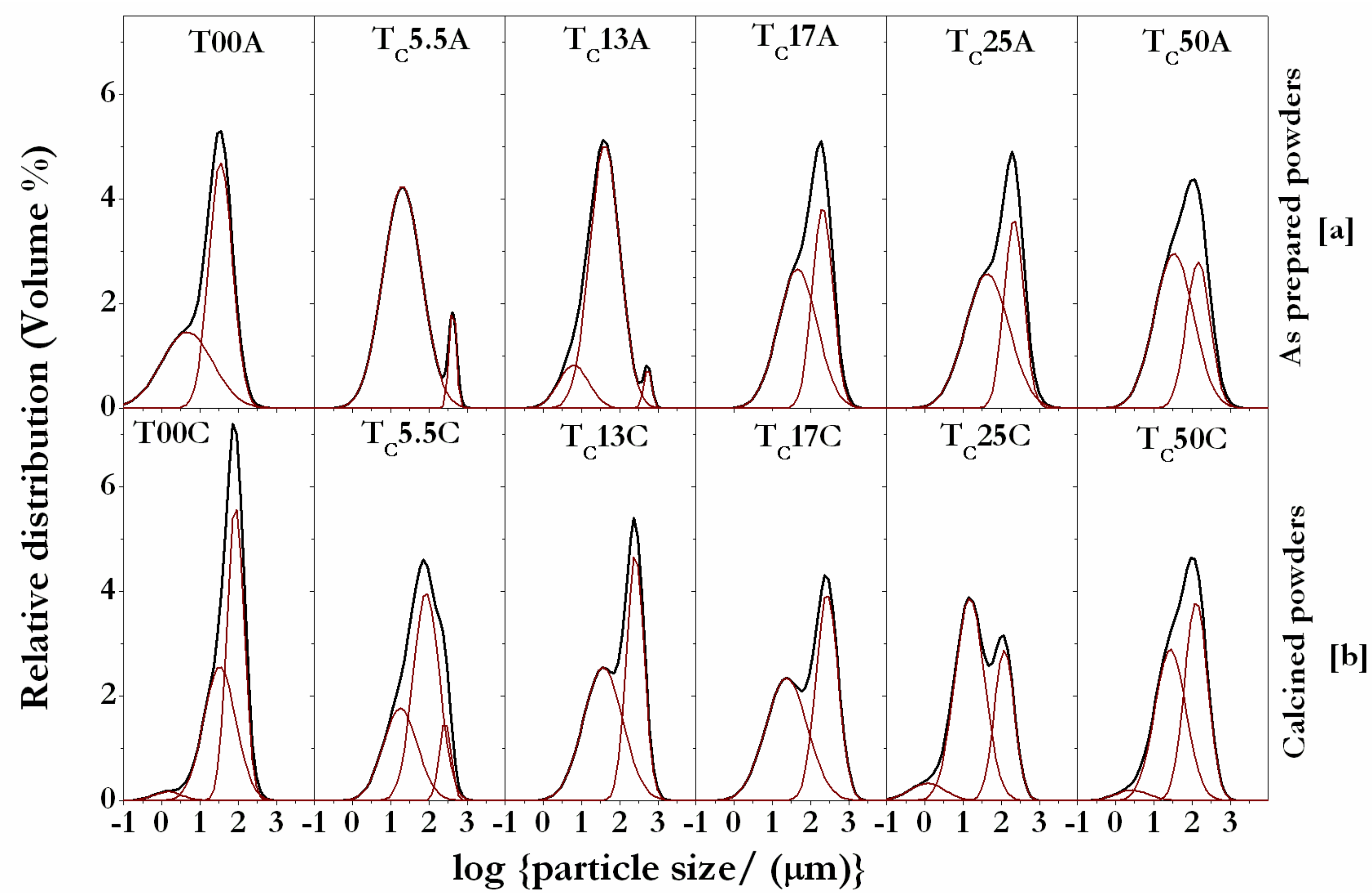

Figure 5.3 Size distribution of particles in the (a) "A" and (b) "C" nc-ThO_2 powders prepared by using citrate gel-combustion method [thick solid line – experimental curve and thin solid line – deconvoluted curve]

5.4.2 Residual Carbon

Carbon residue present in the T_CXXA and T_CXXC powders was found to vary between 137 and 1591 ppm and 105 and 568 ppm respectively (Table 5.2). As expected, the thoria powders prepared by direct denitration were found to contain minimum carbon residue. From the data presented in Table 5.2 it is evident that the nc-ThO_2 powders (calcined) prepared in this study were found to contain much lower carbon residue as compared to the methods reported in the literature [5, 7, 8, 10-12]. Carbon residue in sintered thoria pellets (selected samples) were found to vary between 70 to 150 ppm.

5.4.3 Phase characterization, XCS, lattice strain and stoichiometry

The XRD patterns of thoria powders (T_CXXA and T_CXXC) are presented in Figs. 5.4. The measured values of XCS (Sc [17] and HW [17]) and lattice strain are presented in Table 5.5 and in Fig. 5.5. The crystallite sizes of the T_CXXA thoria powders were found to be 4 – 9 nm (Sc) and 5 - 10 (HW) while that of the T_CXXC powders were found to be between 14 & 19 nm (Sc) and 17 & 22 nm (HW). In all these powders XCS shows nearly uniform change upon calcination. The XCS of both these powders exhibited a very weak dependence on the value of "R". The lattice strain however showed a significant linear dependence on "R" (Fig. 5.5), especially in the T_CXXA powders, similar to the observations made on nc-UO_2 (Chapter 3). Many authors had investigated [1, 5, 10-13, 18-20] the XCS of nc-ThO_2 the details of which are presented in Table 5.5. However, no systematic correlation between XCS and lattice strain has been reported so far. From the data presented in Table 5.5 it is evident that thoria derived ex-oxalate exhibits the lowest XCS and gel-combustion derived thoria exhibit XCS in the range 5-20 nm. Our TEM data (Figs. 5.6-5.7) testifies the mean XCS values obtained through the HW analysis of the XRD data.

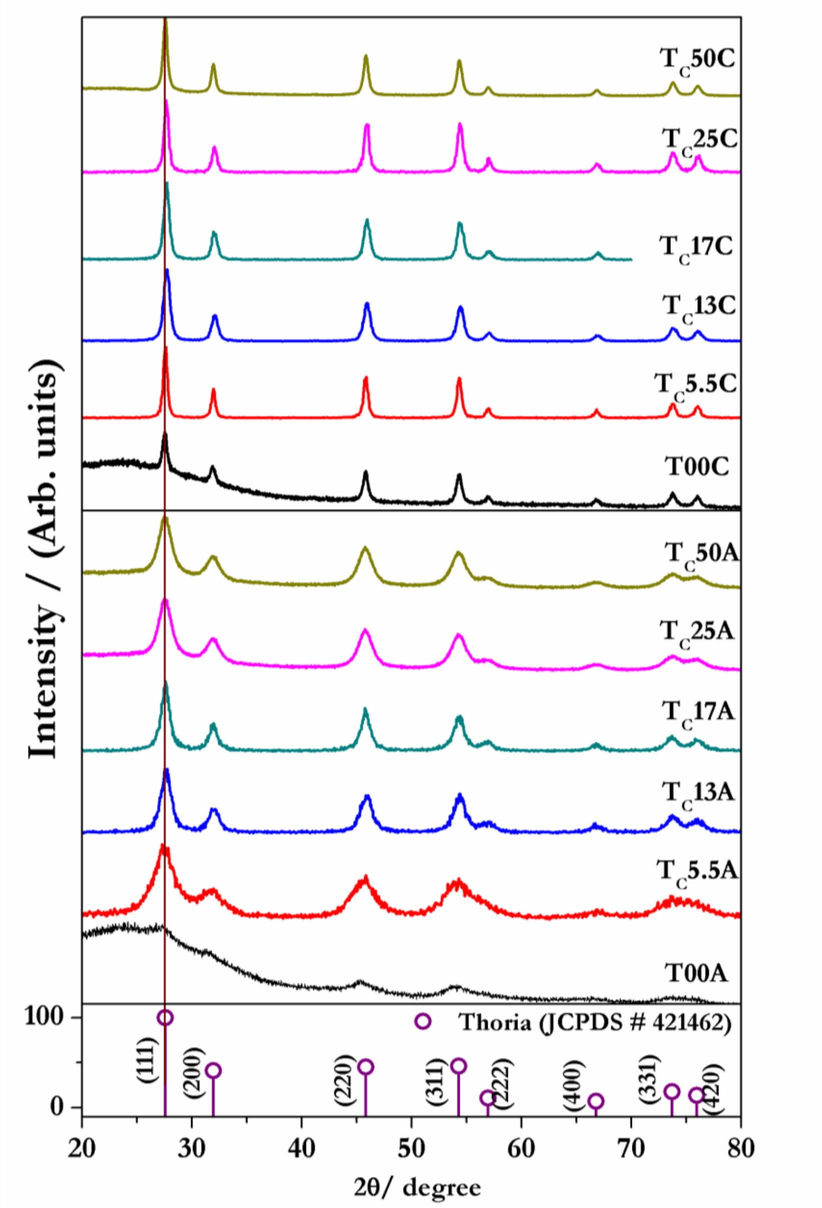

Figure 5. 4 XRD pattern of the "A" and "C" nc-ThO$_2$ powders derived through citrate gel-combustion method

The dimensionless lattice strain of T$_C$XXA powders measured by using HW method was found to be higher than that of T$_C$XXC powders (Figs. 5.5b & 5.5c). This observation is in line with our earlier results on nc-UO$_2$ powders [Chapter 3]. However, in general, it is observed that the dimensionless lattice strain in the T$_C$XXA powders is higher than that of the thoria powders obtained through precipitation method [10].

Table 5.5 XCS and lattice strain of nc-ThO_2 powders measured in this study along with those reported in the literature

Sample	X-ray Crystallite size						TEM
	A			C			A (nm)
	Sc (nm)	HW (nm)	Strain x 10^{-3}	Sc (nm)	HW (nm)	Strain x 10^{-3}	
T0	4	-	-	17	18	0.55	-
$T_C5.5$	4	7	3.01	19	22	0.67	-
T_C13	8	9	4.87	14	15	0.14	11 - 25
T_C17	9	10	6.71	16	22	2.14	6 - 16
T_C25	4	5	2.00	16	17	0.45	-
T_C50	5	6	1.69	17	19	0.60	-

Ref.		Sc (nm)	HW (nm)	TEM (nm)
[1]	**HP**	5	**-**	**-**
	MW	11	**-**	**-**
[18]		20.1 – 43.2	**-**	**-**
[10]		5 - 34	**-**	**-**
[5]		2.2 – 19.3	10 - 11	5-10
[19]		6	-	-
[11]		53 & 90	-	-
[20]		27	23	12
[12]		4.6	-	-
[13]		30	-	10 - 30

Ref. – References; HP-hot plate heating and MW-microwave mode of heating

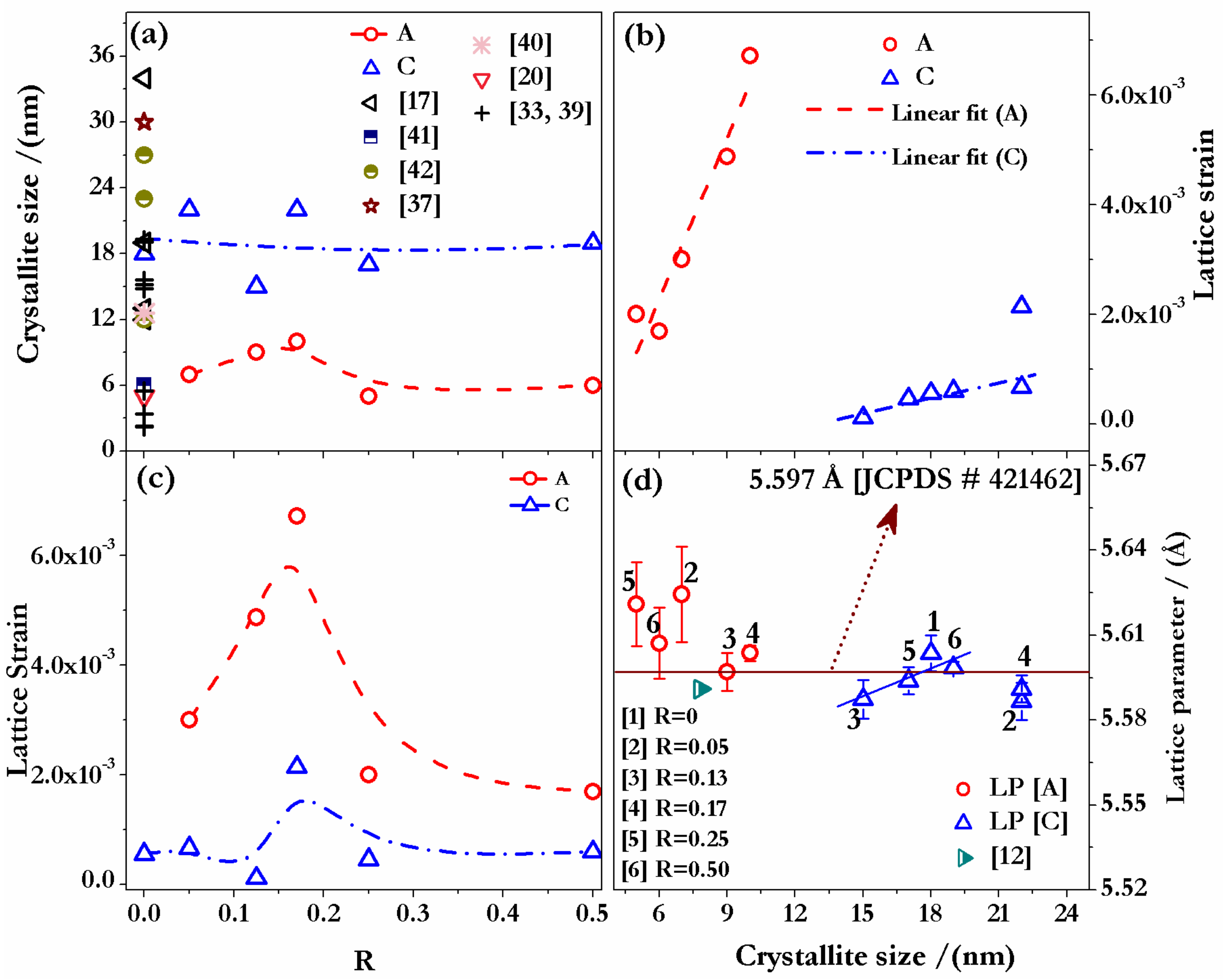

Figure 5.5 (a) Dependence of the XCS (HW method) on R values; (b) variation of lattice strain in crystallites with R values; (c) variation of lattice strain with XCS in "as prepared (A)" and "calcined (C)" thoria powders and (d) variation of the lattice parameter with XCS in nc "A" and "C" thoria powders

The combustion reaction is a self propagating fast reaction, which accentuates the formation of nanocrystallites with a higher lattice strain. However, this lattice strain gets annulled upon calcination (1073 K). The measured values of lattice strain in the T_CXXA and T_CXXC powders (Table 5.5) further support this premise. The lattice strain in the powders derived through volume combustion (T_C17A and T_C17C) was found to be the highest. This is due to the rapid formation of crystallite during the combustion of the mixtures with R = 0.125 and 0.25, which not only disperses the product but also does not allow sufficient time for grain coarsening / annealing of strain.

The lattice parameter (LP) of the thoria powders prepared in this study was computed from their respective X-ray diffractograms. The LP of T_CXXA powders were higher than that of T_CXXC powders (Fig. 5.5d). Further, it was observed that the LP approaches the value cited in JCPDS No. 00-42-1462 (5.597 Å) for powders with XCS 17 nm or more.

High resolution TEM images did not reveal any lattice defects. EELS analysis was also carried on T_C13A and T_C17A samples (Fig. 5.8). The O-K and $N_{4,5}$ ($4d \rightarrow 5f$) edges are presented in Fig. 5.8. Selection rule states that $d_{3/2}$ electrons can only be excited to empty $f_{5/2}$ level which means the relative occupation of $5f_{5/2}$ and $5f_{7/2}$ could be calculated by measuring the area beneath N4 ($4d_{3/2} \rightarrow 5f_{5/2}$) and N5 ($4d_{5/2} \rightarrow 5f_{5/2}, 5f_{7/2}$) peak [21, 22]. The branching ratio [$B = A_{5/2} / (A_{3/2} + A_{5/2})$], where $A_{3/2}$ and $A_{5/2}$ denotes areas within $4d_{3/2}$ and $4d_{5/2}$ peaks [21, 22] corresponding to the N4 and N5 edges of T_C13A and T_C13C were measured from the background corrected spectra. The values of B pertaining to T_C13A and T_C13C powders are 0.5786 and 0.5608. Increase in the integrated area of N4 edge had led to decrease in B value in calcined thoria powders. The measured peak maxima pertaining to N4 and N5 edges are comparable to the values reported earlier [21, 22] for pure Th metal. This corresponds to an oxidation state of (IV). Hence it is reasonable to conclude that the EEL spectrum did not show any evidence for the presence of Th ions in oxidation states other than (IV). Pavelkova et al. [12] had reported the LP of 5.591 Å for the nc-ThO2 powders with an XCS of 7.8 nm. While Tyrpekl et al. [10] had reported the LP of 5.6006 Å (293 K) for the nc-ThO_2 powders. However, so far no confirmatory evidence has been presented to substantiate the origin of substoichiometry in the oxygen sublattice of this oxide.

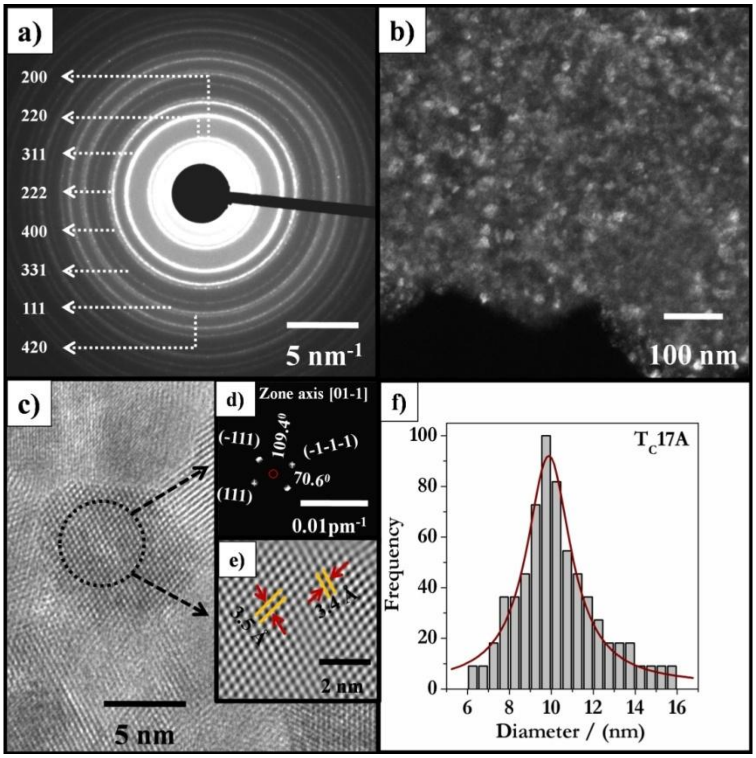

Figure 5.6 *TEM images of T_C17A powders; (a) SAED image; (b) bright field image; (c) HRTEM image of a nanograin; (d-e) FFT and filtered IFFT image revealing zone axis [01-1] and (f) grain size distribution*

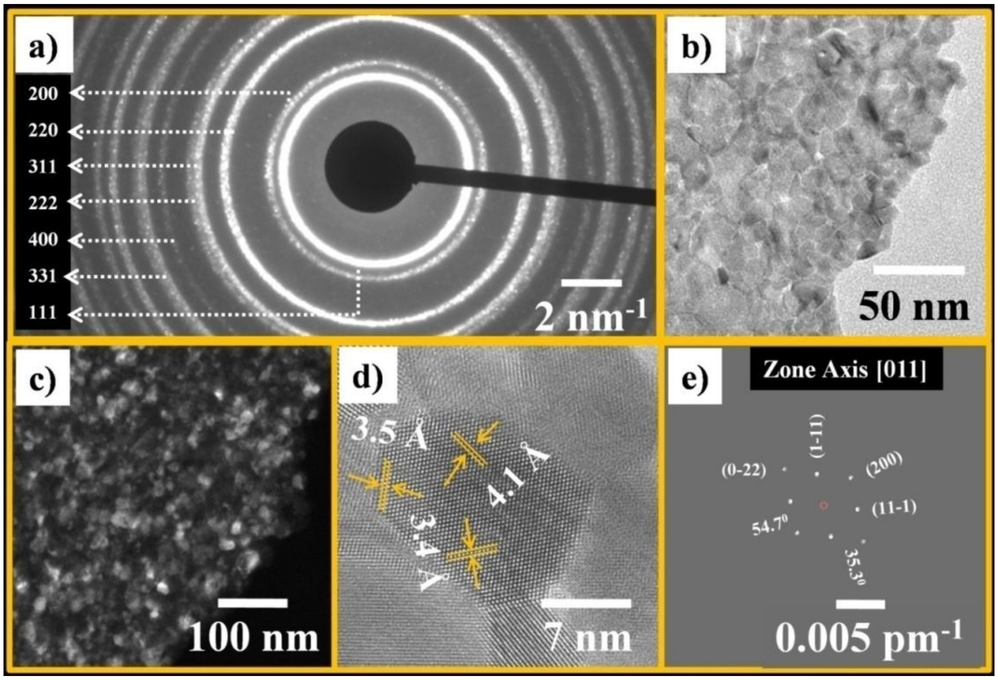

Figure 5.7 *TEM images of T_C13A (ThO_2) powders: (a) SAED image; (b-d) bright field, dark field image and HRTEM image of nano grain and (e) FFT image with the zone axis [011]*

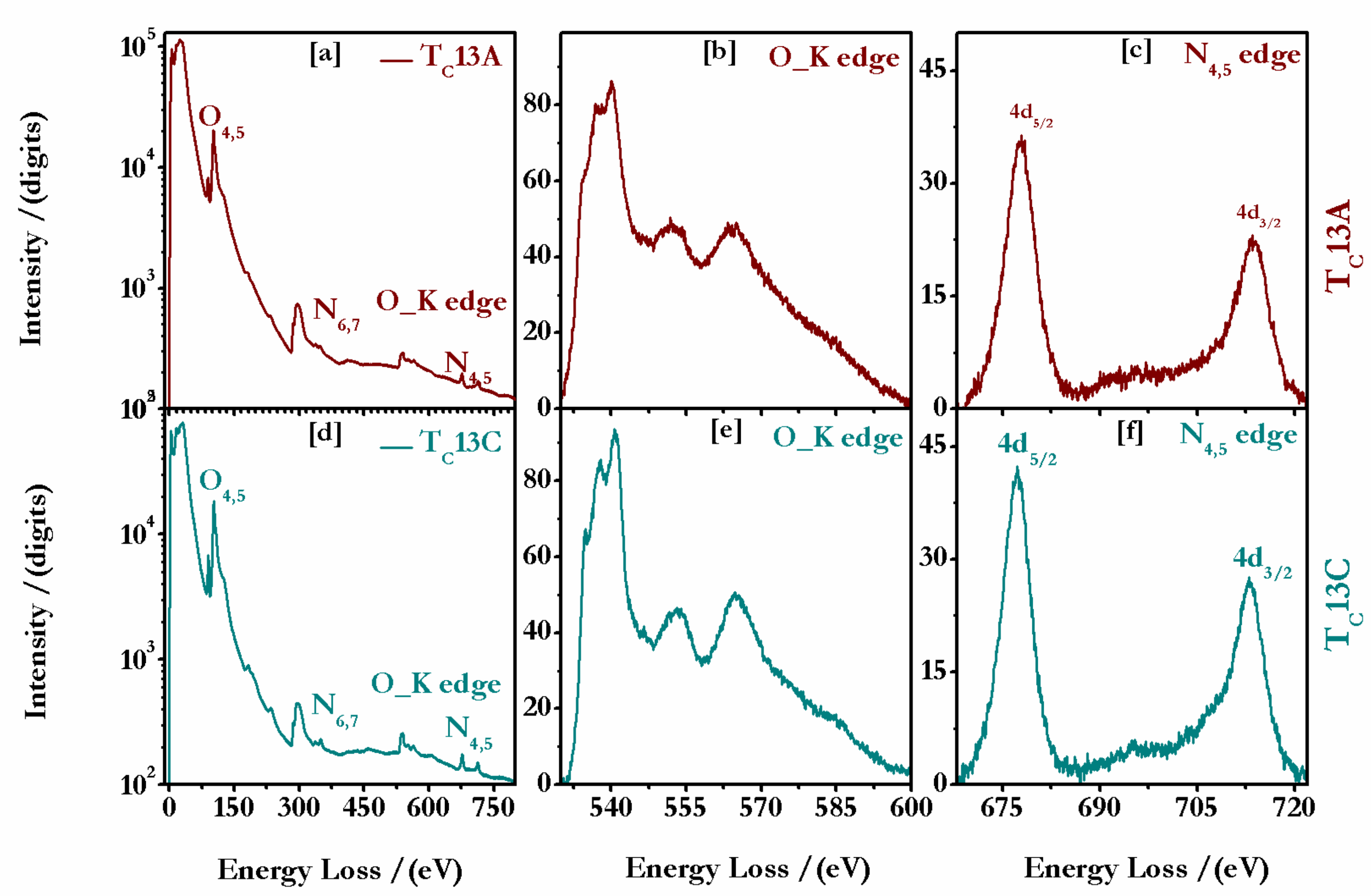

Figure 5. 8 EELS of T_C13A and T_C13C depicting (a & d) background corrected full spectra; (b & e) O-K edges and (c & f) $N_{4,5}$ (4d → 5f) edges

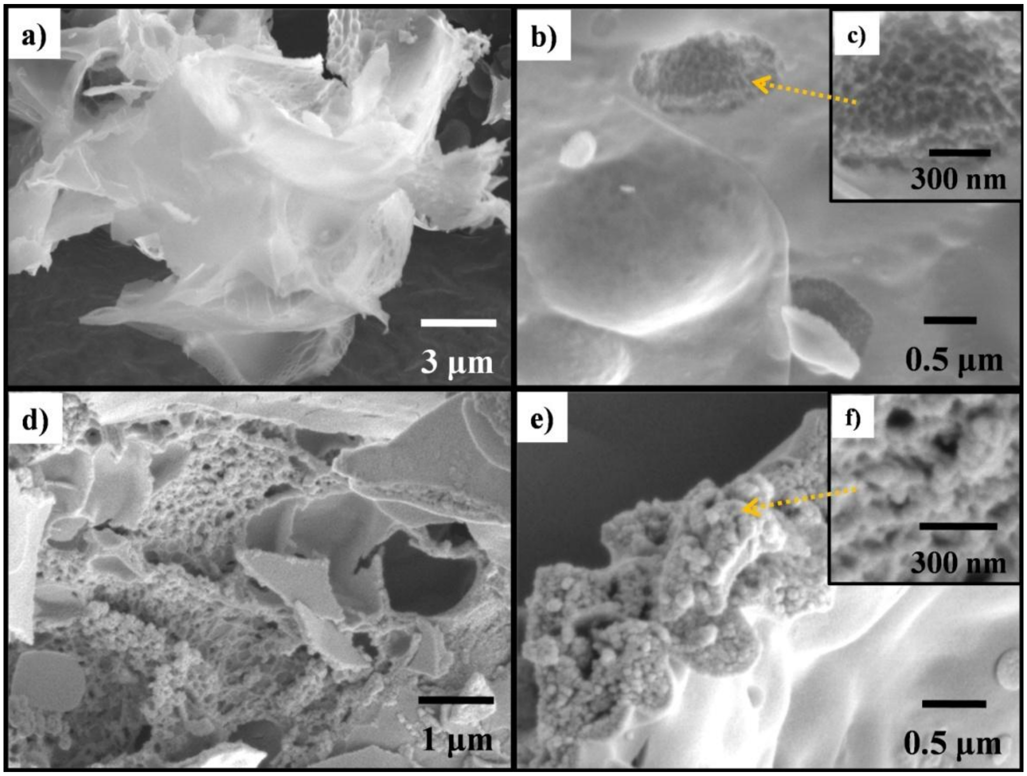

Figure 5.9 SEM images of thoria powders (a-c) T_C17A and (d-f) T_C25A

5.4.4 Microstructural analysis by using SEM and TEM

Low magnification images showed a flaky pattern (Fig. 5.9) while the high magnification SEM images revealed that the T_C17A and T_C25A comprised a network of porosity (Fig. 5.9). It was also observed that these powders comprised both micro and macropores (Fig. 5.9).

TEM investigations carried out on the powders T_C13A and T_C17A (Fig. 5.6 – 5.7) revealed a broccoli like pattern with porous morphology. Bright field and dark field images of T_C17A powders confirmed the presence of nanograins with interconnected pores. The SAED images of T_C13A and T_C17A powders (Figs. 5.6a and 5.7a) confirmed the presence of fluorite structure and nanocrystallity. The "d-spacing" measured in this powder were comparable to those cited in the standard JCPDS pattern (No. 00-42-1462). The grain size distribution was mainly unimodal with a maxima at 10 nm.

5.5 Compaction and sintering of nanocrystalline thoria powders

5.5.1 Green density (ρ_G)

It was observed that the ρ_G of the thoria pellets increases with the CP (Fig. 5.10a & Table 5.8). The plot depicting the variation of ρ_G with the CP reveals a discontinuity in the slope at a compaction pressure of 175 MPa in all these powders. Further, it is observed that the values of the ρ_G varies in the following order $\rho_{G(TC13C)} < \rho_{G(TC17C)} < \rho_{G(TC25C)} < \rho_{G(TC50C)} < \rho_{G(TC5.5C)} < \rho_{G(T00C)}$, irrespective of the CP. It was observed that this trend is akin to the trend in the variation in the ρ_B of these powders. Thoria powders which comprised near unimodal size distribution of particles did not yield pellets with high ρ_G, while the powders that comprised multimodal size distribution of particles yielded compacts with high ρ_G. Thoria powders derived through direct denitration method yielded fragile compacts when compacted at 60 MPa.

The maximum green density that could be obtained was 58.2 ± 0.6 % T.D (T_C13C) and 60.2 ± 0.2 % T.D (T_C17C - 353 MPa). Further, it was observed that the green compacts of these powders (T_C13C and T_C17C) showed sufficient handling strength even when a CP as low as 60 MPa was employed. The powders T00C, T_C5.5C and T_C50C (set I) exhibited higher ρ_G than T_C13C, T_C17C and T_C25C (set II). This trend is similar to that observed in their ρ_B i.e. $\rho_{G(set\ I)} > \rho_{G(set\ II)}$. The higher fraction of fines in the (set II) powders probably led to a lower ρ_G. Chandramouli et al. [1] had employed a CP of 200 MPa to compact nc-thoria powders. However, these authors have not reported the values of ρ_G. It was observed that the ρ_G values obtained in this study for nc-ThO_2 powders are higher as compared to those reported earlier (Table 5.6). In addition, the thoria compacts derived in this study are superior compared to those reported earlier [5, 7, 8, 12, 18, 23, 24] as these nc-ThO_2 powders did not require any additional consolidation aids viz., pre-compaction, grinding, addition of lubricants or binders during compaction.

Table 5.6 Comparison of ρ_G of thoria compacts reported in the literature

Reference	CP; Lubricant/binder	ρ_G
[23]	345 MPa; stearic acid	59.6 – 60.3 %
[7]	-	56 – 64 %
[24]	200 MPa; zinc stearate	56 %
[18]	276 MPa; zinc stearate	56 – 64 % T.D
[5, 8]	Pre & post compaction-120 MPa and 200 MPa	50 % TD
[12]	500 MPa; stearic acid	53.8 % T.D

5.5.2 Studies on the sintering of nc-ThO$_2$

Both CS and TSS experiments were carried out with nc-ThO$_2$ powders (T$_C$13C: 317 MPa) derived through "volume combustion" (Table 5.7). Our results revealed that the "TSS$_2$" carried out at a final temperature of 1773 K, yielded a denser product as compared to TSS$_1$ (T$_C$13S$_1$) and CS (T$_C$13S$_{CS1}$ and T$_C$13S$_{CS2}$) (Table 5.7). Hence, these thoria compacts were sintered by using the "TSS$_2$ method" at a final sintering temperature of 1773 K (Table 5.7). Hence, thoria compacts were sintered by using the TSS at a final sintering temperature of 1773 K (TSS$_2$).

The ρ_S are presented in Fig. 5.10b and in Table 5.8. These were found to vary between 79.3 ± 0.2 % to 98.9 ± 0.3 % T.D. Harada et al. [25] obtained a ρ_S of 75 % T.D for the thoria powders derived through denitration. These authors compacted the thoria powders blended with stearic acid (binder) and CCl$_4$ (lubricant) at 138 MPa. The T00C powders are in fact powders derived through direct denitration. Our results show that the processing protocol used in this study resulted in a density more than that reported by Harada et al. [25], despite the fact that no binder or lubricant was used in our work. This highlights the fact that the "TSS$_2$" helps enhance the ρ_S. The dependence of the ρ_S of these two sets of powders set I and set II on the CP followed a trend quite opposite to that observed in the variation of ρ_G, i.e. $\rho_{S\ \mathrm{set\ II}} > \rho_{S\ \mathrm{set\ I}}$.

Table 5.7 Sintering parameters and ρ_S of ThO_2 (T_C13C; 317 MPa)

ρ_G	**CS_1** **(T_C13S_{CS1})**	**CS_2** **(T_C13S_{CS2})**	**TSS_1** **(T_C13S_1)**	**TSS_2** **(T_C13S_2)**
		% T. D.		
56.7 ± 0.0	95.8 ± 0.1	96.1 ± 0.1	96.6 ± 0.8	97.8 ± 0.3

CS_1 – 1673 K 4h **CS_2** - 1773 K 4h **TSS_1** Step 1 - 1873 K 30 min; Step 2 - 1673 K 4 h **TSS_2** Step 1 - 1873 K 30 min; Step 2 - 1773 K 4 h

Table 5.8 ρ_G and ρ_S of thoria pellets (sintered by using TSS_2 method)

CP (MPa)	**Density / (%T.D)***											
	T00C	**T00S_2**	**T_C5.5C**	**T_C5.5S_2**	**T_C13C**	**T_C13S_2**	**T_C17C**	**T_C17 S_2**	**T_C25C**	**T_C25S_2**	**T_C50C**	**T_C25S_2**
	ρ_G	**ρ_S**	**ρ_G**	**ρ_S**	**ρ_G**	**ρ_S**	**ρ_G**	**ρ_S**	**ρ_G**	**ρ_S**	**ρ_G**	**ρ_S**
60	59.0 ± 0.5	-	58.2 ± 0.9	84.9 ± 0.6	45.6 ± 0.7	94.8 ± 0.3	47.7 ± 0.2	95.4 ± 0.5	49.2 ± 0.7	93.5 ± 0.4	52.9 ± 0.5	83.5 ± 0.2
120	62.5 ± 1.3	79.3 ± 0.2	61.4 ± 0.5	89.5 ± 0.5	49.9 ± 0.3	97.8 ± 0.7	51.6 ± 0.3	95.9 ± 0.3	53.7 ± 0.5	94.2 ± 0.5	56.5 ± 0.6	88.4 ± 0.9
180	65.4 ± 0.4	80.6 ± 0.4	64.5 ± 0.6	91.1 ± 0.3	53.5 ± 0.3	97.9 ± 0.7	55.3 ± 0.2	97.4 ± 0.4	57.9 ± 0.5	95.8 ± 0.8	59.9 ± 0.2	90.7 ± 0.6
243	66.7 ± 0.3	82.6 ± 0.2	65.6 ± 0.7	92.2 ± 0.2	55.8 ± 0.5	**98.8 ± 0.3**	57.2 ± 0.4	97.6 ± 0.2	58.9 ± 0.5	96.5 ± 0.2	62.0 ± 0.3	92.2 ± 0.6
317	67.9 ± 1.4	83.8 ± 0.3	68.4 ± 0.5	92.5 ± 0.3	56.7 ± 0.3	**98.9 ± 0.3**	58.8 ± 0.5	**98.2 ± 0.7**	59.6 ± 1.1	96.7 ± 0.4	63.1 ± 0.9	95.3 ± 0.5
353	68.4 ± 0.2	84.9 ± 0.2	68.0 ± 0.1	93.1 ± 0.2	58.2 ± 0.6	**98.3 ± 0.7**	60.2 ± 0.2	97.6 ± 0.2	61.7 ± 0.3	96.9 ± 0.2	64.8 ± 0.2	95.5 ± 0.2

*represents the mean of five measurements

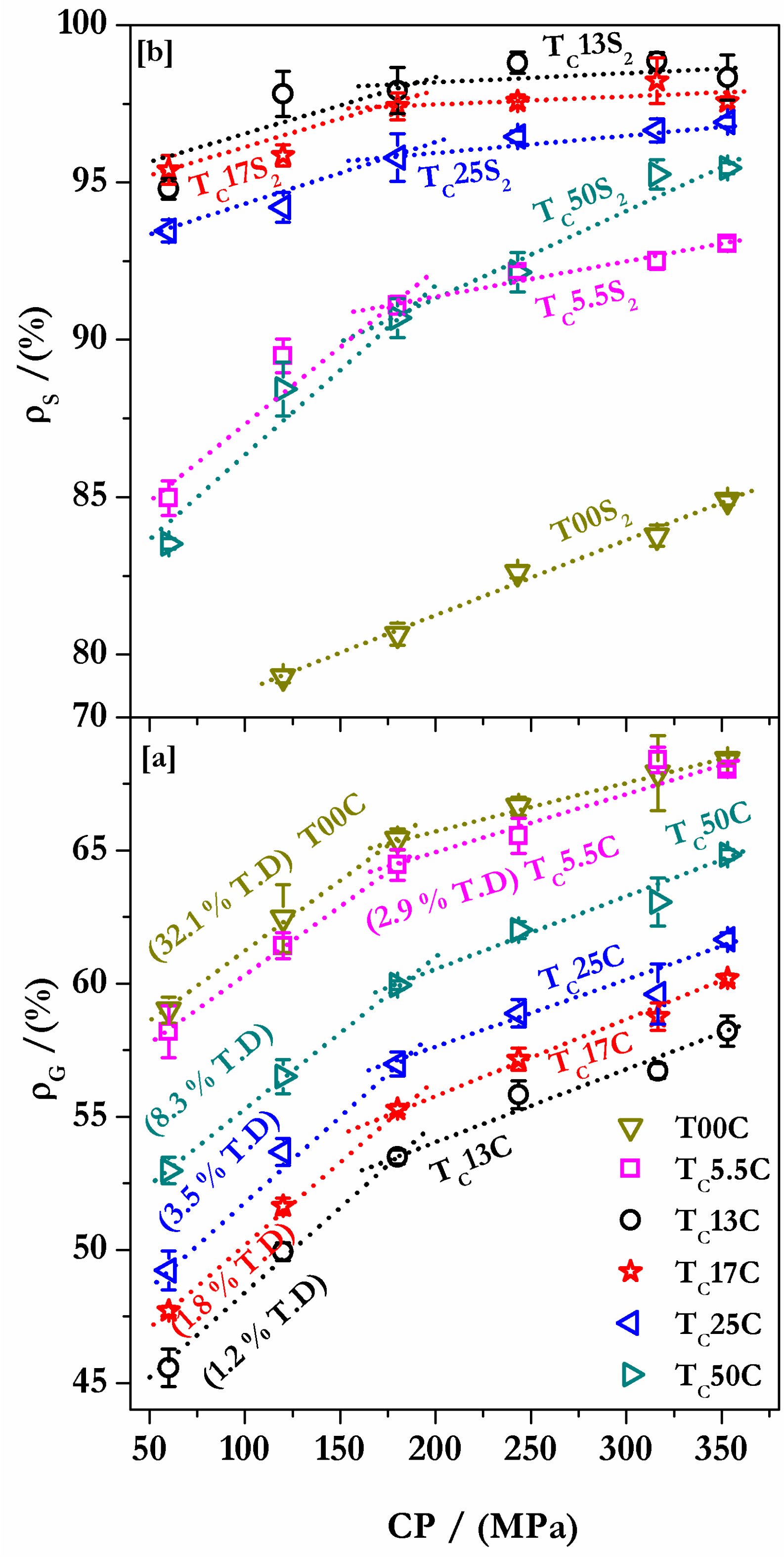

Figure 5.10 Variation of (a) ρ_G and (b) ρ_S with CP [ρ_B of the respective thoria powders are presented in parenthesis]

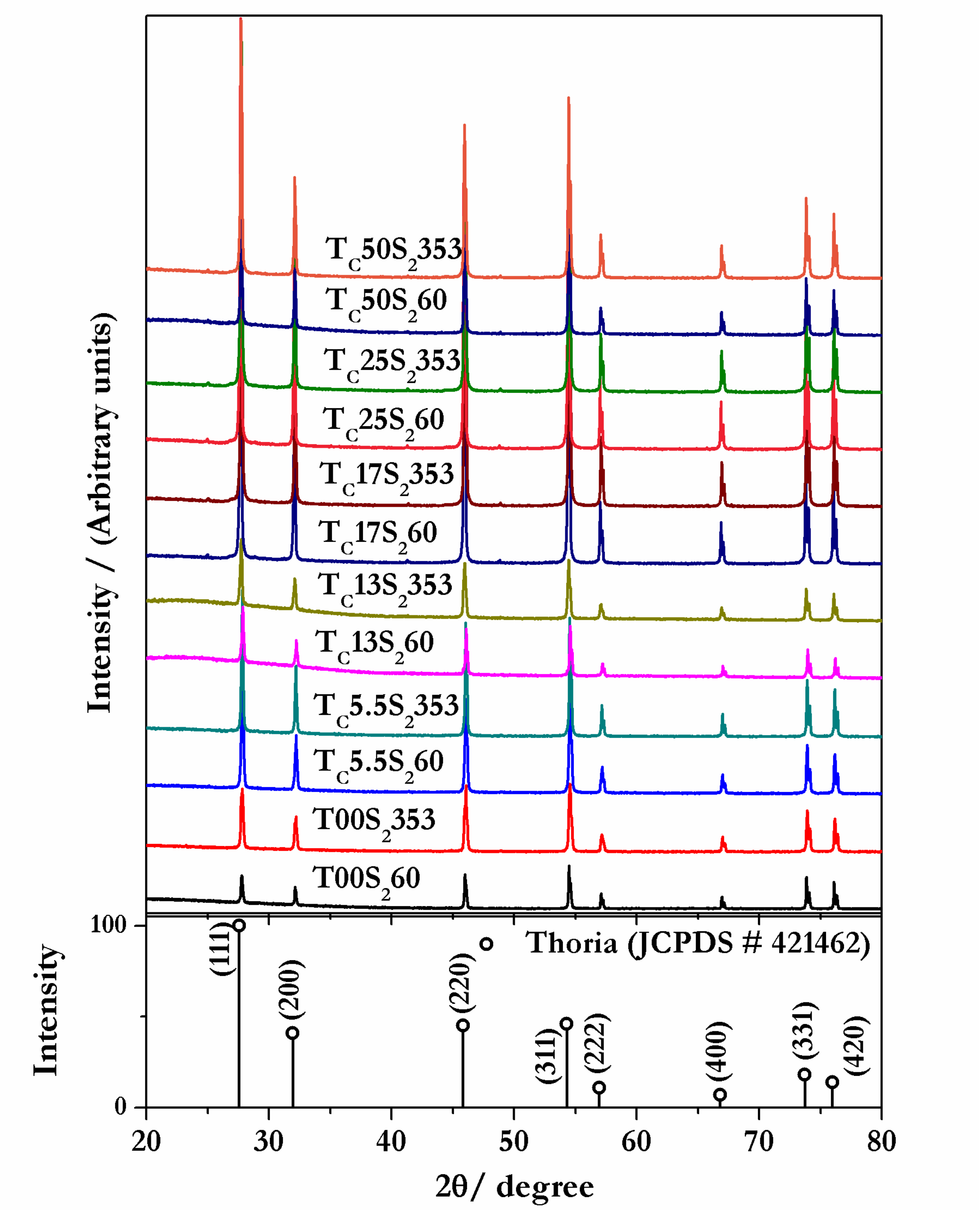

Figure 5.11 XRD patterns of some sintered thoria monoliths

The XRD patterns of sintered thoria monolith are presented in Fig. 5.11. ρ_S of T_C13C, T_C17C and T_C25C thoria monoliths varied from 93.5 ± 0.4 % to 98.9 ± 0.3 % T.D. A CP as low as 60 MPa was found to be sufficient to obtain high ρ_S. The ρ_S of the T_C13C compacts [243 MPa

(1773 K)] is marginally higher (98.8 ± 0.3 % T.D) than those obtained at 317 MPa [97.8 ± 0.3 % T.D (1773 K)]. This observation reveals that nc-ThO_2 could be sintered by the TSS method to just about the same density but by employing a lower CP. This is the highest ρ_S reported so far for citrate gel-combustion derived nc-ThO_2 powders. However, removal of 1-2 % porosity from these monoliths would be a challenging task. White et al. [18] obtained sintered monoliths whose densities ranged from 81.4 – 96 % T.D (276 MPa; 1923 K and He-6%H_2). Yayli et al. [24] sintered thoria monoliths of 96.0 % T.D (200 MPa; 1973 K 4 h and Ar-10% H_2). Purohit et al. [11] had reported a ρ_S of 97.0 % T.D (187 MPa; 1573 K 3h and air). However, these authors did not report detailed microstructural investigations of the sintered products obtained by them [1, 5, 8, 18, 23, 24].

Fig. 5.12 depicts the temperature dependence of the sintered densities of thoria, prepared through different routes reported in earlier investigations. From the data presented in Fig. 5.12 it is evident that the thoria derived ex-oxalate [23] when sintered by using CS yields only lower ρ_S (≈86 % T.D.). The results reported in refs. [1, 5, 8, 11, 26, 27] reveal that for sintered ThO_2, densities above 95 % T.D. could be obtained at temperatures as low as 1550 K. Ex-tannate powders [23], glycine combustion product [11], citrate gel-combustion derived powder [1] and ex-deagglomerated oxalate powders [5] of thoria have all yielded high densities. However, information on the microstructure of the sintered products obtained from them [5, 11, 23] is either limited or not available. Further, citrate gel-combustion derived powders when sintered beyond a certain threshold temperature could yield undesirably low densities owing to “run-away” sintering [8].

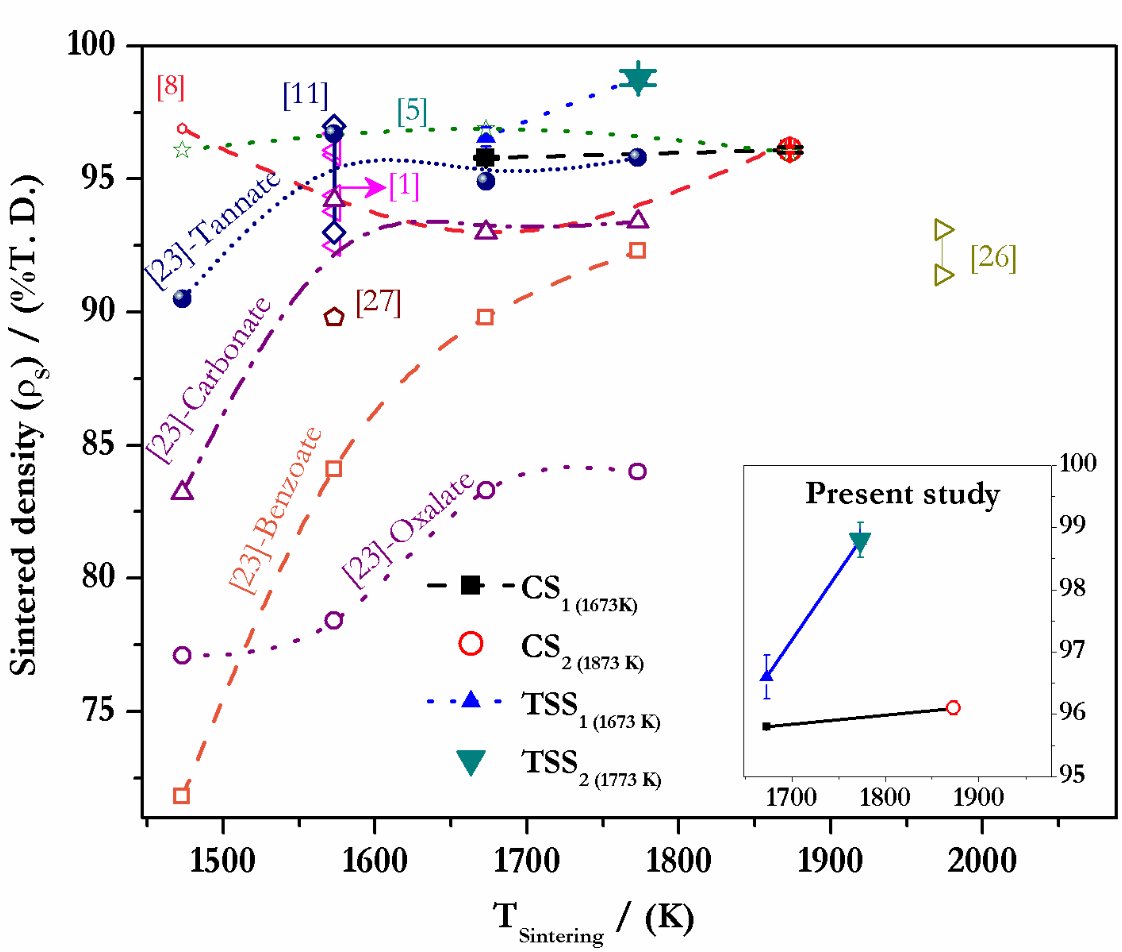

Figure 5.12 Effect of $T_{Sintering}$ on the ρ_S of ThO_2

Our investigations (1673 K) on the "TSS_2" of nc-UO_2 presented in Chapter 3, reveals that this technique yields a product with a high density and a desirable microstructure. Even though the results reported in refs. [1, 5, 8, 11, 26, 27] show high densities, the usefulness of these methods need to be reinvestigated for they do not provide information on the microstructure [1, 5, 8, 11, 26, 27] and temperature dependence [11] of the ρ_S. Our results on the "TSS_2" sintering of ThO_2 clearly indicate that the ρ_S reported in this study (98.8 ± 0.3 % T. D; 243 MPa) is the highest among the values reported so far at 1773 K. Further a monotonous increase in ρ_S is being reported for nc-ThO_2 for the first time when the final temperature is raised from 1673 to 1773 K.

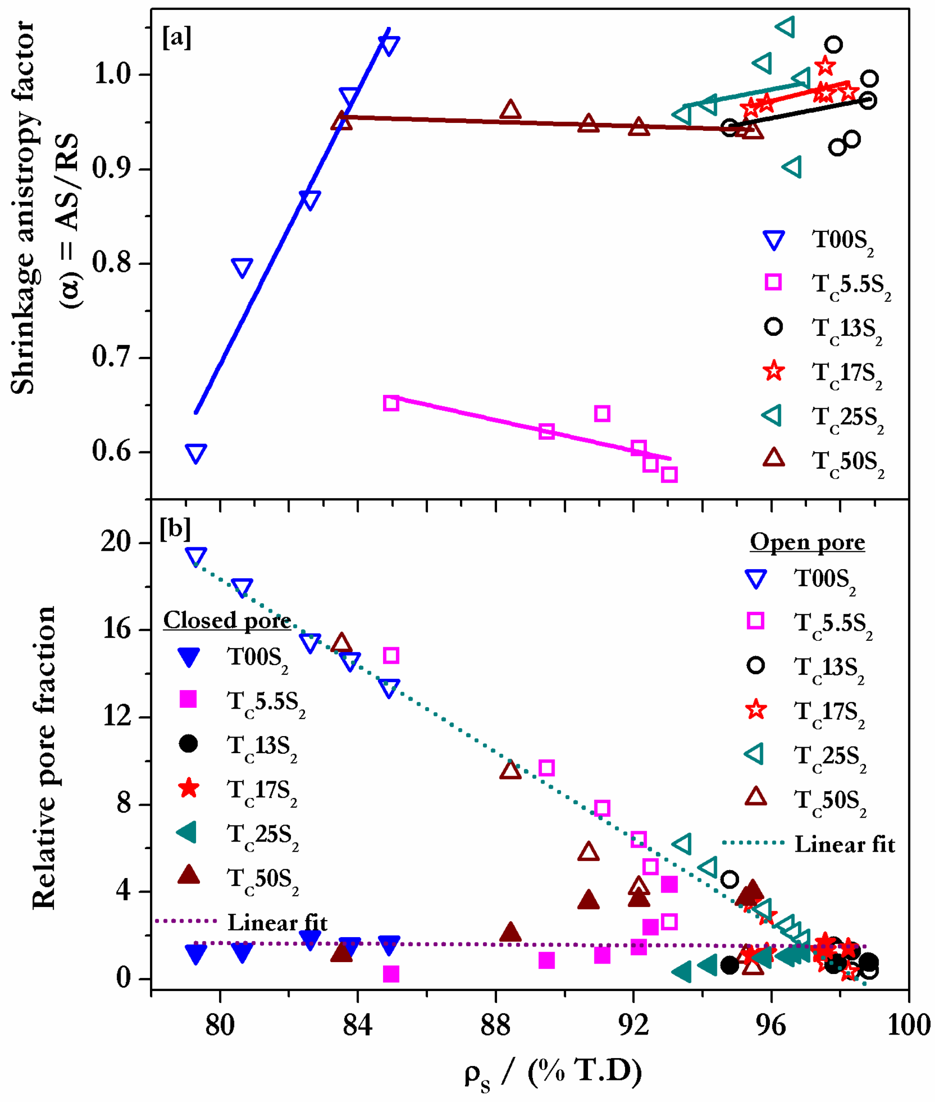

Figure 5.13 Dependence of a) shrinkage anisotropy factor (α) and (b) open and closed porosity on ρ_S in the sintered ThO_2 monoliths

The variation in the relative pore fraction (open and closed pore) and shrinkage anisotropy factor (α) [14] with the ρ_S is given in Fig. 5.13. Fig. 5.13a reveals that α is linearly correlated with the ρ_S. Further, the variation is less pronounced for the compacts made from T_C13C, T_C17C, T_C25C and T_C50C. This figure (Fig. 5.13) also reveals that T00C and T_C5.5C compacts exhibited differential densification while all other compacts showed uniform (isotropic) densification. These results are important from an industrial point of view to obtain defect free sintered bodies with near net shapes [14, 28]. As expected, the relative fraction of pores varies linearly with the ρ_S. This plot (Fig. 5.13b) also reveals that the relative pore fraction nearly becomes equal in all compacts when their ρ_S approaches 97 % T.D.

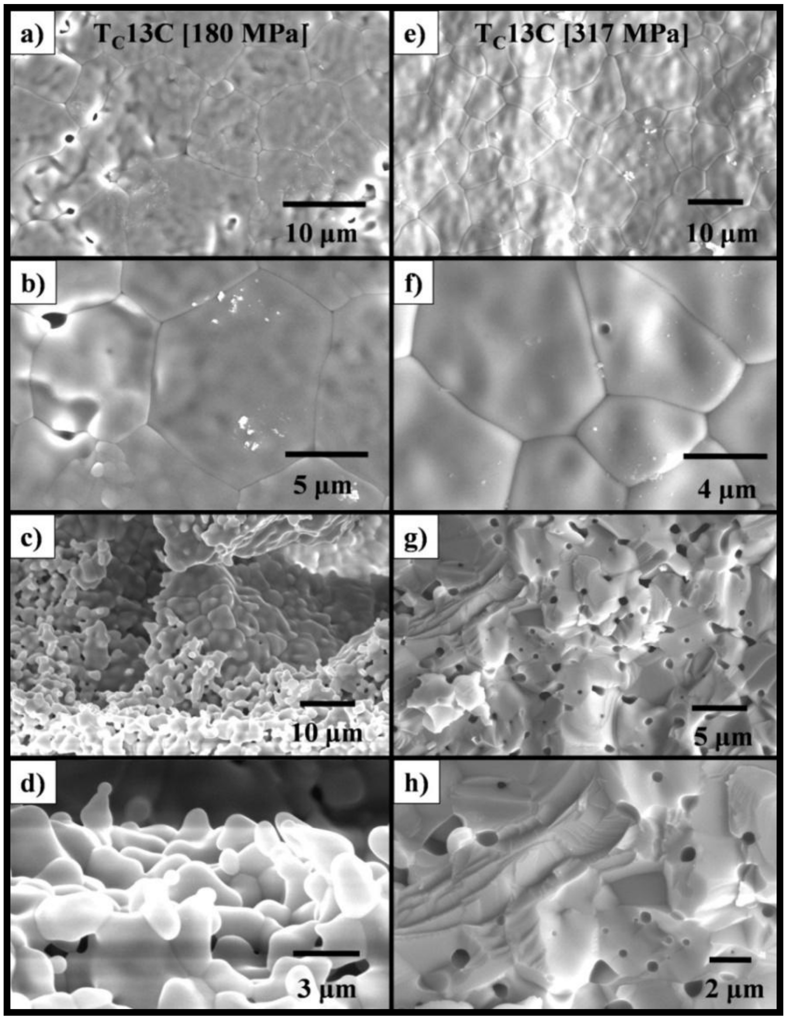

Figure 5.14 SEM images of sintered T_C13C pellets compacted at (a-d) 180 MPa and (e-f) 317 MPa [(a, b, e & f) sintered surface showing well defined grain boundaries and (c, d, g & h) fractured surface showing intra and intergranular pores]

5.5.3 Morphological analysis by using SEM

Microstructure of the sintered thoria monoliths are presented in Figs. 5.14-5.16. The SEM images reveal that these monoliths comprised uniform grains with well-defined grain boundary (faceted morphology) and near unimodal size distribution of grains with their size ranging between 6 – 15 µm. Surface morphology of the sintered thoria shows that majority of the grains possess pentagonal or hexagonal boundaries. Investigations of a fractured surface revealed the smaller grains submerged into the larger one (Ostwald ripening [29]) and that the grains in the fractured surface are also faceted.

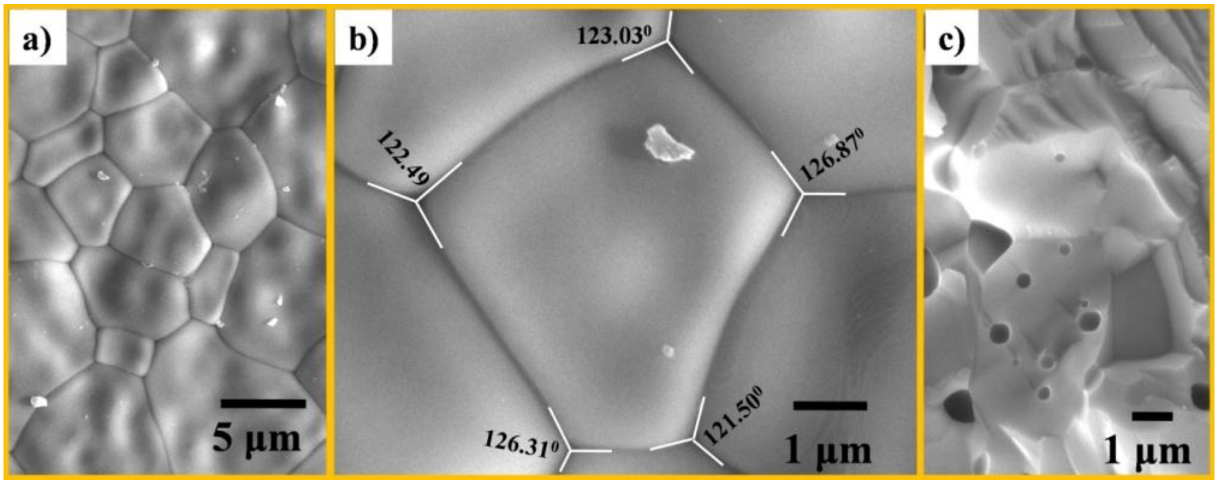

Figure 5.15 (a-c) SEM images of sintered pellets of thoria (TC13S$_2$-317 MPa); (a) pellet surface revealing faceted grains; (b) typical pentagonal grains revealing ≈121-127^0 dihedral angle and (c) Image of fractured surface revealing intra and intergranular pores

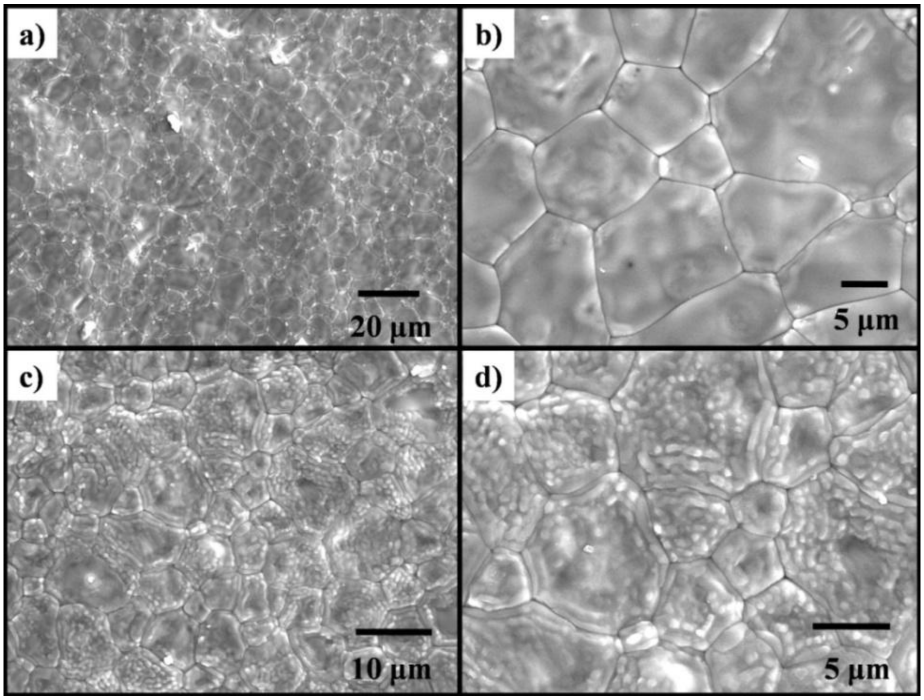

Figure 5.16 SEM images of sintered T$_C$13C pellets (353 MPa) (a) unpolished pellet surface revealing uniform grains; (b) high magnification image of pellet surface showing faceted grains; (c) low magnification image of the polished fractured surface showing uniform grains and (d) high magnification image of the fractured polished sintered surface showing well defined grain boundaries

5.6 Conclusions from the investigations on nc-ThO_2

Nc-ThO_2 powders were prepared by using citrate gel-combustion method in bulk quantities by varying the fuel to nitrate mole ratio (R = 0 to 0.50). The systematic dependence of the properties of nc-ThO_2 powders on R was investigated. It was observed that the ρ_B, SSA, PSD, XCS and lattice strain showed a systematic dependence on the R value. The combustion reaction in the mixture with an R value of 0.50 was investigated with DTA, DSC and mass spectrometry. Direct evidence for consumption of oxygen during combustion was observed for the first time. It was observed that the mixture with R values 0.13 and 0.17 exhibited vigorous and moderate volume combustion respectively. Microstructural investigations revealed that the volume combustion derived thoria powders were porous and comprised aggregates of nanograins. TEM investigation reaffirmed the nanocrystallinity. For the first time, EELS investigation was carried out on the nc-ThO_2 powders and the branching ratio (B) was calculated for both the "as prepared" and "calcined" powders. No evidence could be obtained for the existence of thorium in multiple oxidation states. TEM investigations also revealed that the nc-ThO_2 comprised unimodal grain size distribution with their size ranging between 6 - 16 nm with maxima at 10 nm.

It was observed that the volume combustion derived nc-ThO_2 powders were highly sinterable. A CP of 243 MP and TSS with a final sintering temperature of 1773 K is sufficient to sinter it to a ρS of 98.8 ± 0.3 % T.D for TC13C powders. Microstructural analysis of polished and thermally etched sintered thoria monoliths revealed that it comprised uniform faceted grains with well-defined grain boundaries. For the first time, α was estimated and it revealed that the ThO_2 compacts had undergone near isotropic shrinkage. This work describes a cost and energy efficient method for the production of high density pellets and small crucibles from nc-ThO_2.

References

[1] V. Chandramouli, S. Anthonysamy, P.R. Vasudeva Rao, J. Nucl. Mater. 265(3) (1999) 255-261.

[2] M. Bobtelsky, B. Graus, J Am Chem Soc 76(6) (1954) 1536-1539.

[3] A. Varma, A.S. Mukasyan, A.S. Rogachev, K.V. Manukyan, Chem. Rev. 116(23) (2016) 14493-14586.

[4] K.C. Patil, Chemistry of Nanocrystalline Oxide Materials: Combustion Synthesis, Properties and Applications, World Scientific Publishing Co. Pvt. Ltd., Singapore, 2008.

[5] K. Ananthasivan, S. Anthonysamy, A. Singh, P.R. Vasudeva Rao, J. Nucl. Mater. 306(1) (2002) 1-9.

[6] J.M. Pope, K.C. Radford, J. Nucl. Mater. 52(2) (1974) 241-254.

[7] T.J. Burke, Characterization of commercial thorium oxide powders (AWBA development program), West Mifflin, PA, USA, 1982.

[8] K. Ananthasivan, S. Balakrishnan, S. Anthonysamy, R. Divakar, E. Mohandas, V. Ganesan, J. Nucl. Mater. 434(1) (2013) 223-229.

[9] L. Wang, R. Zhao, X.-w. Wang, L. Mei, L.-y. Yuan, S.-a. Wang, Z.-f. Chai, W.-q. Shi, CrystEngComm 16(45) (2014) 10469-10475.

[10] V. Tyrpekl, J.-F. Vigier, D. Manara, T. Wiss, O. Dieste Blanco, J. Somers, J. Nucl. Mater. 460 (2015) 200-208.

[11] R.D. Purohit, S. Saha, A.K. Tyagi, J. Nucl. Mater. 288(1) (2001) 7-10.

[12] T. Pavelková, V. Čuba, E. de Visser-Týnová, C. Ekberg, I. Persson, J. Nucl. Mater. 469 (2016) 57-61.

[13] T. Yousefi, M. Torab-Mostaedi, H.G. Mobtaker, A.R. Keshtkar, J. Nucl. Mater. 479 (2016) 633-638.

[14] M.N. Rahaman, Sintering of Ceramics, CRC Press, Boca Raton, Florida, 2008.

[15] R. Chaim, R. Marder, C. Estournés, Z. Shen, Adv. Appl. Ceram. 111(5-6) (2012) 280-285.

[16] A. Mukhopadhyay, B. Basu, Int. Mater. Rev. 52(5) (2007) 257-288.

[17] V. Mote, Y. Purushotham, B. Dole, J. Theor. Appl. Phys. 6(1) (2012) 6.

[18] G.D. White, L.A. Bray, P.E. Hart, J. Nucl. Mater. 96(3) (1981) 305-313.

[19] S. Dash, A. Singh, P.K. Ajikumar, H. Subramanian, M. Rajalakshmi, A.K. Tyagi, A.K. Arora, S.V. Narasimhan, B. Raj, J. Nucl. Mater. 303(2) (2002) 156-168.

[20] M. Moeini, A. Malekzadeh, S.J. Ahmadi, M. Hosseinpour, Mater. Lett. 81 (2012) 99-101.

[21] K.T. Moore, Micron 41(4) (2010) 336-358.

[22] G. van der Laan, K.T. Moore, J.G. Tobin, B.W. Chung, M.A. Wall, A.J. Schwartz, Phys. Rev. Lett. 93(9) (2004) 097401.

[23] V.K. Moorthy, A.K. Kulkarni, T. Indian Ceram. Soc. 22(4) (1963) 116-129.

[24] A. Yayli, S. Kırtay, E. Oktay, A. Van, M.T. Aybers, L. Çolak, Key Eng. Mater. 264-268 (2004) 305-308.

[25] Y. Harada, Y. Baskin, J.H. Handwerk, J. Am. Ceram. Soc. 45(6) (1962) 253-257.

[26] P. Balakrishna, B.P. Varma, T.S. Krishnan, T.R.R. Mohan, P. Ramakrishnan, J. Nucl. Mater. 160(1) (1988) 88-94.

[27] V. Chandramouli, S. Anthonysamy, P.R. Vasudeva Rao, R. Divakar, D. Sundararaman, J. Nucl. Mater. 231(3) (1996) 213-220.

[28] R. Chaim, M. Levin, A. Shlayer, C. Estournes, Adv. Appl. Ceram. 107(3) (2008) 159-169.

[29] H.G. Yang, H.C. Zeng, J. Phys. Chem. B 108(11) (2004) 3492-3495.

Chapter 6

Synthesis, Conventional Sintering and SPS of nanocrystalline Yttria

This chapter describes the experiments on the VCR in the citrate gels containing the $Y(NO_3)_3$ *and the studies on the sintering of nc-*Y_2O_3 *derived by using this reaction.*

6.1 Starting material

Yttrium nitrate was used as such. The starting materials used in the preparation of the combustion mixtures were devoid of impurities that would significantly alter the characteristics of the gel-combustion derived powders.

6.2 The combustion reaction

VCR was observed in the mixtures containing yttrium nitrate with an R value of 0.17. The plausible reaction pertaining to the VCR in the preparation of Y_2O_3 is given in Eqn. (6.1).

$$2Y(NO_3)_3 + C_6H_8O_7 + 3O_2 \rightarrow Y_2O_3 + 6NO_2 + 6CO_2 + 4H_2O \quad (6.1)$$

6.3 Powder characterization

ρ_B of all the “as prepared” yttria powders were lower than that of their “calcined” counterparts (Table 6.1). Upon calcination the yttria powders showed a significant increase (300 %) in the ρ_B which were comparable to those reported in earlier investigations [1, 2].

Size distribution of particles in the “as prepared” and “calcined” powders of yttria is presented in the Fig. 6.1 and in Table 6.2. From these data it is evident that the “as prepared” powders comprised particles with lower size as compared to the calcined products derived from them. The influence of the relative distribution of size fractions on the ρ_B of nc-UO_2 has been explained in chapter 3. A similar trend is observed among nc-Y_2O_3 as well.

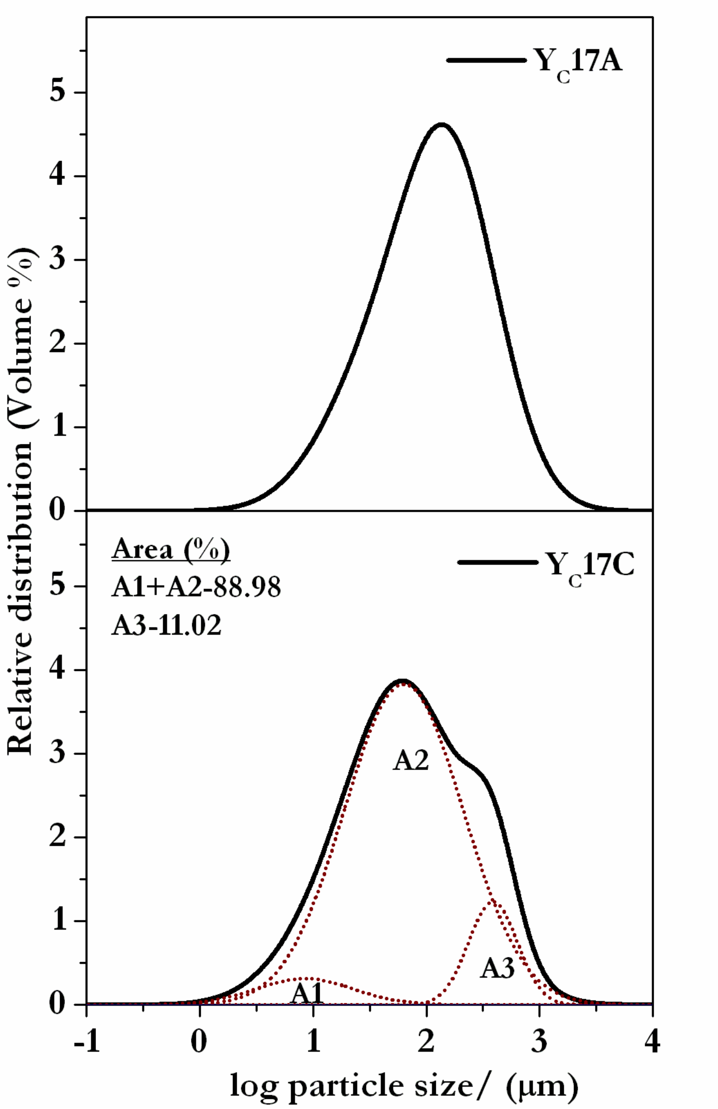

Figure 6.1 Distribution of sizes among particles in the "A" and "C" yttria powders (Thick solid lines – experimental curve, thin solid line – deconvoluted curves)

The size distribution of particles in the calcined powders was nearly bimodal and comprised a larger fraction of the fines (below 100 μm) than their "A" precursors. The latter exhibited a nearly unimodal distribution. Thus the presence of fines would have helped increase the ρ_B of the calcined yttria powders. The SSA values of the "A" powders were higher as compared to that of the "C" powders derived from them. Hence, it is evident that calcination leads to a reduction in the SSA and porosity due to grain coarsening. It is observed that the values of the ρ_B and SSA are inversely correlated.

Table 6.1 Characteristics of the nc-yttria powders derived through VCR

Sample	R	ρ_B (% T. D)	RC (ppm)	SSA (m^2g^{-1})	XCS Sc (nm)	XCS HW (nm)	XCS Strain x 10^{-3}
Y_C17A	0.166	0.6	1350	57	12	13	1.02
Y_C17C	0.166	1.8	621	24	18	19	0.15

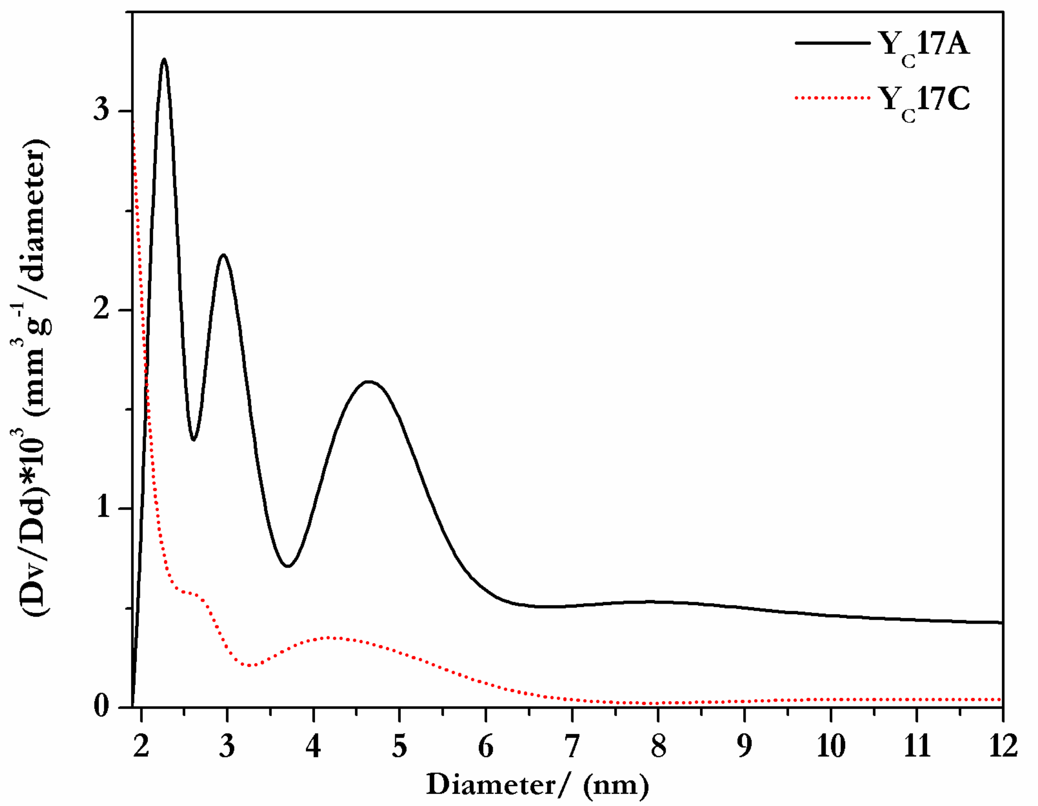

Figure 6.2 Size distribution of pores in nc-yttria powders

Table 6.2 Size distribution among particles and porosity in nc-yttria powders

Sample	Particle size distribution (Vol %) 10 vol. % of sample has size less than (μm)	50 vol. % of sample has size less than (μm)	90 vol. % of sample has size less than (μm)	Average size of the pore (nm)	Maximum size of the pore (nm)	Specific pore volume (mm^3g^{-1})
Y_C17A	12	68	275	2.27	5.4	71
Y_C17C	11	64	364	1.89	2.1	36

Size distribution of pores in Y_2O_3 (Fig. 6.2) powders derived by using the BET N_2 adsorption isotherm are presented in Table 6.2. The specific pore volume of these powders was found to vary from 34 mm^3g^{-1} to 71 mm^3g^{-1}, and it decreased by a factor of 2 upon calcination (Y_2O_3: 71 mm^3g^{-1} to 36 mm^3g^{-1}). These observations further substantiate the fact that pore elimination and grain coarsening take place during calcination.

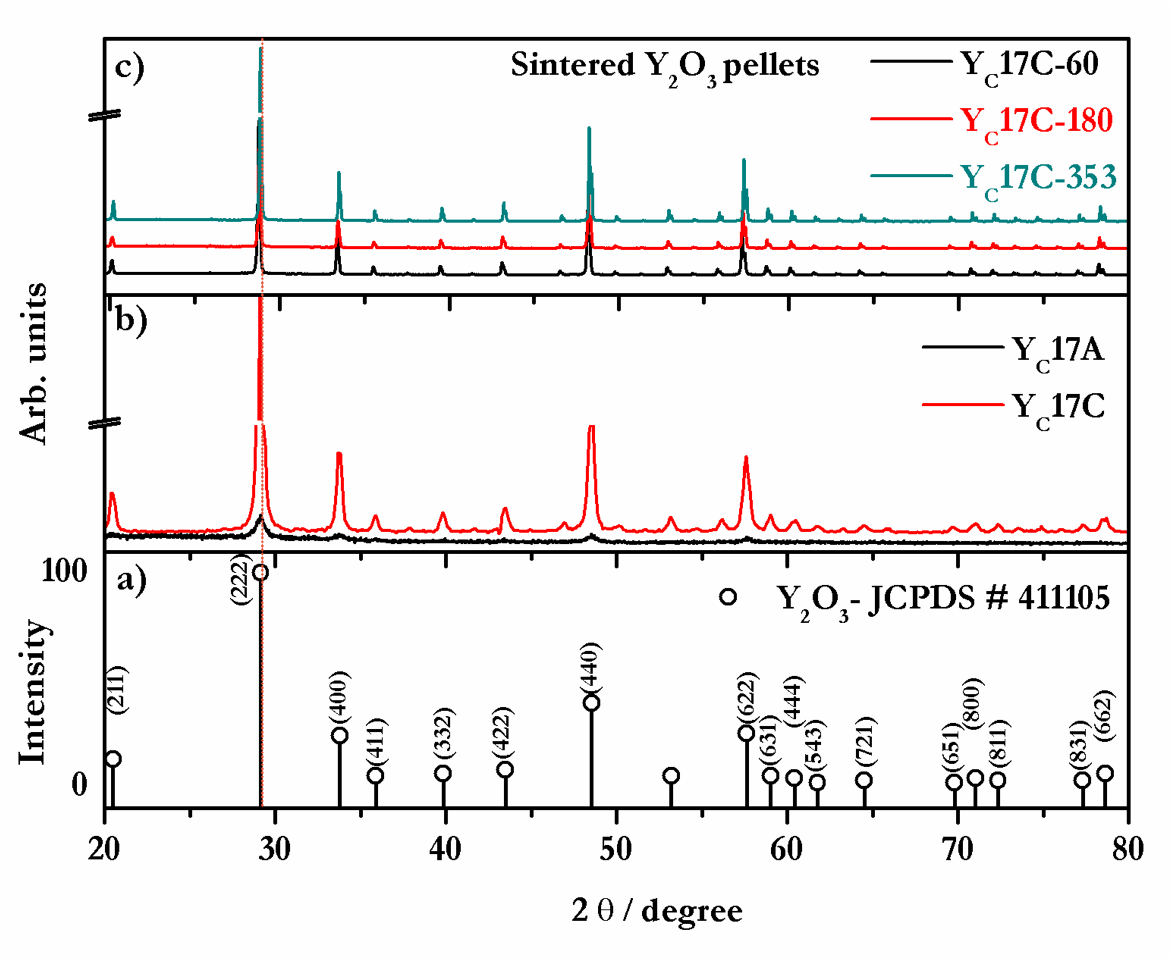

Figure 6.3 XRD of yttria a) JCPDS pattern [# 411105]; b) "A" and "C" volume combustion derived powders and c) sintered yttria monoliths

The XRD patterns of the powders are presented in the Fig 6.3. The "A" powders were found to possess crystallites with a mean size of about 13 nm. Upon calcination these crystallites grew to about 19 nm. The lattice strain in the "A" powders, estimated by the HW method [3] was found to decrease by a factor of 7 (Table 6.1) after calcination. It was observed that the error (due to the strain component) in the estimates of the crystallite size obtained by the Sc method was rather insignificant. This observation is quite different than the trends observed in the XCS of nc-urania [Chapter 3] derived through citrate gel-combustion. Probably the precipitation of U_3O_8 and its conversion back into UO_2 would have induced a higher lattice strain in the latter. It is evident from the data presented in Table 6.1 that the “A” powders had a higher carbon residue, than the “C” powders.

6.4 Microstructural investigations on nc-Y_2O_3 powders

The SEM images of the “A” powders are presented in Fig. 6.4. These images show that these powders comprise irregular agglomerates. An image of the “A” yttria powder at a higher magnification confirms the presence of nano pores. The TEM images also confirm the same (Fig. 6.5). Microstructural characterization (TEM) of volume combustion derived Y_2O_3 powders further ascertained that these powders comprised grains of uniform size in the nano regime (20 – 30 nm). SAED patterns confirmed both their size and nanocrystallinity (Figs. 6.5a-6.5c). HRTEM images (Fig. 6.5d and 6.5f) of these samples depict the values of the “d” spacings that are in agreement with the standard values cited in JCPDS [Y_2O_3 – 00-41-1105].

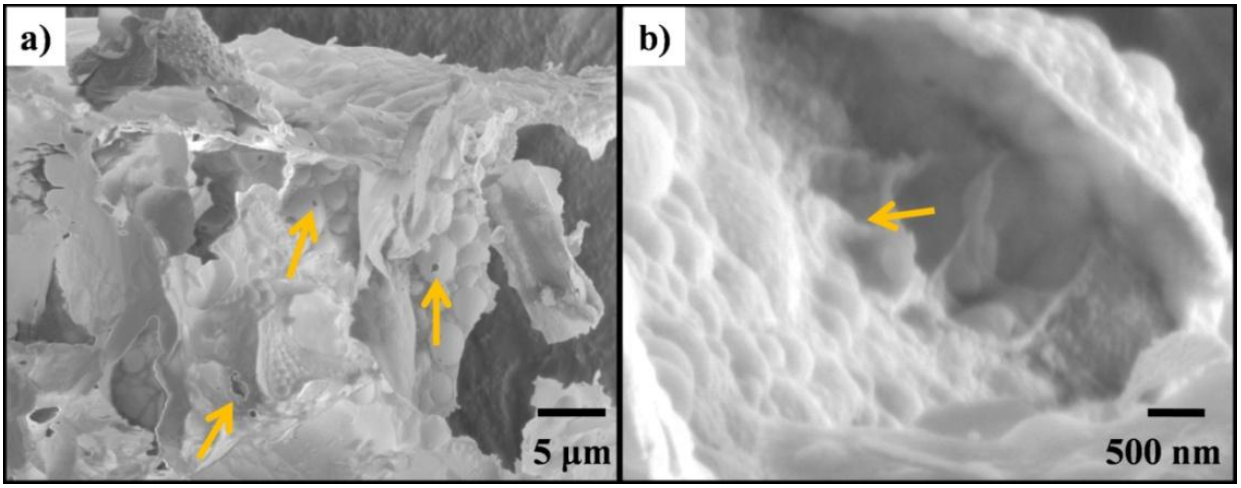

Figure 6.4 SEM images of powders a) and b) “as-prepared” Y_2O_3 powders (Y_C17A)

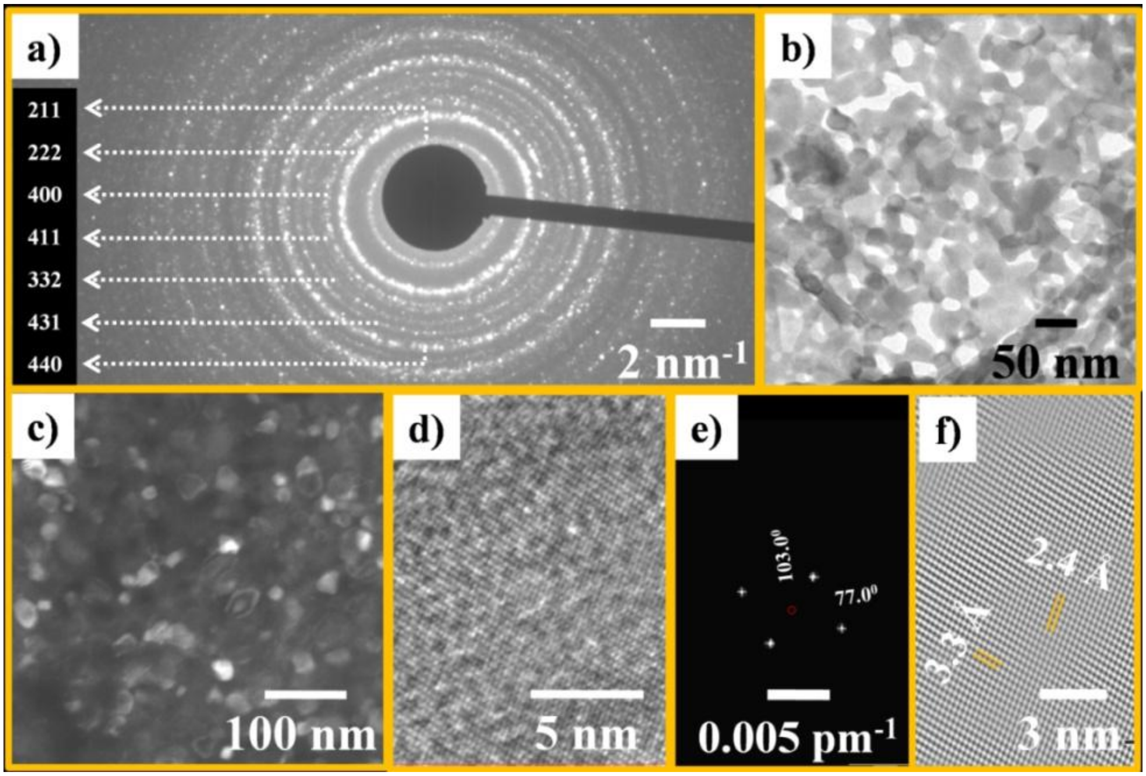

Figure 6.5 TEM images of Y_C*17A powders: (a) SAED image; (b) bright field image revealing nano grains; (c) dark field image revealing nano grains; (d) HRTEM image of nano grain within the selected area; (e) FFT image and (f) filtered IFFT image*

6.5 Compaction and sintering of nc-Y_2O_3

6.5.1 Green density (ρ_G)

The dependence ρ_G of the nc-Y_2O_3 powders on the CP was studied to optimize the compaction process (Fig. 6.6a). The ρ_G verses CP plot of yttria could be divided into two linear regions. In the "first region" from 60 – 180 MPa a linear correlation between ρ_G and CP was observed. Beyond this CP there was no significant increase in the ρ_G with the CP. These experiments revealed that a ρ_G of about 54 % T.D. could be obtained at a pressure of 317 MPa (Y_2O_3), which was used to prepare the pellets for sintering.

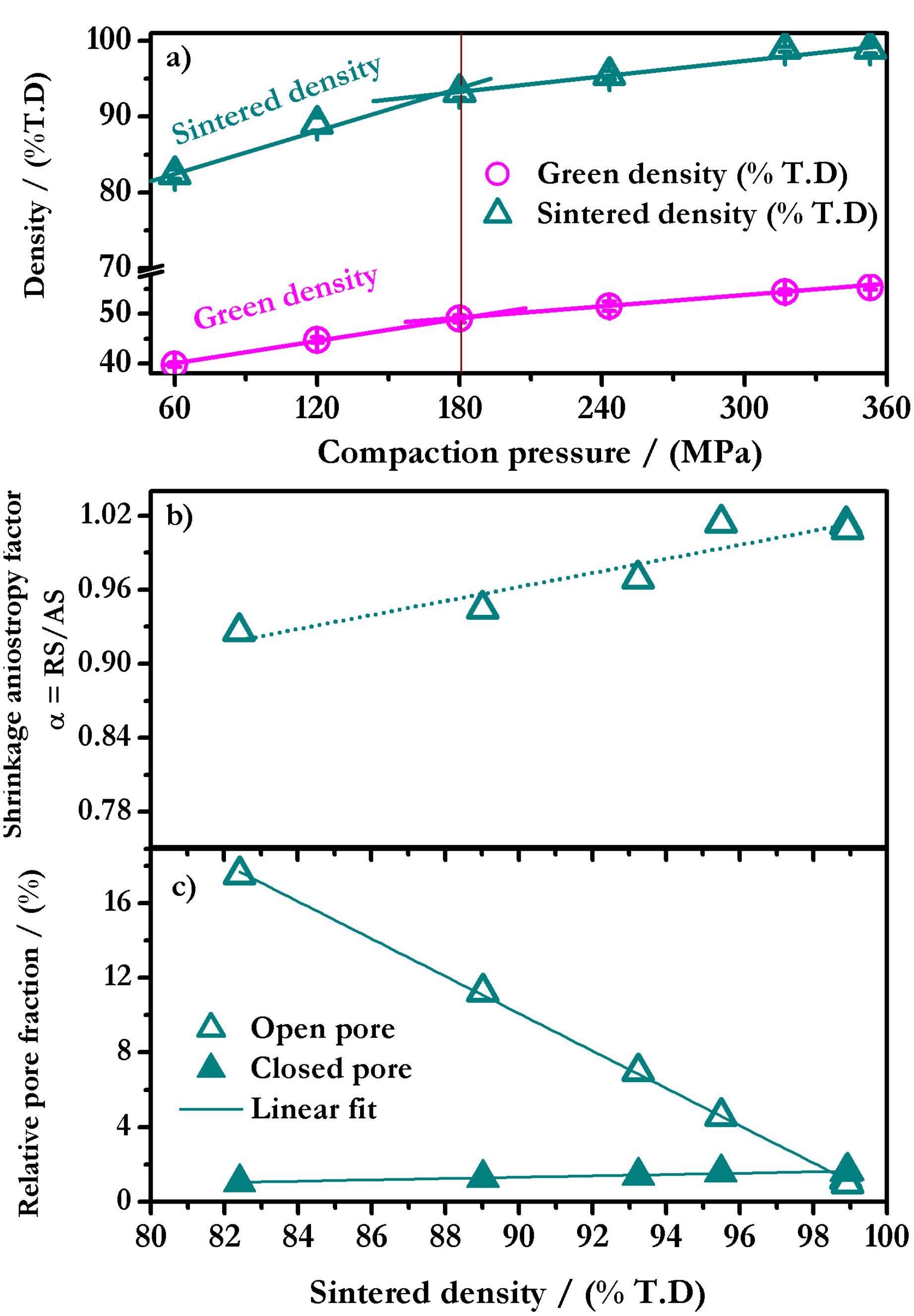

Figure 6.6 (a) variation of ρ_G and ρ_S with the CP; (b) dependence of shrinkage anisotropy factor (α) with the ρ_S and (c) dependence of open and closed pore fraction with the sintered density

6.5.2 Sintering of nc-Y_2O_3

Tables 6.3-6.4 depict the characteristics of the compacts. The data presented in Table 6.3 reveals that the "TSS^Y_1" sintering leads to a better densification as compared to that of CS (CS^Y_1

and CS^{Y}_{2}). It is interesting to note that in the "TSS^{Y}_{1}" method, a final temperature as low as 1673 K is sufficient to obtain a ρ_S of 98.9 % T. D. Hence, Y_2O_3 compacts were sintered by using the TSS_1 at a final sintering temperature of 1673 K. The variation of ρ_S with the CP reveals two regions (separated at 180 MPa) and in both these regions the ρ_S is linearly correlated with the CP. A maximum ρ_S of about 98.9 % T. D was obtained at 317 MPa and 353 MPa which indicates that a CP of 317 MPa is sufficient to obtain yttria monoliths of 99 % T. D (grain size < 3 μm). It was also observed that the shrinkage anisotropy factor (α) [4] and relative pore fraction are linearly correlated with the compaction pressure (Fig. 6.6).

Table 6.3 Sintering parameters and ρ_S of Y_2O_3 (Y_C17C; 317 MPa)

ρ_G	**CS^{Y}_{1}** Y_C13S_{CS1}	**CS^{Y}_{2}** Y_C13S_{CS2}	**TSS^{Y}_{1}** Y_C13S_1	**TSS^{Y}_{2}** Y_CXXS_2
		% T. D		
54.4 ± 0.4	98.2 ± 0.4	98.3 ± 0.1	98.9 ± 0.1	98.4 ± 0.4

CS^{Y}_{1} – 1673 K 4h **CS^{Y}_{2}** - 1773 K 4h **TSS^{Y}_{1}** Step 1 - 1873 K 30 min Step 2 - 1673 K 4 h **TSS^{Y}_{2}** Step 1 - 1873 K 30 min Step 2 - 1773 K 4 h

Table 6.4 Characteristics of yttria compacts

P (MPa)	**ρ_G (% T.D)**	**ρ_S (% T.D)**
60	39.8 ± 0.5	82.4 ± 0.6
120	44.7 ± 0.5	89.0 ± 0.8
180	49.0 ± 0.7	93.2 ± 0.8
243	51.5 ± 0.9	95.5 ± 0.5
317	54.4 ± 0.4	98.9 ± 0.3
353	55.4 ± 0.5	98.9 ± 0.6

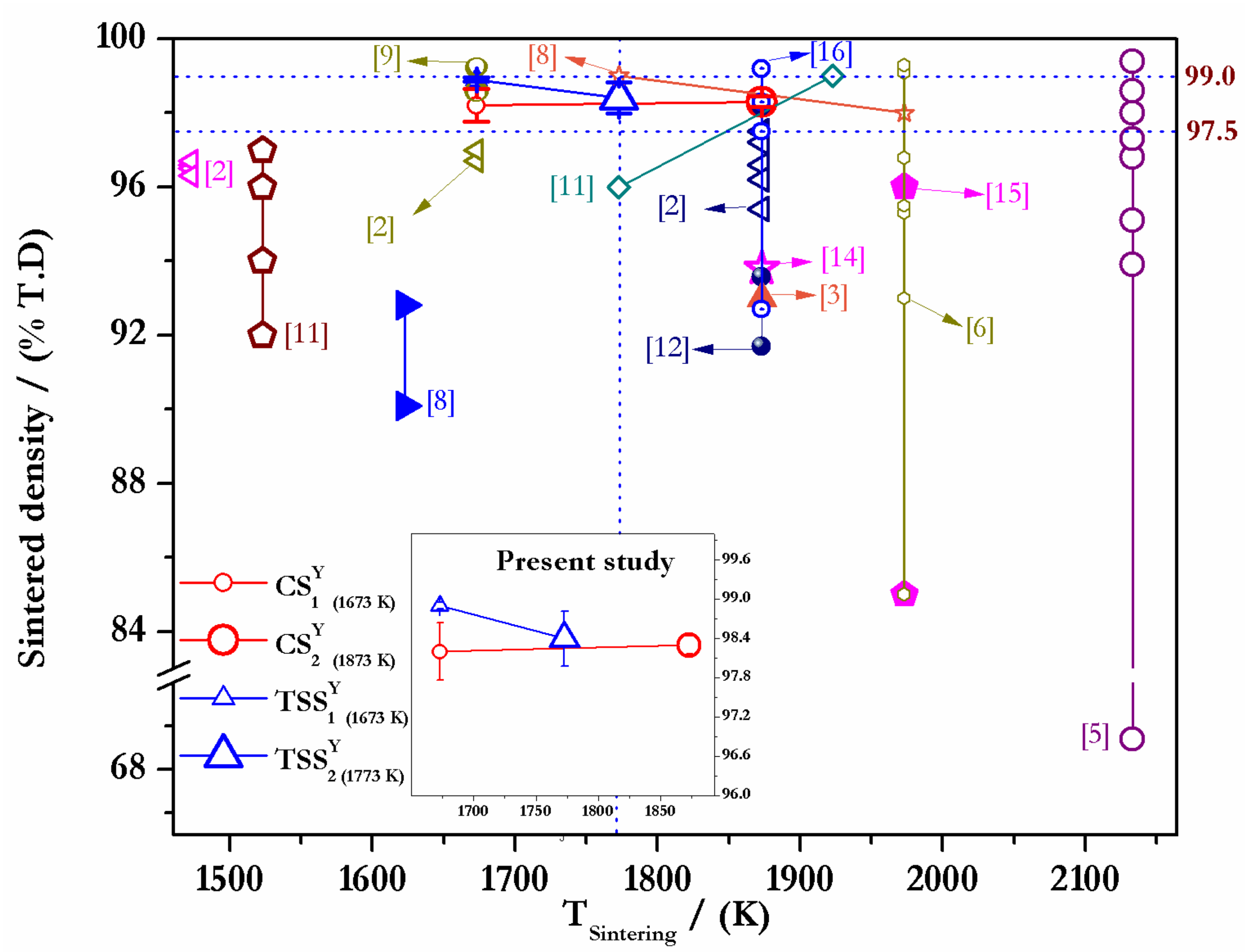

Figure 6.7 Dependence of the sintered density of Y_2O_3 with the sintering temperature ($T_{Sintering}$)

Fig. 6.7 depicts the temperature dependence of the ρ_S of yttria prepared through different routes reported in earlier investigations [2, 5-16]. From the data presented in this Fig. 6.7 it is evident that sintering of yttria by the conventional method yields samples with a lower ρ_S. These powders could be sintered to full density by doping aliovalent cations in yttria [8, 12], vacuum sintering at high temperature [10] or by using hot isostatic pressing [6]. But these methods require either deliberate addition of impurities or are energy intensive. However, recent studies have revealed that yttria could be sintered to very high densities (≤ 97 % T. D.) by tailoring the methods used for both the powder preparation [6, 17] as well as sintering [8, 17, 18]. Fig. 6.8 shows the SEM images of the sintered pellets.

In the present study, we have also reaffirmed that CS could also be used to sinter Y_2O_3 to a high density but elimination of the final residual porosity (1-2 %) is extremely difficult. From Fig. 6.6 and Fig. 6.7 it is evident that the TSS method yields highly sintered products (99 % T.D) at a sintering temperature as low as 1673 K. Upon increasing the final temperature to 1773 K the ρ_S was found to decrease marginally to 98.4 % T. D.

Table 6.5 Comparison of ρ_S of yttria monoliths reported in the literature

Ref.	Method	Sintering temperature / Condition	ρ_S (% T. D)
[12]	glycine gel-combustion	1873 K / Air	98.2
[5]	precipitation	2133 K / Vacuum	99.4
[9]	glycine gel-combustion	1673 K / Air	99.0
[10]	yttrium carbonate	1873 K / Vacuum	99.0
[16]	yttrium carbonate	1873 K / Air	99.2

From the data presented in Table 6.5, it is evident that yttria powders were sintered at temperature higher than 1673 K in earlier investigations [5, 9, 10, 12, 16]. Further, the spread in the values of ρ_S of yttria observed in the present study is quite insignificant as compared to those cited in earlier investigations [6, 9, 12]. The preparation method presented here is amenable for scale-up. In addition owing to the reduced quantities of fuel (citric acid) employed, the sintered product has only insignificantly low amounts of carbon residue.

6.5.3 Spark plasma sintering of nc-Y_2O_3

Calcined VCR derived nc-Y_2O_3 powder was used as such without any further processing step in the SPS studies. Nc-Y_2O_3 powders were sintered at 1873 K at a heating rate of 100 K min^{-1} and 50 MPa. These pellets were calcined in air at 1873 K for 1 h to remove the graphite adhering to their surface and were subjected to further analysis viz., phase identification, densification and microstructural investigation. XRD pattern pertaining to the spark plasma sintered pellets revealed that they comprised c-Y_2O_3 and that the carbon residue in the sintered compacts after annealing in air at 1673 K for 1 h was found to be 647 ppm (Table 6.6).

Table 6.6 Sintered density of yttria monolith derived through SPS

Material	**Sample Index**	**Initial phase composition**	**Heating rate (K min^{-1})**	**ρ_S (% T. D)**	**RC (ppm)**	**T_s**
Y_2O_3	Y_C17C	c	100	99.3 ± 0.2	647	1873 K 7 min

c – cubic and T_s - Sintering schedule

Table 6.7 Comparison of ρ_S of yttria monoliths derived by using SPS with the reported values in the literature

Ref.	**Method**	**TS / time / pressure (MPa)**	**ρ_S (% T. D)**	**Average grain size (µm)**
[19]	commercial nc-Y_2O_3	1673 K/ 5 min / 100	98.5	4
		Above 1673 K	93 - 94	5 – 6
[20]	commercial nc-Y_2O_3	923 K / - / 83	-	0.10
		1123 K / - / 83	-	0.50
		1123 K / - / 83	-	0.7
		1873 K / - / 83	98	-
[21]	hydrothermal	1773 K /- /100	99.6	1 - 1.12
[22]	commercial Y_2O_3/ ball milled	1473 K to 1873 K / - / 100	98 - 99	0.24 - 2

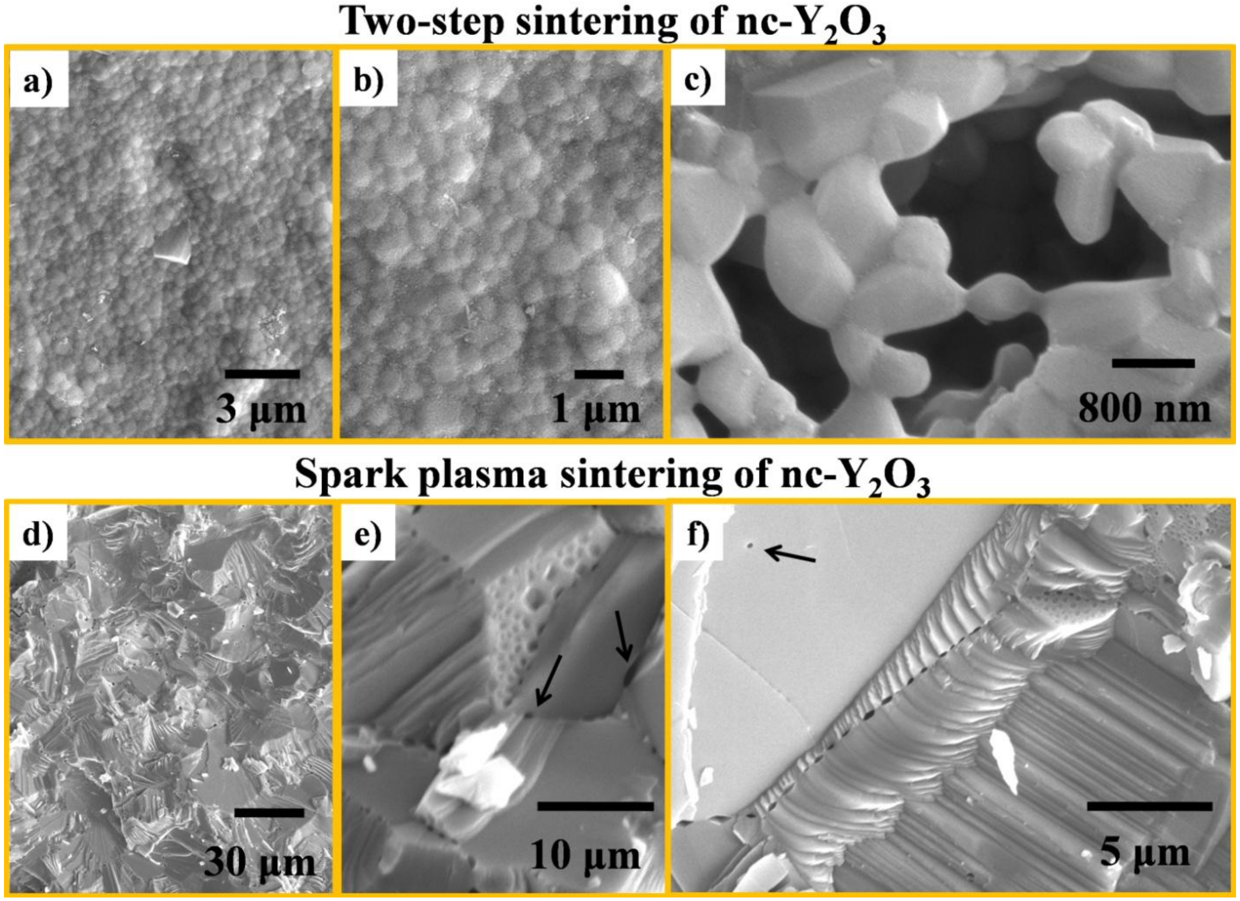

Figure 6.8 *SEM images of sintered pellets of yttria (a-c)TSS*$_1$ *and (d-f) SPS; (a) pellet surface revealing fine grains, (b) high magnification image of pellets surface revealing nearly uniform grains, (c) Image of fractured pellet surface, (d) low magnification image of fractured pellet surface, (e) high magnification images of fractured pellet surface revealing entrapped closed pores and (e) high magnification images of fractured pellet surface revealing isolated pore and intragranular cracks*

The ρ_S of this compact was found to be 99.3 ± 0.2 % T.D (Table 6.6). Visual examination of this compact did not reveal any defects viz., cracks or hour glassing. Many authors (Table 6.7) had derived nc-Y_2O_3 powders by using different method (hydrothermal method, precipitation, etc.) and had sintered these powders by using SPS with different sintering schedules. However, no reports so far been published in the literature pertaining to SPS of nc-Y_2O_3 powders derived through citrate gel VCR.

Thus, from the foregoing discussion it is evident that the ρ_S of the yttria monoliths derived in this study by SPS are comparable to those reported in the literature (Table 6.7).

Microstructural investigation of the SPS monoliths of nc-Y_2O_3, (SEM) had revealed that the compacts had undergone uniform densification with no visible pores. However, higher magnification images of fractured surface revealed the presence of closed pores. These images also revealed that grains are faceted and had a typical size ranging from 6-12 μm. Further optimization is required to obtain nanostructured (grain size < 1 μm) monoliths.

6.6 Conclusions drawn from the investigations on nc-Y_2O_3

It was demonstrated for the first time that VCR takes place in mixtures containing yttrium nitrate with citric acid with an R value of 0.17. The powders derived through VCR were found to be nanocrystalline, fine grained and highly porous (60 - 70 mm^3g^{-1}).

All the powders comprised nc aggregates. It was demonstrated that the ρ_B, SSA, PSD, XCS and the morphology of these powders were unique as compared to the powders derived through other methods reported in the literature [2, 5-16]. Microstructural analysis of the “A” powders carried out by using TEM confirmed the presence of nc c-Y_2O_3. Both TEM and SEM investigations revealed that these powders possessed nano pores.

The calcined products were found to be highly sinterable. It was demonstrated that Y_2O_3 pellets with a density as high as 98.9 % T. D. could be produced by using the “two-step sintering” method (TSS^{Y}_{1}) at a final temperature as low as 1673 K. Shrinkage anisotropy factor (α) and relative pore fraction of sintered Y_2O_3 were linearly correlated with the compaction pressure. Similarly, it was observed that citrate gel-combustion derived nc-Y_2O_3 could be sintered to a density of 99.3 % T. D by using SPS (1873 K 7 min; 50 MPa and grain size: 6-12 μm).

References

[1] S. Balakrishnan, K. Ananthasivan, K.C. Hari Kumar, Ceram. Int. 40(5) (2014) 6777-6785.

[2] S. Balakrishnan, K. Ananthasivan, K.C. Hari Kumar, Ceram. Int. 41(4) (2015) 5270-5280.

[3] V. Mote, Y. Purushotham, B. Dole, J. Theor. Appl. Phys. 6(1) (2012) 6.

[4] M.N. Rahaman, Sintering of Ceramics, CRC Press, Boca Raton, Florida, 2008.

[5] M.D. Rasmussen, G.W. Jordan, M. Akinc, O. Hunter, M.F. Berard, Ceram. Int. 9(2) (1983) 59-60.

[6] A. Dupont, A. Largeteau, C. Parent, B. Le Garrec, J.M. Heintz, J. Eur. Ceram. Soc. 25(12) (2005) 2097-2103.

[7] S.V. Chavan, K.T. Pillai, A.K. Tyagi, Mater. Sci. Eng. B 132(3) (2006) 266-271.

[8] H.R. Khosroshahi, H. Ikeda, K. Yamada, N. Saito, K. Kaneko, K. Hayashi, K. Nakashima, J. Am. Ceram. Soc. 95(10) (2012) 3263-3269.

[9] W.-J. Kim, J.Y. Park, S.J. Oh, Y.S. Kim, G.-W. Hong, I.-H. Kuk, J. Mater. Sci. Lett. 18(5) (1999) 411-413.

[10] N. Saito, S.-i. Matsuda, T. Ikegami, J. Am. Ceram. Soc. 81(8) (1998) 2023-2028.

[11] A.L. Micheli, D.F. Dungan, J.V. Mantese, J. Am. Ceram. Soc. 75(3) (1992) 709-711.

[12] R.V. Mangalaraja, S. Ananthakumar, J. Mouzon, M. Lopez, C.P. Camurri, M. Oden, J. Ceram. Soc. Jpn. 117(1371) (2009) 1258-1262.

[13] A.S. Kumar, A.R. Durai, T. Sornakumar, Mater. Lett. 58(11) (2004) 1808-1810.

[14] J. Mouzon, M. Odén, Powder Technol. 177(2) (2007) 77-82.

[15] K. Richardson, M. Akinc, Ceram. Int. 14(2) (1988) 101-108.

[16] H. Gong, D.-Y. Tang, H. Huang, T.-S. Zhang, J. Ma, Mater. Chem. Phys. 112(2) (2008) 423-426.

[17] X.-H. Wang, P.-L. Chen, I.W. Chen, J. Am. Ceram. Soc. 89(2) (2006) 431-437.

[18] I.W. Chen, X.H. Wang, Nature 404(6774) (2000) 168-171.

[19] R. Chaim, R. Marder, C. Estournés, Z. Shen, Adv. Appl. Ceram. 111(5-6) (2012) 280-285.

[20] H. Yoshida, K. Morita, B.-N. Kim, K. Hiraga, M. Kodo, K. Soga, T. Yamamoto, J. Am. Ceram. Soc. 91(5) (2008) 1707-1710.

[21] M. Ghaderi, R. Shoja Razavi, M.R. Loghman-Estarki, S. Ghorbani, Ceram. Int. 42(13) (2016) 14403-14410.

[22] L. An, A. Ito, T. Goto, J. Eur. Ceram. Soc. 32(5) (2012) 1035-1040.

Chapter 7

Synthesis, Characterization and Sintering of Nanocrystalline HfO_2 and YSH powders by SMS

This chapter deals with the results obtained in the investigations on the bulk synthesis and sintering of nc-HfO_2 and nc-YSH powders by using salt melt synthesis.

7.1 Purity of starting material and the final product

The cationic impurities present in $HfCl_4$ were insignificantly low (Table 7.1) and are unlikely to influence the characteristics of the final products. The latter were found to contain lesser quantities of impurities (Table 7.2).

7.2 The salt melt synthesis (SMS) of nc-Hafnia

The salt melt synthesis (SMS) has been used in the past for the preparation of ceramic powders to prepare single phase materials with minimum impurities [1, 2]. The SMS involves the decomposition of a precursor in a pool of alkali metal nitrates. The reaction that ensues could be viewed based on the Lux-Flood concept [3], as an acid-base reaction, in which a base donates its oxide ion to an acid. Kerridge [4] and Durand et al. [5] had carried out extensive work on SMS. Benamira et al. [6] had demonstrated that m-HfO_2 could be prepared by the reaction between $HfCl_4$ and an equimolar mixture of $NaNO_3$ and KNO_3 at 723 K. Ternary mixtures containing 7 mol% $NaNO_3$, 53 mol% KNO_3, and 40 mol % $NaNO_2$ are quite stable up to about 873 K [7]. In the presence of oxygen, this mixture could be held without decomposing up to about 973 K. The decomposition of $NaNO_3$ and $NaNO_2$ could be described based on the equilibria [7, 8], represented in the equations (7.1) to (7.4). It is clear from these equilibria that a mixture richer in nitrate would be more oxidizing. Further, the nitrate ion decomposes through the formation of NO_2^-. Thus nitrite rich mixtures would be less oxidizing because of the lesser oxygen availability by virtue of the equilibrium described in eqn. (7.1) which would be shifted towards the left, in the presence of excess nitrite.

$$[\mathrm{NO_3^-}] \leftrightarrow [\mathrm{NO_2^-}] + \frac{1}{2}(\mathrm{O_2}) \tag{7.1}$$

$$2[\mathrm{NO_2^-}] \leftrightarrow [\mathrm{O^{2-}}] + \frac{3}{2}(\mathrm{O_2}) + (\mathrm{N_2}) \tag{7.2}$$

$$2[\mathrm{NO_2^-}] \leftrightarrow [\mathrm{O^{2-}}] + (\mathrm{NO_2}) + (\mathrm{NO}) \tag{7.3}$$

$$\mathrm{K_{Eq}} = \frac{\mathrm{a_{NO_2^-}}}{\mathrm{a_{NO_3^-}}}\,\mathrm{p_{o_2}^{\frac{1}{2}}} \tag{7.4}$$

Thus carrying out the reaction under the flow of argon helps accelerate the forward reaction leading to the formation of the products given in the equations (7.1) to (7.3). The nitrite rich mixtures exhibit less vigorous reaction.

The reactions in the melt could be described through eqns. (7.5-7.6) which represent the extreme conditions of reacting $HfCl_4$ with either the alkali nitrate [eqn. (7.5)] or the alkali nitrite alone [eqn. (7.6)], respectively.

$$\begin{aligned}&4[\mathrm{NaNO_3}] + 4[\mathrm{KNO_3}] + 3[\mathrm{HfCl_4}] \\ &\qquad \leftrightarrow 3[\mathrm{HfO_2}] + (\mathrm{O_2}) + 8(\mathrm{NO_2}) + 4[\mathrm{NaCl}] + 4[\mathrm{KCl}] + 2\mathrm{Cl_2}\end{aligned} \tag{7.5}$$

$$[\mathrm{HfCl_4}] + 4[\mathrm{NaNO_2}] \leftrightarrow [\mathrm{HfO_2}] + 2(\mathrm{NO_2}) + 2(\mathrm{NO}) + 4[\mathrm{NaCl}] \tag{7.6}$$

$$4(\mathrm{NO}) \leftrightarrow 2(\mathrm{N_2O}) + (\mathrm{O_2}) \tag{7.7}$$

Thus the gaseous products would contain different oxides of nitrogen [eqn. (7.7)]. In the mixtures rich in nitrate which are more oxidizing, the O_2 and NO_2 would be present while less oxidizing mixtures would lead to the formation of NO_2 and NO. It is reported in Ref. [9] that evolution of N_2 is brought about only when the reaction is carried out in a closed container. When the melt is allowed to decompose in an open vessel, evolution of NO, NO_2 and O_2 would be observed [9]. From the visual observation it was evident that NO_2 does evolve during the course of the reaction. Y. Du and D. Inman [10] proposed that $AlCl_3$ reacts with molten nitrate (or nitrite) mixture to form α-Al_2O_3 with the liberation of NO and NO_2. These researchers [10] also showed that the reaction mechanism was altered by the composition of the melt and the experimental conditions. Thus by changing the composition of the melt (varying nitrite content) the reaction mechanism could be altered. Du et al. [11] have reported that the addition of a Lux-Flood base would reduce the reaction temperature due to increase in basicity. In this study, even though no attempt was made to elucidate the kinetics of the salt melt reaction, thermal analysis coupled with evolved gas analysis (EGA) was carried out on all mixtures. These results are discussed below.

Table 7.1 ICP-MS analysis of $HfCl_4$ powders

Elements	Li	Ca	Sr	Ba	Ti	Zr	Al	Ga	Ta	As	Bi	Fe	Mo	Ni	Si	Cr
ppm	0.1	0.3	1.2	1.2	53	81	2.7	0.1	5.1	2.1	3.0	0.6	0.2	0.3	0.1	<.0.2

Table 7.2 Analysis of HfO_2 by ICP-OES, AAS# and Ion selective electrode*

Elements	Sample	Na#	K#	Zr	Si	Cl*
ppm	m-HfO_2	10.1	2.1	3.0	7.1	<1
	c-HfO_2	14.4	3.5	2.6	6.3	<1
	30YSH	11	2.5	2.8	6.6	<1

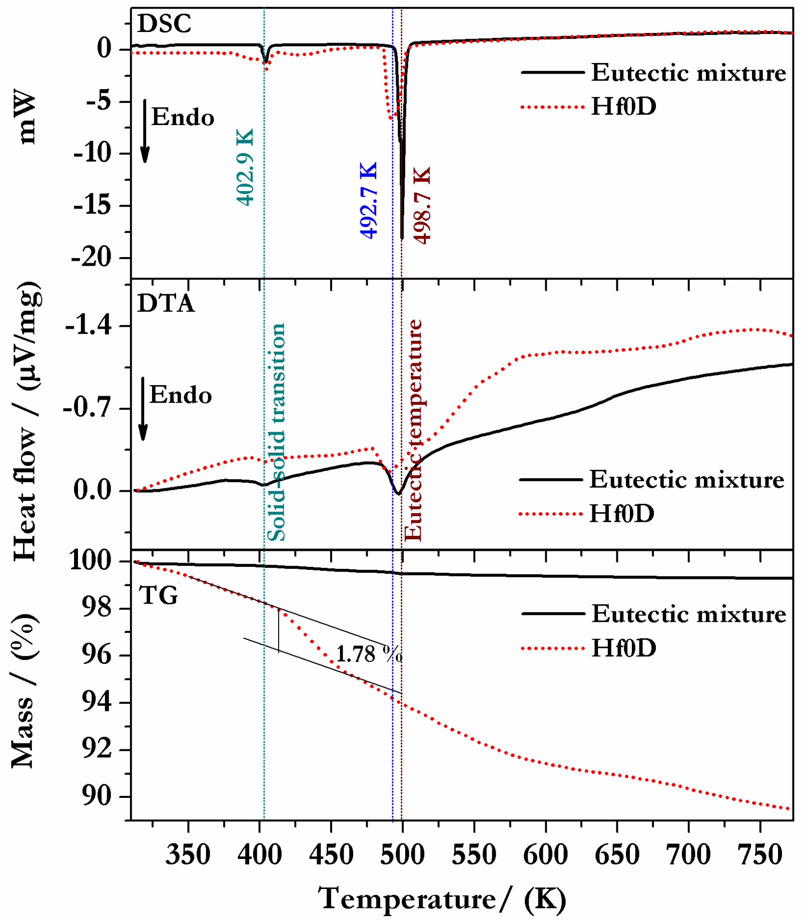

Figure 7.1 Thermal analyses of the salt mixtures revealing the heat effects during the salt melt reaction [where, Hf0D –hafnia powders prepared without the use of $NaNO_2$]

7.3 Thermal analysis of salt mixture

The DSC curves depict the heat effect during the course of the reaction (Fig. 7.1). Data cited in the literature [7] pertaining to KNO_3-$NaNO_3$ and KNO_3-$NaNO_3$-$NaNO_2$ (HITEC®) [12] reveal that these systems are being studied extensively and that the solid state transitions as well as melt equilibria are being investigated in order to establish the pertinent phase diagrams. Recent investigations revealed that in the subsolidus region, a phase transition occurs at 367 K and 390 K in the systems KNO_3-$NaNO_3$-$NaNO_2$ (HITEC®) [12] and KNO_3-$NaNO_3$ [13] respectively.

Thermogram, DTA curve, DSC curve and evolved gas analyses of the salt mixtures are presented in Figs. 7.1-7.3. The endotherms observed at 403 K and 499 K in the DSC curves of the pure nitrate mixture (Fig. 7.1) and TG-DTA-MS are in agreement with the temperatures pertaining to the subsolidus transformation reported in the literature and the pseduobinary eutectic isotherm. Additionally, it was observed that the eutectic mixture is thermally stable till 773 K (TG and EGA). The mass loss of 0.2% observed at the eutectic temperature could be ascribed to the loss of water of crystallization. No exothermic peak was observed in the DTA curve at the eutectic temperature in all these mixtures. However, weight loss corresponding to gas evolution (mass spectra) was observed. This is probably due to the following phenomena which take place simultaneously; fusion (endothermic) and oxidation of $HfCl_4$ (exothermic). Since, 80 % of the melt contains the eutectic mixture the heat effect pertaining to the exothermic reaction probably gets masked by that due to the endothermic fusion.

Even though DTA curves obtained with the other salt mixtures reveal that the eutectic isotherm shifts to lower values with the addition of $NaNO_2$ while there is no change in the subsolidus phase transformation temperature (Fig. 7.2). It is observed that the salt melt reaction takes place close to the eutectic isotherm. This was further reaffirmed by evolved gas analysis (evolution of NO, NO_2, Cl_2, O_2 and HCl).

In general it was observed that the relative proportion of NO gas liberated increases with $NaNO_2$ addition whereas evolution of Cl_2 was observed only in mixtures without $NaNO_2$ (Fig. 7.3). Liberation of HCl and N_2O [eqn. (7.7)] was observed when $NaNO_2$ was present in the mixture. However, the relative proportion of these gases was less compared to that of NO (Fig. 7.3). Traces of O, O_2 and NO_2 were also observed (Fig. 7.3). The presence of O could be due to the gas phase dissociation of oxygen during ionization in the mass spectrometer. However, the presence of both O_2 and O testify the release of oxygen during the reaction. From the foregoing it is evident that the reaction mechanism is significantly altered when nitrite is added to the reaction mixture.

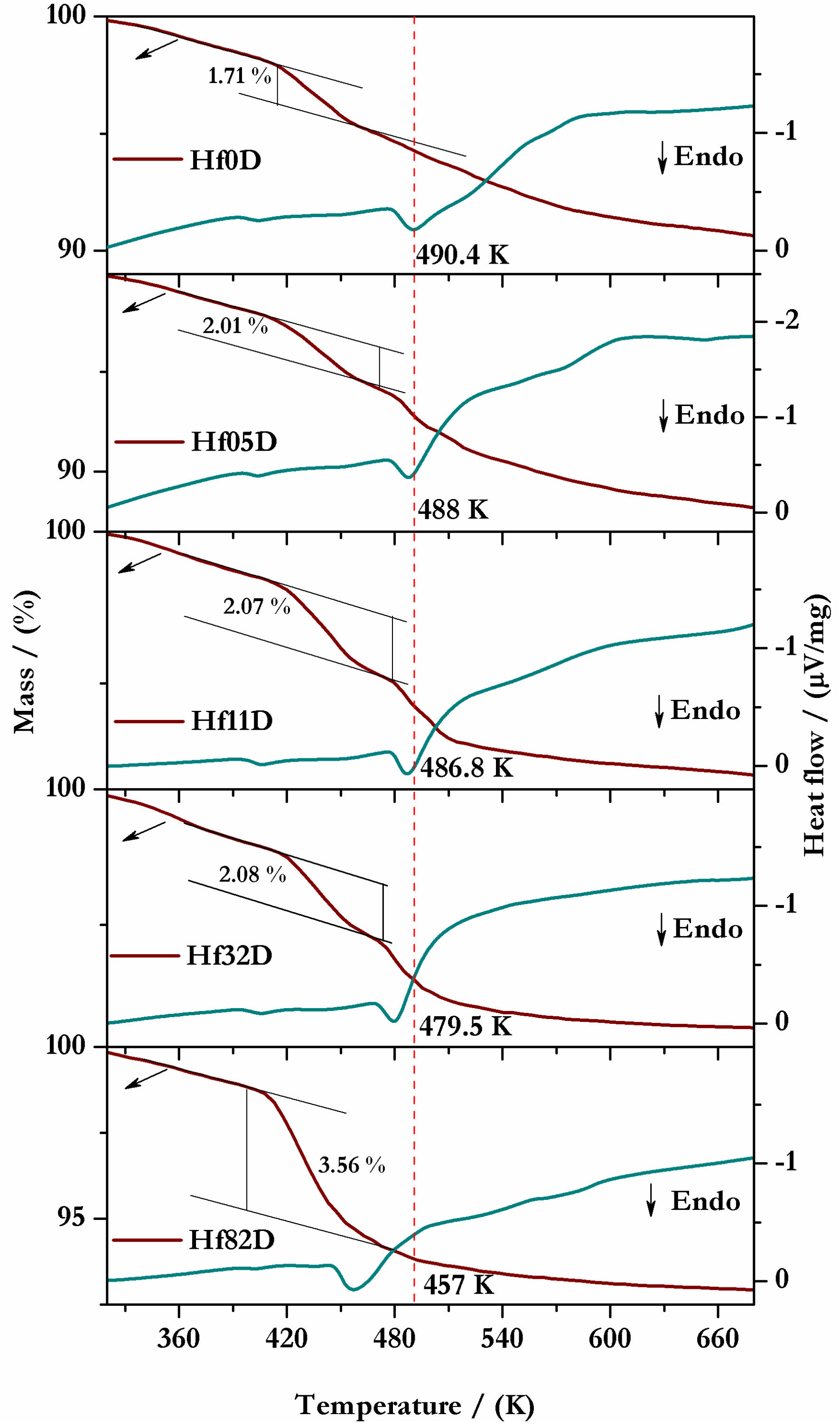

Figure 7.2 Thermal analyses of salt mixtures with varying Φ values (where Φ = 0, 0.055, 0.11, 0.32 and 0.82) revealing the shift in the eutectic temperature

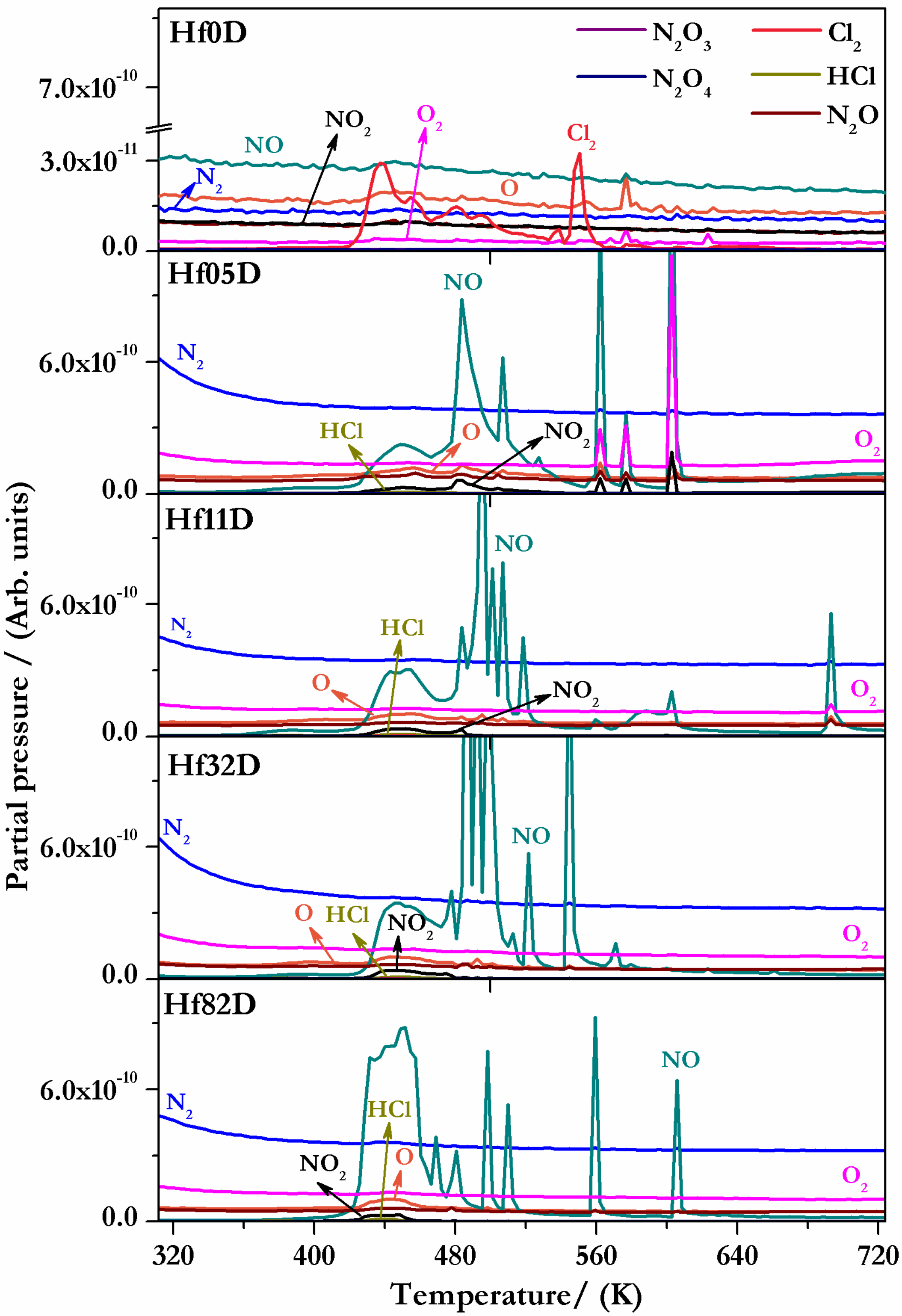

Figure 7.3 Evolved gas analysis of the reaction mixtures with varying Φ values (where Φ = 0, 0.055, 0.11, 0.32 and 0.82)

Table 7.3 Characteristics of HfO_2 powders obtained through SMS from mixtures with different composition

Sample	Φ	ρ_B (Mg m^{-3})	RC (ppm)	SSA (m^{2}g^{-1})	XCS (nm)											
					673 K			873 K			1073 K			1473 K		
					Sc	HW	Strain x10^{-2}	Sc	HW	Strain x10^{-2}	Sc	HW	Strain x10^{-2}	Sc	HW	Strain x10^{-2}
Hf0D	0	1.58	498	81	7	13	0.983	12	16	0.356	16	22	0.214	52	99	0.143
Hf05D	0.05	1.72	618	68	8	13	0.905	14	21	0.334	20	25	0.185	68	138	0.147
Hf11D	0.11	1.67	528	57	9	14	0.584	14	25	0.377	31	36	0.171	41	113	0.172
Hf32D	0.32	1.66	621	38	9	26	0.411	15	27	0.255	23	32	0.167	39	83	0.127
Hf82D	0.82	1.52	717	26	22	38	0.131	23	38	0.115	23	39	0.105	55	130	0.132

$$\Phi = \frac{\text{Moles of } NO_2^-}{\text{Moles of } NO_3^-}$$

7.4 Bulk density (ρ_B), PSD and SSA of nc-HfO_2 powders

The characteristics of the powders obtained in this study are listed in Table 7.3. From the results presented it is evident that the ρ_B of nc-HfO_2 powders prepared in this study varies from 1.52 – 1.72 Mg $m^{-3}$and it is not a strong function of the concentration of nitrite in the melt. These powders were found to be free flowing and thus make an ideal press feed.

Size distribution of particles in the "as prepared" nc-hafnia powders is presented in Fig. 7.4. From these data it is evident that these powders are nearly unimodal and comprised particles with a mean size of 10 μm.

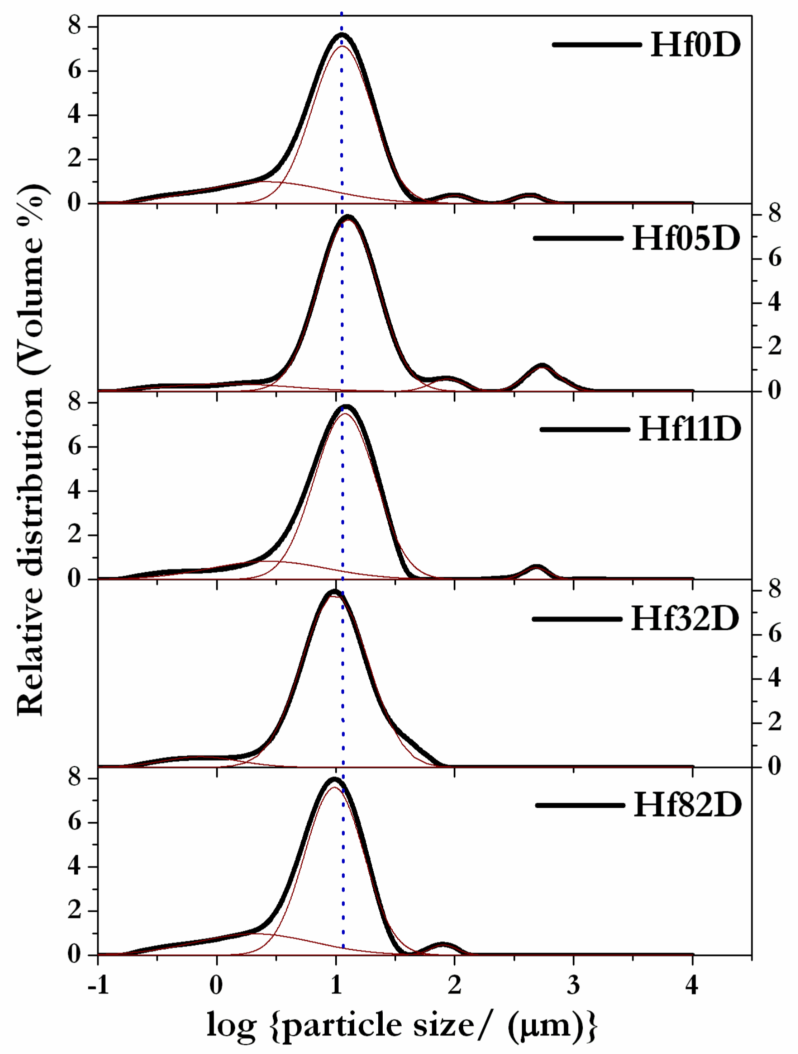

Figure 7.4 Distribution of sizes among particles in nc-HfO_2 powders prepared by using SMS (Thick solid lines - experimental curve and thin solid lines -deconvoluted curves)

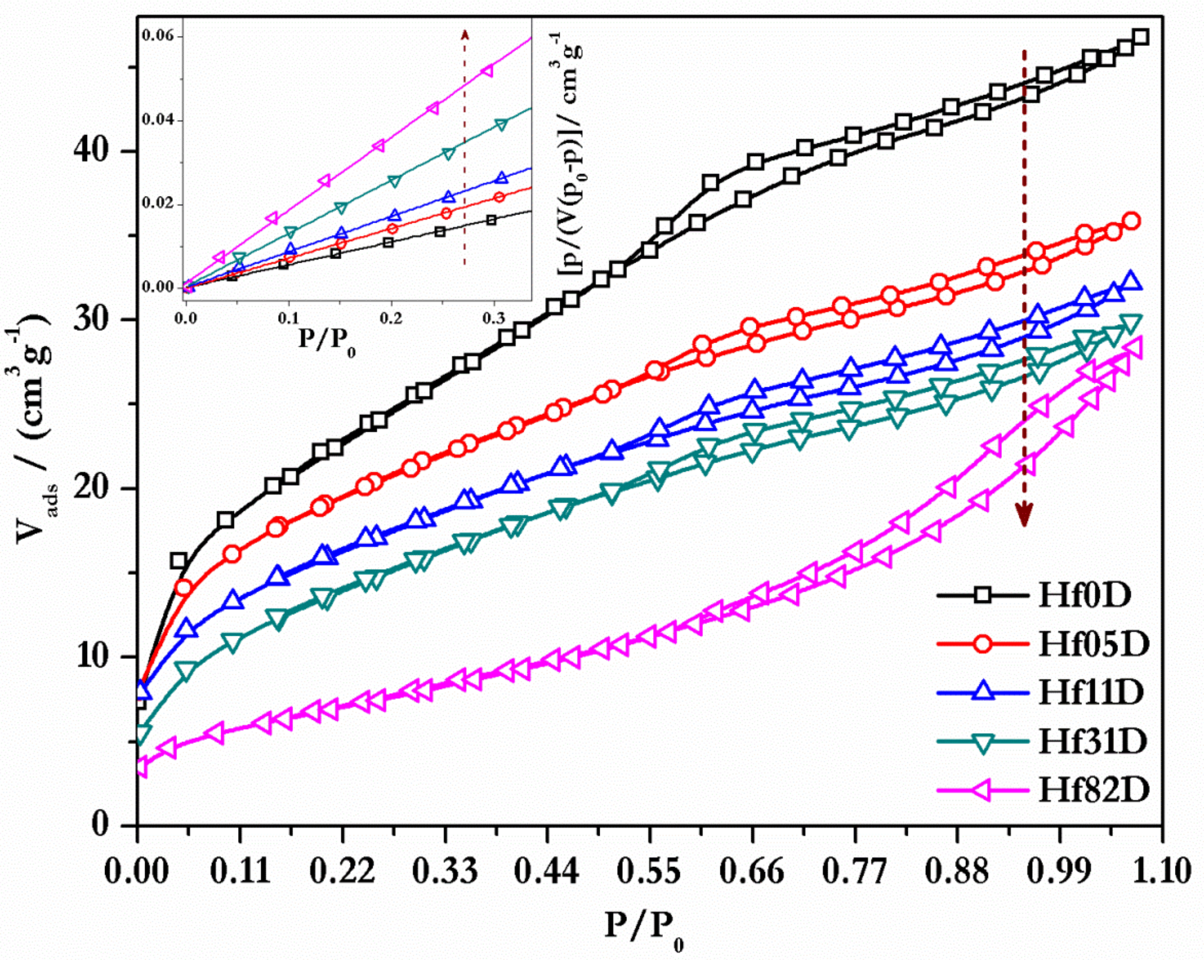

Figure 7.5 Adsorption isotherms of nc-HfO_2 derived through SMS, inset shows linear BET plot

The adsorption isotherms of the nc-HfO_2 obtained in this study are depicted in Fig. 7.5 along with their respective linear BET plots. From the hysteresis in the adsorption-desorption limbs of these isotherms, it is evident that these samples possess micropores. Further, the hysteresis patterns are identical revealing the similarity in the distribution of sizes of pores. The SSA of these nc-HfO_2 powders were found to vary systematically with the value of Φ (Fig. 7.6a). The SSA is related to the grain (crystallite) size which in turn is strongly influenced by the course of the decomposition reaction. The highly oxidizing nitrate rich melts (Φ = 0) yield powders with a SSA of 81 m^2 g^{-1}. When the same reaction is performed in a mixture rich in the nitrite (Φ = 0.82) the surface area is brought down to a value of 25 m^2 g^{-1} (Fig. 7.6a).

During the chemical separation of the hafnium oxide from the solidified reaction mass, the latter had to be treated with propan-2-ol. Hence, the final product was found to have carbon residue of about 700 ppm (Table 7.3).

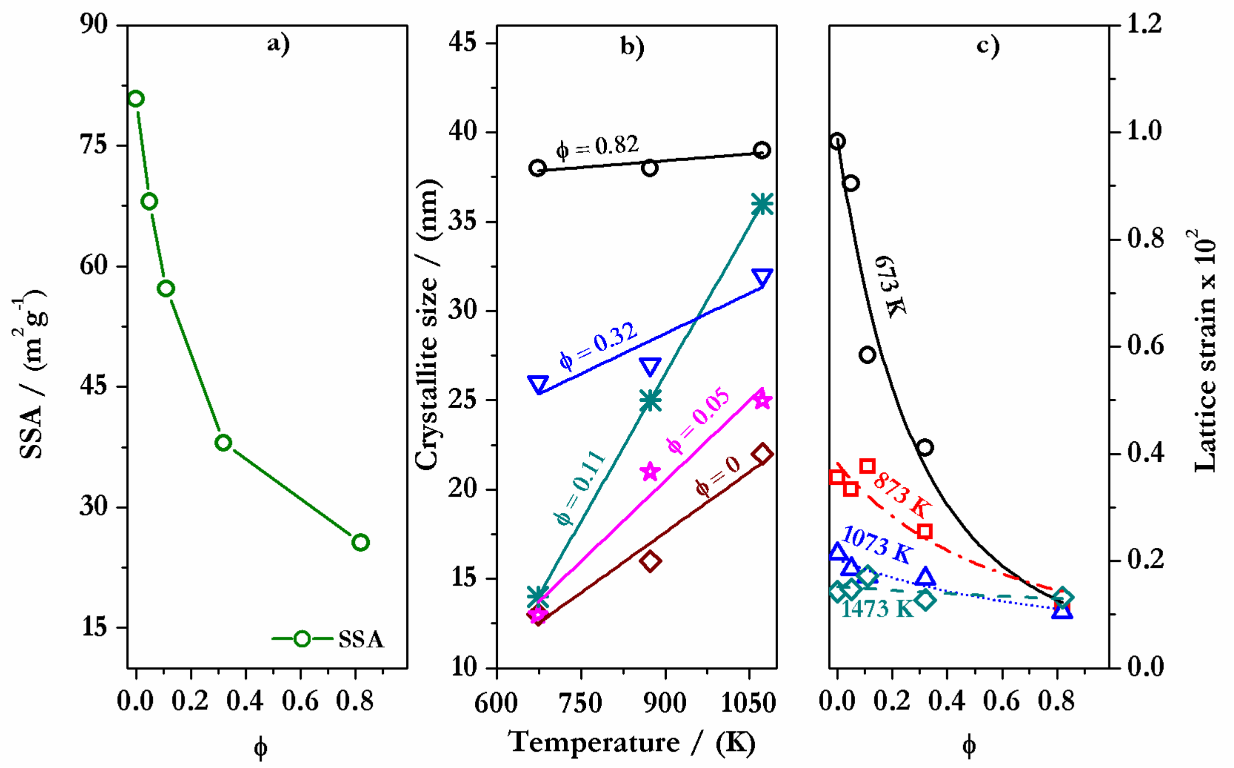

Figure 7.6 *(a) Dependence of the SSA of the powders on the composition of the melt (Φ); (b) Linear correlation of the XCS with the calcination temperature and (c) Dependence of the lattice strain on both the calcination temperature and on the value of ϕ*

7.5 Phase identification, XCS, lattice strain and microstructure of nc-HfO_2

Hafnium oxide exists in the monoclinic form HfO_2 ($P2_1/c$) which is thermodynamically stable under ambient conditions [14, 15]. Above 1973 K it transforms into the tetragonal ($P4_2/nmc$) phase [15] and finally takes the cubic form (Fm3m) at temperatures above 2873 K [15]. The XRD patterns pertaining to the products obtained in this study are presented in Fig. 7.7.

All the powders synthesized in this study excepting Hf82D were found to comprise the monoclinic form of this oxide. The powder Hf82D was the cubic analogue. It retained the cubic phase even upon further heating upto 1073 K. However, when heated at 1473 K it transformed into the monoclinic phase. Thus, for the first time the salt melt technique has been gainfully used for synthesizing metastable c-HfO_2 at a temperature as low as 673 K. Since this was observed only with the fusion mixture that was rich in nitrite, it is apparent that the latter aids the formation of the metastable cubic phase. Ling Gao et al. [16] synthesized Mn doped cubic HfO_2, $Hf_{1-x}Mn_xO_{2-\delta}$ with x=0.5 which was stabilized at room temperature. These authors suggested that the high temperature cubic phase is stabilized in $Hf_{0.70}Mn_{0.30}O_{2-\delta}$ due to the presence of variable oxidation state of Mn ions which in turn affects the oxygen vacancy. Further, the oxidation state of Mn depends on the synthesis atmosphere and temperature. We observed the stabilization of the cubic phase, in the present study in the powders prepared from melts in which the oxygen availability is rather less compared to the rest. Further, plausibly annealing in air at high temperature restores the monoclinic form by the re-introduction of oxygen into the lattice. XRD pattern pertaining to the same powders that were heated in air at 1473 K supports this phase reversal. The HRTEM images (Fig. 7.8) show that the cubic phase is devoid of cationic inclusions. XRD patterns of c-HfO_2 do not show any peak splitting at higher diffraction angle which indicates that the product (cubic phase) were formed without tetragonal phase. In addition, the XRD pattern of c-HfO_2 does not show any asymmetry in the peaks pertaining to (200), (311) and (222). However, no evidence could be obtained to establish the oxygen stoichiometry and it is not certain if the oxygen deficiency in the melt or the sluggish reaction is responsible for the stabilization of the cubic phase. These results indicate the absence of the tetragonal phase formation and hence it could be concluded that c-HfO_2 phase has not been formed by the stabilization of the cubic to tetragonal phase.

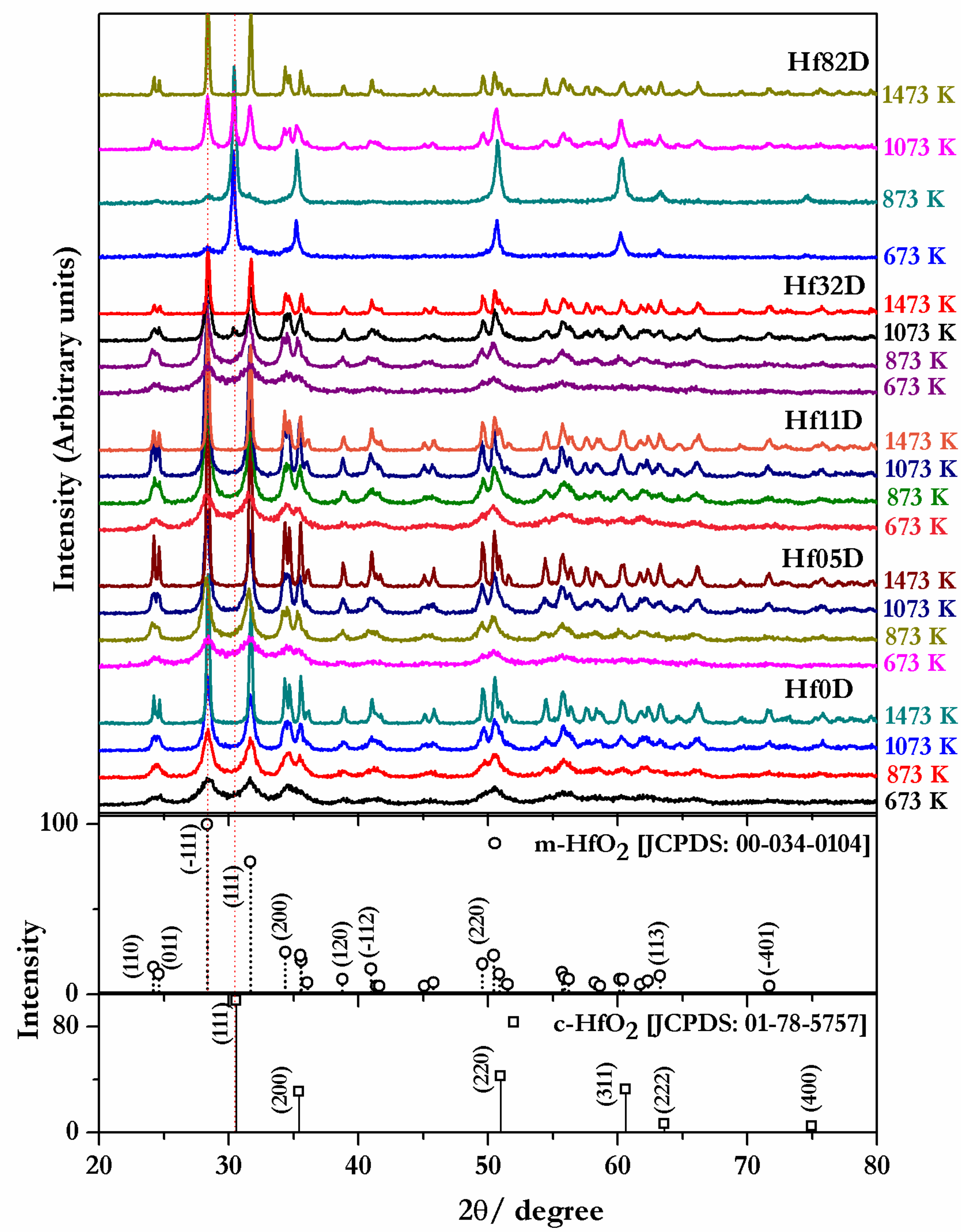

Figure 7.7 XRD pattern of the HfO_2 powders derived through SMS annealed at different temperature

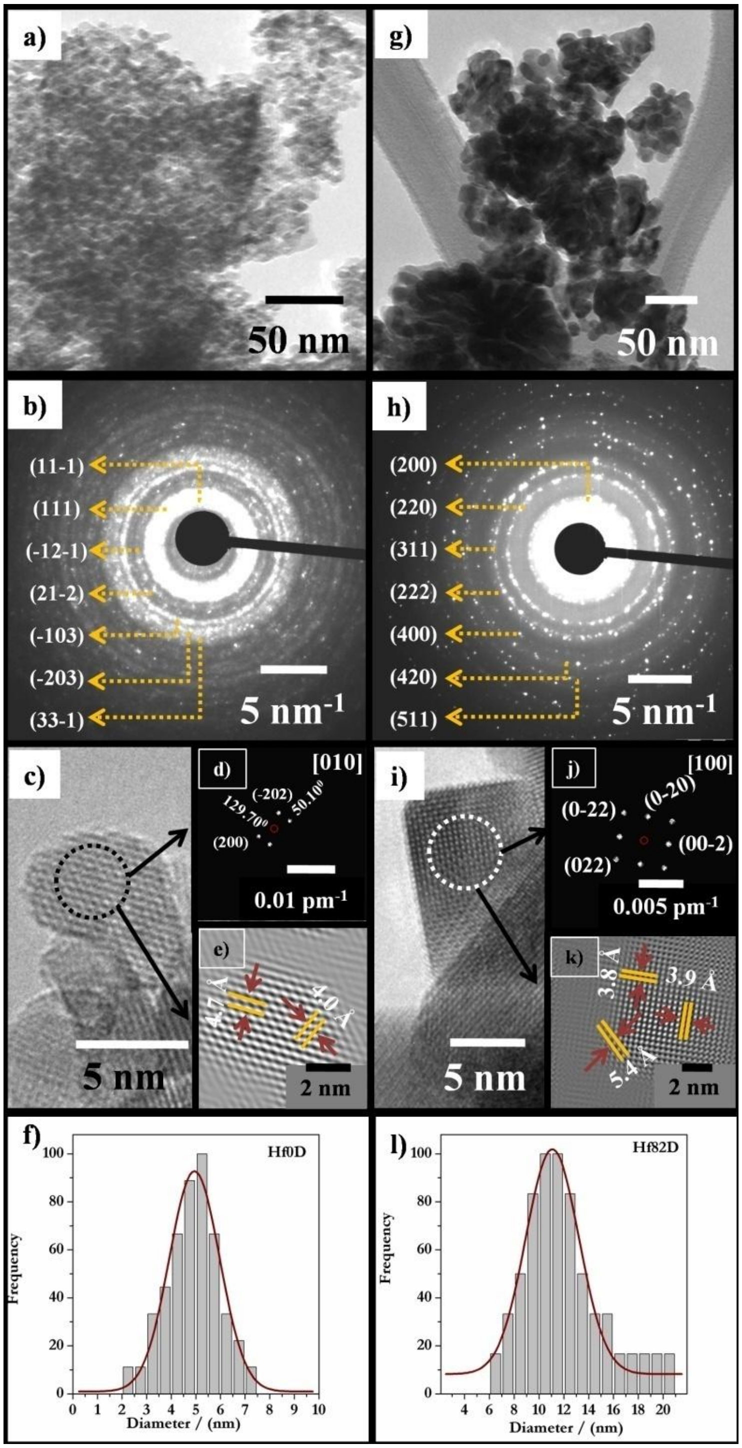

Figure 7.8 *TEM images of HfO_2 powders derived through SMS: [a-f] m-HfO_2 (Hf0D): (a) bright image revealing nano grains; (b) SAED image; (c) HRTEM image of nano grains; (d-e) FFT and filtered IFFT image revealing zone axis [010]; (f) grain size distribution of m-HfO_2 [g-l] c-HfO_2 (Hf82D) (g) dark field image revealing nano grains; (h) SAED image; (i) HRTEM image of nano grains; (j-k) FFT and filtered IFFT image revealing zone axis [100]; (l) grain size distribution of c-HfO_2*

Analysis of X-ray diffractograms revealed that these powders were nanocrystalline. The XCS determined by using the Sc method [17] was found to be less than the estimates of the same obtained through the HW [17] analysis of the XRD data. A closer look at the values of the XCS pertaining to the powders obtained by calcination up to 1073 K reveals that the XCS increases linearly with the calcination temperature (Fig. 7.6b). In an earlier study it was observed that the XCS of nc-ThO_2 obtained by decomposition of thorium oxalate exhibited an exponential dependence on the calcination temperature [18]. Allred et al.[1] reported that the XCS of thoria derived from thorium oxalate increases exponentially with the calcination temperature. Ananthasivan et al. [18] confirmed this trend for thorium oxalate product from aqueous and non-aqueous media. Thus, it is evident that the calcination temperature strongly influences the XCS of nc-oxide powders. Nc powders would coarsen even at relatively low temperatures employed for calcining their precursors. For the hafnia powders synthesized in this study probably the threshold temperature for the onset of grain coarsening lies between 1073 K and 1473 K as evidenced by the substantial increase in the XCS, when calcined at 1473 K.

The lattice strain in the powders obtained in the present study, elucidated through HW analysis of the XRD data are presented in Table 7.3. The dependence of lattice strain on both the calcination temperature and the composition of the fusion mixture are depicted in Fig. 7.6b. From these data it is evident that the lattice strain in all these powders except Hf82D decreases progressively with both the calcination temperature and the quantity of nitrite in the melt (Fig. 7.6c). Calcination reduces the lattice strain through annealing. It is evident from the TG-DTA-MS curve (Fig. 7.3) that the formation of nc c-HfO_2 takes place at around 457 K. The powder Hf82D prepared from a mixture with $\Phi = 0.82$ possesses minimum residual lattice strain which does not seem to vary significantly with the calcination temperature. Thus, when the melt

---

[1] V. D. Allred et al. *J. Phys. Chem.*, **1957**, *61* (1), 117–120.

was maintained at 673 K for 1 h, c-HfO_2 had undergone both annealing as well as grain coarsening (Fig. 7.6b & 7.6c).

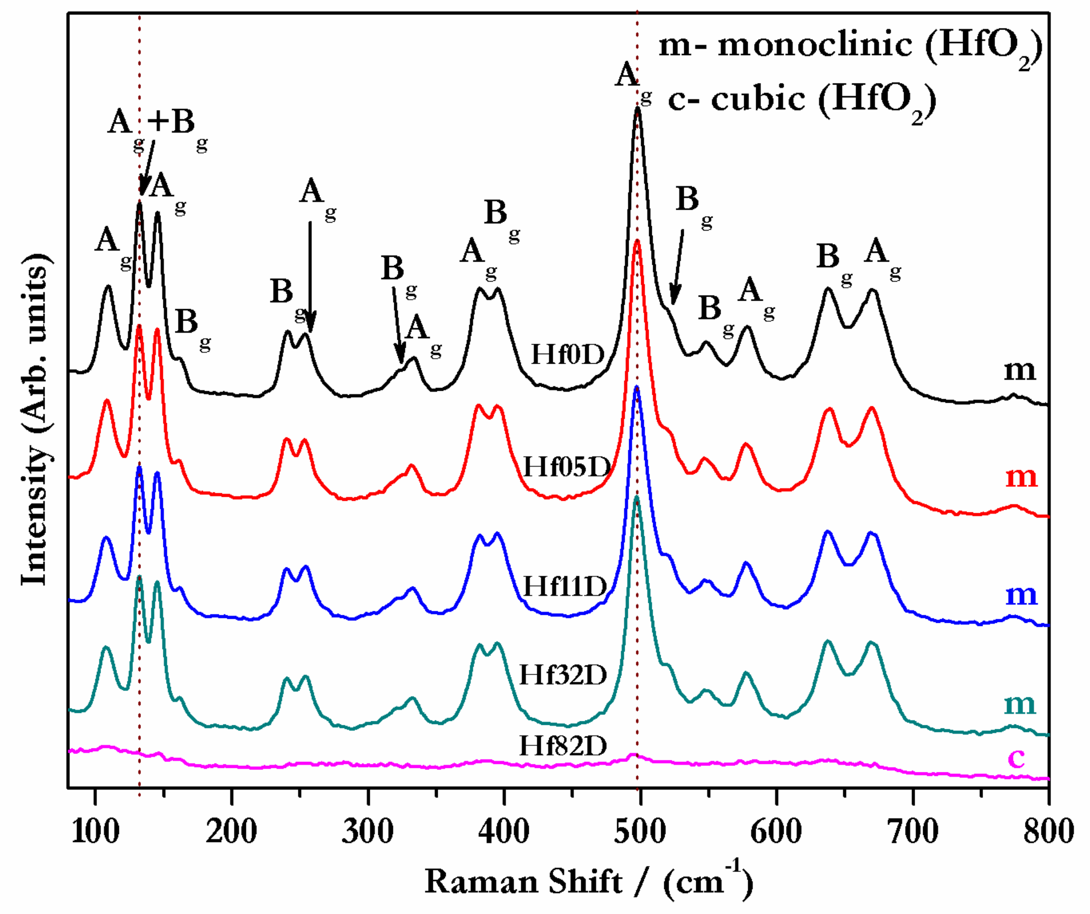

Figure 7.9 Raman spectrum of nc-HfO_2 powders prepared with varying Φ value (where Φ = 0, 0.055, 0.11, 0.32 and 0.82) revealing the absence of the tetragonal phase

7.6 Raman spectroscopy investigations on nc-HfO_2

The optical phonon modes of m-HfO_2 (space group: $P2_1/c$) [14] and c-HfO_2 (space group: Fm3m) [14] were obtained by using group theoretical analysis [19, 20]:

$$\Gamma(\text{Monoclinic}) = 9A_g\,(R) + 9B_g\,(R) + 8A_u\,(IR) + 7B_u\,(IR) + 2B_u\,(a) + A_u\,(a) \tag{7.8}$$

$$\Gamma\,(\text{Cubic}) = F_{2g}\,(R) + F_{2u}\,(IR) + F_{1u}\,(a) \tag{7.9}$$

where: R = Raman mode; IR = Infrared mode and a = Acoustic mode. The unit cell contains 4 formula units that result in 36 degrees of freedom. Since all modes in the monoclinic phase are non-degenerate 18 Raman bands are expected. The c-HfO_2 unit cell contains only 1 formula unit; leading to 3 phonon modes [a Raman active mode, an Infrared active mode and an acoustic mode]. Raman spectra (Fig. 7.9) of all nc-hafnia powders (except Hf82D) are similar to those reported in the literature [19, 21, 22] for m-HfO_2. Additionally, the Raman shifts observed in this study for the nanocrystalline m-HfO_2 are in agreement with the data presented in Ref. [23]. Studies by Rui Wu et al. [19] showed that the band observed at 133 cm^{-1} in m-HfO_2 is due to overlapping of the bands at 134 cm^{-1} (A_g) and 131 cm^{-1} (B_g) and cannot be resolved by a conventional instrument. Nanocrystalline m-HfO_2 powders prepared in this study also exhibit a Raman band at 132 cm^{-1} that could be due to the combination of two frequencies mentioned above. Nanocrystalline c-HfO_2 powders prepared in this study do not show any Raman active mode in the spectrum. The increased width of the Raman bands (from 10 cm^{-1} for the bulk to 18.98 cm^{-1} for the present sample) is indicative of phonon confinement effects.

7.7 Microstructural investigation on nc-HfO_2

Microstructural characterization (TEM) of the m-HfO_2 and c-HfO_2 powders further ascertained that these powders comprised grains with uni-modal distribution of size [Hf0D: 3-8 nm and Hf82D: 6-21 nm] (Fig. 7.8). The SAED patterns confirmed the presence of m-HfO_2 - $P2_1/c$ [14] - (Hf0D) and c-HfO_2 - Fm3m [14] - (Hf82D). SAED image also confirmed their nanocrystallinity (Fig. 7.8).

The d-spacings derived from the diffraction patterns were comparable to the standard JCPDS pattern [m-HfO_2 – PDF No. 00-034-0104; c-HfO_2 – PDF No. 01-078-5757]. Both bright and dark field images revealed the presence of nanograins. The HRTEM images (Fig. 7.8) of these samples depict the values of the “d” spacing that are in agreement with the values (JCPDS) mentioned above. The Fast Fourier Transform images (FFT) of both m-HfO_2 and c-HfO_2 were comparable with the FFT image generated with appropriate zone axes.

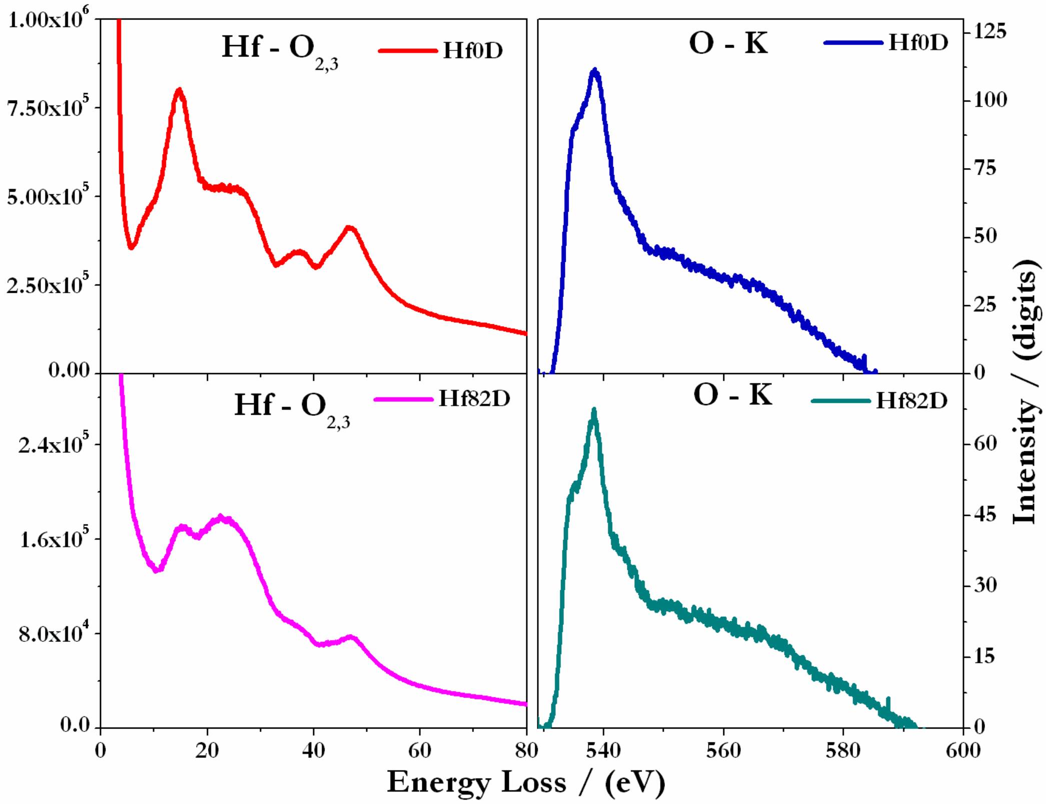

Figure 7.10 EELS of m-HfO_2 ($\Phi = 0$) and c-HfO_2 ($\Phi = 0.82$) powders depicting $O_{2,3}$, O-K and Hf-$M_{4,5}$ edges

EELS was used to understand the characteristics of the bonding in nc-HfO_2 [m-HfO_2 (HfθD) and c-HfO_2 (Hf82D)] (Fig. 7.10). Presence of oxygen defects [24], crystallinity [25, 26] and cationic inclusions [26] in the unit cell will influence the characteristics of the EEL spectrum at both low and high loss regions [26]. Hence, EEL spectra of the nc-hafnia powders prepared in this study were compared and analyzed with that of the microcrystalline sample. In the low loss region, O-K edge and $M_{4,5}$ edges in the samples (m-HfO_2 and c-HfO_2) reveal that the peaks are broad and the energy corresponding to the onset of these peaks are shifted compared to that observed in the bulk sample (annealed at high temperature-1273K) [27]. Rauwel et al. [26] have reported that the reduction in peak intensities and shift in peak onset could plausibly be due to the presence of oxygen vacancies and nano size (quantum confinement). Thus, these observations further suggest the presence of oxygen vacancies. Mizoguchi et al. [28] reported the partial density of states (pDOS) on O-K edge in the three polymorphs (monoclinic, tetragonal and cubic form) of HfO_2. Calculation pertaining to pDOS [28] shows that the O-K edge observed in both the cubic and tetragonal phase is sharp as compared to that in the monoclinic phase. This variation has been ascribed to the octahedral (O_h) symmetry [26, 28, 29]. In c-HfO_2, the tetrahedral (T_d) oxygen is coordinated to 4 Hf atoms while the m-HfO_2 contains two different O atoms coordinated with 3 and 4 Hf atoms respectively [26, 28, 29]. The low loss and O-K edge fine splitting would not be visible in an EEL spectrometer with an energy resolution of 0.6 eV [26]. In this study, m-HfO_2 exhibited a broad peak (O-Kedge) with maxima at 538.8 eV, while c-HfO_2 exhibited a sharp peak with maxima at 538.4 eV. A closer look at the O-Kedge in c-HfO_2 shows that it comprises two peaks, which when resolved through deconvolution is shown to comprise two peaks with their maxima at 534.8 eV and 538.4 eV. These values are in good agreement with the values reported in the literature [29]. Hf $M_{4,5}$ edges in m-HfO_2 are observed at 1684 eV and 1699 eV while for c-HfO_2 they are found at 1684 and 1697 eV. In general it was observed that the intensities of all the peaks in the powder Hf0D (m-HfO_2) were higher than those in the powder Hf82D (c-HfO_2). Since the EEL spectrum corresponding to Hf^{4+} occurs in the higher energy range (≈1700 eV) it was not possible to resolve it to delineate the contributions from Hf in other oxidation states.

7.8 Compaction and sintering of nc-HfO_2

7.8.1 Green density (ρ_G)

In order to enhance densification in nc powders and to obtain compacts with uniform microstructure, the characteristics of the powders used for making green compacts need to be appropriately tailored. In general the ρ_G of all the powders were nearly identical, probably due to similar size distribution of particles, in the latter. The relative ρ_G of hafnia pellets exhibit a linear positive correlation (38.1 ± 0.7 % T.D to 54.8 ± 0.5 % T.D) with the CP (60 to 353 MPa) (Table 7.4 and Fig. 7.11a) and nitrite content in the salt mixture. In addition, these nc powders could not be compacted to a very high density owing to higher frictional resistance [30-32]. Further, the powder Hf32D yielded green compacts with a higher density which could be due to the presence of excess fine fraction of particles. Chaim et al. [32] had reported that the particle which deviates from sphericity would require higher CP as compared to spherical particles owing to the presence of large interparticle frictional force in the former. The particles in the powder Hf82D were cuboidal and faceted, while the rest of the powders comprised irregular particles. Thus, it is reasonable to assume that a higher degree of “asphericity” in the Hf82D powders could have led to a lower ρ_G.

Table 7.4 ρ_G of HfO_2 derived through salt melt synthesis

CP	Hf0D	Hf05D	Hf11D	Hf32D	Hf82D
(MPa)			% T.D		
60	41.2 ± 0.9	38.1 ± 0.7	39.6 ± 0.3	44.1 ± 0.5	39.4 ± 0.3
120	43.8 ± 0.2	41.9 ± 0.5	43.0 ± 0.3	46.7 ± 0.6	42.5 ± 0.3
180	46.5 ± 0.2	44.1 ± 0.3	45.4 ± 0.4	48.6 ± 0.7	43.6 ± 0.6
244	48.4 ± 0.7	46.3 ± 0.6	47.6 ± 0.9	50.3 ± 0.6	45.4 ± 0.4
317	50.3 ± 0.3	48.2 ± 0.9	49.4 ± 0.3	52.3 ± 0.5	47.3 ± 0.6
353	51.9 ± 0.5	49.0 ± 0.5	50.2 ± 0.7	54.8 ± 0.5	47.9 ± 0.2

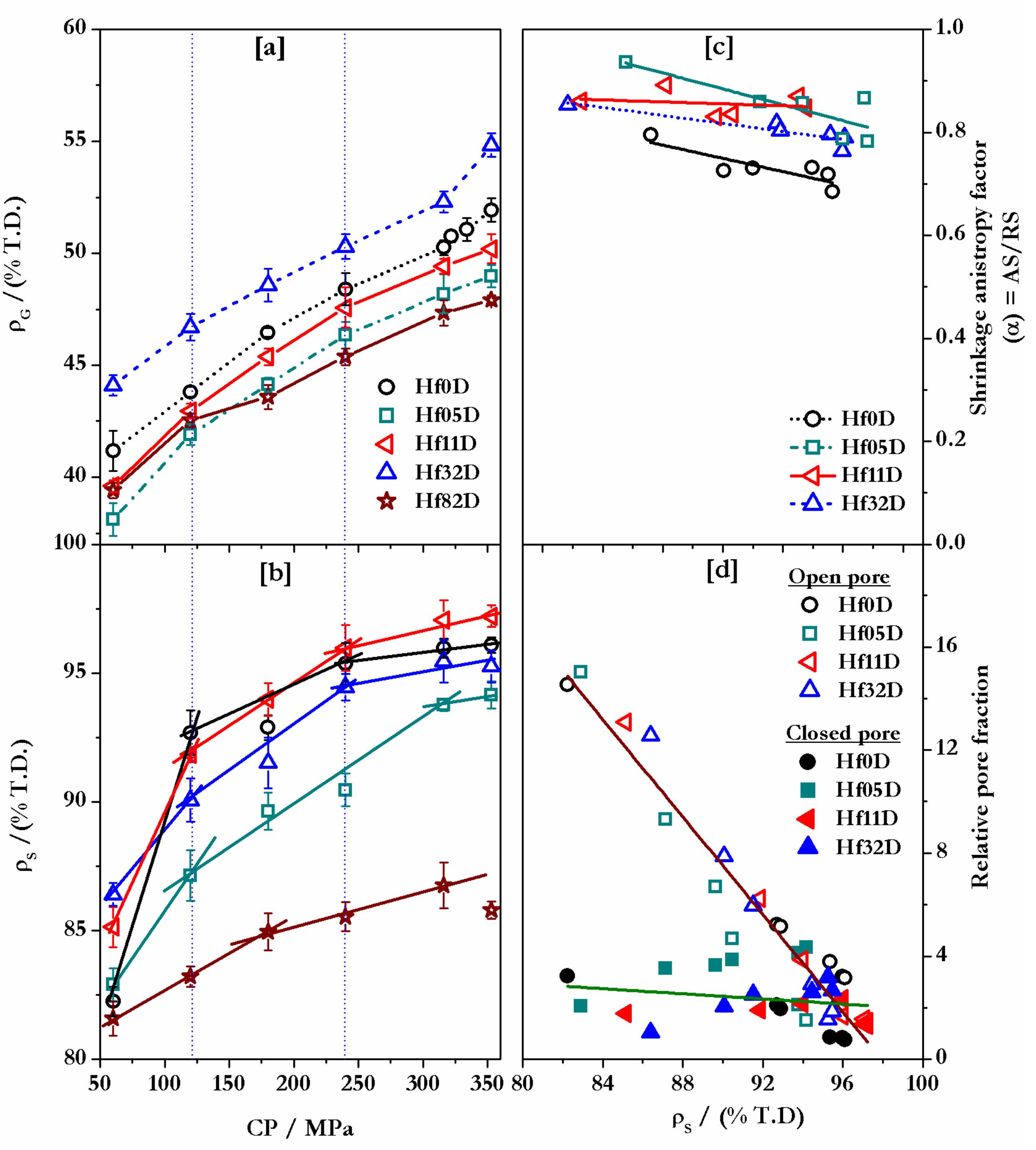

Figure 7.11 *Variation of (a) ρ_G and (b) ρ_S with the CP; (c) variation of shrinkage anisotropy factor (α) with the ρ_S and (d) dependence of pore fraction on the ρ_S*

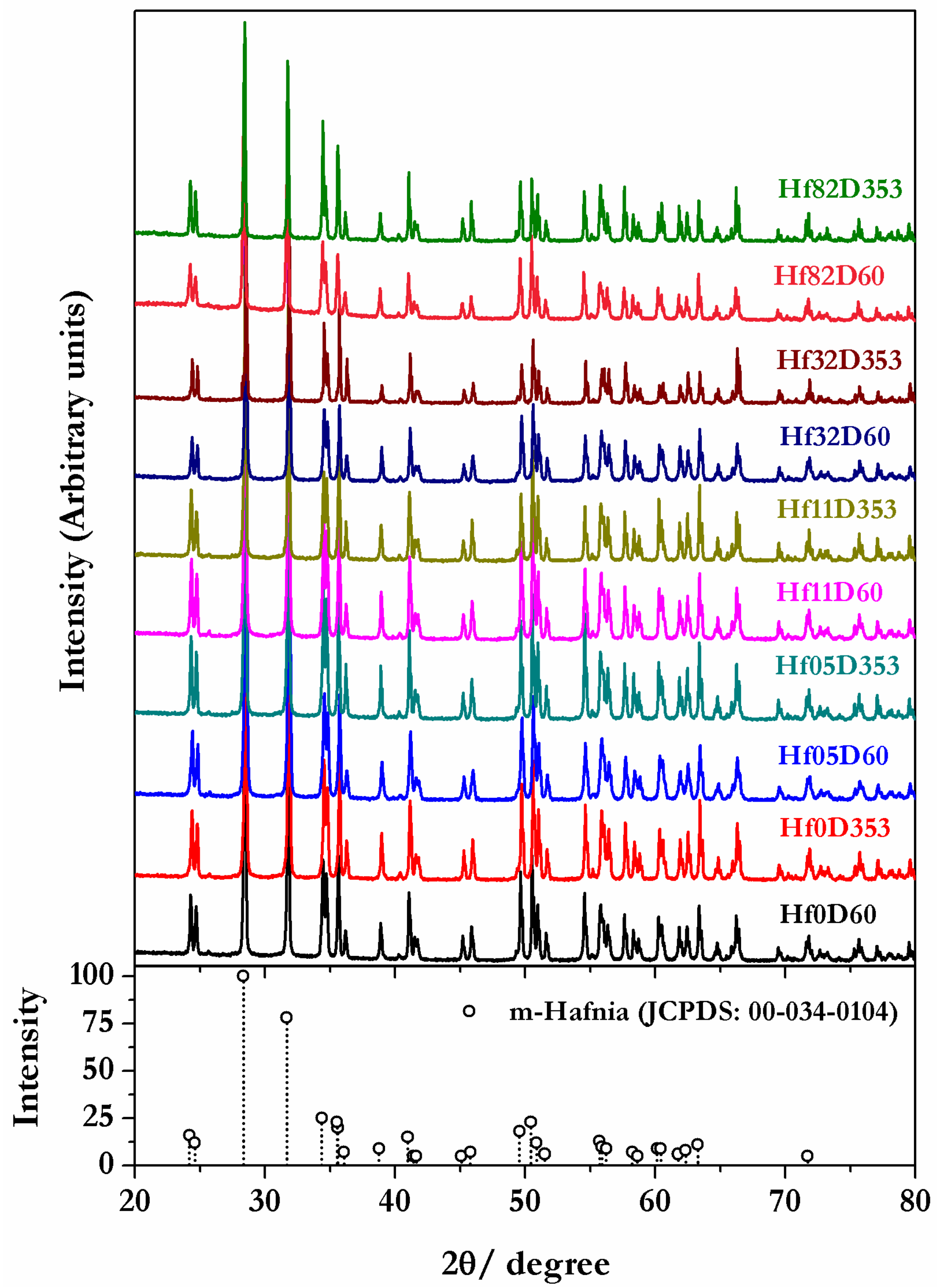

Figure 7.12 XRD of sintered HfO_2 monoliths

7.8.2 Phase characterization and carbon residue in sintered hafnia monoliths

Selected samples of sintered hafnia monoliths were analyzed by using XRD (Fig. 7.12), which revealed that they comprised the thermodynamically stable, room temperature, monoclinic phase. The XRD analysis further reaffirms that even though the powders Hf82D initially comprised the cubic phase at the end of the sintering cycle they had reverted back to the thermodynamically stable m-HfO_2 phase. The XRD patterns are indexed appropriately by comparing them with those reported in JCPDS (m-HfO_2 - JCPDS No. 00-034-0104). According to the ASTM (C1076-09 [33]) specification, hafnia to be used in nuclear applications should contain carbon residue below 1000 ppm. Selected samples of sintered hafnia monoliths were analyzed for carbon residue and it was observed that it was varying between 81 to 151 ppm. Hence, this procedure could be deployed for the production of nuclear grade HfO_2.

7.8.3 Sintering and microstructural investigations on HfO_2 monoliths

To optimize the sintering, selected samples of hafnia powders were compacted at 317 MPa and were sintered by using both CS ($HfYD_{CS1}$, $HfYD_{CS2}$ and $HfYD_{CS3}$) and TSS (TSS_1 and TSS_2) procedures (Chapter 2). The ρ_S are presented in Tables 7.5 & 7.6. These data reveal that the monoliths derived through TSS_2 method had sintered better as compared to those subjected to CS. Hence, all the hafnia powders were compacted at 60, 120, 180, 244, 317 and 353 MPa and were sintered in air by using the TSS_2 method.

The characteristics of the sintered pellets derived through TSS_2 are presented in Table 7.6 and in Fig. 7.11b. In general, it was observed that all the hafnia compacts (except Hf82D) had undergone better densification when sintered by using the TSS_2 method. The TSS_2 method with final sintering temperature of 1773 K and a CP of 353 MPa yield monoliths with a high ρ_S (94.2 ± 0.5 T.D to 97.2 ± 0.4 % T.D). It was observed that Hf0D and Hf11D compacts had undergone higher densification as compared to all other compacts. Their ρ_S were found to be almost identical and were independent of the CP. The ρ_S values of Hf32D were found to be marginally higher than that of Hf05D owing to a higher ρ_G of the former. Hf82D compacts had yielded monoliths with ρ_S ranging between 81.6 ± 0.7 % to 86.6 ± 0.9 % T.D. These values are indeed much lower as compared to that of the rest.

Table 7.5 Sintering parameters and ρ_S of HfO_2 (317 MPa; CS and TSS method)

Sample	**ρ_G**	**ρ_S**				
		CS_1 **$HfYD_{CS1}$**	**CS_2** **$HfYD_{CS2}$**	**CS_3** **$HfYD_{CS3}$**	**TSS_1** **$HfYDS_1$**	**TSS_2** **$HfYDS_2$**
	% T. D.					
Hf0D	50.3 ± 0.3	90.5 ± 0.6	91.4 ± 0.2	94.1 ± 0.6	94.9 ± 0.3	96.0 ± 0.4
Hf05D	48.2 ± 0.9	89.0 ± 0.1	90.4 ± 0.2	92.2 ± 0.3	92.9 ± 0.2	93.8 ± 0.3
Hf11D	52.3 ± 0.5	91.1 ± 0.7	91.3 ± 0.2	94.8 ± 0.5	95.1 ± 0.5	97.1 ± 0.8

$Y = \Phi * 100$

CP - 317 MPa
CS_1 – 1673 K 4 h
CS_2 – 1773 K 4 h
CS_3 – 1873 K 4 h
TSS_1 Step 1 - 1873 K 1 h; Step 2 - 1673 K 4 h
TSS_2 Step 1 - 1873 K 1 h; Step 2 - 1773 K 4 h

Table 7.6 Characteristics of sintered HfO_2 monoliths derived through TSS_2 method

CP (MPa)	**Hf0D**	**Hf05D**	**Hf11D**	**Hf32D**	**Hf82D**
			% T.D		
60	82.2 ± 0.6	82.9 ± 0.6	85.1 ± 0.8	86.4 ± 0.4	81.6 ± 0.7
120	92.7 ± 0.9	87.2 ± 0.1	91.8 ± 0.1	90.1 ± 0.8	83.2 ± 0.4
180	92.9 ± 0.5	89.6 ± 0.7	94.0 ± 0.6	91.5 ± 0.9	85.0 ± 0.7
244	95.4 ± 0.8	90.5 ± 0.6	96.0 ± 0.9	94.5 ± 0.5	85.5 ± 0.6
317	96.0 ± 0.4	93.8 ± 0.3	97.1 ± 0.8	95.5 ± 0.8	86.6 ± 0.9
353	96.1 ± 0.3	94.2 ± 0.5	**97.2 ± 0.4**	95.3 ± 0.6	85.8 ± 0.3

These monoliths Hf82D were found to have undergone significant “warping” and had cracks on the pellet surface. Cubic HfO_2 reverts to the monoclinic form at around 1073 K. Recently Piluso et al. [15, 34] had reported that the phase transformation of hafnia crystals is accompanied by a volumetric expansion of about 3.4 % (from the tetragonal to monoclinic phase upon cooling) which induces cracks. Thus, from the above discussion it is evident that the phase transformation from the metastable cubic to the stable monoclinic phase is responsible for the poor sinterability of Hf82D.

The shrinkage anisotropy factor (α) [35] and relative pore fraction (ratio of open/closed porosity to that of total porosity) were measured to understand the extent of densification and to evaluate the quality of the final sintered product (Fig. 7.11c & Fig. 7.11d). The desirable value of relative pore fraction is less than 2 % while that of shrinkage anisotropy factor is 1. Dependence of the relative pore fraction on ρ_S reveals that the open pore fraction decreases while the closed pore fraction increases (marginally) with the ρ_S (Fig. 7.11d). Fig. 7.11d also reveals that the fraction of both open and closed pores becomes nearly equal at around 96 % T.D. Further, this plot reveals that the removal of closed pores from hafnia monolith is tedious and to remove the residual porosity further optimization is necessary. The shrinkage anisotropy factor (α) [35] of hafnia monoliths were found to be linearly correlated with their ρ_S (Fig. 7.11c).

Microstructures of sintered hafnia pellets (Hf0D; 60 MPa and Hf0D; 353 MPa) are shown in Fig. 7.13. The SEM images reveal that the hafnia monoliths compacted at 60 MPa (Fig. 7.13a -b) exhibit both intra and intergranular pores on both the polished as well as the fractured surfaces. The hafnia monoliths derived from the greens compacted at 353 MPa showed the presence of faceted grains with dihedral angles ranging between 109^0 to 130^0 (Fig. 7.13d-e). The values of the dihedral angle suggest that sintering has proceeded nearly up to the “final stage”

[35, 36]. The polished surfaces also showed the presence of well defined grain boundaries with grain size ranging between 1 µm to 3 µm. Point scan by using energy dispersive X-ray analysis of sintered hafnia monoliths revealed that it comprised only hafnia and was devoid of any other impurity.

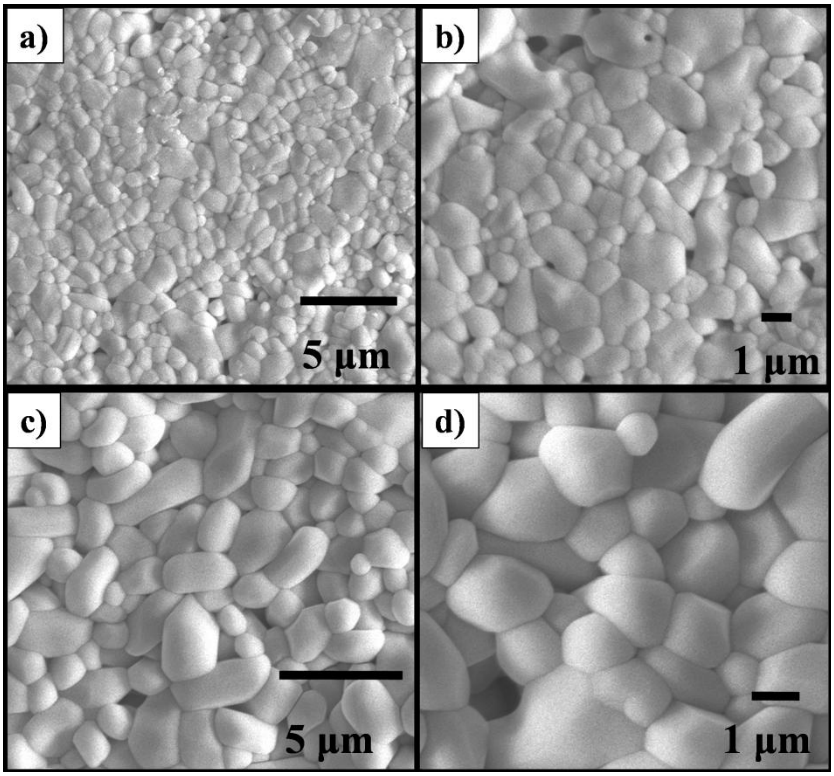

Figure 7.13 Sintered Hf0D (a-b) 60 MPa and (c-d) 353 MPa; SEM images of Hf0D (a & c) low magnification image of 60 MPa and 353 MPa monoliths; (b & d) high magnification image of 60 MPa and 353 MPa monoliths

7.8.4 Crucibles from nc-HfO_2

It was observed that nc-HfO_2 powders compacted at 353 MPa pressure and sintered by using TSS_2 had yielded monoliths with the highest ρ_S. By using this method the powders Hf0D and Hf11D could be sintered to a maximum density of about 96 % T.D. Hence, these two powders were chosen for making crucibles. The powders Hf0D and Hf11D were compacted at 353 MPa and sintered by using TSS_2 method. The sintered densities of Hf0D and Hf11D crucibles were found to be 95.8 ± 0.3 % T.D and 97.0 ± 0.1 % T.D respectively. It was observed that these sintered crucibles were devoid of any visual defects viz., cracks, chipping, deformation and end-capping (Fig. 7.14). These crucibles were parted and were subjected to microstructural analysis by using SEM. The fractured surfaces were found to possess grains with sizes ranging between 1 – 4 μm. Both Hf0D and Hf11D sintered crucibles could be used for melting uranium bearing alloys. Hf11D crucibles are more suitable for they contain a lesser porosity (< 3%).

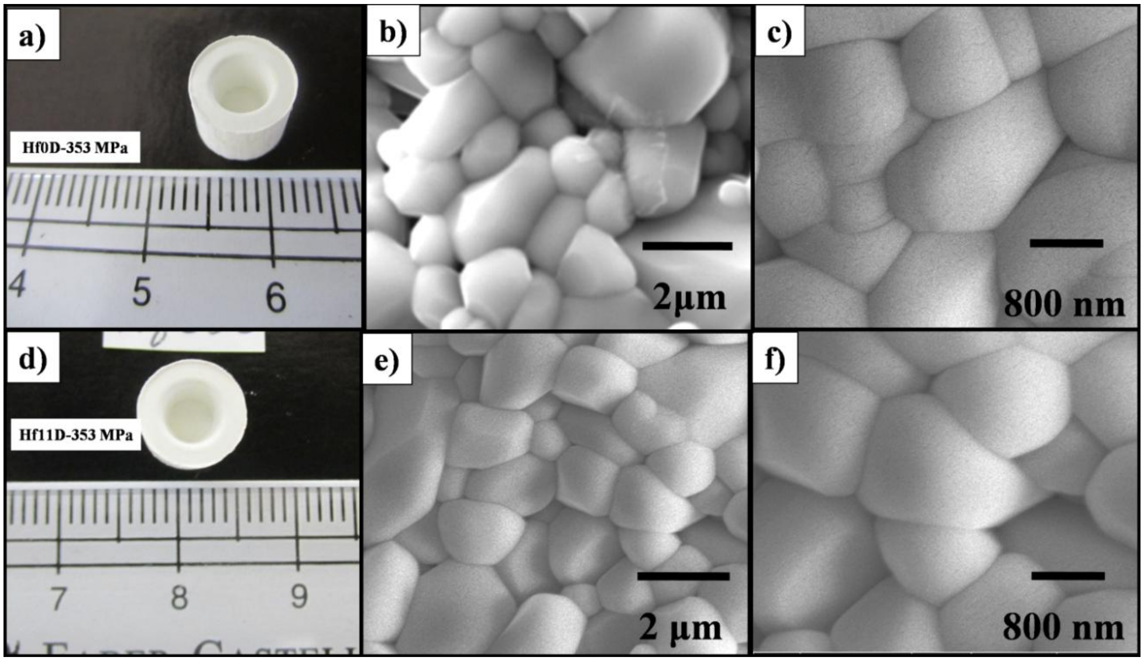

Figure 7.14 (a-c) Hf0D sintered cup derived with 353 MPa pressure and (d-f) Hf11D derived with 353 MPa pressure; (a and d) photograph of sintered hafnia crucibles and (b and e) low magnification SEM image fractured surfaces of sintered HfO_2 crucibles and (c & f) high magnification SEM image fractured surfaces of sintered hafnia crucibles

7.9 Conclusions drawn from the preparation of nc-HfO_2 by SMS and its sintering

For the first time nc powders of metastable c-HfO_2 was prepared by the SMS. It was also demonstrated that either the metastable cubic form or the thermodynamically stable monoclinic form could be derived at room temperature by tailoring the composition of the melt.

The addition of nitrite to the salt melt mixture probably brings about a reduction in the oxygen potential of the melt which in turn controls the reaction kinetics as well as the characteristics of the product. The SSA and lattice strain decreased with the nitrite content while the XCS showed a reverse trend. Microstructural analysis of these powders by using TEM reaffirmed their nanocrystallinity as well as their crystallite size estimated from XRD (20 to 40 nm). Further, both XRD and Raman spectra ascertained that the starting mixtures with Φ values of 0 - 0.32 and 0.82 yielded m-HfO_2 and c-HfO_2 respectively. Comparison of the Raman spectra pertaining to both microcrystalline and nc samples revealed that the latter exhibited broader peaks due to quantum confinement. EELS of m-HfO_2 (Φ = 0) and c-HfO_2 (Φ = 0.82) were consistent with the observations made in the other investigations. However, further direct evidence in support of the presence of Hf in an oxidation state lower than 4+ could not be obtained.

A CP of 353 MPa was required to compact and sinter hafnia to a ρ_S of 97.2 ± 0.4 % T.D by using TSS_2 method. Point scan (EDS) of hafnia powders and sintered monoliths did not reveal the presence of any impurity. Morphological analysis of polished and thermally etched sintered monoliths revealed the presence of uniform grains with well-defined grain boundaries. The dihedral angle in sintered hafnia monoliths was found to be varying between 119-130^0. Shrinkage anisotropic factor (α) revealed that the hafnia compacts had undergone near isotropic shrinkage. Small crucibles made out of both Hf0D and Hf11D were devoid of visual cracks and physical defects.

7.10 Salt melt synthesis and two-step sintering of nc-YSH powders

The reaction observed in the preparation of YSH through SMS was quite similar to those observed in the preparation of HfO_2. The generalized equation pertaining to the salt melt synthesis of nanocrystalline YSH powders could be written as given in eqn. (4):

$$\begin{gathered}[\mathrm{NaNO_3}] + [\mathrm{KNO_3}] + [\mathrm{xY(NO_3)_3.6H_2O}] + (1-\mathrm{x})[\mathrm{HfCl_4}] \rightarrow [\mathrm{Y_xHf_{1-x}O_{2-0.5x}}] + \\ (1.75\mathrm{x})(\mathrm{O_2}) + (2+3\mathrm{x})(\mathrm{NO_2}) + [\mathrm{NaCl}] + [\mathrm{KCl}] + 6\mathrm{x}(\mathrm{H_2O}) + (1-2\mathrm{x})(\mathrm{Cl_2})\end{gathered} \tag{7.4}$$

The XRD pertaining to YSH containing 6 mol% of yttrium indicated the presence of both m-HfO_2 and c-YSH phase whereas nc-YSH powders containing 10-30 mol % yttrium revealed the presence of only the cubic phase.

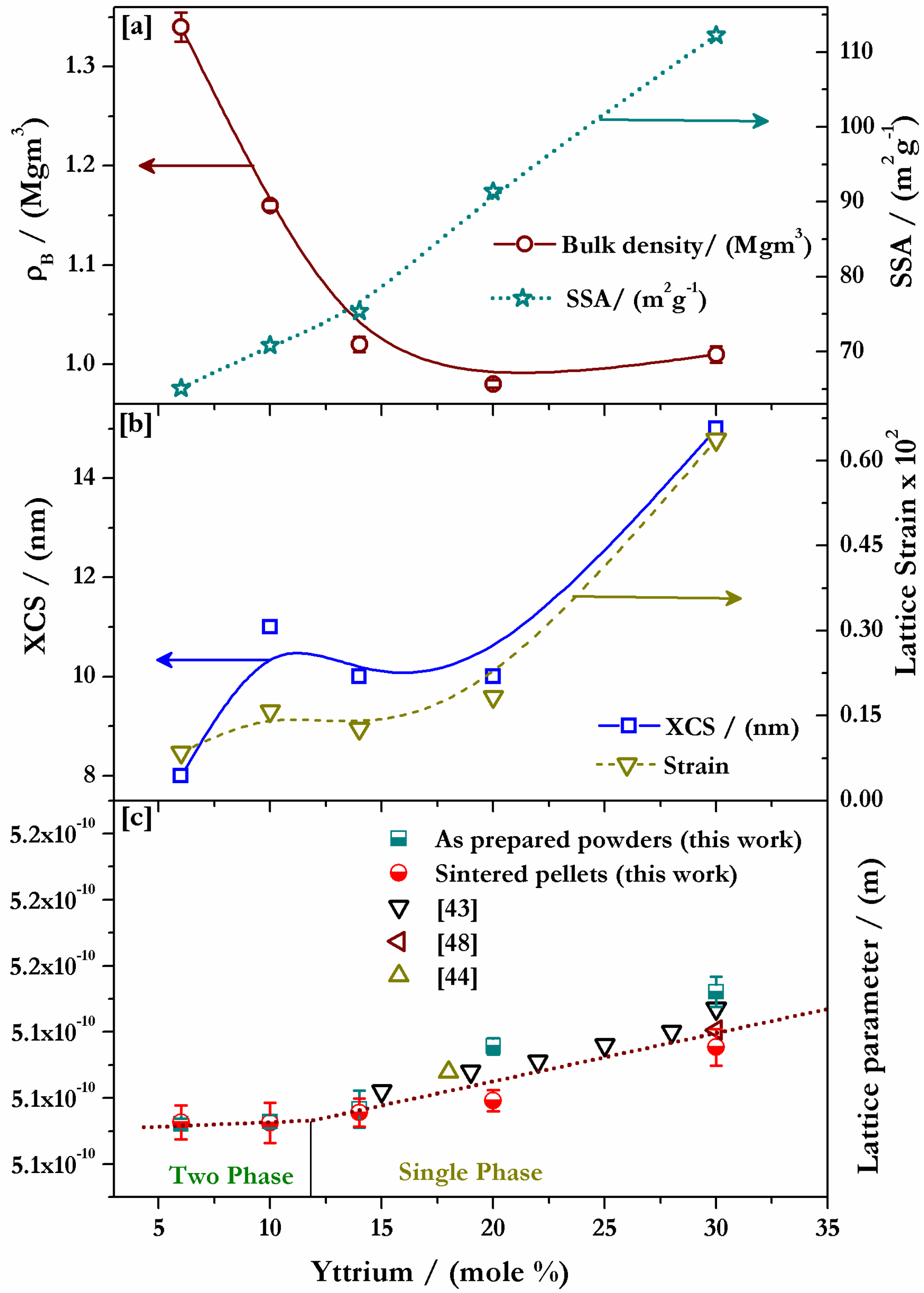

Figure 7.15 (a) Dependence of the ρ_B and SSA with yttrium content; (b) Dependence of XCS and lattice strain with yttrium content; (c) variation of lattice parameter with yttrium (mole %)

Table 7.7 Characteristics of nc-YSH powders

Sample	ρ_B (Mg m^{-3})	RC (ppm)	SSA (m^{2}g^{-1})	XCS (nm)			Particle size distribution		
				Sc	HW	Strain x10^{-2}	10 vol. % of sample has size less than (µm)	50 vol. % of sample has size less than (µm)	90 vol. % of sample has size less than (µm)
6YSH	1.34	415	65	7	8	0.085	4	12	38
10YSH	1.16	263	71	9	11	0.158	5	16	47
14YSH	1.02	425	75	9	10	0.127	4	14	38
20YSH	0.98	485	91	8	10	0.183	5	17	49
30YSH	1.01	451	112	7	15	0.637	7	21	80

7.11 Bulk density (ρ_B), PSD and SSA

The powder characteristics of nc-YSH powders are presented in Table 7.7. The ρ_B of the nc-YSH powders decreases exponentially with the yttrium content (Fig. 7.15a). The decrease in ρ_B with the quantity of dopant was found to be more pronounced up to a dopant concentration of 14 mole % Y, beyond which there was no appreciable change. This variation in ρ_B could be due to the variation in the size distribution of particles (Fig. 7.16). From the Fig. 7.16 it is evident that all YSH powders exhibit bimodal size distribution of particles with the maximum size fraction at around 10 μm (about 81 % of the fraction of particles possessed an average size of 10 μm).

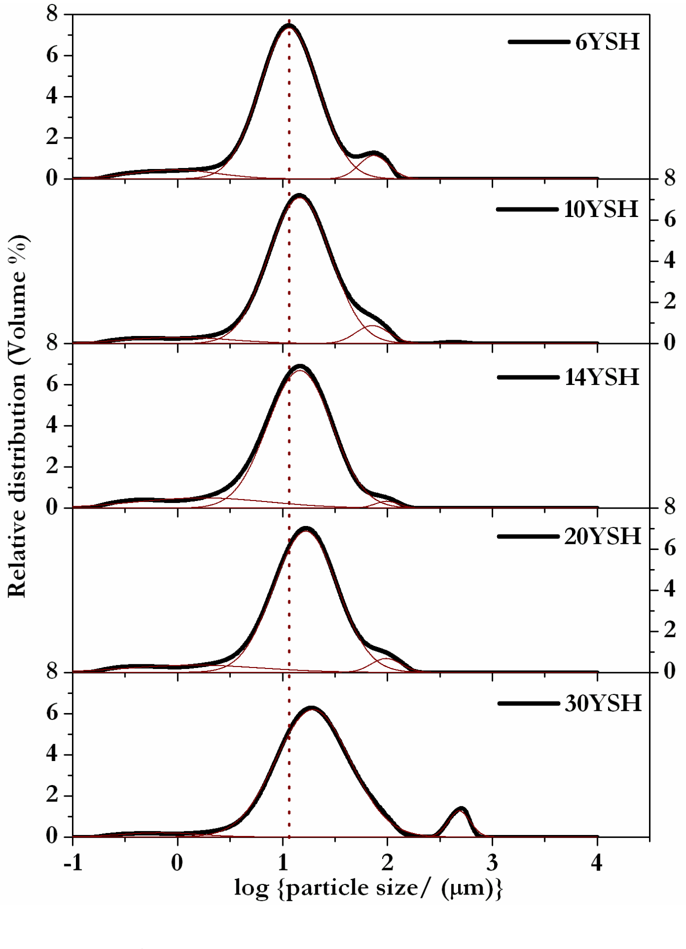

Figure 7.16 Size distribution of particles in nc-YSH powders (Thick solid lines – experimental curve, thin solid line – deconvoluted curves)

It is evident from Fig. 7.16 that 6YSH powders possess two size fractions of particles (lower fraction: ≈ 92 % and higher fraction: ≈ 8 %). All other powders exhibited a “near unimodal” size distribution of particles. A closer observation reveals that increase in the yttrium content shifts the peak maxima towards a higher size fraction (Fig. 7.16).

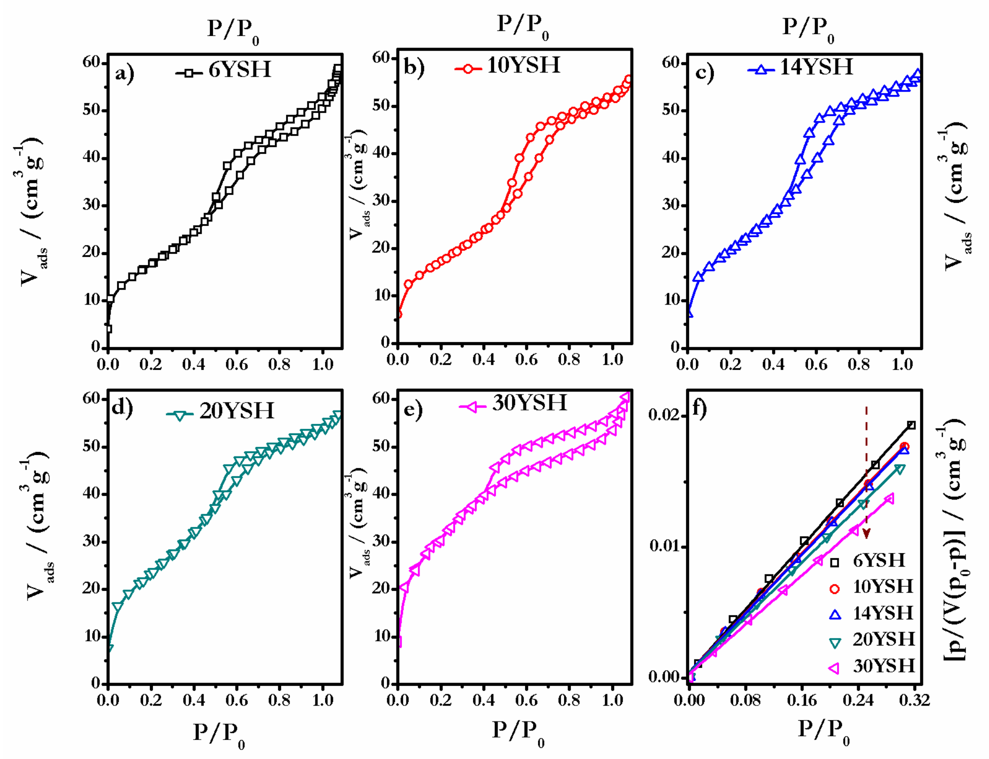

Figure 7.17 (a-e) BET adsorption isotherm of nc-YSH derived through SMS and (f) linear BET adsorption isotherm

All the YSH powders possessed high SSA (65 to 112 m^2g^{-1}, Fig. 7.15a) and were higher compared to that reported for powders prepared by precipitation [37]. Fig. 7.15a shows the variation of SSA of nc-YSH powders with yttrium content. The adsorption isotherms and the corresponding linear BET isotherm plots pertaining to the nc-YSH powders are depicted in Fig. 7.17. The hysteresis in their adsorption isotherm suggested that these powders were microporous. Further, the BET adsorption isotherms reveal that the slope decreases with yttrium addition. In other words, this plot (Fig. 7.15a) indicates that the SSA of YSH powders increases with yttrium content as a result of formation of microporosity (hysteresis in BET isotherm). Probably interparticle cohesion was also enhanced due to Y^{3+} doping.

7.12 Carbon residue

The impurity levels in nanocrystalline powders which are to be used in sensor [38] and nuclear application should be within 1000 ppm [33]. The YSH powders obtained in this study were found to contain carbon residue varying from 250 – 500 ppm. Thus, this method does not necessitate additional calcination step for removing the residual carbon. Hence, these nanopowders could be used as such without any further processing.

7.13 Phase identification, XCS and lattice strain

The XRD patterns pertaining to the YSH powders are presented in Fig. 7.18. From this figure (Fig. 7.18) it is evident that these powders comprise only the cubic phase. However, the powder 6YSH comprised both the monoclinic and cubic phases. Porter and Heuer [39] have reported that the volume fraction of monoclinic phase present in c-YSH could be evaluated from the XRD pattern by considering the multiplicity factor and linear absorption coefficient of m-HfO_2 and c-YSH phases. It was found that 6YSH powders contain 21 % and 79 % of m-HfO_2 and c-YSH phase. The volume fraction of c-YSH in 6YSH was higher as compared to the values reported in reference [15]. Thus, it could be concluded that SMS helps in stabilizing a higher fraction of YSH phase as compared to the solid state route [15].

The XCS values derived by using both Sc [17] and HW [17] are in good agreement except for those pertaining to the 30YSH powders (Table 7.7 & Fig. 7.15b). This difference in XCS between the Sc and HW estimate in 30YSH could be attributed to lattice strain. The Sc method leads to erroneous XCS values especially for nc materials possessing high lattice strain [40]. The measured values of the lattice parameter pertaining to all the YSH powders are shown in Fig.15c. It is observed that the lattice parameter increases with yttrium addition [41] (Fig. 7.15c). The empirical (Vegard's) equation [42] was used as the reference to compare the measured values of lattice parameter. The lattice parameter of powders reported in this study (Fig. 7.15c) is marginally higher (0.15 %) as compared to those reported in other investigations [42-44]. However the powders employed in the studies reported in references [18, 43, 44] were microcrystalline.

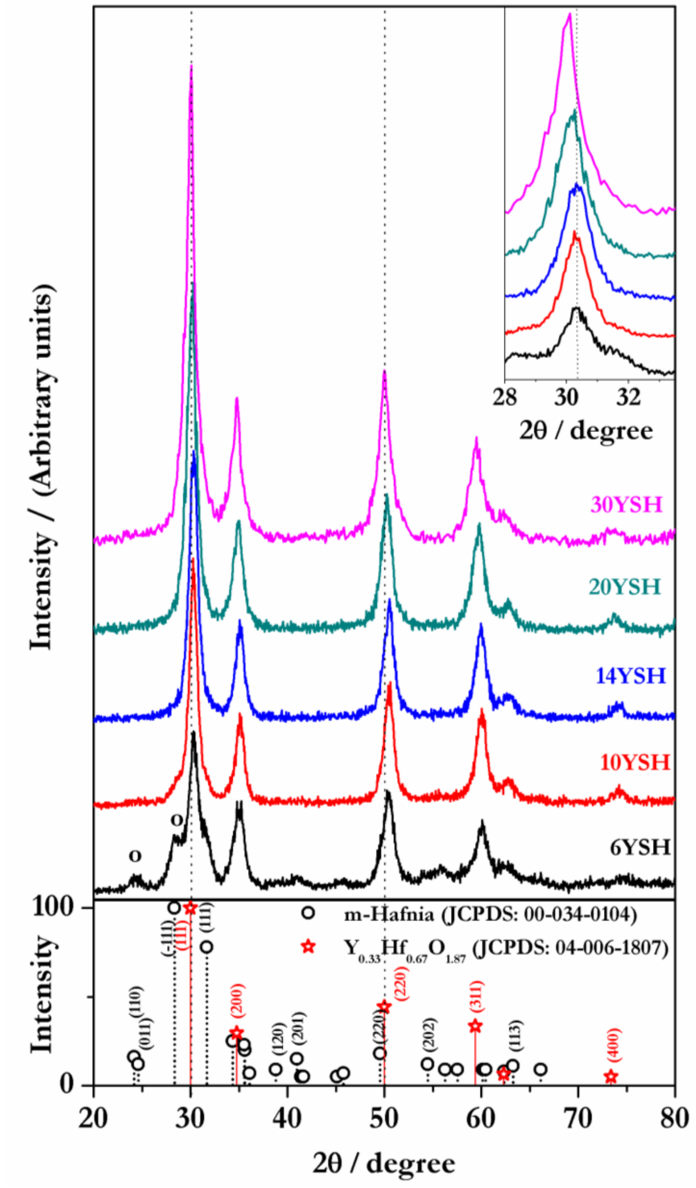

Figure 7.18 XRD pattern of nc-YSH powders derived through SMS

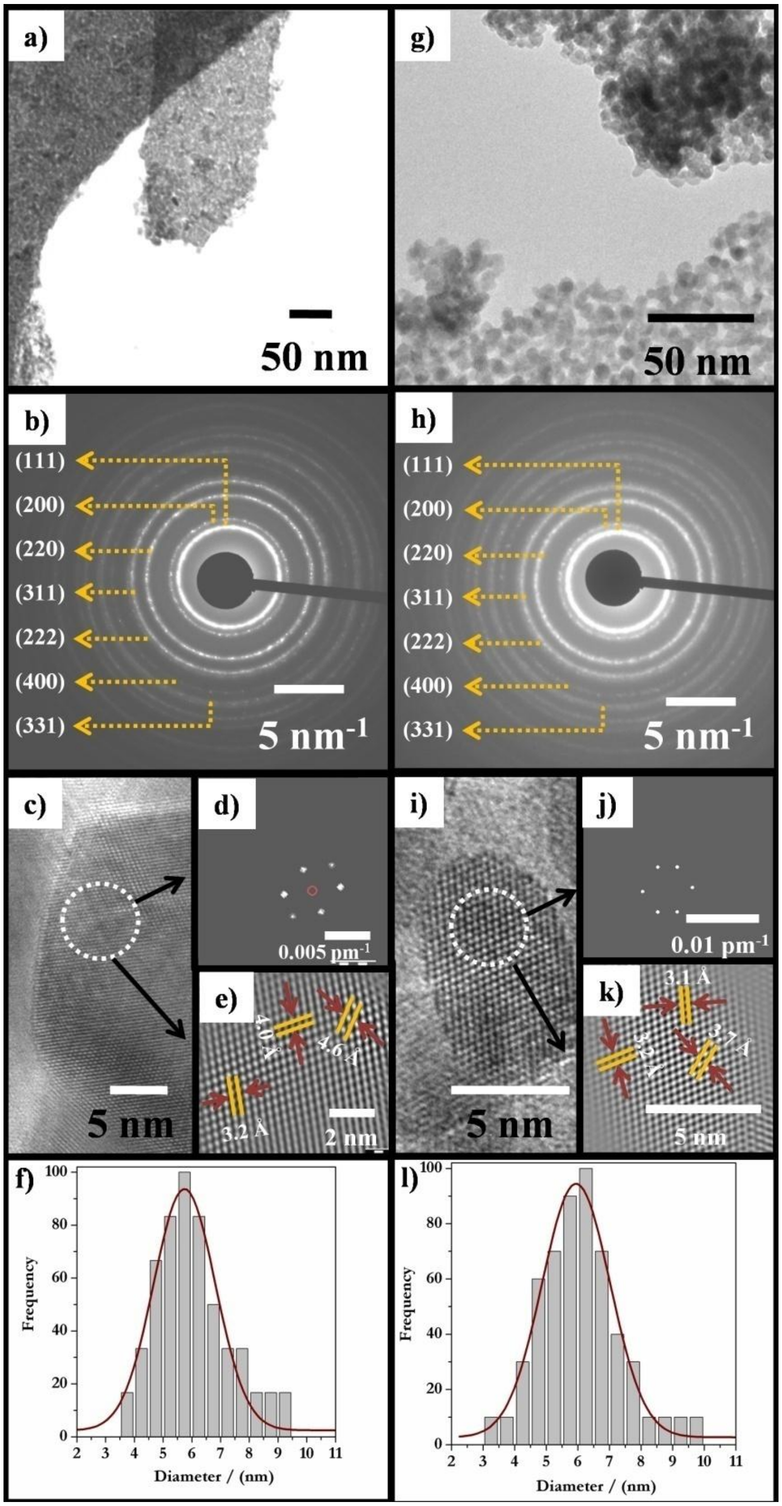

Figure 7.19 *TEM images of YSH [10YSH (a-f) and 14YSH (g-l)] revealing: (a & g) bright field image showing uniform nano grains; (b & h) SAED image revealing the cubic phase; (c & i) HRTEM image revealing nano grains; (d & j) FFT of selected area; (e & k) IFFT of the corresponding FFT and (f & l) grain size distribution plot*

7.14 Microstructural analysis by using SEM and TEM

TEM investigation also revealed a “near unimodal” distribution of grains (Fig. 7.19). The unimodal distribution of sizes among the agglomerates as well as grains is possibly due to homogeneous nucleation and growth. Both 10YSH and 14YSH powders revealed that the YSH powders (Fig. 7.19) comprised unimodal size distribution of grains with maxima ranging between 5-6 nm (Fig. 7.19f & Fig. 7.19*l*). SAED patterns of 10YSH and 14YSH confirmed their nanocrystallinity and that they comprise cubic phase (Fig. 7.19b & Fig. 7.19h). HRTEM images (Fig. 7.19c & Fig. 7.19i) of these samples depict the values of the “d-spacings” that are in agreement with the values cited in JCPDS [YSH [45] – PDF No. 04-006-1807]. It was also observed that the grain sizes measured from TEM images are comparable with the XCS [10YSH (Sc: 9 nm, HW: 11 nm) and 14YSH (Sc: 9 nm, HW: 10nm)]. Elemental mapping and “point mode” analysis on YSH powders for yttrium by using SEM revealed that it is distributed uniformly in the YSH powders and the measured dopant concentrations (approximately) are comparable to the values pertaining to the overall composition.

7.15 Sintering of nc-YSH

7.15.1 Green pellets

Compaction experiments revealed that the ρ_G of all the YSH pellets increase linearly (35 % T. D to 47 % T. D) with the CP (60 MPa to 353 MPa). Table 7.8 and Fig. 7.20a depict the characteristics of these green compacts. The ρ_G values obtained in this study are rather low possibly due to the smaller size of agglomerates and lack of multi modal distribution of sizes [31]. Segal et al. [46] had reported that if the powders contain weak or no agglomerates, it would result in uniform distribution of pores in the compacts and sintering of such compacts would result in monoliths with very high density. Similarly, Ma et al. [47] had shown that the green pellets derived with multimodal size distribution of particles has a detrimental effect on the density due to differential densification during the final stage of sintering as well as multimodal size distribution of grains in the final product. Variation in ρ_G with the CP obtained for all the different powders did not show any significant variation. This could be attributed to the similarity in the particle size distribution in them.

Table 7.8 ρ_G of YSH pellets derived through SMS

CP (MPa)	**6YSH**	**10YSH**	**14YSH**	**20YSH**	**30YSH**
			% T.D		
60	35.8 ± 0.5	34.8 ± 0.3	34.8 ± 0.7	36.0 ± 0.3	36.0 ± 0.7
120	39.0 ± 0.1	37.9 ± 0.1	38.0 ± 0.3	39.2 ± 0.4	37.4 ± 0.1
180	41.0 ± 0.6	40.1 ± 0.1	39.6 ± 0.4	41.6 ± 0.4	40.5± 0.3
244	44.1 ± 0.4	42.7 ± 0.2	42.5 ± 0.6	43.6 ± 0.4	42.3 ± 0.2
317	45.8 ± 0.3	44.9 ± 0.2	44.3 ± 0.2	45.8 ± 0.2	44.3 ± 0.4
353	47.3 ± 0.1	45.9 ± 0.2	45.5 ± 0.2	46.6 ± 0.3	45.2 ± 0.4

7.15.2 Phase characterization and carbon residue in sintered YSH monoliths

Fig. 7.21 shows the X-ray diffraction patterns pertaining to the sintered YSH. These patterns were indexed appropriately by comparing them with the standard JCPDS pattern [m-HfO_2 – JCPDS No. 00-034-0104; c-YSH – JCPDS No. 04-006-1807]. Lattice parameter values of the sintered YSH pellets were determined and are presented in Fig. 7.15c. The values of lattice parameter derived were compared with those cited in the literature [43, 44, 48]. An empirical equation presented in ref. [48] was also used to derive the lattice parameter of YSH as a function of its yttrium content [mol %] (Fig. 7.15c). These values are in agreement with the data presented in ref. [43, 44, 48]. Fig. 7.15c also reveals that the lattice parameters of the “as prepared” nc-YSH powders were higher as compared to that of the sintered YSH as well as those predicted by the empirical equation. This deviation could be due to the increased lattice strain in the nanocrystalline YSH. Fig. 7.15b shows that lattice strain increases with yttrium addition and that calcination anneals the lattice strain and leads to grain coarsening. Carbon residue of the randomly selected sintered YSH pellets was found to vary from 51 – 140 ppm.

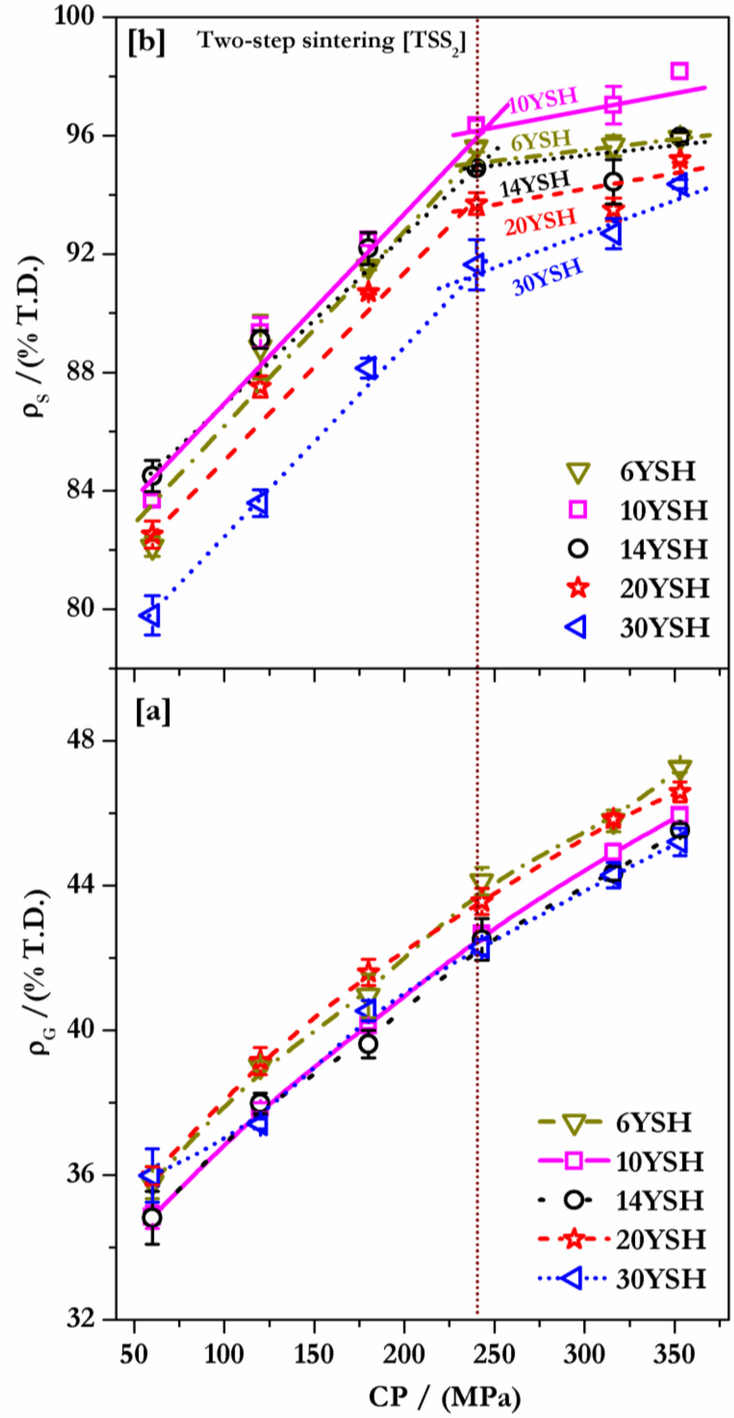

Figure 7.20 Variation of (a) ρ_G *and (b)* ρ_S *with the CP*

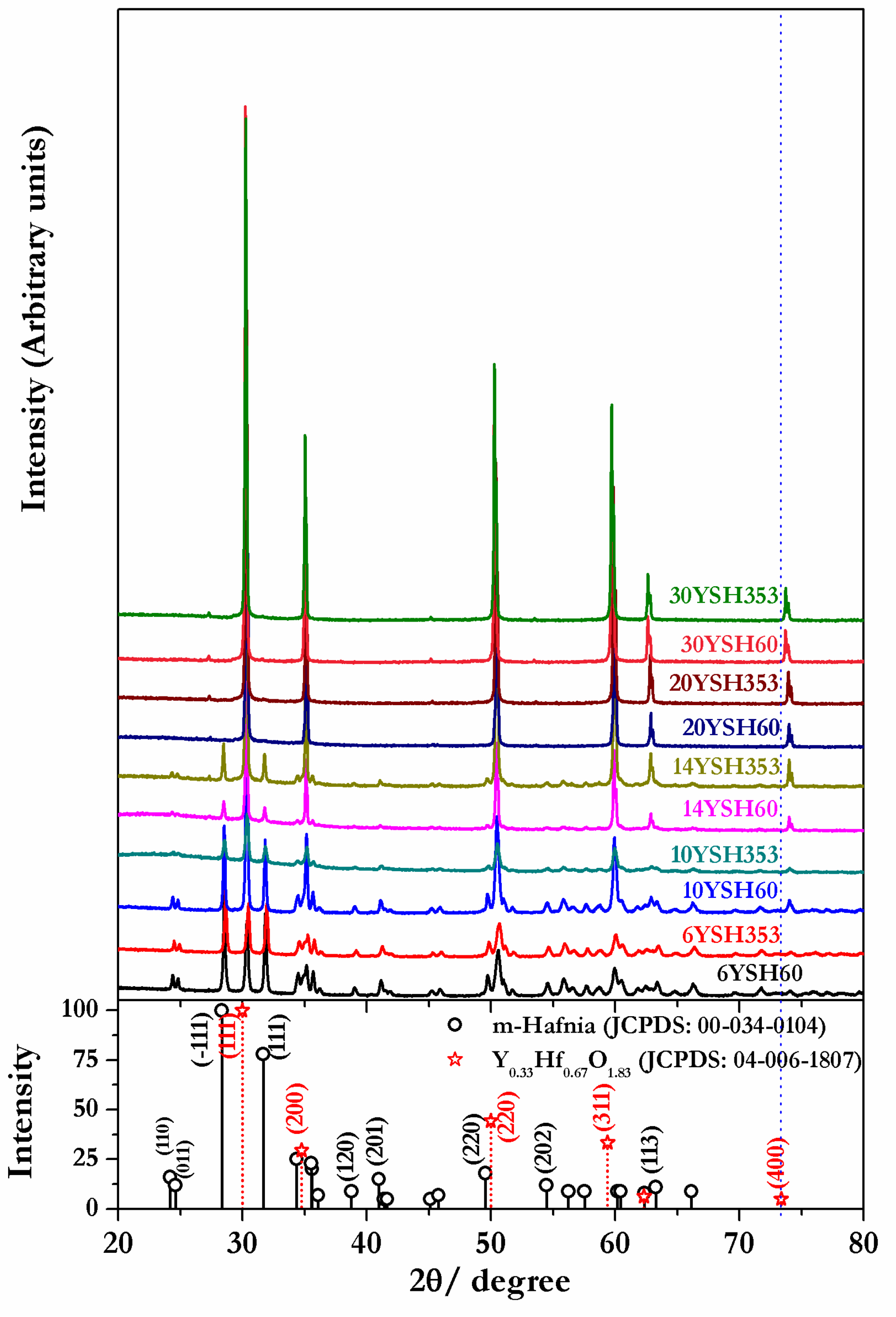

Figure 7.21 XRD pertaining to sintered YSH monoliths

7.15.3 Sintering nc-YSH and microstructural investigations on sintered YSH monoliths

To identify an appropriate sintering procedure and its impact on the final densification, selected samples of YSH pellets were sintered by using CS (xxYSH$_{CS1}$, xxYSH$_{CS2}$ and xxYSH$_{CS3}$) and TSS (TSS$_1$ and TSS$_2$) procedures (Chapter 2). The values of the ρ_S are tabulated in Table 7.9 - 7.10. The pellets sintered by TSS_2 showed better densification as compared to those sintered by TSS_1 and CS (Table 7.9 - 7.10). Hence, the TSS_2 method was used to sinter all the YSH compacts.

Table 7.10 and Fig. 7.20b depicts the variation in the ρ_S with the CP pertaining to the YSH pellets derived through TSS_2. In general, it was observed that doping HfO_2 with Y^{3+} leads to a decrease in ρ_S (except for 10YSH). TSS_2 method with a final temperature as low as 1773 K (353 MPa) yields monoliths with a high ρ_S (94.4 ± 0.2 % T.D to 98.2 ± 0.3 % T.D). These values of ρ_S were higher than those reported in the literature [15, 34, 43, 48]. Fig. 7.20 depicts the variation in the green and sintered densities of the YSH powders. The sintered densities are directly correlated with the corresponding green densities. The green density is found to decrease with the Y^{3+} content in the starting material. However the XCS and SSA are found to increase with the Y^{3+} content. The increase in the former is due to grain coarsening. Size distribution of particles of YSH powders reveals that the formation of larger size fraction of particles was found to increase with Y^{3+} doping (Fig. 7.16) i.e., agglomeration increases with yttrium doping and compaction of these powders would result in compacts with lower green density. Thus more Y^{3+} doping led to an increase in the size fraction of larger particles and inefficient packing. This in turn brought down the green density and the corresponding sintered density. Thus the effect of interparticle cohesion seems to overwhelm the influence due to increased SSA.

The increase in SSA and BD is probably due to the introduction of microporosity in the powder. However, the particles (i.e. agglomerates of crystallites) grow with Y^{3+} doping (Fig. 7.16). Thus the increased porosity and inefficient packing in the bimodal powders have brought down the BD. Moreover the trend in the variation in the green density with Y^{3+} content indicates that the fracture of particles becomes progressively difficult with Y^{3+} doping. This leads to diminished values of green density. Thus, even though the SSA increases with Y^{3+} doping, a commensurate increase in the sintered density is not observed.

XRD analysis of sintered YSH monoliths revealed that a single phase solid solution is formed only when the Y^{3+} concentration is more than 20 mol %, below which the products were only partially stabilized (biphasic) (Fig. 7.21).

In order to optimize the process parameters for obtaining a final product with a desirable density, the variation of α (shrinkage anisotropy factor) [35, 49] and relative pore fraction with ρ_S are compared (Fig. 7.22a). It is observed that α is linearly correlated with the ρ_S (0.75 - 0.95). Rahmann [35] had reported that α is inevitable but its magnitude needs to be kept optimum. Additionally, Exner and Giess [49] have shown that α increases (0.3 – 0.7) with the ρ_S (60 – 99 % T.D) and it is independent of the size and shape of the particles. These studies [49] were conducted on jagged and spherical powders of dimension 6 μm and 13 μm. The results obtained in this study do follow a linear variation and are in line with the results obtained by Exner and Giess [49]. However, the values of α are quite high compared to that pertaining to micron sized particles. Thus, it could be concluded that the nc-YSH sinters with uniform AS and RS. Relative pore fraction plot (Fig. 7.22b) reveals that the open pore fraction decreases while the closed pore fraction increases (marginally) with the CP. Fig. 7.22b also reveals that the critical CP is about 353 MPa wherein both closed and open pore fraction were nearly equal (at around 96 % T.D) and are at their minimum.

Table 7.9 Sintering parameters and ρ_S of YSH monoliths (317 MPa; CS and TSS method)

Sample	ρ_G	ρ_S				
		CS_1	**CS_2**	**CS_3**	**TSS_1**	**TSS_2**
		$xxYSH_{CS1}$	**$xxYSH_{CS2}$**	**$xxYSH_{CS3}$**	**$xxYSHS_1$**	**$xxYSHS_2$**
		% T. D				
10YSH	44.9 ± 0.2	75.4 ± 0.4	90.8 ± 0.1	92.3 ± 0.1	92.2 ± 0.3	97.0 ± 0.6
20YSH	45.8 ± 0.2	71.8 ± 0.8	82.9 ± 0.7	84.6 ± 0.1	85.1 ± 0.3	93.5 ± 0.4

xx - mole fraction of yttrium (in %)

CP - 317 MPa

CS_1 – 1673 K 4 h

CS_2 – 1773 K 4 h

CS_3 – 1873 K 4 h

TSS_1
Step 1 - 1873 K 1 h
Step 2 - 1673 K 4 h

TSS_2
Step 1 - 1873 K 1 h
Step 2 - 1773 K 4 h

Table 7.10 ρ_S of YSH monoliths which were sintered by using the TSS_2 method

CP (MPa)	**6YSH**	**10YSH**	**14YSH**	**20YSH**	**30YSH**
			% T. D		
60	82.1 ± 0.3	83.7 ± 0.2	84.5 ± 0.5	82.5 ± 0.5	79.8 ± 0.7
120	88.9 ± 1.1	89.4 ± 0.5	89.1 ± 0.3	87.5 ± 0.4	83.6 ± 0.5
180	91.6 ± 0.1	92.5 ± 0.2	92.2 ± 0.6	90.7 ± 0.1	88.2 ± 0.3
244	95.6 ± 0.2	96.3 ± 0.2	94.9 ± 0.1	93.7 ± 0.4	91.6 ± 0.9
317	95.7 ± 0.4	97.0 ± 0.6	94.4 ± 0.8	93.5 ± 0.4	92.7 ± 0.5
353	95.9 ± 0.2	98.2 ± 0.3	96.0 ± 0.2	95.2 ± 0.1	94.4 ± 0.2

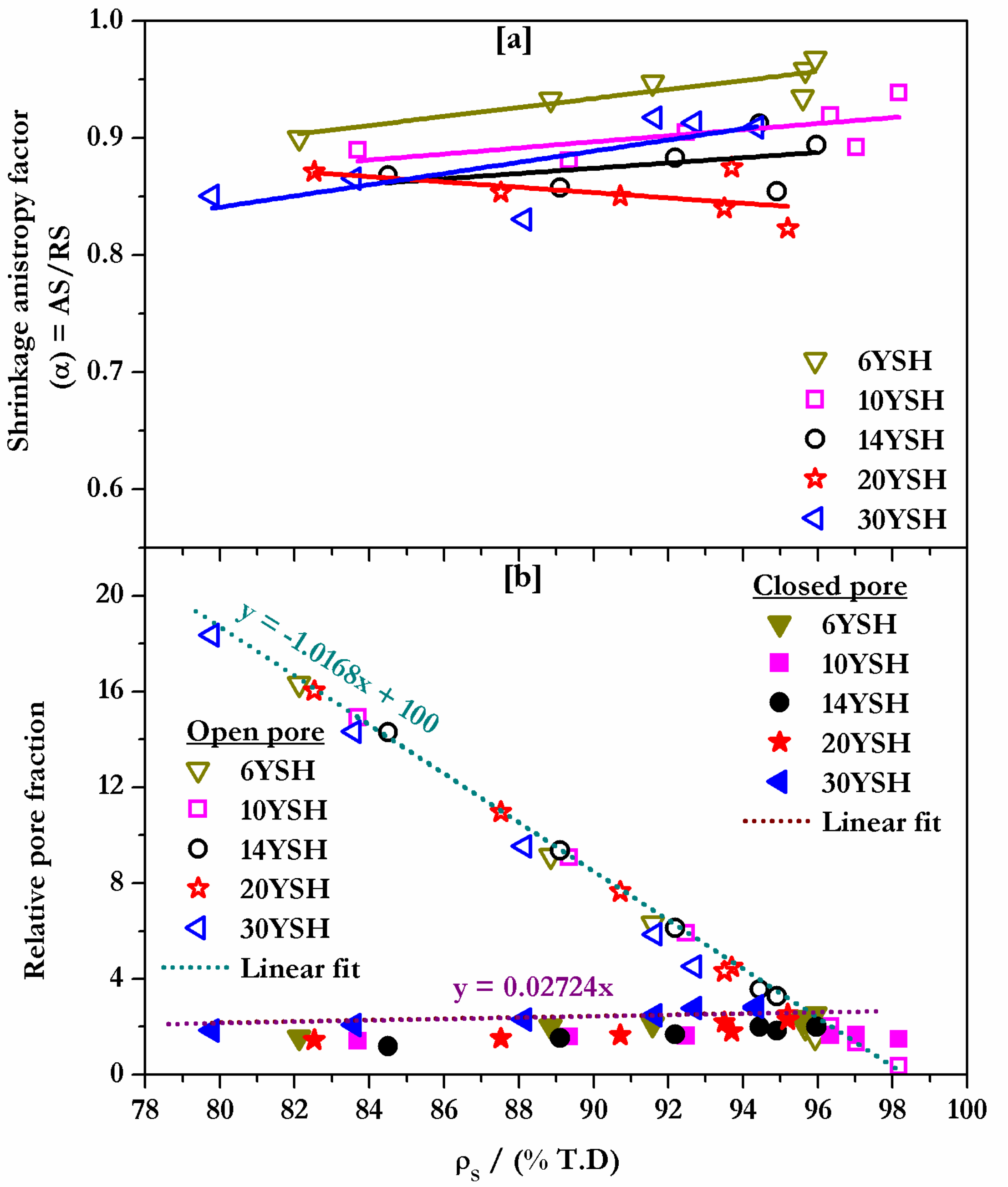

Figure 7.22 (a) Variation in the shrinkage anisotropy factor (α) with the sintered density [TSS_2] and (b) Interdependence of the volume fractions of open and closed pore with sintered density [TSS_2]

Microstructural investigation of the sintered 30YSH pellets are shown in Figs. 7.23 – 7.24. The images (Figs. 7.23 – 7.24) reveal that the Y^{3+} and Hf^{4+} are uniformly distributed in the sintered 30YSH monolith. SEM of sintered 30YSH monolith (60 MPa) show the presence of both inter and intergranular pores at the surface as well as in the fractured surface. The SEM image of 30YSH monoliths (compacted at 353 MPa) reveals many interesting features such as faceted grains with well defined grain boundaries, presence of pentagonal grains with a dihedral angle of 121 - 127^0 and uniform distribution of yttrium and hafnium on the surface. Additionally, it also reveals that the grain size varies from 5 - 12 µm (YSH derived by using TSS_2).

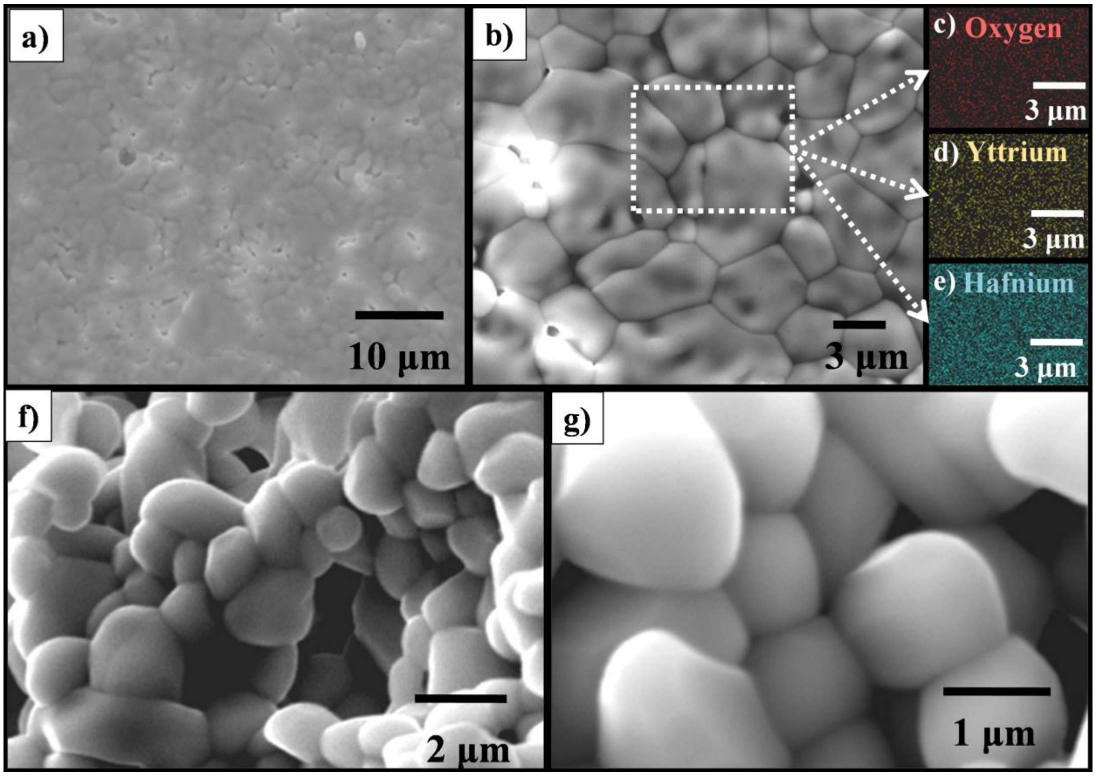

Figure 7.23 SEM images obtained with sintered 30YSH pellets (60 MPa) (a-b) porous sintered surfaces, (c-e) elemental mapping/distribution of oxygen, yttrium and hafnium on the selected sintered surface of YSH and (f-g) image of the fractured sintered surface revealing intra and intergranular pores

7.15.4 YSH crucibles

In general it was observed that the nc-YSH powders compacted at 353 MPa and sintered by the TSS_2 method had yielded monoliths with the highest ρ_S. Among the YSH powders, 10YSH had yielded a final sintered density of 98.2 ± 0.3 % T.D which is the highest among the values obtained in this study. The XRD studies revealed that the 20YSH and 30YSH powders had yielded monoliths comprising complete solid solution. Hence, among the nc-YSH powders, 30YSH was selected for making crucibles. In addition crucibles were also made out of 10YSH powders in order to understand the effect of phase segregation on the integrity (cracks, chipping and shape distortion) [15] of the sintered YSH crucibles (Fig. 7.25). It was observed that the ρ_S of 10YSH and 30YSH crucibles were 97.8 ± 0.1 % T.D and 94.1 ± 0.3 % T.D respectively. Further, the sintered crucibles (10YSH and 30YSH) were devoid of cracks and physical defects (layering, cracks, end-capping and hour glassing) (Fig. 7.25). Even though 10YSH powders yielded a marginally higher ρ_S, the crucibles made from 30YSH were preferred for they would be more suitable for applications that involve thermal cycling.

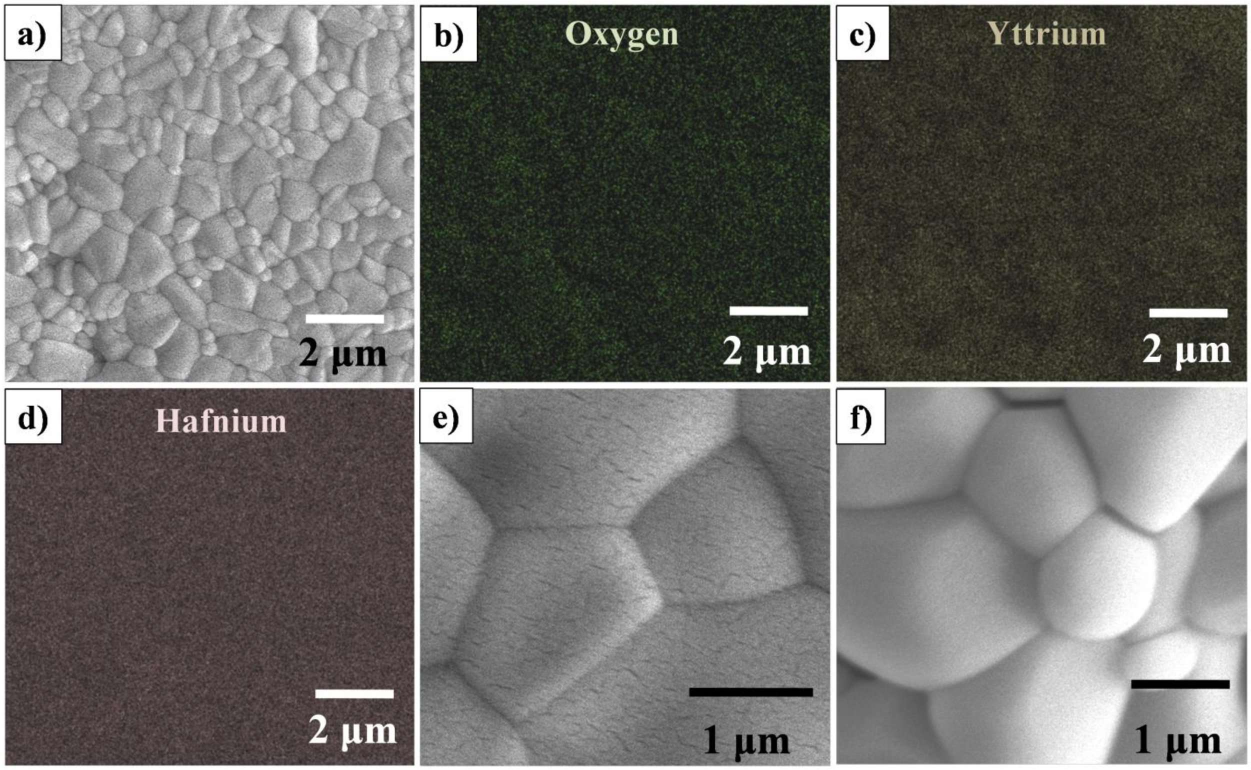

Figure 7.24 *SEM images obtained with sintered 30YSH pellets (353 MPa) (a & e) sintered surfaces, (b-d) elemental mapping/distribution of oxygen, yttrium and hafnium on the sintered YSH and (e) typical pentagonal grains revealing ≈ 121 - 127^0 dihedral angle and (f) image of fractured surface revealing grain coarsening*

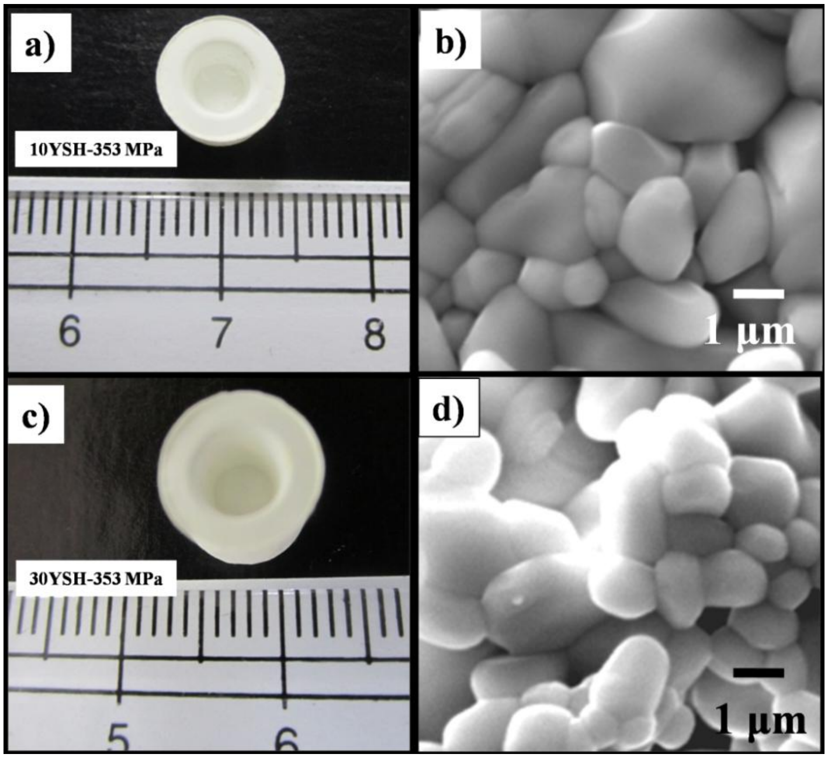

Figure 7.25 (a-b) 10YSH sintered cup derived with 353 MPa pressure and (c-d) 30YSH derived with 353 MPa pressure; (a and c) photograph of sintered YSH cup and (b and d) SEM image fractured surfaces of sintered YSH cups

7.16 Conclusions drawn from the synthesis and sintering of nc-YSH

For the first time fine grained nc-YSH powders were prepared by using SMS. It was observed that the yttrium content significantly influences the powder characteristics. Size distribution analysis revealed that the YSH powders exhibited near unimodal size distribution with maxima at 10 μm. The SSA, XCS, lattice strain and lattice parameter increased with yttrium addition while their ρ_B showed the reverse trend. TEM investigations reaffirmed the presence of nanograins with unimodal size distribution of grains and SAED further ascertained the presence of a fluorite solid solution. All powders exhibited monotonic increase in ρ_G with the CP. A compaction pressure of 353 MPa was found optimum in order to sinter YSH compacts containing 10 mol % of yttrium to a sintered density of 98.2 ± 0.3 % T.D by using the “two-step” sintering (TSS_2). Point scan and area mapping for constituent elements in the YSH powders and sintered monoliths confirmed the presence of uniform distribution of yttrium and hafnium. Morphological analysis of polished and thermally etched sintered monoliths revealed the presence of uniform grains with well-defined grain boundaries. The dihedral angle in sintered YSH monoliths was found to be varying between 121-127^0. Shrinkage anisotropic factor (α) revealed that the YSH compacts had undergone near isotropic shrinkage. Small crucibles made out of both 10YSH and 30YSH were devoid of visual cracks and physical defects.

7.17 SPS studies on nc-HfO_2 and nc-yttria stabilized hafnia (YSH) powders

Nc-HfO_2 and nc-YSH powders prepared via SMS were used as such in the SPS studies. Nc-HfO_2 powders were indexed as Hf0D (m-HfO_2) and Hf82D (c-HfO_2) while YSH powders were indexed as YSH bearing a prefix that indicated the yttrium content in mole %. The detailed experimental procedure employed in the preparation of nc m-HfO_2 and c-HfO_2 powders and YSH are described in Chapter 2. Hf0D were prepared without the use of sodium nitrite ($\Phi = 0$) while the c-HfO_2 powders were prepared with Φ value of 0.82.

7.17.1 SPS of nc-hafnia powders

XRD patterns (Fig. 7.26) reveal that the metastable c-HfO_2 powders had reverted back to the monoclinic phase upon SPS. The carbon residue in the sintered monoliths was found to vary between 500 to 734 ppm.

The characteristics of the spark plasma sintered pellets are presented in Table 7.11. ρ_S of these monoliths reveal that both the monoclinic and cubic hafnia powders could be sintered to a density of about 98 % T.D. Further, visual examination of these monoliths revealed that these monoliths were intact with no visible physical defects viz., cracks, hour glassing or deformation. However, pellets made out of nc c-HfO_2 powder when sintered by using the TSS or CS methods had undergone warping and some pellets were found to be cracked. These could be attributed to the phase reversal during sintering. Comparison of the ρ_S of Hf0D monoliths obtained by using different heating routines reveal that the rate of heating does not strongly influence the ρ_S of the final product. Nc-HfO_2 undergoes better densification than nc-YSH. The heating rate does not affect the ρ_S. SPS is energy and cost efficient, as expected, for obtaining the monoliths with about 98 % T.D, ρ_S.

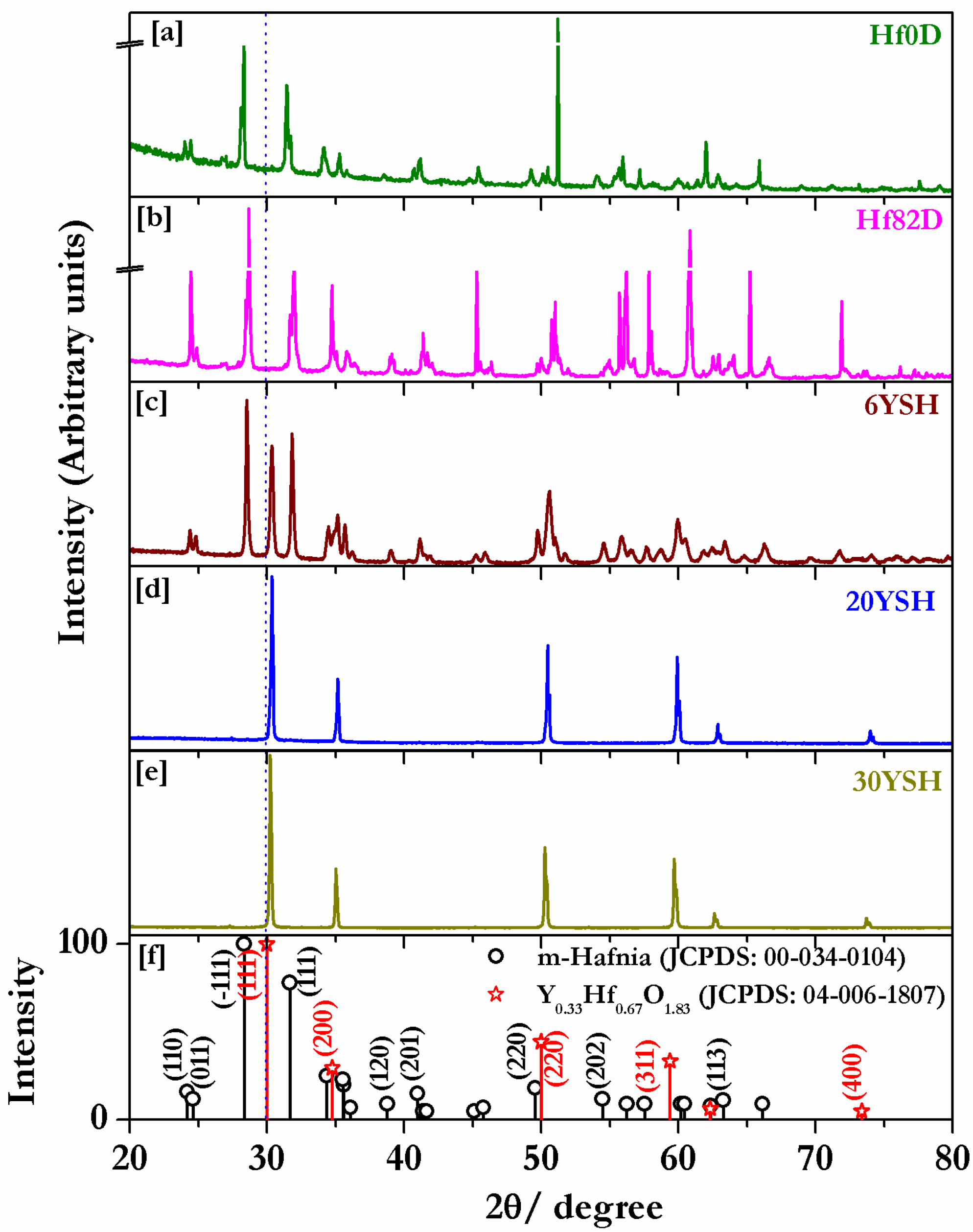

Figure 7.26 XRD patterns pertaining to spark plasma sintered monoliths (a-b) Hafnia (c-e) YSH and their (f) JCPDS pattern

Table 7.11 Characteristics of SPS sintered pellets

Material	Sample Index	Initial phase composition	Heating rate (K min^{-1})	ρ_S (% T. D.)	RC (ppm)	T_s
HfO_2	Hf0D	m	50	98.6 ± 0.2	503	1873 K 7 min
	Hf0D	m	100	98.8 ± 0.1	515	
	Hf82D	c (63 %) & m (37 %)	50	98.5 ± 0.2	719	
	Hf82D		100	97.9 ± 0.2	734	
YSH	6YSH	c (79 %) & m (21 %)	100	97.1 ± 0.2	502	
	20YSH	c	100	97.3 ± 0.6	613	
	30YSH	c	100	96.2 ± 0.3	455	

m- monoclinic, c - cubic, RC - carbon residue; T_s - Sintering schedule

The data pertaining to the synthesis and sintering of nc-hafnia powders are rather scant. Further, no reports have been published so far on the SPS of nc-HfO_2 powders. Our study is the “first of its kind”, on the SPS of pure nc-HfO_2 powders. Recently Dusan et al. [50] had sintered commercial hafnia powders in air (compacted at 440 MPa) without the addition of any sintering aid to a density of 66.1 % T.D (1573 K 3h 30 min) and 90.9 % T.D (1773 K 3 h 30 min). Piluso et al. [15, 34] had compacted hafnia powders by using semi-isostatic pressing in the presence of binder and plastizier and sintered to a density of 95.1 % T.D (1973 K 30 min). However, these compacts cracked during sintering due to phase transformation. Matovic et al. [51] had prepared hafnia powders by the solid state route, compacted at 150 MPa with no sintering additives and sintered these green compacts at different temperatures and obtained the following ρ_S viz., 88 % T.D (1573 K 2h), 94 % T.D (1673 K 2h) and 97 % T.D (1773 K 2h). Lakhlifi et al. [52] had sintered hafnia powders derived through precipitation method, compacted at 200 MPa and sintered the green pellets in air at different temperatures ranging between 1973 K to 2173 K to obtain final products with densities 89.6 T.D.% to 95.4 % T.D. (1973 K 2 h), 93.1 % T.D and 87.7 % T.D (2073 2h). Thus, it could be concluded that SPS had led to better densification than conventional method.

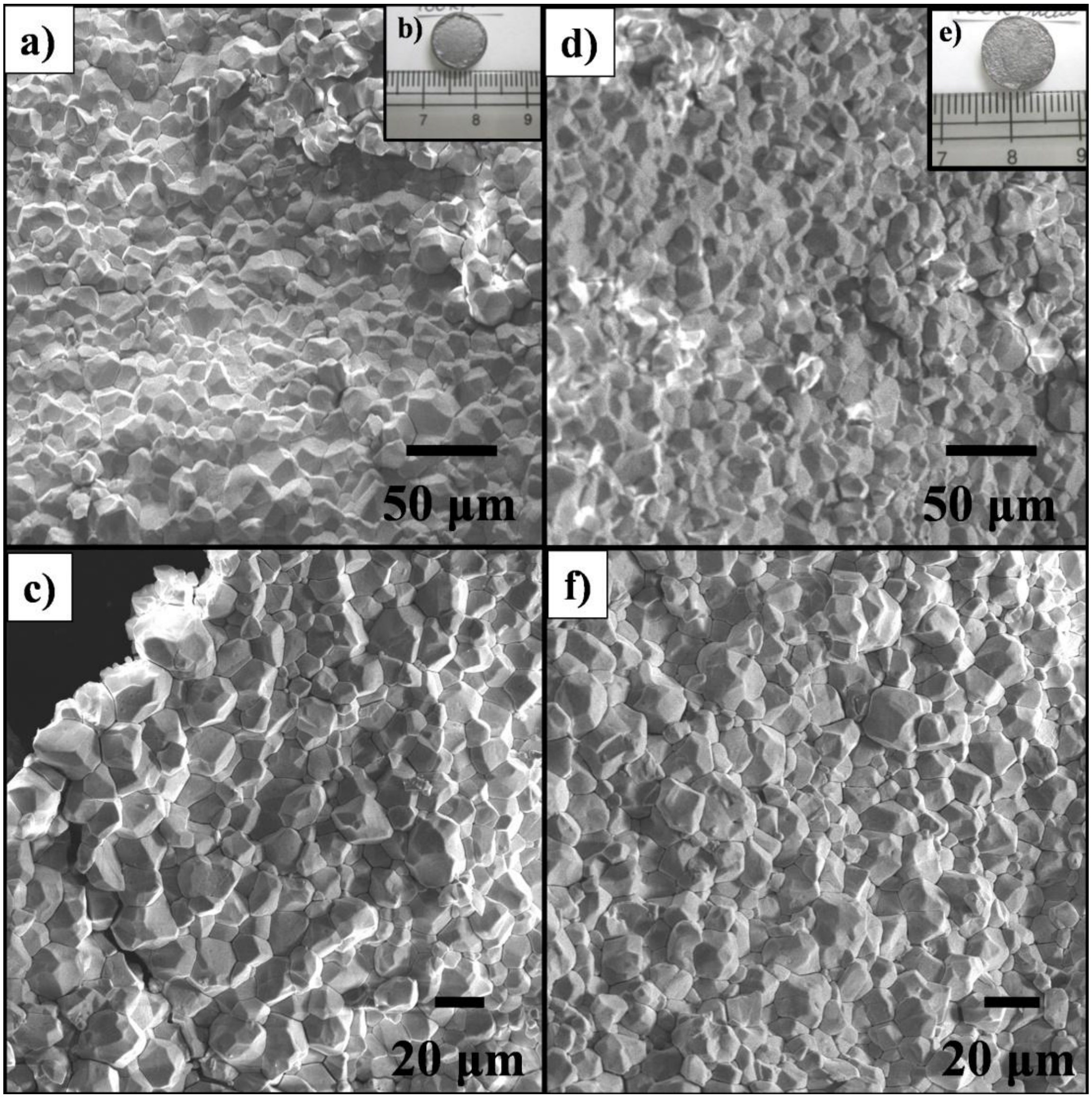

Figure 7.27 SEM images of (a-c) Hafnia (Hf0D); (d-f) Hafnia (Hf82D); (b & e) image showing "as prepared" hafnia pellets covered with graphite layer; (a & d) low magnification images of fractured pellet surface and (c & f) high magnification images showing faceted grains

Table 7.12 Comparison of the ρ_S of HfO_2 and YSH monoliths reported in the Literature

Reference	Sample	Method	CP (MPa)	ρ_G (% T.D)	S_m	T_s	ρ_S (% T.D)
[50]	HfO_2	Comm	440	51.7	C (air)	1573 K 3 h 30 min	66.1
						1773 K 3 h 30 min	90.9
					C (Ar)	1573 K 3 h 30 min	66.1
						1773 K 3 h 30 min	90.9
[15]	HfO_2	Comm	-	-	C (air)	1873 K 30 min	95.1*
	HfO_2 + *P* 40						72.0
	HfO_2 + *P* 70						48.0
	HfO_2 + 5 X						88.3
	HfO_2 + 8 X						91.2
[34]	HfO_2	Comm	0.1 to 30	-	C (air)	1873 K 1h	**98.5***
	HfO_2 + 1 X						96.6
	HfO_2 + 3 X						92.5
	HfO_2 + 5 X						91.6
	HfO_2 + 8 X						88.8
[51]	HfO_2	Re-Ox	150	-	C (air)	1573 K 2 h	88.0
						1673 K 2h	94.0
						1773 K 2 h	**97.0**
[52]	HfO_2	Flash reaction	200	45.6	C (air)	1973 K 2h	89.6
						1973 K 4h	95.4
						2023 K 2h	93.1
						2073 K 2h	87.7
	HfO_2 + 3 X	Thde		45.2	C (air)	1973 K 2h	67.4
						1973 K 4h	63.4
						2073 K 2h	65.2
						2173 K 2h	67.4
	HfO_2 + 10 X	Thde		43.4	C (air)	1973 K 2h	62.3
						1973 K 4h	59.2
						2073 K 2h	62.1
						2173 K 2h	63.9
[53]	HfO_2 + 15 X	*S*	57	-	SPS	1873 K 5 min	95.3
[54]	HfO_2	Comm	160 (IP)	-	C (air)	1473 K 1h	45.0
						1673 K 1h	75.0
						1823 K 1h	90.0
						1873 K 1h	94.0
						1923 K 1h	95.0
	HfO_2 + 5 X					1873 K 1h	88.5
	HfO_2 + 8 X						86.5
[55]	HfO_2 + 8 X	Thde	345	-	C (air)	2273 K 1h	92.0
	HfO_2 + 10 X						94.5
	HfO_2 + 12 X						93.4
	HfO_2 + 14 X						90.8
	HfO_2 + 16 X						91.5
	HfO_2 + 18 X						90.7
	HfO_2 + 20 X						89.4
[48]	$Hf_{0.7}Y_{0.3}O_{2-\delta}$	Ball milled	100	-	C (air)	1923 K 10h	74.6
			200				80.7
			400				96.3
			500				97.5
			100		SPS	1923 K 3min	96.0
This study	HfO_2 (Hf11D)	SMS	353	50.2	TSS_2	Step 1: 1873 K 30min	**97.2**
	30YSH			45.2		Step 2: 1773 K 4h	94.4
	HfO_2		50	-	SPS	1873 K 7 min	**98.8**
	30YSH						**97.3**

*P - porous agent (vol%); X - mol% Y_2O_3; Thde - thermal decomposition; Comm – commercial powder; C - conventional method; IP - Isostatic pressing; CP - compaction pressure; T_s - Soaking temperature/duration; S_m - sintering method; S - external gelation sol-gel technique; Re-Ox - Reduction-oxidation and * - cracked*

7.17.2 Microstructural and compositional analyses of hafnia monoliths (SPS)

Microstructures of the hafnia consolidated through SPS is presented in Fig. 7.27 and Fig. 7.28. Both Hf0D and Hf82D show dense grains with no visible pores. Thus, it is evident that crucibles obtained through SPS would be ideal for melting applications. Low magnification and high magnification images of fractured pellet surfaces of Hf0D and Hf82D show uniform distribution of grains with faceted morphology. EDS investigation (point scan) revealed that no major impurities were present within the detection limits. The grain size of SPS was found to be in the range 5 – 25 μm while the CS and TSS_2 derived compacts had grain size varying between 5 – 12 μm and 1 – 4 μm respectively.

7.17.3 SPS of nc-YSH powders

XRD analysis of spark plasma sintered pellets revealed that all the compacts except 6YSH comprised only the cubic phase while the latter consisted of both cubic and monoclinic phases. The carbon residue was found to vary between 455 to 613 ppm.

All YSH pellets were sintered at 1873 K at a heating rate of 100 K min^{-1}. Their ρ_S was in the range of 96 to 97 % T.D. Bu et al. [48] had sintered ball milled YSH powders by using both the conventional and SPS techniques. These authors [48] had reported that the ρ_S of $Hf_{0.70}Y_{0.30}O_{2-x}$ monoliths were 97.5 % T.D (1923 K 10 h) and 96 % T.D (1873 K 3 min) respectively. In addition, they had also reported that $Hf_{0.70}Y_{0.30}O_{2-x}$ had undergone better densification when sintered by CS as compared to SPS. However, these authors had employed a CP of 500 MPa and had sintered at 1923 K for 10 h to obtain a ρ_S of 97.5 % T.D. The powder obtained in this study 30YSH had undergone better densification (marginally higher) than those reported by Bu et al. [48] (both in the SPS and conventional method). Tyrpekl et al. [53] had prepared YSH ($Hf_{0.85}Y_{0.15}O_{2-x}$) by employing the external gelation method and the derived beads that were sintered by using SPS at 1873 K for 5 min. The sintered density of these monoliths were found to be 95.3 ± 0.6 % T.D which is lower than the values reported in the present study. Zhao et al. [54] had prepared YSH by milling hafnia powders along with 5 mol% and 8 mol% of yttria. These ball milled powders were sintered in air by using the conventional method and were found to yield final products with ρ_S of 88.5 % T.D and 86.5 % T.D (1873 K 1 h). However, it was observed that these monoliths comprised both the monoclinic and cubic phases and had undergone poor densification. Piluso et al. [34] had published a patent on the preparation and sintering of dense YSH monoliths to be used in nuclear core melting simulation experiment. These authors had varied the yttria content from 0.50 mol% to 8 mol% and had sintered the compacts in air by using CS (1873 K 1 h). The ρ_S of these monoliths were found to vary between 96.6 % T.D (1 mol% Y_2O_3) and 88.8 % T.D (8 mol% Y_2O_3). The ρ_S of YSH monoliths (96.2 % T.D to 97.3 % T.D) reported in this study is the highest among the values reported so far for nc-YSH. Further, a CP as low as 50 MPa and sintering temperature of 1873 K with 7 min holding time was sufficient to sinter it to the above mentioned ρ_S. Thus, from the foregoing it is evident that the YSH powders derived in this study had undergone better densification when the SPS technique was used, rather than the CS and TSS method.

7.17.4 Microstructural and compositional analyses of YSH monoliths

SEM image of spark plasma sintered 30YSH monoliths is presented in Fig. 7.28. The fractured pellet surface shows that these pellets are highly dense with no visible pores. However, at higher magnification dents with size ranging between 0.10 to 0.40 μm were observed within the grains. These dents could have been formed due to the closure of pores. High and low magnification images of fractured pellet surface revealed the presence of uniform distribution of grains with their size ranging between 10 μm and 30 μm. Further, the grains were highly faceted suggesting that the sintering had proceeded up to the final stage. EDS (point scan and elemental mapping) revealed that the mean atom fraction of Hf (in the cation sublattice) was about 0.69 and that Y was distributed uniformly in the YSH matrix.

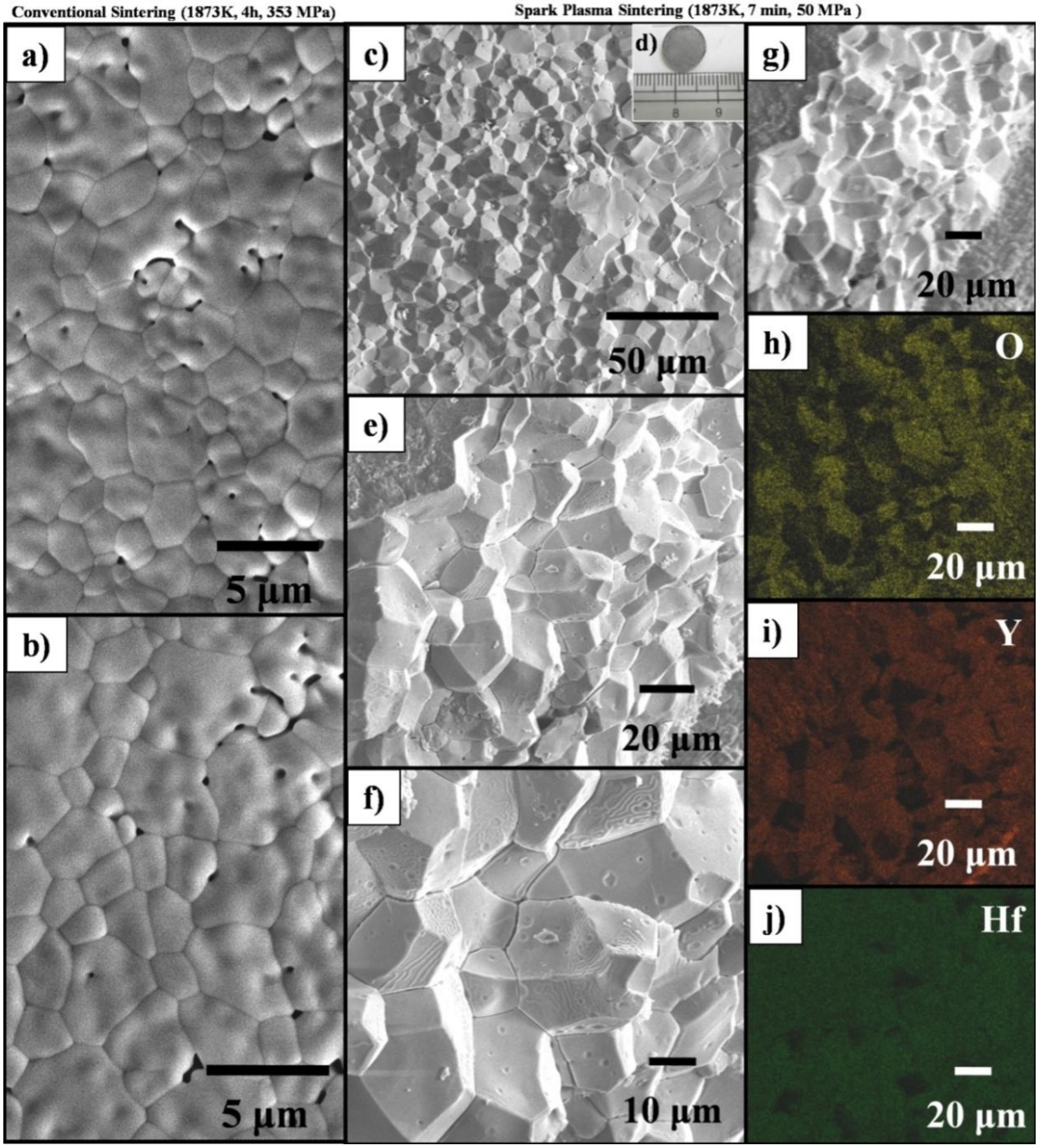

Figure 7.28 SEM images of sintered 30YSH monoliths: (a-b) Conventional sintering (1873 K; 4h; air; 353 MPa) and (c-j) SPS (1873 K; 7 min; 50 MPa) c) low magnification images of fractured pellet surface; (d) image showing "as prepared" pellets covered with graphite layer; (e-f) low magnification image showing well defined grain boundaries and faceted grains; (g) a typical fractured pellet surface showing faceted grains and (h-j) elemental mapping pertaining to image (g) which shows the uniform distribution of respective elements in the YSH matrix

7.18 Conclusions drawn from spark plasma sintering studies

Spark plasma sintering studies of nc-hafnia and nc-YSH powders derived through SMS revealed that a CP as low as 50 MPa and sintering temperature of 1873 K for 7 min is sufficient to obtain dense monoliths of about 99 % T.D (HfO_2 - 98.8 % T.D and YSH - 97.3 % T.D respectively. Both visual and microscopic examinations of sintered monoliths did not reveal any cracks or defects. EDS analysis and area mapping for constituent elements in the sintered monoliths (YSH) confirmed the presence of uniform distribution of yttrium and hafnium. SEM investigations of polished and thermally etched sintered monoliths revealed the presence of uniform distribution of grains with well-defined grain boundaries with their grain sizes varying between 5 - 25 μm (HfO_2) and 10 - 30 μm (YSH). Higher magnification images of fractured surface of YSH monoliths revealed the presence of dents with their size ranging between 0.30 μm to 0.40 μm. Further investigations are required to optimize the sintering parameters to obtain submicron sized grains.

7.19 Compatibility test with molten uranium

Compatibility test was carried out in the sintered crucibles of hafnia (Hf11D; 353 MPa; TSS_2) and YSH (10YSH; 353 MPa; TSS_2) by using the “spot technique” [56-58]. These investigations had revealed that the molten uranium was non-reactive with the crucible surface and the globule of molten uranium could be removed easily (non-wetting) even after repeating the experiments for three times in the same crucible. The fusion temperature of uranium was measured by using two color pyrometer and it was found to be 1403 ± 5 K. Visual examination of both sample and interior of the crucible surface after first two trial experiment did not show any blackening of either crucible or sample surface, however, blackening of sample surface was observed on the third trial.

These crucibles (Hf11D and 10YSH) were subjected to microstructural examination after fracturing and polishing (Fig. 7.29). The microstructure of the inner surface of the crucibles did not reveal adherence of uranium metal or contamination of the crucible surface with uranium. Further, to ascertain this fact, EDS investigation (point scan) was also conducted. All these investigations reaffirmed the absence of the uranium in the interior surface of the crucible. Thus, from the preliminary investigation, it could be concluded that both hafnia and YSH sintered crucibles are compatible with molten uranium. Further experiments are required to reaffirm the utility of these crucibles with more reactive uranium bearing alloys.

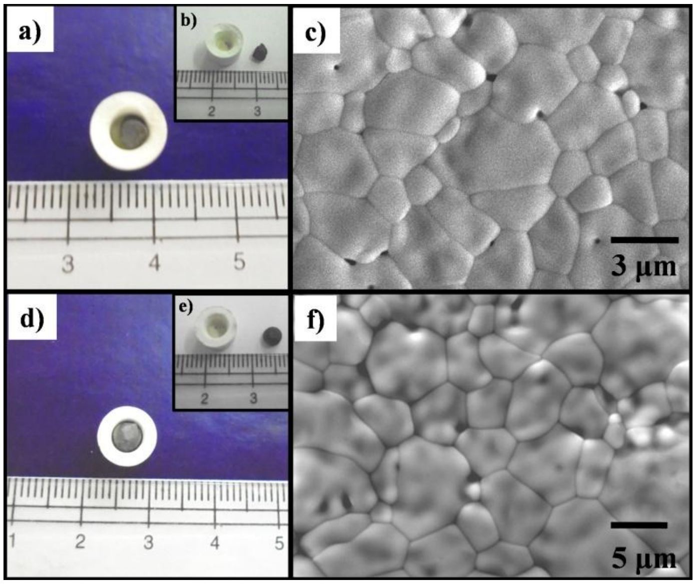

Figure 7.29 (a-c) Hf11D sintered crucible (353 MPa) and (d-f) 10YSH sintered crucible (353 MPa); (a & d) photograph of Hf11D and 10YSH crucibles holding molten uranium respectively; (b & e) photograph showing non-wetting molten uranium separated from Hf11D and 10YSH crucibles respectively; (c-f) SEM images of fractured and polished interior surface Hf11D and 10YSH crucibles (images were taken after compatibility test)

7.20 Conclusions drawn from the compatibility test

Preliminary investigations carried out on the sintered crucibles of hafnia and YSH had revealed that these crucibles could be used for holding uranium bearing alloys. Visual examination of both the sample and interior surface of the crucible did not show the presence of uranium. Further, these crucibles were non-wetting and could be reused. Microstructural investigations also revealed the absence of uranium in the interior surface of the crucible.

References

[1] X. Liu, N. Fechler, M. Antonietti, Chem Soc Rev 42(21) (2013) 8237-8265.

[2] T. Ouyang, K. Cheng, Y. Gao, S. Kong, K. Ye, G. Wang, D. Cao, J. Mater. Chem. A 4(25) (2016) 9832-9843.

[3] H. Flood, T. Forland, Acta Chem. Scand. 1 (1947) 592-604.

[4] D.H. Kerridge, Pure Appl Chem (1975) 355-371.

[5] B. Durand, J.P. Deloume, M. Vrinat, Mat. Sci. Forum (152-153) (1994) 327-330.

[6] A. Benamira, J.-P. Deloume, B. Durand, J. Mater. Chem. 9(10) (1999) 2659-2662.

[7] R.I. Olivares, Sol. Energy 86(9) (2012) 2576-2583.

[8] C.M. Kramer, Z.A. Munir, J.V. Volponi, Thermochim. Acta 55(1) (1982) 11-17.

[9] K.H. Stern, High Temperature Properties and Thermal Decomposition of Inorganic Salts with Oxyanions, CRC Press, Boca Raton, 2000.

[10] Y. Du, D. Inman, J. Mater. Chem. 6(7) (1996) 1239-1240.

[11] Y. Du, P. Rogers, D. Inman, J. Mater. Sci. 31(13) (1996) 3361-3364.

[12] A.G. Fernández, H. Galleguillos, E. Fuentealba, F.J. Pérez, J. Therm. Anal. Calorim. 122(1) (2015) 3-9.

[13] D.J. Rogers, G.J. Janz, J. Chem. Eng. Data 27(4) (1982) 424-428.

[14] J. Wang, H.P. Li, R. Stevens, J. Mater. Sci. 27(20) (1992) 5397-5430.

[15] P. Piluso, M. Ferrier, C. Chaput, J. Claus, J.-P. Bonnet, J. Eur. Ceram. Soc. 29(5) (2009) 961-968.

[16] L. Gao, L. Zhou, J. Feng, L. Bai, C. Li, Z. Liu, J.-L. Soubeyroux, Y. Lu, Ceram. Int. 38(3) (2012) 2305-2311.

[17] V. Mote, Y. Purushotham, B. Dole, J. Theor. Appl. Phys. 6(1) (2012) 6.

[18] K. Ananthasivan, S. Balakrishnan, S. Anthonysamy, R. Divakar, E. Mohandas, V. Ganesan, J. Nucl. Mater. 434(1) (2013) 223-229.

[19] W. Rui, Z. Bo, L. Qian, J. ZhenYi, W. WenBo, M. WenYan, Z. XiaoDong, J. Phys. D: Appl. Phys. 45(12) (2012) 125304.

[20] X. Zhao, D. Vanderbilt, Phys. Rev. B 65(23) (2002) 233106.

[21] C.W. Li, M.M. McKerns, B. Fultz, Phys. Rev. B 80(5) (2009) 054304.

[22] P.E. Quintard, P. Barbéris, A.P. Mirgorodsky, T. Merle-Méjean, J. Am. Ceram. Soc. 85(7) (2002) 1745-1749.

[23] I. Villa, A. Vedda, M. Fasoli, R. Lorenzi, N. Kränzlin, F. Rechberger, G. Ilari, D. Primc, B. Hattendorf, F.J. Heiligtag, M. Niederberger, A. Lauria, Chem. Mater. (2016) 3245–3253.

[24] C. Li, Y. Yao, X. Shen, Y. Wang, J. Li, C. Gu, R. Yu, Q. Liu, M. Liu, Nano Res. 8(11) (2015) 3571-3579.

[25] H. Nienhaus, V. Kravets, S. Koutouzov, C. Meier, A. Lorke, H. Wiggers, M.K. Kennedy, F.E. Kruis, J. Vac. Sci. Techno. B 24(3) (2006) 1156-1161.

[26] P. Rauwel, E. Rauwel, Probing the electronic structure of HfO_2 polymorphs via electron energy loss spectroscopy, in: A. Méndez-Vilas (Ed.), Microscopy: Advances in Scientific Research and Education: Series 62, Formatex Research Center, Spain (2014) 875-886.

[27] M.P. Agustin, L.R.C. Fonseca, J.C. Hooker, S. Stemmer, Appl. Phys. Lett. 87(12) (2005) 121909.

[28] T. Mizoguchi, M. Saitoh, Y. Ikuhara, J. Phys.: Condens. Matter 21(10) (2009) 104212.

[29] P. Rauwel, E. Rauwel, C. Persson, M.F. Sunding, A. Galeckas, J. Appl. Phys. 112(10) (2012) 104107.

[30] J.R. Groza, Nanostruct. Mater. 12(5) (1999) 987-992.

[31] A. Mukhopadhyay, B. Basu, Int. Mater. Rev. 52(5) (2007) 257-288.

[32] R. Chaim, M. Levin, A. Shlayer, C. Estournes, Adv. Appl. Ceram. 107(3) (2008) 159-169.

[33] ASTM C1076-09 (2015), Standard Specification for Nuclear Grade Hafnium Oxide Pellets, ASTM International, West Conshohocken, PA 2015.

[34] P. Piluso, M. Ferrier, J.P. Bonnet, Patents US 2009/0305027 A1, 2009.

[35] M.N. Rahaman, Sintering of Ceramics, CRC Press, Boca Raton, Florida, 2008.

[36] R. Castro, K. van Benthem, Sintering: Mechanisms of Convention Nanodensification and Field Assisted Processes, Springer Berlin Heidelberg, 2012.

[37] W. Zhou, S.V. Ushakov, A. Navrotsky, J. Mater. Res. 27(7) (2012) 1022-1028.

[38] G. Niu, H.-D. Kim, R. Roelofs, E. Perez, M.A. Schubert, P. Zaumseil, I. Costina, C. Wenger, Sci. Rep. 6 (2016) 28155.

[39] D.L. Porter, A.H. Heuer, , J. Am. Ceram. Soc. 62(5-6) (1979) 298-305.

[40] B.R. Rehani, P.B. Joshi, K.N. Lad, A. Pratap, Indian J. Pure Appl. Phys. 44 (2006) 157-161.

[41] D.-J. Kim, Lattice Parameters, J. Am. Ceram. Soc. 72(8) (1989) 1415-1421.

[42] J. Bu, P.G. Jönsson, Z. Zhao, Ceram. Int. 41(2015) 2611-2615.

[43] J.D. Schieltz, J.W. Patterson, D.R. Wilder, J. Electrochem. Soc. 118(8) (1971) 1257-1261.

[44] H. Fujimori, M. Yashima, S. Sasaki, M. Kakihana, T. Mori, M. Tanaka, M. Yoshimura, Chem. Phys. Lett. 346(3–4) (2001) 217-223.

[45] A.M. Gavrish, B.Y. Sukharevskii, E.I. Zoz, A.E. Solovieva, Inorg. Mater. 9 (1973) 232-235.

[46] D. Segal, J. Mater. Chem. 7(8) (1997) 1297-1305.

[47] J. Ma, L.C. Lim, J. Eur. Ceram. Soc. 22(13) (2002) 2197-2208.

[48] J. Bu, P.G. Jönsson, Z. Zhao, Ceram. Int. 41(2) (2015) 2611-2615.

[49] H.E. Exner, E.A. Giess, J. Mater. Res. 3(1) (2011) 122-125.

[50] D.A. Pejaković, J. Lumin. 130(6) (2010) 1048-1054.

[51] B. Matovic, J. Pantic, J. Lukovic, M. Cebela, S. Dmitrovic, M. Mirkovic, M. Prekajski, Ceram. Int. 42(1) (2016) 615-620.

[52] A. Lakhlifi, M. Taha, P. Satre, Y. Jorand, G. Fantozzi, M. Roubin, Ceram. Int. 23(4) (1997) 349-359.

[53] V. Tyrpekl, M. Holzhäuser, H. Hein, J.-F. Vigier, J. Somers, P. Svora, J. Nucl. Mater. 454(1–3) (2014) 398-404.

[54] J. Zhao, Y. Zhang, H. Gong, Y. Zhang, X. Wang, X. Guo, Y. Zhao, Ceram. Int. 41(4) (2015) 5232-5238.

[55] J.D. Schieltz, J.W. Patterson, D.R. Wilder, J. Electrochem. Soc. 118(8) (1971) 1257-1261.

[56] K. Ananthasivan, Development of Methods and Materials for the Determination of Solid to Liquid Phase Transformation Temperatures in Alloys, PhD Thesis, University of Madras, 2002.

[57] S. Balakrishnan, K. Ananthasivan, K.C. Hari Kumar, J. Alloys Compd. 689 (2016) 751-758.

[58] K. Ananthasivan, S. Balakrishnan, I. Kaliappan, S. Anthonysamy, R. Pankajavalli, P.R.V. Rao, J. Alloys Compd. 468(1) (2009) 275-279.

Chapter 8

Conclusions

8.1 Synthesis, Characterization and Sintering of Nanocrystalline Urania

Nc-urania powders were synthesized by using citrate gel-combustion in bulk quantities for the first time. The systematic dependence of the reaction as well as the properties of these nanocrystalline powders on the composition of the combustion mixture (R) was investigated. The course of the combustion reaction is these mixtures were measured with the help of DSC for the first time. These results showed that the rate of this reaction is strongly influenced by the composition of the combustion mixture (R). Mixtures with an R value of 0.25 showed a markedly different behavior compared to the rest and underwent “volume combustion”.

Upon storage the oxygen stoichiometry of the UO_2 powders was found to change with time, plausibly due to the facile oxidation of these nc powders. All the powders possessed a flaky morphology and comprised agglomerates of nanocrystallites of α-U_3O_8 or UO_2. The morphology and microstructure of the powders derived from the mixture with the R value of 0.25 were very different from the rest. HRTEM investigations reaffirmed the nanocrystallinity and revealed the presence of faceted nano crystallites and nano pores. The EELS study confirmed the covalency as expected.

It was observed that the ρ_B, XCS, size distribution of pores and particles, morphology of the powders and their microstructure showed a strong dependence on the value of R. The variation in the bulk density with R and its correlation with the size distribution of particles were investigated. For the first time an attempt was made to de-convolute the particle size distribution data. The contributions from the different size fractions were found to correlate well with the ρ_B.

The variation in lattice strain in nc-UO_2 derived through citrate gel-combustion and its dependence on size is being reported for the first time. Two distinct regimes viz., nc regime and the microcrystalline regime could be delineated by analyzing the variation in the lattice strain with the XCS. Further analytical models are required, in order to understand the relation between the lattice strain and the distribution of sizes. It appears that the combustion mixtures with R values ranging from 0.25 to 0.50 would yield powders that are most suitable further processing.

Elucidation of a reaction mechanism for the combustion synthesis of uranium oxide was carried out for the first time. The sample gels were analyzed by using TG-DTA-MS and DSC. Three exothermic peaks were observed in both the DTA and DSC analyses. The proposed reaction mechanism was supported by the mass spectrometric analysis of the evolved gases. The E_a estimated for the first two thermal events were 152 ± 6 and 179 ± 8 kJ mol^{-1} respectively. The E_a for the third thermal event (crystallization of U_3O_8) was found to be 166 ± 7 kJ mol^{-1}. In this study gels with a fuel to oxidant ratio of 0.25 were investigated. However, the reaction mechanisms and the activation energies will depend on the fuel (citric acid) to oxidant (nitrate) ratio of the gels. Further investigations are required to study the systematic variation of citrate gel-combustion of urania with different fuel to nitrate ratio (R).

Systematic investigation on sintering of nc-UO_2 powders derived through citrate gel-combustion method was carried out for the first time. Sintering was carried out by using three different methods, viz., i) conventional method, ii) low temperature two-step sintering ($LTTSS_1$) and iii) low temperature two-step sintering ($LTTSS_2$). Among these two-step sintering $LTTSS_2$ was found most suitable. Powders derived from starting mixtures with an R value of 0.10 and 0.25 were found to be highly sinterable and yielded a maximum sintered density of ≈ 98 % T.D with uniform grains. Through optimization trials, 180 MPa and $LTTSS_2$ were found to be the ideal conditions to obtain high density UO_2 pellets. Shrinkage anisotropy factor (α) of sintered UO_2 monoliths were investigated for the first time. Relative size fraction of open and closed pore fraction of sintered UO_2 monoliths were also investigated. The method employed in this study has led to a new fabrication procedure which would be energy and cost efficient for obtaining UO_2 pellets with a uniform grain size of about 1-10 μm.

8.2 Preparation of UO_2 foam and porous UO_2 pellets

UO_2 foam was successfully prepared for the first time by using a sucrose-gel precursor. This comprised both meso and macro pores and possessed good handling strength. However, the presence of large amounts of carbon residue would limit their utility for the intended application, viz., DOR, owing to the electronic conductivity brought about by carbon. Typically 30 to 40% porosity would be ideal for the DOR process. However, the densities of these foams are far lower than the optimum value suitable for the end use.

A fuel to oxidant ratio (R) of 0.25, a CP of 180 MPa and a TSS_3 with a maximum temperature of 1473 K were found to be the optimum conditions for obtaining a product with a desirable density of about 60 to 70 % T. D.

8.3 Synthesis, Characterization and Sintering of Nanocrystalline Thoria

Nc-ThO_2 powders were prepared by using citrate gel-combustion method in bulk quantities by varying the fuel to nitrate mole ratio (R = 0 to 0.50). The systematic dependence of the properties of nc-ThO_2 powders on R was investigated. It was observed that the ρ_B, SSA, PSD, XCS and lattice strain showed a systematic dependence on the R value. The combustion reaction in the mixture with an R value of 0.50 was investigated with DTA, DSC and mass spectrometry. Direct evidence for the consumption of oxygen during combustion is being reported for the first time. It was observed that the mixture with R values 0.13 and 0.17 exhibited vigorous and moderate volume combustion respectively. Microstructural investigations revealed that the volume combustion derived thoria powders were porous and comprised aggregates of nanograins. TEM investigation reaffirmed their nanocrystallinity. For the first time, EELS investigation was carried out on the nc-ThO_2 powders and the branching ratio (B) was calculated for both the "as prepared" and "calcined" powders. No evidence could be obtained for the existence of thorium in multiple oxidation states. TEM investigations also revealed that the nc-ThO_2 comprised unimodal grain size distribution with their size ranging between 6 - 16 nm with maxima at 10 nm.

It was observed that the volume combustion derived nc-ThO_2 powders were highly sinterable. A compaction pressure of 243 MPa and TSS with a final sintering temperature of 1773 K were found suitable to sinter the compacts prepared from T_C13C powders to a ρ_S of 98.8 ± 0.3 % T.D. Microstructural analysis of polished and thermally etched sintered thoria monoliths revealed that they comprised uniform faceted grains with well-defined grain boundaries. For the first time, sintering anisotropy factor (α) was estimated and it revealed that the ThO_2 compacts had undergone near isotropic shrinkage during sintering. This work describes a cost and energy efficient method for the production of high density pellets and small crucibles from nc-ThO_2.

8.4 Synthesis, Conventional Sintering and SPS of Nanocrystalline Yttria

It was demonstrated for the first time that VCR takes place in mixtures containing yttrium nitrate with citric acid with an R value of 0.17. The powders derived through VCR were found to be nanocrystalline, fine grained and highly porous.

All the powders comprised nc aggregates. It was demonstrated that the ρ_B, SSA, PSD, XCS and the morphology of these powders were unique as compared to the powders derived through other methods reported in the literature [1-13]. Microstructural analysis of the "A" powders carried out by using TEM confirmed the presence of nc c-Y_2O_3. Both TEM and SEM investigations revealed that these powders possessed nano pores.

The calcined products were found to be highly sinterable. It was demonstrated that Y_2O_3 pellets with a density as high as 98.9 ± 0.1 % T. D. could be produced by using the "two-step sintering" method (TSS^{Y}_{1}) at a final temperature as low as 1673 K. Shrinkage anisotropy factor (α) and relative pore fraction of sintered Y_2O_3 were linearly correlated with the compaction pressure. Similarly, it was observed that citrate gel-combustion derived nc-Y_2O_3 could be sintered to a density of 99.3± 0.2 % T. D by using SPS (1873 K 7 min; 50 MPa and grain size: 6-12 μm).

8.5 Salient features of the results obtained from citrate gel-combustion synthesis of nc-urania, nc-thoria and nc-yttria

Nc-urania nc-thoria and nc-yttria powders were synthesized by using citrate gel-combustion in bulk quantities (about 30 - 60 g) for the first time. The systematic dependence of the reaction as well as the properties of these nc powders on the composition of the combustion mixture (R) was investigated. Thermal analysis of citrate gels containing thorium nitrate or uranyl nitrate were carried out with the help of DSC for the first time (nc-urania and nc-thoria). These results showed that the rate of this reaction is strongly influenced by the composition of the combustion mixture (R). It was demonstrated for the first time that "volume combustion reaction" takes place in citrate gels containing thorium nitrate, yttrium nitrate and uranyl nitrate with citric acid at an R value of 0.125, 0.17 and 0.25 respectively.

It was observed that the ρ_B, XCS, size distribution of pores and particles, morphology of the powders and their microstructure showed a strong dependence on the value of R. The morphology and microstructure of the powders through volume combustion were very different from the rest. HRTEM investigations reaffirmed the nanocrystallinity of the final products and revealed the presence of faceted nano crystallites and nano pores in them. The variation in the ρ_B with R and its correlation with the size distribution of particles were investigated. For the first time an attempt was made to de-convolute the particle size distribution data. It was observed that the number of modes in size distribution of particles had a correlation with the ρ_B value. The ρ_B of the powders with tetra modal and trimodal distributions was higher than that of the bimodal powders. Variation in the lattice strain in these nc-powders and their correlation with the XCS is being reported for the first time. Two regimes could be delineated (nc-urania) viz., nc regime and microcrystalline regime wherein the former exhibited a higher lattice strain even after annealing at higher temperature while the latter exhibited the conventional microcrystalline powder property.

Systematic investigation on sintering of nc powders derived through citrate gel-combustion method was carried out by using three different methods, viz., i) conventional method - CS, ii) two-step sintering - TSS_1 and iii) TSS_2. For the first time, shrinkage anisotropy factor (α) pertaining to the sintering of compacts made out of nc UO_2, ThO_2 and Y_2O_3 was estimated. It was established that these compacts had undergone near isotropic shrinkage. The method employed in this study has led to a new fabrication procedure which would be energy and cost efficient for obtaining highly sintered pellets (UO_2, ThO_2 and Y_2O_3) with uniform grain size.

8.6 Salt melt synthesis and sintering of nc-HfO_2 and nc-YSH

A procedure based on the salt melt synthesis that employed molten mixtures of KNO_3 and $NaNO_3$ along with different amounts of $NaNO_2$ was optimized to obtain nc m-HfO_2, c-HfO_2 and YSH powders in bulk, with fine grain size and uni-modal size distribution of particles. It was also demonstrated that either the metastable cubic form or the thermodynamically stable monoclinic form could be derived at room temperature by tailoring the composition of the melt. It was also observed that the yttrium content (for YSH preparation) and nitrite content (for HfO_2 preparation) significantly influence the powder characteristics. The SSA and lattice strain of nc-HfO_2 decreased with the nitrite content while the XCS showed a reverse trend. Microstructural analysis of m-HfO_2 and c-HfO_2 powders by using TEM reaffirmed their nanocrystallinity as well as their crystallite size estimated from XRD (20−40 nm). Further, XRD, TEM and Raman spectra ascertained that the starting mixtures with Φ values of 0−0.32 and 0.82 yielded m-HfO_2 and c-HfO_2 respectively. Comparison of the Raman spectra pertaining to both microcrystalline and nc samples (HfO_2) revealed that the latter exhibited broader peaks due to quantum confinement. EELS of m-HfO_2 ($\Phi = 0$) and c-HfO_2 ($\Phi = 0.82$) were consistent with the observations reported in earlier investigations [14-17]. Direct evidence in support of the presence of Hf in an oxidation state lower than 4+ could not be obtained.

In the nc-YSH derived through SMS, SSA, XCS, lattice strain and lattice parameter increased with the yttrium content while the BD showed a reverse trend. TEM investigations reaffirmed the presence of nanograins with unimodal size distribution and SAED further ascertained the presence of fluorite solid solution.

All nc HfO_2 and YSH powders exhibited monotonic increase in ρ_G with the CP. A CP of 353 MPa was required to compact and sinter hafnia to a ρ_S of about ≈ 97-98 % T.D by using TSS_2 method. Point scan and area mapping for constituent elements in the YSH powders and sintered monoliths confirmed the presence of uniform distribution of yttrium and hafnium. Morphological analysis of polished and thermally etched sintered monoliths of HfO_2 and YSH revealed the presence of uniform grains with well-defined grain boundaries. The dihedral angle in sintered hafnia YSH monoliths was found to be varying between 121-127^0 and 109-130^0. Shrinkage anisotropic factor revealed that the both hafnia and YSH compacts had undergone near isotropic shrinkage.

Small crucibles could be made out of both 10YSH and 30YSH by die casting and could be sintered to high densities and were devoid of cracks and physical defects. Selected powders of HfO_2 and YSH were used in the fabrication of cups and the compatibility of these cups with molten U at 1405 K was tested. These investigations revealed that these could be used for U metal melting since the cups were compatible with molten U at 1420 K.

8.7 Spark Plasma Sintering of nc-HfO_2 and nc-YSH

SPS of nc-HfO_2 (SMS) and nc-YSH (SMS) was carried out for the first time to prepare dense pellets. Nc- HfO_2 and nc-YSH revealed a maximum sintered density of 98.8% and 97.3% T.D. respectively. SEM investigation revealed that the grain sizes were varying from 9 - 25 μm (both HfO_2 and YSH). However, further optimization of experimental parameters is required in order to obtain nanograined monoliths (HfO_2 and YSH) by using SPS.

8.8 Scope for future work

These investigations suggest that the following studies could be taken up in future:

- Further experiments need to be carried out with the porous pellets prepared by the method reported here. This warrants further optimization trails for the preparation of porous ThO_2 and UO_2 pellets.
- The kinetics of gel-combustion reaction of Th^{4+} containing gels had not been investigated so far. This needs to be taken up.

- In order tot understand the coarsening and densification in nc powders vis-à-vis their microcrystalline counterparts, further dilatometry experiments need to be taken up on the sintering of nc powders.
- Only preliminary trails have been carried out on the SPS of nc-HfO2 and nc-YSH. Even though substantial reduction in grain growth has been achieved, nanograined (< 100 nm) monoliths could not be prepared. Further optimization trails need to be undertaken, in order to accomplish the same.
- Effect of nitrite to nitrate mole ratio and the influence of yttrium content on the stability of nanocrystalline YSH structures could be investigated.
- The effect and the influence of salt mixtures containing chlorides, nitrate and/or nitrite of lithium, sodium and/or potassium on the formation of nanocrystalline metastable hafnia and YSH powders could be investigated.
- Experiments pertaining to the utility of sintered hafnia and YSH crucibles with more reactive uranium bearing alloys could be taken up.
- Mechanical properties of sintered compacts viz., ductility, hardness, impact resistance, and fracture toughness could be compared with their respective microstructures.
- Further, the mechanical properties of sintered monoliths derived by using different processing techniques could also be compared.

References

[1] M.D. Rasmussen, G.W. Jordan, M. Akinc, O. Hunter, M.F. Berard, Ceram. Int., 9 (1983) 59-60.

[2] A. Dupont, A. Largeteau, C. Parent, B. Le Garrec, J.M. Heintz, J. Eur. Ceram. Soc. 25 (2005) 2097-2103.

[3] S. Balakrishnan, K. Ananthasivan, K.C. Hari Kumar, Ceram. Int. 41 (2015) 5270-5280.

[4] S.V. Chavan, K.T. Pillai, A.K. Tyagi, Mater. Sci. Eng. B 132(3) (2006) 266-271.

[5] H.R. Khosroshahi, H. Ikeda, K. Yamada, N. Saito, K. Kaneko, K. Hayashi, K. Nakashima, J. Am. Ceram. Soc. 95 (2012) 3263-3269.

[6] W.-J. Kim, J. Y. Park, S. J. Oh, Y.S. Kim, G.-W. Hong, I.-H. Kuk, J. Mater. Sci. Lett. 18 (1999) 411-413.

[7] N. Saito, S.-i. Matsuda, T. Ikegami, J. Am. Ceram. Soc. 81 (1998) 2023-2028.

[8] A.L. Micheli, D.F. Dungan, J.V. Mantese, J. Am. Ceram. Soc. 75 (1992) 709-711.

[9] R.V. Mangalaraja, S. Ananthakumar, J. Mouzon, M. Lopez, C.P. Camurri, M. Oden, J. Ceram. Soc. Jpn. 117 (2009) 1258-1262.

[10] A.S. Kumar, A.R. Durai, T. Sornakumar, Mater. Lett. 58 (2004) 1808-1810.

[11] J. Mouzon, M. Odén, Powder Technol. 177 (2007) 77-82.

[12] K. Richardson, M. Akinc, Ceram. Int. 14 (1988) 101-108.

[13] H. Gong, D.-Y. Tang, H. Huang, T.-S. Zhang, J. Ma, Mater. Chem. Phys. 112 (2008) 423-426.

[14] I. Villa, A. Vedda, M. Fasoli, R. Lorenzi, N. Kränzlin, F. Rechberger, G. Ilari, D. Primc, B. Hattendorf, F.J. Heiligtag, M. Niederberger, A. Lauria, Chem. Mater. (2016) 3245–3253.

[15] C.W. Li, M.M. McKerns, B. Fultz, Phys. Rev. B 80 (5) (2009) 054304.

[16] W. Rui, Z. Bo, L. Qian, J. ZhenYi, W. WenBo, M. WenYan, Z. XiaoDong, J. Phys. D: Appl. Phys. 45 (2012) 125304.

[17] P.E. Quintard, P. Barbéris, A.P. Mirgorodsky, T. Merle-Méjean, J. Am. Ceram. Soc. 85 (2002) 1745-1749.